

Sediment dynamics on intertidal mudflats

A study based on in situ measurements and numerical modelling

Zhu, Qin

DOI

[10.4233/uuid:5f094e4b-fef9-4216-abbe-3277adc90b28](https://doi.org/10.4233/uuid:5f094e4b-fef9-4216-abbe-3277adc90b28)

Publication date

2017

Document Version

Final published version

Citation (APA)

Zhu, Q. (2017). *Sediment dynamics on intertidal mudflats: A study based on in situ measurements and numerical modelling*. [Dissertation (TU Delft), Delft University of Technology].
<https://doi.org/10.4233/uuid:5f094e4b-fef9-4216-abbe-3277adc90b28>

Important note

To cite this publication, please use the final published version (if applicable).
Please check the document version above.

Copyright

Other than for strictly personal use, it is not permitted to download, forward or distribute the text or part of it, without the consent of the author(s) and/or copyright holder(s), unless the work is under an open content license such as Creative Commons.

Takedown policy

Please contact us and provide details if you believe this document breaches copyrights.
We will remove access to the work immediately and investigate your claim.

Sediment dynamics on intertidal mudflats

A study based on *in situ* measurements and numerical modelling

基于现场观测和数值模拟的淤泥质潮滩沉积动力过程研究

Sediment dynamics on intertidal mudflats

A study based on *in situ* measurements and numerical modelling

Proefschrift

Ter verkrijging van de graad van doctor
aan de Technische Universiteit Delft,
op gezag van de Rector Magnificus prof. ir. K.C.A.M. Luyben,
voorzitter van het College voor Promoties,

en

East China Normal University,
op gezag van de Rector Magnificus prof. Q. Chen,
in het openbaar te verdedigen
op woensdag 22 maart 2017 om 12.30 uur

door

Qin ZHU

Bachelor of science in de fysica
geboren te Shanghai, China.

Dit proefschrift is goedgekeurd door de

promotors: Prof. dr. S.L. Yang
Prof. dr. ir. Z.B. Wang
copromotor: Dr. ir. B.C. van Prooijen

Samenstelling promotiecommissie:

Rector Magnificus	voorzitter
Prof. dr. S.L. Yang	East China Normal University, promotor
Prof. dr. ir. Z.B. Wang	Technische Universiteit Delft, promotor
Dr. ir. B.C. van Prooijen	Technische Universiteit Delft, copromotor

Onafhankelijke leden:

Prof. dr. ir. M.J.F. Stive	Technische Universiteit Delft
Prof. dr. ir. J.C. Winterwerp	Technische Universiteit Delft
Prof. dr. P.X. Ding	East China Normal University
Prof. dr. T.J. Andersen	Københavns Universitet

The doctoral research has been carried out in the context of an agreement on joint doctoral supervision between East China Normal University, China and Delft University of Technology, the Netherlands.



Front cover: Sheet erosion on Southeastern Chongming mudflat

Back Cover: Kapellebank mudflat

Copyright © 2017 by Qin Zhu (Email: zhuqin0612@msn.cn).

Printed by: Proefschriftmaken.nl

ISBN: 978-94-6295-607-0

All rights reserved. No part of the material protected by this copyright notice may be reproduced or utilized in any form or by any mean, electronic or machanical, including photocopying, recording or by any information storage and retrieval system, without the prior permission of the author.

Abstract

The accumulation of fine-grained sediments forms broad and mildly sloped tidal flats in intertidal zones. Tidal flats are widely distributed in coastal areas, especially in areas that are characterized by large tidal ranges, abundant resources of fine-grained sediments, seabeds with small slopes, and weak wave forces. Tidal flats are important sedimentary coastal environments, and tidal flat processes are closely related to the patterns of human activity and economic development. Progradational tidal flats provide space for both the expansion of salt marshes and human activity. For example, the land area of Chongming Island in the Yangtze Estuary has increased by 120% via the reclamation of salt marshes. In addition, tidal flats serve as flood defence systems by dissipating waves to protect large populations along coastline areas. However, tidal flats have been subjected to pressures by a drastic decrease in sediment supplies with sea level rise due to climate change and human impacts (e.g., damming in the river basin). **Knowledge of sediment dynamics is fundamental to developing a better understanding of mechanisms of erosion and deposition.** These are crucial for predicting future evolutionary patterns the protection and re-construction of tidal flats.

In situ measurements serve as an important and useful approach to studying the sediment dynamics of tidal flats. Most studies on sediment dynamics in intertidal zones have focused either on intra-tidal and neap–spring variations in current velocity and suspended sediment concentrations (SSCs) based on instrument records collected during tidal submersion or on bed-level changes based on surveys undertaken when the tidal flats are emerged. However, the way in which **intra-tidal** bed-level changes are associated with hydrodynamic and sedimentary processes is key to understanding the mechanisms of tidal flat erosion and deposition. Furthermore, tidal flats are shallow environments subjected to both wave and current forces. It is thus critical to study sediment dynamics on intertidal flats based on integrated measurements of *in situ* waves, tidal currents, SSC and bed-level changes. Additional to *in situ* measurements, numerical models will be essential to integrate the knowledge and make predictions for the development of

intertidal areas.

The overall objective of this study is to understand the sedimentary processes and bed-level changes under combined wave–current action forces on intertidal flats. Therefore, we use an integrated approach with *in situ* measurements of waves, tidal currents, SSC and bed-level changes at high temporal and spatial resolutions using advanced instruments under different wind conditions in combination with numerical modelling. First, we identify and quantify erosion and deposition stages by comparing and linking the total bed shear stress under combined wave–current action (τ_{cw}) with the critical bed shear stress for erosion (τ_e), which is derived from measured soil mechanical characteristics of bed sediment. Second, we simulate intra-tidal bed-level changes by calculating the erosion and deposition rates, using the data as obtained from the field campaigns. A combination of measurements and simulations is used to further our understanding of erosion-deposition mechanisms and improve the given model. **The main research question** is to find a sound relation between the bed-level changes and sediment transport under combined wave–current action. **The key techniques** applied to address this question are: operating instruments measuring *in situ* waves, tidal currents, SSC levels, and bed-level changes; quantifying τ_{cw} and τ_e ; and choosing appropriate erosion and deposition rate modelling strategies.

In this study, we examine three intertidal flats of different exposure levels: the **Nanhui Foreland mudflat**, which faces an open sea area with a fetch of at least 100 km and which forms an absolute open flat; the **Southeastern Chongming mudflat**, which is a moderate open flat with offshore shoals of several kilometres between the flat area and sea; and the **Kappellebank mudflat**, which is a weakly open (sheltered) flat located at the outer bend of a channel in the Westerschelde Estuary. On the three intertidal flats, we carried out integrated observations of water depths, wave parameters, current profiles, turbulent velocities, SSC levels at specific heights, SSC profiles, and bed-level changes using wave-loggers, ADVs (Acoustic Doppler Velocity meters), ADCPs (Acoustic Doppler Current Profilers), OBSs (Optic Backscatter Sensors), and ASM (Argus Surface Meter). During the observation periods, we collected suspended sediment samples, surface bed sediment samples, and mini-core samples; we carried out instrument data calibrations and measurements of grain size distributions, water content, and diatom biomass. By applying widely used calculation models, we calculated the total bed shear stress levels under combined wave–current action τ_{cw} (via Grant-Madsen, van Rijn, and Soulsby wave–current interaction models), critical shear stress for erosion τ_e , erosion rates E , settling velocities ω_s , deposition rates D , and sediment transport rates Q_s . The measured and calculated parameters were used to demonstrate variations in hydrodynamic forces at intra-tidal, spring–neap, and storm scales; temporal and spatial variations in SSC; and bed stability distributions and hydrodynamics and their mechanical interpretations. The findings were further used to formulate the bed-level change (BLC) model.

1. Dynamic variations on intertidal flats

The measurements on the mudflats resulted in large data sets (1680 hours) for various parameters at the three locations. The results can be summarized as follows.

Nanhui Foreland mudflat: wind speed was 1.7–19.7 m/s and averaged 5.9 m/s during the observation period. Tidal range varied from 1.4–5.0 m and averaged 3.7 m. Near-bed current velocity was from 0.001–0.51 m/s and averaged 0.17 m/s. Significant wave height (H_s) ranged from 0.01–3.92 m and averaged 0.32 m. τ_c ranged from 0.0005–3.58 Pa and averaged 0.56 Pa; τ_w ranged from 0–1.62 Pa and averaged 0.15 Pa; and τ_{cw} ranged from 0.02–4.79 Pa and averaged 0.72 Pa. τ_{cw} was dominated by tidal currents during much of the tidal submersion period and was dominated by waves when the water depths were less than 1 m. τ_{cw} followed a V-shaped time series, whereby the τ_{cw} values were high during flood and ebb peaks and low during high water periods. The average τ_{cw} value during spring tides was 0.65 Pa, which was greater than that observed in neap tides (0.35 Pa). During storm periods, τ_{cw} significantly increased to 2.13 Pa.

Southeastern Chongming mudflat: wind speed was 0.4–10.8 m/s and averaged 6.0 m/s during the observation period. Tidal range varied from 0.9–4.7 m and averaged 2.7 m. Near-bed current velocity ranged from 0.004–0.51 m/s and averaged 0.18 m/s. H_s ranged from 0.07–0.46 m and averaged 0.21 m. τ_c ranged from 0.01–2.43 Pa and averaged 0.52 Pa; τ_w ranged from 0.01–1.68 Pa and averaged 0.22 Pa; and τ_{cw} ranged from 0.04–2.47 Pa and averaged 0.66 Pa. The average τ_{cw} during strong wind and normal weather periods (average wind speeds of 6.8 m/s and 2.6 m/s, respectively) were 1.07 Pa and 0.35 Pa, respectively.

Kapellebank mudflat: wind speed was 0–18.0 m/s and averaged 5.6 m/s during the observation period. Tidal range varied from 3.2–5.3 m and averaged 4.5 m. Near-bed current velocity ranged from 0.001–0.47 m/s and averaged 0.20 m/s. H_s ranged from 0.005–0.43 m and averaged 0.06 m. τ_c ranged from 0.0004–2.27 Pa and averaged 0.14 Pa; τ_w ranged from 0–1.26 Pa and averaged 0.08 Pa; and τ_{cw} ranged from 0.002–2.55 Pa and averaged 0.18 Pa. τ_{cw} values before, during and after storm periods were 1.32 Pa, 2.10 Pa, and 0.57 Pa, respectively.

2. Critical shear stress for erosion τ_e on intertidal flats and its comparison with τ_{cw}

Nanhui Foreland mudflat: the median grain size (d_{50}) of surface sediment on the middle flat was 34 μm ; the water content of the surface 2 mm and 10 mm layers was 72% and 34%, respectively, and those of τ_e were 0.085 Pa and 0.119 Pa, respectively. On low flats, the d_{50} of surface sediment was 21 μm ; water content was 73%; and τ_e was 0.084 Pa. The flat showed an erosion tendency, as τ_{cw} was larger than τ_e by over 90% during the observation period. Under normal weather conditions, $\tau_{cw} < \tau_e$ was found during high slack water periods, and this lasted for 15% of the tidal submersion period; however, this was the case for 0% of the storm period and for 19.3% and 26.5 % of the spring and neap

tide periods, respectively.

Southeastern Chongming mudflat: the d_{50} of surface sediment was 34 μm ; water content was 32%; τ_e was 0.29 Pa. Freshly deposited sediment was looser and finer, d_{50} was 26 μm ; water content was 98%; and τ_e was 0.14 Pa. τ_{cw} was greater than τ_e for 88.3% of the observation period. $\tau_{cw} < \tau_e$ was found for 6.1% of the tidal submersion period during neap and moderate tide periods, and this coincided with strong wind events. The same condition was found in 23.1% of the normal weather periods.

Kapellebank mudflat: the d_{50} of surface sediment was 20.2–30.6 μm ; water content was 106–148%; and τ_e was 0.11–0.13 Pa. In the vertical dimension, τ_e increased from 0.11 Pa to 0.75 Pa within the uppermost 11 cm layer. Without biological effects, τ_{cw} was greater than τ_e for 21.6% of the observation period. $\tau_{cw} < \tau_e$ conditions were found in 53.9% and 85.9% of tidal submersion periods during spring and neap tides, and these conditions accounted for 86.9% of the storm period. Diatom presence enhanced τ_e to 0.44 Pa, representing 4 times the value of abiotic τ_e .

3. SSC variations on intertidal flats

Nanhui Foreland mudflat: near-bed SSC in the middle flat area varied from 0.4–4.8 kg/m^3 ; average SSC values at 6 cm, 15 cm, 35 cm and 75 cm were 3.1 kg/m^3 , 1.8 kg/m^3 , 1.4 kg/m^3 , and 1.0 kg/m^3 , respectively. Near-bed SSC in lower flat areas varied from 0.02–19.9 kg/m^3 , and the average SSC values were measured at 10 cm, 35 cm, 50 cm and 100 cm as 4.4 kg/m^3 , 2.4 kg/m^3 , 2.2 kg/m^3 , and 1.7 kg/m^3 , respectively. Vertical SSC profiles identified during typical flood and ebb stages following a logarithmic trend, i.e., SSC increased gradually with height, whereas vertical SSC profiles were L-shaped during slack water periods. The background SSCs in middle and low flats were 1.4 kg/m^3 and 2.0 kg/m^3 , respectively. Substantial volumes of suspended sediment that settled during slack water periods formed a near-bed fluid mud layer. The thicknesses of fluid mud layers lasting for 0.5–1 h under normal weather conditions in middle and low flats were < 6 cm and 20–40 cm, respectively. During storm periods, the thickness of fluid mud layers increased to 48 cm when the background SSC value increased to 3.3 kg/m^3 . In addition, 30 cm fluid mud layers likely formed during peak flood/ebb periods.

Southeastern Chongming mudflat: near-bed SSC varied from 0.005–3.64 kg/m^3 and averaged 0.91 kg/m^3 . There were three stages in the measurement duration: strong wind event (average wind speed of 6.9 m/s), bed recovery stage when winds were weak (average wind speed of 3.5 m/s), and second wind event (average wind speed of 5.4 m/s). Average SSC values during these three stages were 0.44 kg/m^3 , 1.53 kg/m^3 , and 2.4 kg/m^3 , respectively.

Kapellebank mudflat: near-bed SSC values varied from 0.01–8.5 kg/m^3 and averaged at 0.53 kg/m^3 . The average SSC values were 0.48 kg/m^3 and 0.58 kg/m^3 during normal weather and storm periods, respectively.

4. Bed-level changes on intertidal flats

Intra-tidal bed-level changes in the Nanhui Foreland mudflat show that erosion occurred during peak flood and ebb periods while accretion occurred under high slack water conditions during periods of normal weather. The maximum intra-tidal erosion depth was 2–3 cm, exceeding the net intertidal bed-level change of 0.7 cm. On low flats, the bed levels were in equilibrium during periods of calm weather. The maximum bed variations was only 2.2 cm. During storm periods, bed-level changes measured via ADV and buried-plate methods showed maximum variations of 8–9 cm, but they were found to be in poor agreement due to the occurrence of sheet erosion. ADV measurements show that rapid accretion (9.5 cm in two tidal cycles) and degradation (5.6 cm in one tidal cycle) occurred during later stages of storm periods and after storms. These processes were closely related to the formation and migration of edges resulting from sheet erosion.

On the Southeastern Chongming mudflat, bed degradation of 10.6 cm occurred over 11 tidal cycles during strong wind events, whereas bed accretion levels of 8.3 cm occurred in the following 5 recovery tidal cycles. Overall, bed-level changes in the mudflat were more significant than those found along the salt marsh, with maximum values observed in the middle flat area. Buried-plate measurements show that during erosion, 3 cm of bed degradation occurred in the middle flat area, whereas lower and upper flat areas showed bed-level variations of ± 0.5 cm; during recovery stages, accretion was greatest in the middle flat area (2.3 cm), followed by those in the lower flat area (1.5 cm) and in the transitional zone between flat and marsh areas (0.8 cm). The lowest value was found in the salt marsh area (0.4 cm).

The maximum variations in low, low-to-middle and middle Kapellebank mudflat area were 11.8 cm, 4.3 cm and 3.6 cm, respectively. Significant bed degradation processes occurred only in low flat areas during storm events. Intra-tidal bed-level changes show that bed degradation only occurred when water depths were less than 1 m, and the bed levels were stable or accretional during the remaining tidal submergence period.

5. Relationships between sediment dynamic processes on intertidal flats

Sediment dynamic processes respond to tides, wind conditions and sediment properties at intra-tide, neap–spring tides, and storm time scales. Erosion and deposition stages alternate due to the balance between τ_{cw} and τ_e and as a result of background SSC values. During tidal submergence periods, erosion occurred during peak flood and ebb periods, whereas deposition generally occurred during slack water periods. Deposition stages were shortened and even disappeared under storm conditions.

Sediment dynamic processes on intertidal flats exhibit neap–spring cyclicality in calm weather conditions. Wind events, which are random, interrupt this neap–spring cyclicality pattern. Our study shows that the effects of waves on intertidal flat sediment dynamics cannot be ignored, even for meso-macrotidal sheltered mudflats subjected to strong wind conditions, which are weaker than those of storm conditions. The effects of waves become more pronounced when flats are open.

Bed degradation during storm periods results from an increase in τ_{cw} . Wind enhances τ_{cw} in the following two ways: (1) wave orbital velocities are increased due to enhanced wave heights driven by winds, which lead to an increase in τ_w ; and (2) wind driven flows increase τ_c in the τ_{cw} model. One form of wind-driven flow involves extra turbulence superimposed on original turbulence resulting from tidal currents, with mean flow speeds maintaining the neap–spring cyclicity. The other form involves wind-driven flows resulting from the abnormal flow structures found on at interface of a flat and channel, which breaks the intra-tidal cyclicity of current speeds. Bed accretion is favourable after wind events under the following conditions: (1) when abundant sediment is delivered through high-energy tidal flows, and often during spring tidal periods; (2) when tidal asymmetry favours flood dominance, leading to higher levels of onshore sediment transport; (3) when τ_d exceeds τ_{cw} long enough to promote sediment deposition; and (4) when high SSC levels enhance flocculation, in turn promoting sediment settlement.

6. BLC (bed-level change) model and its applications

Based on our understanding both of the relationships between τ_{cw} , τ_e , τ_d , SSC and bed-level changes and of the classical Partheniades-Krone erosion-deposition model, we constructed a BLC model using the measured parameters as input. Measurements and simulations were used to investigate effects of strong wind events on sediment dynamics in intertidal mudflats, to quantify the erosion parameter τ_e and M (erosion coefficient) and to study the influence of wind events on these variables. Our results show that the sediment that was freshly deposited after wind events is much looser: the water content was found to be 3 times that of more consolidated bed sediment before the examined wind event, and M decreased by 60%. Vertically, τ_e decreased following a power function, and the magnitude of M was 10^{-3} – 10^{-4} s/m without presenting a significant tendency with depth. This result indicates that τ_e cannot be simplified as a constant in depth in erosion-deposition and morphological models and that M can be used as a constant in depth.

The BLC model was used to determine whether τ_d should be introduced into the deposition model. We define falling sediment motion as ‘settling’ and the product of sediment settling as ‘deposition’: sediment always settles under the influence of gravity, whereas sediment deposition resulting in bed accretion occurs when τ_{cw} falls below a certain threshold, which is τ_d . Therefore, we suggest employing τ_d , which is valued at 0.5 – $1 \tau_e$.

This study furthers our understanding of characteristics and mechanisms of physical processes in intertidal mudflats by investigating large- to small-scale processes using qualitative and quantitative measures based on single indicators and well as a combination of multidisciplinary parameters. We also construct and improve a model that simulates morphological changes in intertidal mudflats and provide suggestions for the model’s parameterization. In addition, part of the work described in this study provides insight into studies conducted in similar disciplines, e.g., coastal engineering, which is related to

sediment dynamics, coastal ecology, which concerns bed stability, and coastal environmental studies, which concern fine-grained sediment transport processes.

The novelties of this thesis are as follows: (1) we proposed and deployed a combined approach to *in situ* measurement and numerical modelling to improve methodologies for studying sediment dynamics in intertidal mudflats. First, technical difficulties experienced when measuring simultaneous waves, current velocities, SSC values and bed-level changes in intertidal flats at a high resolution were addressed. Second, the BLC model was designed to apply τ_{cw} , τ_e , τ_d , E and D calculations based on *in situ* measured data, and simulated BLC values were found to be in good agreement with measured BLC values. (2) We focused on wind effects not only at the storm level but also at weaker levels (strong wind; speed < 10 m/s). We found that even for semi-open tidal flats, strong winds substantially affect sediment dynamics on intertidal flats.

We recommend that future works highlight the importance of **integrated *in situ* measurements of bottom boundary layers under combined wave–current action conditions** to the study of sediment dynamics. This study shows that: i) as intertidal flats are shallow water environments, the H_s/h ratio is likely to be larger than 0.25 in these areas, causing near-bed velocities in three dimensions to be influenced by surface waves; ii) in highly turbid areas, fluid mud layers often form within 50 cm above the bed. Because fluid mud layers are occasionally only several centimetres thick, this is where the OBS probe must be placed; and iii) 70% of sediment transport occurs within 50 cm above the bed, indicating that estimations of sediment flux in the bottom boundary layer are vital to understanding sediment transport processes occurring in intertidal flats. This study also presents ways to better **describe bottom boundary conditions** in BLC or other morphological models: i) wet-dry treatments (or critical depths) in numerical models should be improved, as our results show that significant bed-level changes occur under very shallow conditions (0.3–1 m) both in open and sheltered flats; ii) values of τ_e and M should be specified, and their vertical distributions should be considered in the layered bed model; and iii) seasonal variations in diatom biomass, which is a stabilizer, should be considered when formulating bed descriptions. Further work must take destabilizers (e.g., macro benthic animals) into account and should quantify biotic effects on τ_e .

Key words: Sediment dynamics; Intertidal zone; Mudflat; *In situ* measurements; Numerical model; Combined wave–current action; Wind; Bottom boundary layer; the Yangtze Estuary; the Hangzhou Bay; the Westerschelde Estuary

Samenvatting

De accumulatie van fijn sediment vormt brede en flauwe intergetijdengebieden. Intergetijdengebieden komen op grote schaal voor in kustgebieden, met name in gebieden die worden gekenmerkt door grote getijde amplitudes, overvloedig aanbod van fijn sediment, zeebodems met flauwe hellingen en geringe golfwerking. Intergetijdengebieden zijn belangrijke kustsystemen en processen op intergetijdengebieden zijn sterk gerelateerd aan de lokale (economische) ontwikkeling en menselijke activiteiten. Uitbouwende intergetijdengebieden bieden ruimte voor zowel de uitbreiding van de schorren en als voor menselijke activiteiten. De oppervlakte van het eiland Chongming in de monding van de Yangtze is bijvoorbeeld met 120% gestegen door de inpoldering van de schorren. Daarnaast dienen intergetijdengebieden als bescherming tegen overstromingen door golven te dempen. Intergetijdengebieden staan echter onder druk door een drastische afname van de sediment beschikbaarheid (bijvoorbeeld dammen in het stroomgebied) en door zeespiegelstijging als gevolg van de klimaatverandering en menselijke invloed. **Kennis over sediment dynamiek is van fundamenteel belang voor een beter begrip van de mechanismen van erosie en afzetting**, die cruciaal zijn voor het voorspellen van toekomstige ontwikkeling van intergetijdengebieden.

In situ metingen dienen als belangrijke en waardevolle methode voor het bestuderen van de sediment dynamiek van intergetijdengebieden. De meeste studies in deze gebieden waren gericht op intra-getijde en doortij-springtij variaties in stroomsnelheid en sediment concentraties. Wijzigingen van het bodemniveau werden meestal gemeten als de intergetijdengebieden droogvallen. De manier waarop het bodemniveau verandert op **intra getijde tijdschaal** als gevolg hydrodynamische en sedimentaire processen vormt echter de sleutel tot het begrijpen van de mechanismen achter erosie en sedimentatie op intergetijdengebieden. Bovendien, intergetijdengebieden zijn ondiepe gebieden, die onderworpen zijn aan de forcering door zowel stroming als

golven. Het is daarmee cruciaal om de sediment dynamiek op intergetijdengebieden te bestuderen op basis van geïntegreerde metingen van *in situ* golven, getijdenstromingen, sediment concentraties en bodem-niveau veranderingen. Naast de *in-situ* metingen is het essentieel om de opgedane kennis te verankeren in numerieke modellen om voorspellingen te kunnen maken van de ontwikkeling van intergetijdengebieden, al dan niet als gevolg van menselijke ingrepen.

De hoofddoelstelling van deze studie is het begrijpen van de sediment dynamica en bed-niveau veranderingen onder invloed van stroming en golven op intergetijdengebieden. Daarvoor wordt een geïntegreerde aanpak toegepast van *in situ* metingen van golven, getijdenstromingen, en sediment concentraties en bed-niveau veranderingen bij een hoge temporele en ruimtelijke resolutie met behulp van geavanceerde instrumenten in verschillende windomstandigheden in combinatie met numerieke modellering. Ten eerste identificeren we de stadia van erosie en sedimentatie door vergelijking van de totale bodemschuifspanning onder golf-stroom interactie (τ_{cw}) met de kritische bodemschuifspanning voor erosie (τ_e), die is afgeleid van de gemeten grondmechanische eigenschappen van de bodem. Ten tweede simuleren we bed-niveau veranderingen door het berekenen van de erosie- en sedimentatiesnelheden in het intergetijdengebied. Een combinatie van metingen en simulaties wordt gebruikt om ons begrip van de mechanismen van de erosie-sedimentatie te verbeteren. **De belangrijkste onderzoeksvraag** is het vinden van een heldere relatie tussen de bodem-niveau veranderingen en het sedimenttransport onder golfstroom interactie. **De belangrijkste technieken** die toegepast worden om deze vraag te beantwoorden zijn: toepassen van instrumenten voor het meten van *in situ* golven, getijdenstromingen, SSC niveaus en bed-niveau veranderingen; het bepalen van relaties voor τ_{cw} en τ_e ; en het modelleren van erosie en sedimentatie.

In deze studie onderzoeken we drie intergetijdengebieden met verschillende blootstelling aan golven: het **Nanhui intergetijdengebied** ligt direct aan de open zee en de strijklengte bedraagt ten minste 100 km; het **Zuid-Oost Chongming intergetijdengebied**, een gematigde open gebied met ondiepe platen van enkele kilometers tussen het intergetijdengebied en de open zee; en de **Kapellebank**, een beschermt intergetijdengebied gelegen in de buitenbocht van een geul van de Westerschelde. Op de drie gebieden zijn geïntegreerde waarnemingen uitgevoerd van de waterdiepte, golfparameters, stroming(sprofielen), turbulente snelheden, concentraties (puntmetingen en profielen) en bodemniveaus met behulp van druksensoren, ADVs (Acoustic Doppler Velocimeter), ADCPs (Acoustic Doppler Current Profiler), OBSen (Optic Backscatter Sensor) en ASM (Argus Surface Meter). Tijdens de observatie-periodes zijn monsters genomen van het zwevend sediment en van het sediment aan het oppervlak van het bed en zijn mini-cores gestoken. Deze monsters zijn gebruikt voor de kalibratie van de

instrumenten en voor de bepaling van korrel grootte verdeling, vochtgehalte en de biomassa van diatomeeën. Door toepassing van veelgebruikte rekenmodellen, hebben we de volgende variabelen berekend: totale bodemschuifspanning als gevolg van golven en stroming τ_{cw} (via golfstromingsinteractie modellen van Grant-Madsen, van Rijn en Soulsby); kritische bodemschuifspanning voor erosie τ_c , erosiesnelheden E , valsnelheden ω_s ; depositiesnelheden D en sedimenttransporten Q_s . De gemeten en berekende parameters werden gebruikt om de variaties aan te tonen in hydrodynamische krachten op intragetijden-, doottij/springtij- en stormtijdschalen; temporele en ruimtelijke variaties in sedimentconcentraties aan te tonen; en om de verticale verdeling van bed stabiliteit te bepalen. De bevindingen werden vervolgens gebruikt voor het formuleren van Bed Level Change (BLC) model.

1. Dynamische variaties op intergetijdengebieden

De metingen op de intergetijdengebieden resulteerden in een grote data set (1680 uur metingen) waarbij verschillende variabelen op drie locaties zijn bepaald.

Nanhui Intergetijdengebied: de windsnelheid varieerde tussen 1.7–19.7 m/s en was gemiddeld 5.9 m/s tijdens de observatieperiode. De getijdeslag varieerde van 1.4–5.0 m en was gemiddeld 3.7 m. De stroomsnelheid in de buurt van het bed was 0–0.51 m/s en gemiddelde 0.17 m/s. De significante golfhoogte (H_s) varieerde van 0.01–3.92 m en was gemiddeld 0.32 m. τ_c varieerden van 0.0005–3.58 Pa en was gemiddeld 0.56 Pa; τ_w varieerde van 0–1.62 Pa en was gemiddeld 0.15 Pa; en τ_{cw} varieerden van 0.02–4.79 Pa en was gemiddeld 0.72 Pa. τ_{cw} werd gedomineerd door getijdenstromingen gedurende het grootste deel van de periode dat het gebied onder water stond en werd gedomineerd door de golven, wanneer de waterdiepte minder dan 1 m bedroeg. τ_{cw} volgde een V-vormige tijdreeks, waarbij de τ_{cw} -waarden hoog waren tijdens maximale vloed en eb en laag tijdens periodes van hoog water. De gemiddelde τ_{cw} waarde tijdens springtij was 0.65 Pa en tijdens doottij (0.35 Pa). Gedurende stormperiodes was τ_{cw} aanzienlijk hoger, tot 2.13 Pa.

Het Zuid-Oost Chongming intergetijdengebied: windsnelheid was 0.4–10.8 m/s en gemiddeld 6.0 m/s tijdens de observatieperiode. De getijslag varieerde van 0.9–4.7 m en was gemiddeld 2.7 m. De stroomsnelheden bij de bodem varieerden van 0.04–0.51 m/s en waren gemiddelde 0.18 m/s. H_s varieerde van 0.07–0.46 m en was gemiddeld 0.21 m. τ_c varieerde van 0.01–2.43 Pa en was gemiddeld 0.52 Pa; τ_w varieerde van 0.01–1.68 Pa en was gemiddeld 0.22 Pa; en τ_{cw} varieerde van 0.0004–2.47 Pa met een gemiddelde van 0.66 Pa. De gemiddelde τ_{cw} tijdens sterke wind en periodes van normale weersomstandigheden (gemiddelde windsnelheden van 6.8 m/s en 2.6 m/s, respectievelijk) waren 1.07 Pa en 0.35 Pa, respectievelijk.

Kapellebank: de windsnelheid was 0–18.0 m/s en gemiddeld 5.6 m/s tijdens de observatieperiode. De getijslag varieerde van 3.2–5.3 m en was gemiddeld 4.5 m. De stroomsnelheid bij de bodem varieerde van 0.001–0.47 m/s en was gemiddeld 0.20 m/s.

Hs varieerden van 0.005–0.43 m en was gemiddeld 0.06 m. τ_e varieerde van 0.0004–2.27 Pa en was gemiddeld 0.14 Pa; τ_w varieerde van 0–1.26 Pa en met een gemiddelde van 0.08 Pa; en τ_{cw} varieerde van 0.002–2.55 Pa en was gemiddeld 0.18 Pa. τ_{cw} -waarden vóór, tijdens en na de storm perioden waren 1.32 Pa, 2.10 Pa en 0.57 Pa, respectievelijk.

2. Kritische schuifspanning voor erosie τ_e erosie en de vergelijking met τ_{cw}

Nanhui Intergetijdengebied: de mediane korrelgrootte (d_{50}) van het sediment van de bodem op de middelste deel van het intergetijdengebied was 34 μm ; het watergehalte van de bovenste 2 mm en 10 mm lagen was respectievelijk 72% en 34%; en de kritische schuifspanning voor erosie τ_e was respectievelijk 0.085 Pa en 0.119 Pa. Op de lage delen werd de d_{50} van de ondergrond sediment 21 μm ; het watergehalte was 73%; en τ_e was 0.084 Pa. Het intergetijdengebied neigde naar erosie, aangezien voor meer dan 90% van de observatieperiode de τ_{cw} groter was dan τ_e . Onder normale weersomstandigheden en tijdens hoogwater bleek $\tau_{cw} < \tau_e$, en dit duurde 15% van de getijde periode. Echter, dit was niet het geval voor de stormperiode en 19.3% en 26.5% van de tijd voor de springtij en de doortij periodes.

Zuid-Oost Chongming intergetijdengebied: de d_{50} van de ondergrond sediment was 34 μm ; watergehalte was 32%; τ_e was 0.29 Pa. Recent afgezet sediment was losser en fijner, d_{50} was 26 μm ; watergehalte was 98%; en τ_e was 0.14 Pa. τ_{cw} was groter dan τ_e voor 88.3% van de waarnemingsperiode. $\tau_{cw} < \tau_e$ bleek voor 6.1% van de getijde periode tijdens doortij en gematigde getij periodes, en dit viel samen met de sterke wind gebeurtenissen. Dezelfde voorwaarde werd gevonden in 23.1% van de normale weer periodes.

Kapellebank: de d_{50} van de ondergrond sediment was 20.2–30.6 μm ; watergehalte was 106–148%; en τ_e was 0.11–0.13 Pa. In de verticale dimensie, τ_e steeg van 0.11 Pa tot 0.75 Pa in de bovenste 11 cm. Zonder biologische effecten was τ_{cw} groter dan τ_e gedurende 21.6% van de waarnemingsperiode. $\tau_{cw} < \tau_e$ voorwaarden werden gevonden in 53.9% en 85.9% van getijde perioden tijdens doortij en springtij, en deze voorwaarden golden voor 86.9% van de storm-periode. Diatomee aanwezigheid verhoogde τ_e naar 0.44 Pa, tot 4 keer de waarde van een abiotische τ_e .

3. SSC variaties op intertidal flats

Nanhui intergetijdengebied: de concentratie nabij de bodem in het vlakke centrale deel varieerde van 0.4–4.8 kg/m^3 ; gemiddelden concentraties op hoogtes van 6 cm, 15 cm, 35 cm en 75 cm boven het bed varieerden waren respectievelijk 3.1 kg/m^3 , 1.8 kg/m^3 , 1.4 kg/m^3 en 1.0 kg/m^3 . De concentraties bij de bodem in het lagere deel varieerde van 0.02–19.9 kg/m^3 en de gemiddelde concentraties op 10 cm, 35 cm, 50 cm en 100 cm waren 4.4 kg/m^3 , 2.4 kg/m^3 , 2.2 kg/m^3 en 1.7 kg/m^3 , respectievelijk. Verticale concentratie profielen gedurende typische vloed en eb fases geleidelijk opgevoerd met hoogte een logaritmische trend volgt, terwijl ze L-vormige tij perioden waren. De achtergrond concentraties in midden en laaggelegen flats waren respectievelijk 1.4 kg/m^3 en 2.0 kg/m^3 . Aanzienlijke hoeveelheden zwevende sediment zakten uit tijdens kentering en vormden

een *fluid-mud* laag nabij de bodem. De diktes van fluid mud lagen onder normale weersomstandigheden waren < 6 cm en 20–40 cm voor de midden en lage gebieden en waren aanwezig voor 0.5–1 uur. Tijdens stormperiodes van de storm verhoogde de dikte van de fluid mud laag tot 48 cm en waren de achtergrond concentraties verhoogd tot 3.3 kg/m³. Bovendien vormde zich een 30 cm dikke fluid mud laag tijdens piekperiodes van vloed en eb.

Zuid-Oost Chongming intergetijdengebied: de concentratie bij de bodem varieerde van 0.005–3.64 kg/m³ en was gemiddelde 0.91 kg/m³. Gemiddelde concentraties tijdens sterke wind (gemiddelde windsnelheid van 6.9 m/s), bed herstel fase waarden wanneer winden waren zwak (gemiddelde windsnelheid van 3.5 m/s), en tweede wind gebeurtenis waarden (gemiddelde windsnelheid van 5.4 m/s) 0.44 kg/m³, 1.53 kg/m³ en 2.4 kg/m³, respectievelijk.

Kapellebank: de concentraties bij de bodem varieerde van 0.01–8.5 kg/m³ en waren gemiddeld 0.53 kg/m³. De gemiddelde concentraties waren 0.48 kg/m³ en 0.58 kg/m³ tijdens normaal weer en tijdens storm perioden.

4. bed-niveau veranderingen in intertidal flats

Bodemvariaties op het intergetijdengebied van Nanhui lieten zien dat erosie optrad tijdens pieksnelheden bij eb en bij vloed, terwijl sedimentatie plaatsvond tijdens hoogwater kentering tijdens periodes van normaal weer. De maximale erosiediepte van 2–3 cm, was groter dan de intertidale bodemvariaties van 0.7 cm. Op de lage delen was de bodem in evenwicht met maximale bed niveau variaties op 2.2 cm tijdens periodes van rust weer. Tijdens storm periodes, veranderingen van de bed-niveau gemeten via ADV en begraven-plaat methoden liet maximale variaties van 8–9 cm, maar ze bleken te zijn in slechte overeenkomst als gevolg van het optreden van blad erosie. ADV metingen laten zien dat snelle sedimentatie (9.5 cm in twee getijde cycli) en erosie (5.6 cm in één getijdencyclus) tijdens latere fasen van de storm en na stormen optraden. Deze processen waren nauw verwant aan de vorming en de migratie van bodemvormen als gevolg van *sheet-erosion*.

Op de Zuid-Oost Chongming intergetijdengebieden trad erosie op van 10.6 cm over 11 getijde cycli, tijdens periodes van sterke wind. Sedimentatie van 8.3 cm vond plaats in de opvolgende 5 getijde cycli. In het algemeen zijn de bodemveranderingen op het intergetijdengebied groter dan die langs de schorren, waarbij de maximale waarden waargenomen zijn in het centrale deel. Metingen met de verzonken plaat laten zien dat tijdens de erosieperiode, 3 cm van de erosie van het bed is opgetreden in het centrale deel, terwijl op de onderste en bovenste delen de variaties beperkt bleven tot ±0.5 cm; tijdens de herstel stadia was sedimentatie het grootst in het middengebied (2.3 cm), daarna in het onderste gedeelte (1.5 cm) en de overgangperiode zone tussen het intergetijdengebied en de schorren (0.8 cm). De laagste waarde werd gevonden in het schor (0.4 cm).

De maximale variaties in laag, laag-naar-Midden en Midden Kapellebank waren

11.8 cm, 4.3 cm en 3.6 cm, respectievelijk. Belangrijke erosieprocessen traden voortijdens de storm op in de laaggelegen gebieden. Veranderingen van de bodem tonen dat de erosie alleen optrad voor waterdieptes van minder dan 1 m. De bodem was stabiel of er trad sedimentatie op gedurende de resterende de overige periodes.

5. Relaties tussen de sediment dynamica processen op intergetijdengebieden

Sediment dynamica processen zijn een gevolg van getijden, windomstandigheden en sediment eigenschappen op intragetij, dootij-springtij en en stormgerelateerde tijdschalen. Erosie en sedimentatieperiodes wisselen elkaar af als gevolg van de verhouding tussen τ_{cw} en τ_e en als gevolg van het sediment aanbod. Erosie is opgetreden tijdens pieksnelheden tijdens eb en tijdens vloed, terwijl sedimentatie vooral tijdens (hoogwater) kentering optrad. Sedimentatiefases werden korter of verdwenen zelfs tijdens stormcondities.

De sediment dynamica processen op intertidal flats vertonen een dootij-springtij cycliciteit bij kalm weer. Een stochastische forcering door wind onderbreekt dit cyclische patroon. Onze studie toont aan dat de effecten van golven op de sediment dynamica niet verwaarloosd mag worden op intergetijdengebieden, zelfs niet voor voor meso-macrotidale gebieden. Ook bij sterke windomstandigheden, die zwakker zijn dan die van storm voorwaarden, treden significante effecten op. De effecten van golven zijn wel uitgesprokener als de intergetijdengebieden minder beschut liggen.

Bodemverlaging tijdens storm periodes is het gevolg van een toename van τ_{cw} . Wind versterkt τ_{cw} op de volgende twee manieren: (1) orbitaalsnelheden zijn toegenomen als gevolg van grotere golfhoogten die zijn gedreven door de wind, leidend tot een toename van τ_w ; en (2) windgedreven stroming leidt tot een toename van τ_c in het τ_{cw} -model. Enerzijds zorgt wind-gedreven stroming voor extra turbulentie bovenop de oorspronkelijke turbulentie die voortvloeit uit getijdenstromingen. Anderzijds zorgt windgedreven stroming voor atypische stromingen op de overgang tussen het intergetijdengebied en de geul. Bodemverhoging treedt vooral op na windgebeurtenissen onder de volgende voorwaarden: (1) wanneer voldoende sediment wordt aangevoerd wordt door middel van hoog-energetische getijdenstromen en vaak tijdens springtij periodes; (2) wanneer de getijdestroming vloeddominant is, wat leidt tot meer landwaarts sedimenttransport; (3) als τ_d lang genoeg groter is dan τ_{cw} om depositie te bevorderen; en (4) wanneer hoge sedimentconcentraties leiden tot flocculatie en daarmee tot verhoogde depositie.

6. BLC (Bed Level Change) model en toepassingen

Gebaseerd op het begrip van de relaties tussen τ_{cw} , τ_e , τ_d , sedimentconcentratie en bodemniveau veranderingen, en op basis van het klassieke erosie-depositie model van Partheniades-Krone, hebben we een BLC-model gebouwd met de gemeten parameters als invoer. Metingen en simulaties werden gebruikt om de effecten van sterke wind gebeurtenissen op de dynamiek van het sediment op intergetijdengebieden te bepalen, om

de erosie parameters τ_e en M (erosie coëfficiënt) te kwantificeren en om de invloed van wind gebeurtenissen op deze variabelen te bepalen. Onze resultaten tonen aan dat het sediment dat neergeslagen is direct na de wind gebeurtenissen veel losser is: het watergehalte bleek een factor 3 hoger te zijn dan van het meer geconsolideerde bed sediment van vóór de gebeurtenis en M daalde met 60%. Over de verticaal gezien daalde τ_e volgens een machtsfunctie en de waarde van M bedroeg $10^{-3} \sim 10^{-4}$ s/m zonder een duidelijke variatie over de diepte. Dit resultaat geeft aan dat τ_e niet constant mag worden aangenomen over de bodemdiepte, terwijl M mogelijk als constante gezien kan worden.

Het BLC model werd gebruikt om te bepalen of τ_d benodigd is in de definitie van de depositie term. We definiëren de vallende sediment beweging als ‘bezinken’ en het product van de valsnelheid en de concentratie als ‘depositie’: sediment bezinkt altijd onder invloed van de zwaartekracht, terwijl depositie van sediment dat tot bodemverhoging leidt, optreedt wanneer τ_{cw} kleiner is dan een bepaalde drempelwaarde, oftewel τ_d . We maken daarom gebruik van τ_d , die een waarde heeft van 0.5 – 1 maal τ_e .

Deze studie heeft het begrip van de mechanismen achter de fysische processen op intergetijdengebieden vergroot door het onderzoeken van kleinschalige en grootschalige processen. Hierbij zijn van kwalitatieve en kwantitatieve methodes gebruikt die zijn gebaseerd op enkele indicatoren alsmede op een combinatie van multidisciplinaire parameters. Wij hebben tevens een model opgezet dat morfologische veranderingen op intergetijdengebieden simuleert en we bieden suggesties voor model parameterisatie. Deze resultaten kunnen gebruikt worden voor gerelateerde disciplines, zoals kustwaterbouwkunde en mariene ecologie.

De vernieuwingen in dit proefschrift zijn: (1) wij hebben een gecombineerde aanpak voorgesteld en geïmplementeerd van *in situ* metingen en numerieke modellering ter verbetering van het begrip van de sedimentdynamiek op intergetijdengebieden. Ten eerste zijn technische moeilijkheden bij het gelijktijdig meten op hoge resolute van golven, stroomsnelheden, sedimentconcentraties en bodemniveau veranderingen op intergetijdengebieden aangegeven. Ten tweede is een BLC model opgesteld en zijn de gemeten waarden voor τ_{cw} , τ_e , τ_d , E en D als invoer gebruikt. De resulterende bodemniveau veranderingen waren in goede overeenstemming met de gemeten waarden. (2) We hebben ons gericht op de effecten van wind en daarbij niet alleen op het stormniveau, maar ook op lagere niveau's (sterke wind; snelheid < 10 m/s). We vonden dat zelfs voor beschutte intergetijdengebieden de wind een wezenlijke invloed kan hebben op de sediment dynamiek op intergetijdengebieden.

We benadrukken voor toekomstig onderzoek het belang van **geïntegreerde *in situ* metingen in de grenslaag bij de bodem samenspel golf-stroom interactie omstandigheden** tot de studie van sediment dynamiek. Deze studie toont aan dat: i) snelheden als gevolg van golven nabij de bodem (sterk) driedimensionaal kunnen zijn,

aangezien de verhouding $H_s \text{ zijn} / h$ meestal groter is dan 0.25, vanwege de geringe dieptes.

ii) In gebieden met zeer troebel water kunnen fluid mud lagen ontstaan binnen ca. 50 cm boven het bed. Omdat fluid mud lagen soms slechts enkele centimeters dik zijn, is het belangrijk om een OBS dichtbij de bodem te plaatsen.

iii) 70% van het sedimenttransport treedt op in de laag van 50 cm boven het bed. Dit geeft aan dat schattingen van sediment fluxen in de grenslaag bij de bodem onmisbaar zijn voor het begrijpen van transport processen die zich voordoen op intergetijdengebieden. Deze studie geeft ook manieren voor een betere **beschrijving van randvoorwaarden** in de BLC of andere morfologische modellen:

i) De afhandeling van zeer ondiep water en bijbehorende droogvalprocedures in numerieke modellen moeten worden verbeterd. Onze resultaten tonen aan dat belangrijke bodemniveau veranderingen zich voordoen in zeer ondiep water (0.3-1 m) zowel in open en beschutte gebieden;

ii) waarden voor τ_e en M moeten nader worden gespecificeerd worden, en hun verticale distributies moeten worden beschouwd in een gelaagde bodemmodule; en

iii) seizoensgebonden variaties in diatomee biomassa, een biostabilisator, moeten worden meegenomen in het opstellen van erosieformuleringen. Toekomstig onderzoek moet rekening houden met destabilatoren (bijvoorbeeld macro benthische fauna) en moet de biotische effecten op τ_e kwantificeren .

摘要

潮滩 (Tidal flat) 是细颗粒泥沙 (fine-grained sediments) 在潮间带 (intertidal zone) 堆积形成的宽广、平坦的滩地。潮滩在世界海岸线上 (尤其是潮汐作用显著、细颗粒泥沙来源丰富、岸外海底坡度较小、波浪作用较弱的岸段) 有广泛分布。潮滩不仅是海岸生态系统的重要组成部分, 而且与人类的生存和发展息息相关。潮滩的淤涨和向海推进为盐沼植被的发育以及人类的围垦提供了有利的空间。例如, 近半个世纪长江口崇明岛的面积就因围垦滩涂而增加了 120%。潮滩还具有显著的消浪护岸功能。然而, 在气候变化引起的全球海平面上升以及流域建坝等导致的入海泥沙通量锐减的影响下, 潮滩 (特别是三角洲潮滩) 正面临淤涨减慢或甚至侵蚀的威胁, 迫切需要增强潮滩冲淤机制的认识, 为潮滩的保护或重建提供科学依据。**潮滩沉积动力 (sediment dynamics) 过程是潮滩冲淤机制的核心。**

鉴于潮间带自然环境的复杂性, 现场观测是潮滩沉积动力过程研究的重要手段。已有的研究成果主要反映淹没潮周期内和大小潮周期的潮滩流速和悬沙浓度变化过程以及淹没潮周期内滩面相对高程的净变化。流速和悬沙浓度变化过程的认识是基于潮滩淹没期间的连续仪器记录, 而淹没潮周期内滩面高程的净变化则是在潮滩淹没的间歇 (露出阶段) 的测量。鉴于潮滩是一种浅水-极浅水环境, 波浪的作用不容忽视 (特别是在开敞型潮滩上和强风-风暴条件下)。此外, 不了解淹没期间滩面变化的过程就无法深入揭示滩面变化与水动力和泥沙过程之间的联系, 也就难以真正解释潮滩冲淤的机制。因此, **基于高分辨率波浪、潮流、悬沙和滩面变化系统观测和数值模拟是当前潮滩沉积动力学研究的前沿。**

本文的主要目标是: 1) 通过在不同风况和潮况条件下利用先进仪器在潮滩上开展波浪、潮流、悬沙浓度和滩面变化的连续、高分辨率的系统观测, 探究波流联合作用下的泥沙输运和底床冲淤的变化过程和特征; 2) 结合底床沉积物力学特性

的测定,计算滩面的临界侵蚀剪切应力,与波流联合剪切应力变化过程进行对比,了解淹没期间的侵蚀和淤积阶段;3)通过侵蚀通量和淤积通量的计算,模拟淹没期间的滩面变化过程,与实测的滩面变化进行对比,改进数值模型,深化冲淤机制认识。**拟解决的关键科学问题**是滩面冲淤与波流联合作用下沉积物输运之间的深层联系。**拟解决的关键技术**包括:获取现场连续、高分辨率波浪、潮流、泥沙、底床冲淤数据的先进仪器操作技能;合理的波流联合剪切应力和底床冲淤临界剪切应力的计算模式和参数的选择;合理的侵蚀速率和沉降速率模型的确定。

本文选择**三种开敞程度不同的淤泥质潮滩**作为研究区域。它们分别是:强开敞型的南汇嘴潮滩、中等开敞型的崇明岛东南岸潮滩、弱开敞型(强隐蔽型)的荷兰 Kapellebank 潮滩。南汇嘴潮滩岸外至少有 100 km 的开敞海域;崇明东南岸潮滩岸外数公里有潮间带浅滩沙洲发育,更向海才是开敞海域;Kapellebank 潮滩位于狭长的西斯凯尔特河口内的弯道顶部。本研究利用自制的海底观测架和先进仪器设备,包括**波潮仪**、**声学多普勒流速剖面仪**(ADCP, Acoustic Doppler Current Profiler), **声学多普勒点流速仪**(ADV, Acoustic Doppler Velocity meter), **后向散射浊度计**(OBS, Optical Backscatter Sensor), 配有后向散射浊度计的 C3™型荧光计和**浊度杆**(ASM, Argus Surface Meter)等。分别在三个潮滩上观测同步高分辨率水深、波浪、流速流向剖面、近底三维紊动流速、单点悬沙浓度或悬沙浓度剖面、滩面冲淤等第一手资料,累计观测 1680 小时。在观测过程中还采集了悬浮泥沙样品、表层沉积物样品、短柱状沉积物样品。在实验室进行了沉积物粒度、含水量和硅藻生物量测定,并对仪器参数进行标定。采用国际上流行的计算模型计算了波流联合底床切应力 τ_{cw} (Grant-Madsen 模型, van Rijn 模型和 Soulsby 模型)、底床沉积物临界侵蚀切应力 τ_c 、侵蚀通量 E 、沉速 ω_s 、沉降通量 D 和悬沙输运率 Q_s 等参数。利用上述提及的大量测量和计算资料,分析了潮周期内、大小潮周期和风暴潮周期内水动力变化、悬沙浓度的时空分布、底床抗侵蚀能力分布的特征及其动力机制。建立了基于现场水文泥沙观测的冲淤模型。主要结果和结论如下:

1. 潮滩动力作用的变化

南汇嘴潮滩观测期间的风速为 1.7~19.1 m/s, 平均 5.9 m/s; 潮差为 1.4~5.0 m, 平均 3.7 m; 近底流速为 0.001~0.51 m/s, 平均 0.17 m/s; 有效波高为 0.01~3.92 m, 平均 0.32 m; τ_c 为 0.0005~3.58 Pa, 平均 0.56 Pa; τ_w 为 0~1.62 Pa, 平均 0.15 Pa; τ_{cw} 为 0.02~4.79 Pa, 平均 0.72 Pa。 τ_{cw} 在潮周期内主要受潮汐控制, 浅水(水深 < 1 m) 受波浪控制, 呈现出涨落急阶段大、涨憩阶段小的 V 型变化趋势。 τ_{cw} 平均值在大潮期间 (0.65 Pa) 大于小潮期间的平均值 (0.35 Pa), 在风暴期间显著增加, 平均值达到 2.13 Pa。

崇明东南岸潮滩观测期间风速为 0.4~10.8 m/s, 平均 6.0 m/s; 潮差为 0.9~4.7 m, 平均 2.7 m; 近底流速为 0.004~0.51 m/s, 平均 0.18 m/s; 有效波高为 0.07~0.46 m, 平均 0.21 m; τ_c 为 0.01~2.43 Pa, 平均 0.52 Pa; τ_w 为 0.01~0.68 Pa, 平均 0.22 Pa; τ_{cw} 为 0.04~2.47 Pa, 平均 0.66 Pa。强风事件期间 (平均风速 6.8 m/s) 和正常天气 (平均风速 2.6 m/s) τ_{cw} 平均值分别为 1.07 Pa 和 0.35 Pa。

Kapellebank 潮滩观测期间风速为 0~18.0 m/s, 平均 5.6 m/s; 潮差为 3.2~5.3 m, 平均 4.5 m; 近底流速为 0.001~0.47 m/s, 平均 0.20 m/s; 有效波高为 0.005~0.43 m, 平均 0.06 m; τ_c 为 0.0004~2.27 Pa, 平均 0.14 Pa; τ_w 为 0~1.26 Pa, 平均 0.08 Pa; τ_{cw} 为 0.002~2.55 Pa, 平均 0.18 Pa。风暴前、中、后期 τ_{cw} 平均值分别为 1.32 Pa, 2.10 Pa 和 0.57 Pa。

2. 潮滩沉积物的临界侵蚀切应力 τ_e 及其与 τ_{cw} 的对比

南汇嘴潮滩中潮滩测点表层沉积物中值粒径为 34 μm , 表层 2 mm 和 10 mm 层沉积物含水量分别为 72% 和 34%, τ_e 分别为 0.085 Pa 和 0.119 Pa。低潮滩表层沉积物中值粒径 21 μm , 表层沉积物含水量为 73%, τ_e 为 0.084 Pa。总体上, 90% 的观测时段 $\tau_{cw} > \tau_e$, 反映侵蚀倾向。正常天气下, $\tau_{cw} < \tau_e$ 发生在高水位憩流期, 占淹没时长的 15%, 而风暴期间 $\tau_{cw} < \tau_e$ 发生几率为 0; $\tau_{cw} < \tau_e$ 在大潮和小潮期间发生几率分别为 19.3% 和 26.5%。

崇明东南岸潮滩表层沉积物中值粒径为 34 μm , 含水量为 32%, τ_e 为 0.29 Pa; 风暴过后的新淤沉积物中值粒径为 26 μm , 含水量为 98%, τ_e 为 0.14 Pa。总体上, 88.3% 的观测时段 $\tau_{cw} > \tau_e$, 反映侵蚀倾向。 $\tau_{cw} < \tau_e$ 在小潮至转入大潮阶段的强风天气下发生几率为 6.1%, 在大潮正常天气下为 23.1%。

Kapellebank 潮滩表层沉积物中值粒径为 20.2~30.6 μm , 含水量为 106~148%, τ_e 为 0.11~0.13 Pa。垂向上 τ_e 在表层 11 cm 内向下递增至 0.75 Pa。不考虑生物作用时, 总体上, 21.6% 的观测时段 $\tau_{cw} > \tau_e$, 反映淤积倾向。 $\tau_{cw} < \tau_e$ 在大潮和小潮期间发生几率分别为 53.9% 和 85.9%, 风暴期间为 86.9%。当滩面存在硅藻时, τ_e 为 0.44 Pa, 是无生物作用下 τ_e 的 4 倍。

3. 潮滩上悬沙浓度的变化

南汇嘴潮滩中潮滩悬沙浓度变化范围为 0.4~8.4 kg/m^3 , 近底 6、15、35 和 75 cm 高度平均悬沙浓度为 3.1 kg/m^3 、1.8 kg/m^3 、1.4 kg/m^3 和 1.0 kg/m^3 。低潮滩悬沙浓度变化范围为 0.02~19.9 kg/m^3 , 近底 10、35、50、100 cm 高度平均悬沙浓度为 4.4 kg/m^3 、2.4 kg/m^3 、2.2 kg/m^3 和 1.7 kg/m^3 。近底悬沙浓度垂向分布在涨落急时段呈上小下大的对数分布趋势, 近底水体悬沙浓度分布较均匀 (1~2 kg/m^3) 涨憩阶段呈 L 型分布, 上下层差异明显。背景悬沙浓度在中潮滩和低潮滩分别为 1.4 kg/m^3

和 2.0 kg/m^3 ，悬沙沉降时在近底形成数厘米厚的浮泥层，其厚度在中潮滩 $< 6 \text{ cm}$ ，在低潮滩为 $20\sim 40 \text{ cm}$ ，持续时间 $0.5\sim 1 \text{ h}$ 。风暴期间背景悬沙浓度为 3.3 kg/m^3 ，涨憩阶段浮泥层厚度达到 48 cm ，持续时间可大于 6 h 。此外，在涨急或落急阶段出现 30 cm 厚度浮泥层。

崇明东南岸潮滩近底悬沙浓度变化范围为 $0.005\sim 3.64 \text{ kg/m}^3$ ，平均 0.91 kg/m^3 。悬沙浓度随时间变化规律为：强风（平均风速 6.9 m/s ）作用时段平均悬沙浓度为 0.44 kg/m^3 ；在此之后滩面历经恢复阶段（平均风速 3.5 m/s ），此时平均悬沙浓度 1.53 kg/m^3 ；第二次强风过程（风速 5.4 m/s ）中，平均悬沙浓度为 2.4 kg/m^3 。

Kapellebank 潮滩近底悬沙浓度变化范围为 $0.01\sim 8.6 \text{ kg/m}^3$ ，平均 0.53 kg/m^3 。正常天气和风暴期间平均悬沙浓度分别为 0.48 kg/m^3 和 0.58 kg/m^3 。

4. 潮滩冲淤变化

正常天气下，南汇嘴潮滩在潮周期内总体呈现涨落急冲刷、涨憩淤积的趋势，潮周期内最大侵蚀深度为 $2\sim 3 \text{ cm}$ ，大于潮周期净侵蚀深度（ 0.7 cm ）。低潮滩在风暴前期最大冲淤幅度为 2.2 cm ，滩面处于平衡状态；风暴期间由于存在层状侵蚀，ADV 和埋板法测得结果不一致，但局部最大冲淤都达到 $8\sim 9 \text{ cm}$ 。ADV 测点上，在风暴后期滩面有异常快速淤积，淤积厚度达 9.5 cm ，而在风暴过后有异常刷深 5.6 cm ，这种剧烈变化可能是层状侵蚀边缘出现引起的。

崇明东南岸潮滩中潮滩在强风期间发生侵蚀，历经 11 个潮周期，最大侵蚀深度为 10.6 cm ；滩面恢复过程历经 5 个潮周期，最大淤积厚度为 8.3 cm 。总体上，光滩冲淤幅度大于草滩，埋板法结果表明，侵蚀阶段中潮滩侵蚀深度约为 3 cm ，低潮滩和草滩冲淤范围为 $\pm 0.5 \text{ cm}$ ；淤积阶段，中潮滩淤积幅度最大（ 2.3 cm ），其次是光草滩过渡带（ 1.5 cm ），再次是低潮滩（ 0.8 cm ），草滩淤积幅度最小（ 0.4 cm ）。

Kapellebank 潮滩最大冲淤幅度在低潮滩、中低潮滩和中潮滩依次为 11.8 cm 、 4.3 cm 和 3.6 cm ，风暴期间仅在低潮滩发生明显冲刷过程。潮周期内，滩面冲刷过程只发生在水深小于 1 m 阶段，其余时段滩面相对稳定，无明显冲淤。

5. 潮滩沉积动力过程的相互联系

潮滩沉积动力过程受到潮汐、风况和沉积物特性的共同制约，存在涨落潮、大小潮和风事件的变化。底床的冲或淤不仅取决于 τ_e 和 τ_{cw} 的对比，也取决于背景悬沙浓度。潮滩上存在侵蚀时段和淤积时段的频繁交替。通常情况下，潮周期内的高流速阶段出现侵蚀，而憩流阶段出现淤积。但在风暴天气下，淤积时段明显缩短或甚至消失。

在无风浪影响的情况下，潮滩沉积动力过程表现出明显的潮汐周期循环。但非周期性的风浪干扰往往会打乱潮滩沉积动力过程的周期性。本文的研究表明，波

浪（尤其是强风条件下）在潮滩沉积动力过程中的作用是不能忽视的。即便是在强潮、高度隐蔽性潮滩，波浪的作用有时也很明显。当然，在开敞程度越高的潮滩，波浪的相对作用会越大。

风暴潮周期内 τ_{cw} 增大引起滩面冲刷，风力增强对增强 τ_{cw} 增大体现在以下两方面。其一，风力增大引起波高增大，增加近底波浪轨迹质点运动幅度，从而增大 τ_w 。其二，风生流进一步增大 τ_e ，一种形式是风生湍流向底部传播，虽然平均流速仍表现出大小潮变化规律，但潮流湍流项上叠加了风引起的湍流；另一种形式是风生流，在滩槽过渡带上易形成特殊水流结构，打破潮周期内原有的流速周期性变化。风暴潮后伴随滩面淤积过程，快速淤积通常满足以下条件：i) 大潮期间水流挟沙力增大，带来更多泥沙；ii) 流速和悬沙浓度在潮周期内呈涨潮优势；iii) 水动力减弱 $\tau_{cw} < \tau_d$ 在潮周期内比例增大；iv) 近底悬沙浓度增大，形成絮凝体加速下沉。

6. 冲淤模型的建立和应用

通过上述 τ_{cw} 、 τ_e 、 τ_d ，悬沙浓度和底床冲淤之间关系的建立，结合经典 Partheniades-Krone 冲淤模型，本文建立了结合现场观测资料的冲淤模型，并通过现场观测和数值模型相结合的方法，进一步论证到强风对潮滩沉积动力过程的作用，定量研究冲淤模型中侵蚀参数分布和对强风事件的响应。强风事件过后新淤沉积物含水量是原先半固结沉积物的 3 倍，侵蚀常数 M 减小 60%；垂向上， τ_e 向下呈幂函数减小， M 值数量级为 $10^{-3} \sim 10^{-4}$ s/m，无明显变化趋势。这说明在冲淤模型和地貌模型中，侵蚀常数 τ_e 不应简单定义为常数，而 M 可取常数。

冲淤模型还探讨了 τ_d 在模型中的合理性，试图解决对 τ_d 的争议。本文研究表明，应当区分沉降过程和沉降结果，即沉降过程始终发生，但下沉泥沙能否沉降到滩面上引起滩面实质性淤积，取决于近底动力条件 τ_{cw} 是否能小于一临界值，即 τ_d 。因此，冲淤模型中需引入 τ_d ，取值范围为 $0.5 \sim 1 \tau_e$ 。

本研究有助于淤泥质潮滩沉积动力过程的研究从宏观到微观，从定性到定量、从单一科学指标向多学科指标融合的深化，从而加深对淤泥质潮滩物理特性和过程的认识，并为淤泥质潮滩冲淤演变数值模型的建立和完善提供重要参考数据。此外，本文的部分工作还为相邻学科（如涉及泥沙运动的海岸工程学，涉及底栖动物影响滩面稳定性的生态学和涉及颗粒输移的海岸环境科学等）的深入研究提供借鉴。

本文的创新点有：(1) 突破了潮滩波浪、潮流、悬沙浓度、底床冲淤高分辨率集成观测的技术难点，引入了波流联合作用剪切应力、底床侵蚀临界剪切应力、侵蚀通量和沉降通量等概念，基于沉积动力过程模拟的冲淤值与实测冲淤值高度吻合，从而推动了潮滩沉积动力过程研究方法的创新；(2) 发现波浪即使是在弱开敞

型的强潮潮滩上也可能扮演重要角色，风暴期间的平均 τ_{cw} 可超过正常天气 τ_{cw} 的数倍，且没有 $\tau_{cw} < \tau_e$ 的时段，从而深化了波浪在淤泥质潮滩沉积动力过程中的作用的认识。

今后工作的展望：本文通过分析不同风况下淤泥质潮滩动力沉积要素的变化，强调**近底边界层波流联合综合观测**在沉积动力过程研究中的重要性，因为 i) 潮滩这样的浅水环境容易满足波高水深比大于 0.25 这一条件，此时近底流速就包含波浪轨迹运动；ii) 高浊度潮滩近底 50 cm 以内通常发育有浮泥层，正常天气下发育厚度只有数厘米至十几厘米，因此在此高度上需放置浊度探头；iii) 大部分悬沙输运发生于近底水层内，70%悬沙输运在近底 50 cm 水层内进行。其次，本文对冲淤模型和地貌模型**底边界定义**具有的指导意义有：i) 因模型稳定性限制，通常会设置临界模拟水深（一般为数厘米到数十厘米）。而本文研究结果表明开敞潮滩在极浅水（水深 0.3 ~ 1m）阶段仍然有明显的冲淤，半遮蔽潮滩的低潮滩在此阶段发生剧烈侵蚀，因此模型需要考虑更优化的干-湿处理，降低临界模拟水深；ii) 侵蚀参数 τ_e 和 M 的数值和垂向分布应当考虑在底床层化模型中，对风暴潮模拟尤为重要；iii) 生物作用的季节性分布也应考虑在底床模型中，本文只考虑了硅藻固滩作用，底栖动物的干扰作用定量化研究有待深入。

关键词：沉积动力；潮间带；淤泥质潮滩；现场观测；冲淤模型；波流联合作用；风；近底边界层；长江口；杭州湾；西斯凯尔特河口

Contents

Abstract	i
Samenvatting	viii
摘要	xvi
Contents	xxiii
1 Introduction	1
1.1 Background.....	1
1.1.1 Intertidal flats.....	1
1.1.2 Physical processes of intertidal flats.....	3
1.2 State of the art.....	4
1.2.1 Hydrodynamics forces under combined wave–current action.....	4
1.2.2 Intra-tidal sedimentary processes.....	6
1.2.3 Bed sediment properties.....	6
1.2.4 Response of intertidal mudflat to wind events.....	7
1.2.5 <i>In situ</i> measurements on intertidal flats.....	8
1.3 Objectives.....	10
1.4 Approaches and thesis outline.....	10
2 Study areas	13
2.1 Reasons of choosing the study areas.....	14
2.2 The Yangtze Estuary: Southeastern Chongming mudflat.....	14
2.3 The Hangzhou Bay: Nanhui Foreland mudflat.....	17
2.4 The Westerschelde Estuary: Kapellebank mudflat.....	19
3 Material and methods	23
3.1 <i>In situ</i> measurements setup.....	24
3.1.1 Instrumentation setup.....	24
3.1.2 Bed level measurements.....	29
3.2 Sample collection and analysis.....	30
3.3 Data process and calculations.....	32

3.3.1	Data transformation from the instruments	32
3.3.2	Critical shear stresses	37
3.3.3	Bed shear stresses.....	37
3.3.4	Sediment fluxes.....	43
3.3.5	Index of agreement.....	43
4	Sediment dynamics of Southeastern Chongming mudflat	45
4.1	Effect of waves to near-bed velocities.....	46
4.1.1	Wind condition and hydrodynamic background	46
4.1.1	Spectra of water elevations and velocities	46
4.1.2	Wave–turbulence decomposition	49
4.2	Estimation of bed shear stress	51
4.2.1	Bed shear stresses.....	51
4.2.2	Discussion on pro and cons of the approaches of estimating bed shear stresses	53
4.2.3	Impact of waves on estimating bed shear stresses	55
4.2.4	Impact of instrument settings on estimating bed shear stresses	57
4.2.5	Optimum solution for estimating the total bed shear stress in intertidal areas	58
4.3	Sedimentary processes and bed level changes	59
4.3.1	Sedimentary processes	59
4.3.2	Measured bed level changes	60
4.3.3	The effect of strong winds on bed-level changes.....	62
4.3.4	Bed recovery after wind event.....	63
5	Sediment dynamics of Nanhui Foreland mudflat.....	67
5.1	Physical processes during normal weather.....	68
5.1.1	Winds, tides, waves and currents (measurements in 2009)	68
5.1.2	Bed sediment properties.....	71
5.1.3	Bed shear stresses.....	72
5.1.4	SSC.....	74
5.1.5	Bed-level changes	75
5.2	Relative importance of waves to sediment dynamics on exposed tidal flats ...	76
5.3	Intra-tidal bed-level changes	76
5.4	Physical processes under storm conditions	78
5.4.1	Sedimentary processes during the measurement period in 2014.....	78
5.4.2	Variations in meteorological factors	80
5.4.3	Tides, waves, currents and hydrodynamic forces	82
5.4.4	SSC.....	83
5.5	Variations in the near-bed SSC	85
5.5.1	High near-bed SSC layer on tidal flats during slack water.....	85
5.5.2	High near-bed SSC layer on tidal flats during a storm event	86
5.6	Sediment transport rate in response to storm event.....	88
5.7	Discussion on sedimentary processes associated with hydrodynamic mechanisms on tidal flats.....	89
6	Sediment dynamics of Kapellebank mudflat	91
6.1	Physical processes of sheltered mudflat	92
6.1.1	Tides and waves	92

6.1.2	Bed shear stresses.....	94
6.1.3	Suspended sediment concentration.....	95
6.2	Bed level changes in response to the storm event.....	95
6.2.1	Cross-shore bed level changes.....	95
6.2.2	Effect of flow pattern to sediment transport during storm.....	96
6.3	Spatial variation in the erodibility of mudflats.....	98
6.3.1	Critical shear stress results.....	98
6.3.2	Abiotic and biotic effect on τ_e of surface sediment.....	100
6.3.3	Vertical distribution of erosion threshold.....	102
6.3.4	Summary of spatial variation in erodibility of sheltered mudflat.....	102
7	BLC model.....	105
7.1	Model description.....	106
7.1.1	Erosion rate.....	108
7.1.2	Deposition rate.....	110
7.2	Application 1: Determining of erosional parameters in wind event.....	111
7.2.1	M of surface sediment.....	111
7.2.2	Variation of τ_e and M in response to wind event.....	113
7.3	Application 2: Obtaining a vertical profile of the erosion coefficient (M).....	115
7.4	Application 3: Debate on critical shear stress for deposition (τ_d).....	118
7.5	Limitations of the model.....	119
7.5.1	Mass erosion of mudflat.....	119
7.5.2	Sediment reworking.....	120
7.5.3	Horizontal processes.....	122
8	Synthesis.....	123
8.1	Conclusions.....	124
8.1.1	Sediment dynamic processes in intertidal mudflats of different open levels.....	124
8.1.2	Relationships between sediment dynamic processes in intertidal flats.....	125
8.1.3	BLC model and its applications.....	126
8.2	Novelties.....	126
8.3	Recommendations for future work.....	127
	References.....	130
	Notations.....	149
	Abbreviations.....	151
	Acknowledgements.....	152
	List of publications.....	155
	Curriculum Vitae.....	158

1 Introduction

1.1 Background

1.1.1 Intertidal flats

Coast lines, which are among the most dynamic boundaries on the Earth, include extensive reservoirs of unconsolidated sediments. Tidal flats are widely distributed along the world's coasts (Eisma, 1998). Tidal flats can be classified as sand beaches or mudflats, according to the composition of the bed sediments. The term 'mud' always refers to a mixture of clay fractions (0–4 μm), silt fractions (4–63 μm) and water. In the later text, 'intertidal flat' mainly refers to intertidal mudflats.

Progradational tidal flats provide the groundwork and space for the expansion of salt marshes. The reclamation of upper salt marshes is frequently undertaken to increase the amount of available land for human activities (Wang et al., 2012; Walstra et al., 2015). For instance, the Chongming Island in the Yangtze Estuary has been reclaimed nine times since the 1950s. The area of Chongming Island was increased by more than 120% (from 614 km^2 to 1374 km^2) between 1958 and 2011. All the reclamation projects has increased the land in Yangtze Estuary by 80% between 1958 and 2011 (Du et al., 2016). However, under the impact of river damming and sea level rise, many mudflats in delta fronts are changing from progradational to recessional (e.g., Chu et al., 2006; Blum and Roberts, 2009; Yang et al., 2011).

In addition to this land's value as potential landmass, tidal flats' ecological and environmental functions have become hot topics (Goodwin et al., 2001; Barbier et al., 2008). Intertidal flats are considered to maintain biological diversity. These regions provide habitats and feeding grounds for various species of wildlife (Temmerman et al.,

2013) and act as natural sewage purification systems (Costanza et al., 1997). Additionally, tidal flats act as a flood defence system by dissipating wave energy, which can protect large populations along the coasts (Cooper, 2005; Barbier et al., 2008; Yang et al., 2012).

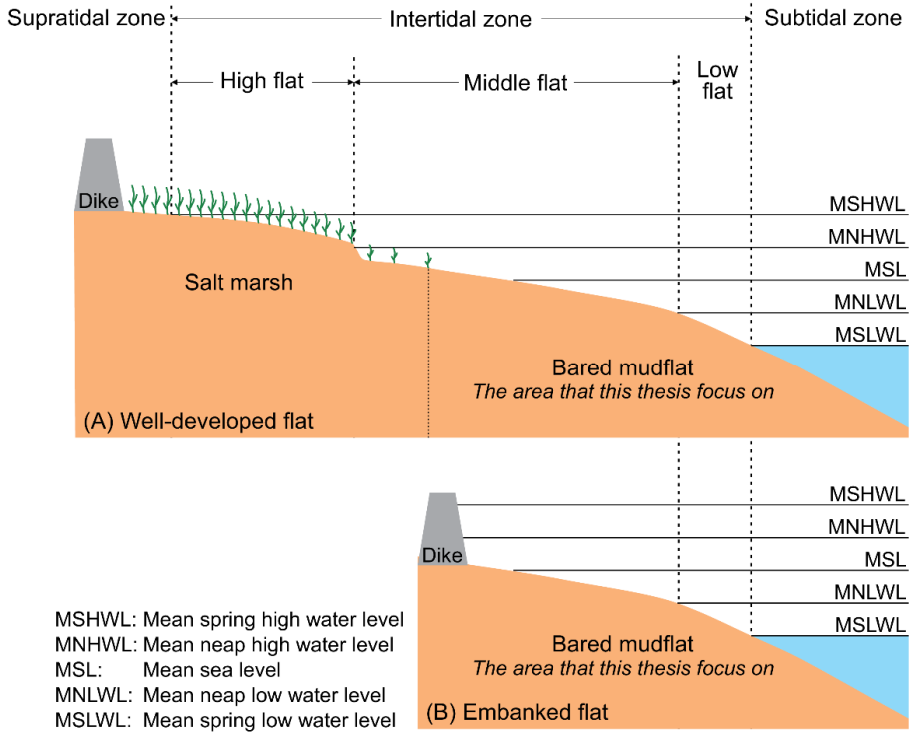


Figure 1.1: Schematized boundaries of tidal flats with fine-grained sediment. This thesis focuses on the physical processes of bared mudflats.

The upper portion of well-developed tidal mudflats is often occupied by salt marshes or mangroves, while the remaining areas are un-vegetated bared mudflats (Figure 1.1A). One example of human activity is that reclaimed tidal flats are shorter, with a very sparsely vegetated or unvegetated marsh (Figure 1.1B). Sometimes, embankments along estuaries protect the land behind them and maintain navigation channels (Figure 1.1B). In this study, we choose three typical types of intertidal flats that represent well-developed flat with salt marshes, remaining mudflat with reclamation, and semi-enclosed flat (see Chapter 2). They are in different open levels.

However, tidal flats have been challenged by effects from both the climate (e.g., sea level rises, more frequent and intense storms) (Emanuel, 2005; Webster et al., 2005; Fan et al., 2006; Harley et al., 2006) and human activities (e.g., damming in the river basin,

engineering along the coasts, mining activities, and over-exploitation of groundwater) (Yang et al., 2011; Dai and Liu, 2013; Wang et al., 2015). Hence, water and sediment discharge from rivers worldwide has decreased (Sanchez-Arcilla et al., 1998; Frihy et al., 2003; Walling, 2006). Numerous studies have shown that the main rivers in China (Yellow River, Yangtze River, and Zhujiang River) have experienced decreasing sediment discharge towards the sea and further influence the environment (Wang et al., 2007; Chu and Zhai, 2008; Dai et al., 2008; Zhang et al., 2008; Hu et al., 2009; Yang et al., 2011; Bi et al., 2014; Dai and Lu, 2014; Dai et al., 2014b; Dai et al., 2015a). In addition, global climate change may increase the frequency and strength of tropical cyclones and storms, which increase the hydrodynamic pressure on intertidal flats (Emanuel, 2005; Webster et al., 2005). Therefore, we must understand and predict the responses of mudflats from both natural and anthropogenic disturbances to protect these regions against future environmental changes.

1.1.2 Physical processes of intertidal flats

The four main components of morphodynamics are hydrodynamics forces, sediment movement, morphological changes, and bed properties (Figure 1.2). Intertidal flats experience complex hydrodynamic forcing, which is an important physical process that affects sediment transport and the shape of tidal flat morphology (Eisma, 1998; Le Hir et al., 2000; de Swart and Zimmerman, 2009; Friedrichs, 2011). Currents and waves are the main hydrodynamic forces in intertidal environments. Currents in intertidal flats are influenced by tidal currents, which are caused by periodical rises and falls in water level, and wind-induced currents. Waves are generated by either local winds or the propagation of offshore waves (swells) (Le Hir et al., 2000; Holthuijsen, 2007).

Sediment movement has been a longstanding research topic because this phenomenon results in morphological changes by coupling with hydrodynamic forces (Pejrup, 1988; Amos and Tee, 1989; Friedrichs, 2011). Sediment movement processes include erosion and deposition (vertical) and suspended sediment transport by advection, bedload transport and gravity-driven sediment transport (horizontal) (Wright et al., 1988; Friedrichs and Wright, 2004; Ma et al., 2010). In this study, we limit ourselves to the first three processes and exclude bedload transport.

In addition to hydrodynamic processes and sediment transport, fine-grained sediment bed properties, especially the erodibility, have been emphasized in recent studies of erosion processes (Maa et al., 1998; Le Hir et al., 2011; Winterwerp et al., 2012; Ge et al., 2015). The critical shear stress for erosion (τ_c) is often set as a constant in numerical models and is the mostly widely used parameter to quantify the erosion rate by the famous Partheniades-Ariathurai erosion formulation. Ge et al. (2015) obtained the τ_c distribution for the Yangtze estuary, Hangzhou Bay and adjacent East China Sea by using the FVCOM (Finite-Volume Community Ocean Model) and retrieved SSC (suspended sediment

concentration) data from satellite images. τ_e varied from 0.1 to 2.0 Pa. This study concluded that the sediment transport model significantly improved the simulation of the distribution and spatial variability of the SSC in Yangtze River Estuary by implementing τ_e distribution.

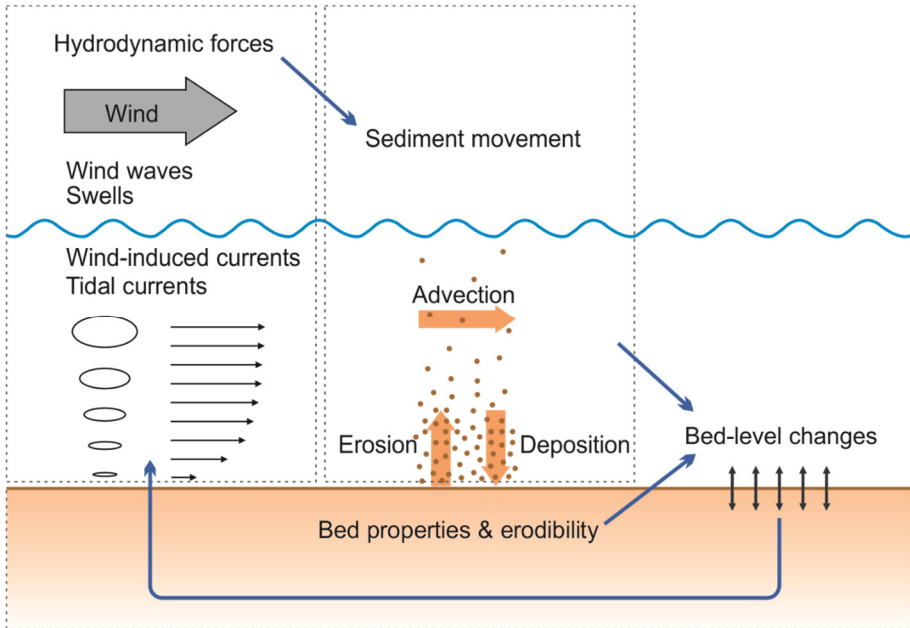


Figure 1.2: Schematized sediment dynamic components involved in tidal flat evolution.

1.2 State of the art

1.2.1 Hydrodynamics forces under combined wave–current action

Bed shear stress, as an indicator of hydrodynamic force, is a critical parameter in sediment dynamics on tidal flats, especially in the calculation of erosion rates (Friedrichs et al., 2000; Friedrichs and Wright, 2004; Wang et al., 2013). The total bed shear stress is the combined contributions from waves and currents. Numerous studies have estimated the total bed shear stress by means of a wave–current interaction model (Grant and Madsen, 1979; Fredsøe, 1984; Christoffersen and Jonsson, 1985; O'Connor and Yoo, 1988; Huyng-Thanh and Temperville, 1990; Myrhaug and Slaattelid, 1990; van Rijn, 1993; Davies and Gerritsen, 1994; Shi et al., 2015), and an overview is given by Soulsby (2005). These wave–current interaction (WCI) models have been widely applied in

numerical models of estuarine and coastal areas (Villaret and Latteux, 1992; Lesser et al., 2004; Warner et al., 2008; Shi et al., 2016). The waves and currents interact in a non-linear way, leading to a total bed shear stress that is not a simple linear addition of wave-induced and current-induced bed shear stress.

The WCI model is an algebraic equation that combines the pure wave-induced and pure current-induced bed shear stresses to obtain the total bed shear stress that accounts for the direction of the waves and currents. The determination of the wave-induced bed shear stress and the current-induced bed shear stress is based on bulk parameters. The wave-induced bed shear stress is generally obtained by using a linear wave theory (Green and Coco, 2007) for a given wave height, wave period, and water depth. The bed shear stresses associated with currents are generally estimated based on the assumption of stationary uniform flow and using the log law; however, this assumption is often violated.

The direct measurement of bed shear stresses presents some difficulties (Grant and Madsen, 1979; Soulsby, 2005). Further advances in acoustic instruments have allowed systematic velocity measurements to be made over longer periods, at higher sampling rates and with greater accuracy (Wang et al., 2006, 2012). The ADV (Acoustic Doppler Velocimeter) makes high-frequency measurements of the 3D velocities at a single point, whereas the ADCP (Acoustic Doppler Current Profiler) measures velocities over a profile. Despite these improvements, the difficulty remains of selecting the most appropriate theory to obtain the current-induced bed shear stress. The most widely used theories are: (1) the LP (log-profile) method; (2) the TKE (turbulent kinetic energy) method; (3) the TKEw (modified TKE) method; (4) the Reynolds stress (RS) method; and (5) the ID (inertial dissipation) method. The LP method uses the mean component of a velocity profile series, whereas the other methods use the turbulent velocity. Kim et al. (2000) systematically compared the current-induced bed shear stresses obtained using the LP, TKE, RS, and ID methods, and found differences of up to 19% between the TKE and LP methods. No significant wave events were recorded. They suggested that all methods should be applied simultaneously to help better estimate bed shear stress. On many tidal flats, the conditions are generally more complex than in their study. As the water depth changes significantly, the relative locations of the fixed measurement positions change. Due to the shallow water depth, wind-driven flow may have a significant influence and disturb the logarithmic flow profile.

Having recognised this inaccuracy, several studies have been conducted to compare some of the above methods of obtaining the bed shear stress (Kim et al., 2000; Andersen et al., 2007). One of the assumptions is that the vertical component of near-bed velocity is not contaminated by waves (see also Stapleton and Huntley, 1995). Wave motion is expected to have a great impact on the velocity distribution near the bed on tidal flats, especially in wavy conditions; e.g., during storms or typhoons.

1.2.2 Intra-tidal sedimentary processes

Sedimentary processes in coastal areas have implications for studies in geomorphology, engineering, ecology, and biogeochemistry (Hooke et al., 1996; Riggs et al., 1998; Schoellhamer et al., 2007; Montserrat et al., 2011). Tidal flats are an important sedimentary coastal environment (Gao, 2009; Friedrichs, 2011), and tidal flat processes are closely connected to patterns of human activity in many regions of the world. Knowledge of sedimentary processes is fundamental to an understanding of the mechanisms of morphological evolution in these areas, and for predicting the future evolutionary trends of mudflat development or decay.

Although numerous studies have been conducted on sedimentary processes and their associated hydrodynamics in intertidal zones, most of them have focused on either: (1) intra-tidal and neap–spring variations in current velocity and SSC (e.g., Pejrup, 1988; Collins et al., 1998; Le Hir et al., 2000; Andersen and Pejrup, 2001; Quaresma et al., 2007), or (2) bed-level changes based on surveys undertaken after ebb and when the tidal flat is exposed to air (e.g., Kirby et al., 1992; de Brouwer et al., 2000; Andersen and Pejrup, 2001; Yang et al., 2003; Fan et al., 2006). These between-tide surveys are useful for measuring the net bed-level changes associated with a succession of tidal cycles, but they are unable to record the details of erosion and deposition within tidal cycles. The magnitudes of erosion and deposition within a tidal cycle may be significantly greater than the net change between tidal cycles. Relatively little is known about sediment exchange processes between the water column and the seabed under combined wave–current action (Andersen et al., 2007; Shi et al., 2012). In particular, it is not clearly known whether fluid mud, or a thin near-bed layer of extremely high SSC (usually $>10 \text{ kg/m}^3$) (Kineke et al., 1996; Ogston et al., 2000), can be formed on tidal flats under calm weathers. There is a great need to integrate high-resolution data on currents, waves, SSC, and bed-level changes during tidal inundation to more fully understand the sedimentary processes occurring on tidal flats.

1.2.3 Bed sediment properties

For cohesive sediment bed, estimation of erosion threshold is important to predict erosion rate of fine-grained sediment, but have remained to be a challenge (Andersen et al., 2007; van Prooijen and Winterwerp, 2010; Salehi and Strom, 2012). Efforts have been made in the last two decades to measure the erodibility of sediment bed, see summary by Le Hir et al. (2008). Some of them carried out measurements in laboratory flumes using artificial kaolinite or homogenous mixtures to study the effect of cohesion on bed strength (Mehta and Partheniades, 1982; Gomez and Amos, 2005; Jacobs et al., 2011). Sediment beds in these experiments, however, were far from the real sediment bed. Others used an alternative approach by placing undisturbed sediment cores in a fitted place of an erosion

device, and making controlled forcing on the sediment surface (Gust and Morris, 1989; Schünemann and Kühn, 1993; Austen et al., 1999; Bohling, 2009; Dickhudt et al., 2009; van Maren et al., 2009). Furthermore, some *in situ* annular flumes could be operated directly on emerged sediment beds (Amos et al., 1992; Widdows et al., 1998; Houwing, 1999; Tolhurst et al., 1999; Paterson et al., 2000; Neumeier et al., 2006). The devices are aimed to study the resuspension characteristics, but operations often can be long and tricky (Le Hir et al., 2008). Different from those various flumes/devices allowing uni-directional flows only, Andersen et al. (2007) read critical erosion shear stress by comparing time series of bed shear stress and high-temporal-resolution bed level changes (also see Salehi and Strom, 2012; Shi et al., 2015). This approach obtains erosion threshold of surface sediment, and asks for accurate estimation of bed shear stress under natural wave-current action.

Erosion threshold for coarser particles, like sands and gravels, are estimated as soon as grain size distributions are known (Shields, 1936; Paphitis and Collins, 2005). According to the previous studies mentioned above, however, when sediment bed is dominated by mud (grain size $\leq 63.5 \mu\text{m}$), sediments are stabilized by cohesive force caused by surface charge acting on each particles (Taki, 2001). van Ledden (2003) further proposed a cohesion triangle diagram, and set a clay content of 7% as the transition between cohesive and non-cohesive mixtures. Critical shear stress for erosion has often been related with bulk density of relative freshly deposited mud (Mehta, 1988; Delo and Ockenden, 1992; Armanini, 1995; Mitchener and Torfs, 1996; Taki, 2001).

In addition, an increasing amount of researches of biological effects on erosion threshold of mud bed (Andersen et al., 2005; Le Hir et al., 2007). Generally, micro-phytobenthos act as stabilizer which form a biofilm in high densities and produce extracellular polymeric substances (EPS) to protect sediment surface against hydrodynamic forces (Austen et al., 1999; Riethmüller et al., 2000; de Brouwer et al., 2005; Andersen et al., 2010; Fang et al., 2014), while meso- and macro-zoobenthos are mainly destabilizer. For instance, benthic bivalve *Macoma balthica* is a bioturbator which increases sediment erosion potential by its burrowing and feeding activities (Willows et al., 1998; Widdows et al., 2000; van Prooijen et al., 2011), and the mud snail *Hydrobia ulvae* increases the erodibility by increasing bed roughness and egesting organic pellets that are easily eroded (Andersen and Pejrup, 2002).

1.2.4 Response of intertidal mudflat to wind events

Numerous studies have sought to clarify the sedimentary processes that act on intertidal mudflats (see Mehta and McAnally (2008) and Friedrichs (2011) for recent overviews). Earlier work on the impacts of combined wave–current action on tidal flats suggests that waves, which are wind-related phenomena, are important agents of mudflat erosion (Green et al., 1997; Christie et al., 1999; Kim et al., 2000; Zhu et al., 2014). Many

studies of wave effects on tidal flat sediment processes and morphology have focused on storm events (Ding et al., 2003; Fan et al., 2006; Palanques et al., 2006; Xu et al., 2015; Maan et al., 2016). Since moderate wave strength may also deeply affect sediment resuspension and transport (Green and Coco, 2014), study of normal wind effects on tidal flat bed-level variability is also needed. In addition, most studies have been based on either field measurements (Yang et al., 2003; Fan et al., 2006; Siadatmousavi and Jose, 2015) or numerical models (Ding et al., 2003; O'Shea and Murphy, 2013; Hu et al., 2015b). Studies combining field measurements and modelling are relatively scarce.

Detailed prediction strategies for bed-level changes over small spatial and temporal scales are still prone to considerable uncertainty. One of the challenges is that several key parameters can be difficult to quantify precisely. For example, the erodibility parameter, the erosion coefficient M , can vary by at least an order of magnitude (Whitehouse et al., 2000). Similarly, validation of erosion models can be limited by the techniques employed to measure bed-level changes at high temporal and vertical resolutions.

1.2.5 *In situ* measurements on intertidal flats

In comparison with those on sandy beaches, the sedimentary processes, morphological changes and their mechanisms on intertidal mudflats are poorly understood (Wang et al., 2006) because *in situ* measurements are difficult to carry out with manpower in intertidal flats. The tall salt marsh before the flat with cohesive fine-grained material, e.g., *Phragmites australis*, whose height is 2.9 ± 0.6 m in the Southeastern Chongming tidal flat (Chapter 2) in the Yangtze River Estuary (Cai et al., 2014), might block the path.

Over the past half century, numerous approaches have been developed to study the morphological development of intertidal flats on various spatial and temporal scales.

(1) The propagation speed and erosion/accretion of intertidal flats and their adjacent areas are often obtained by digitalizing and comparing **bathymetric maps** (Yang et al., 2011; Dai et al., 2014a) and **satellite images** (Han and Yun, 2003; Jangir et al., 2016; Sarmiento et al., 2016) from different years. Bathymetric maps only provide depth information below the 0-m isobath, so this method cannot reveal the details of intertidal flats. Satellite images provide morphological changes of complete tidal areas by analysing the light spectra, although their accuracy must be improved.

(2) **Isotope records** (^{210}Pb and ^{137}Cs) have been widely used to determine the sedimentation rates of intertidal flats (Armentano and Woodwell, 1975; Williams and Hamilton, 1995; Wang et al., 2005). These records provide sedimentation records on a time scale of tens to hundreds of years, which is not sufficient to learn the erosion processes.

(3) **The double/triple-rod method** (Bird, 1986; Yang et al., 2003; Fan et al., 2006; Lawler, 2008; Nolte et al., 2013) is conducted during tidal emersion. The bed elevation

over a larger spatial scale measured during tidal emersion can also be measured by **GIS-based elevation measurements**, including RTK-GPS (Real-Time Kinematic Global Positioning System; Yang et al., 2001) and airborne/ground-based laser altimetry (LiDAR) techniques (Nagihara et al., 2004; Mancini et al., 2013; Millard et al., 2013). Recently, Hu et al. (2015a) developed an **automated SED-sensor** (Surface Elevation Dynamics sensor), which used a series of phototransistors to detect the position changes of the sediment surface. This method may require less labour than the first two methods. These three methods can elucidate the evolution of tidal flats over inter-tidal, neap-spring, storm, seasonal, and even long-term cycles.

(4) In recent decades, **acoustic measurements** have been used to measure bed position changes in high temporal and vertical resolution ($\pm 1\text{--}2$ mm) during tidal submergence. These measurements are achieved either by individual instruments, e.g., ALTUS and Altimeter (Gallagher et al., 1996; Jestin et al., 1998; Thornton et al., 1998; Christie et al., 1999; Saulter et al., 2003; Turner et al., 2008), or by functions in some ADVs (Andersen et al., 2006; Andersen et al., 2007; Zhu et al., 2014; Shi et al., 2015). To date, this approach is the only method that can obtain detailed bed-level changes during tidal submergence.

Since the advances in the technology, field-based instruments have become more portable and easier to handle, and detailed sedimentary processes on intertidal flats have since been studied (Allen and Duffy, 1998; Christie et al., 1999; O'Brien et al., 2000; Wang et al., 2006; Andersen et al., 2007; Quaresma et al., 2007; Shi et al., 2012; Wang et al., 2012). On the mudflat on Jiangsu coast, which is to the north side of the Yangtze Estuary, Wang et al. (1999, 2006, 2012) have carried out the pioneer study on sediment dynamic processes based on *in situ* measurements along Chinese coast. Their MIDAS-400 Customised Data Acquisition System was composed by six electromagnetic current meters, turbidity sensors, logger electronics with conductivity, temperature and pressure sensors, battery pack and cables. The studies showed that the MIDAS-400 system can be utilized to collect high-resolution hydrodynamic and sediment dynamic data under the condition of wave–current interactions on intertidal flats, and is a useful tool to study material transport processes.

In addition to the aforementioned bed-level changes, three basic elements are considered in *in situ* measurements. (1) Waves are often transformed from the water depth, which is sampled in high frequencies. Recently, directional wave gauges that use acoustic surface tracking have been developed, e.g., AWAC (acoustic wave and current profiler, Nortek) and the Workhorse ADCP (acoustic Doppler current profiler, RD Instruments). (2) ADVs (acoustic Doppler velocity meter) and ADCPs have been used more often to measure current velocities than magnetic velocity meters in recent years. (3) The optics and acoustics have been used to measure the suspended sediment concentrations (SSC) (Thorne et al., 2007). Optical backscatter sensors (OBS) are the most frequently and

widely used method, while a more sophisticated instrument that uses laser diffraction has been developed to measure both the SSC and particle size distribution.

1.3 Objectives

The main objectives of this study are as follows:

- Study the sedimentary processes and bed-level changes under combined wave–current action forces on intertidal flats by carrying out integrated *in situ* measurements of waves, tidal currents, SSC and bed-level changes at high temporal and spatial resolutions using advanced instruments under different wind conditions;
- Demonstrate erosion and deposition stages by comparing the total bed shear stress under combined wave–current action (τ_{cw}) with critical bed shear stress for erosion (τ_e), which is derived from measured soil mechanical characteristics of bed sediment;
- Simulate intra-tidal bed-level changes by calculating the erosion and deposition rates. A combination of measurements and simulations is used to further our understanding of erosion–deposition mechanisms and improve the given model.

1.4 Approaches and thesis outline

The approaches to achieving the aforementioned objectives are presented in Figure 1.3. The study areas and observation sites, and why we chose these locations, are introduced in Chapter 2. Chapter 3 illustrates comprehensive *in situ* observations in the three study areas, including the instruments (usages and settings) and sampling work. Besides, calculation of sediment dynamic parameters are presented in Chapter 3.

Chapters 4–6 demonstrate the sediment dynamic processes (e.g., water depth, wave height, wave period, current velocities, suspended sediment concentration, bed-level changes, water content and grain size distribution of bed sediments) interpolated from instruments or measurements. Discussion related to the objectives is also presented in these three chapters. In Chapter 7, we describe a BLC model incorporated with inputs by using the *in situ* measured parameters. Implementations of this model (detecting the effects of strong wind, calibrating the erosional parameters, and discussing sediment deposition motion) are presented.

Chapter 8 integrates the relevant findings and presents important conclusions and outlooks for future studies.

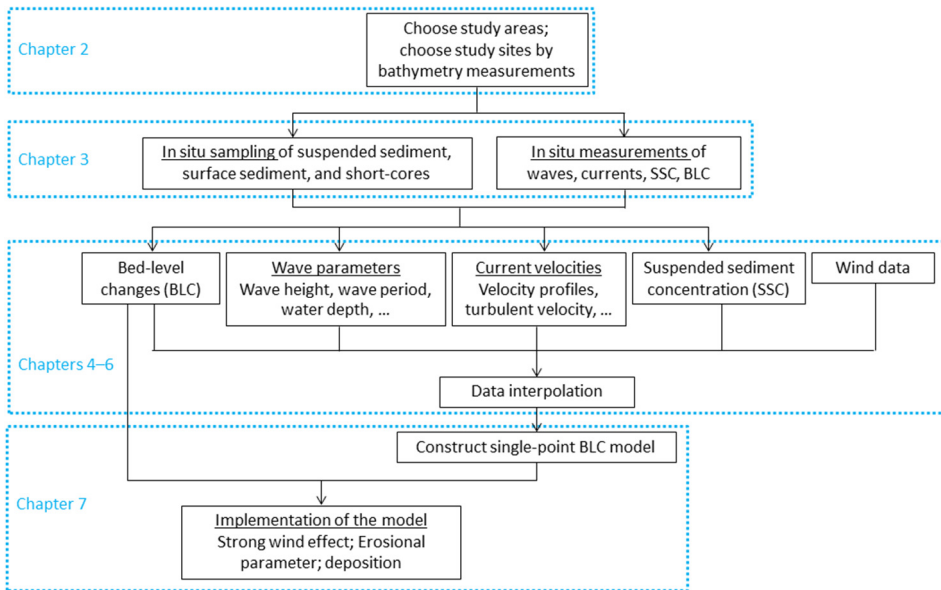
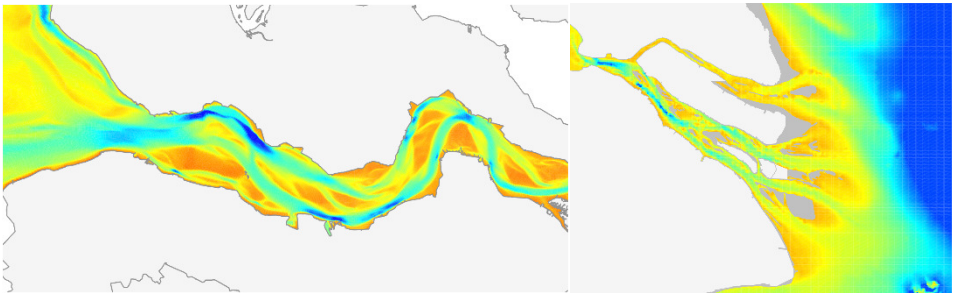


Figure 1.3: The approach and outline of this thesis.

2 Study areas

This chapter illustrates the following three study areas and reasons of choosing them: Southeastern Chongming mudflat in the Yangtze River Estuary (semi-open), Nanhui Foreland mudflat in Hangzhou Bay (open), and Kapellebank mudflat in the Westerschelde Estuary (sheltered).



2.1 Reasons of choosing the study areas

The Yangtze Estuary has great economical meaning with respect to human settlement in large-density and land use. Moreover, estuaries are also important shipping routes, which stimulate the economic development. So as the Westerschelde Estuary to the Netherlands and Belgium. Southeastern Chongming mudflat and Nanhui Foreland mudflat in the Yangtze River Estuary and Kapellebank mudflat in the Westerschelde Estuary are chosen in this study. Bed sediment of the three intertidal flat are dominated by mud (fine grained sediment with grain size less than $63\ \mu\text{m}$), thereby the three tidal flats are called 'mudflat'. The other similarity is that they are all meso-tidal or macro-tidal flats. Tidal ranges are 2.5 m, 3.2 m and 4.5 m in Southeastern Chongming mudflat, Nanhui Foreland mudflat, and Kapellebank mudflat, respectively.

Difference among the three intertidal mudflats is the morphological characteristics. Southeastern Chongming mudflat is a well-developed flat (Figure 1.1A) having salt marsh on the upper flat. It is a semi-open tidal flat which is connected with a shoal by a secondary channel. Nanhui Foreland mudflat has been affected by reclamation projects carried out since 1999. Remained flats (Figure 1.1B) of southern Nanhui Foreland mudflat has limited nature salt marsh, with some even being protected by artificial cliff. It is located in the transition zone between two estuaries, which is an open tidal flat exposed to waves and strong tidal currents. Kapellebank mudflat is a fringing tidal flat, which is semi-enclosed and less impacted by waves, in the Westerschelde Estuary. Salt marsh development depends on local hydrodynamic conditions. Upper part of Kapellebank mudflat is around mean sea level, so that rare vegetation is found on this flat. They are the three typical types of intertidal flats in an estuary: open and semi-open flats are often seen in the estuarine front, while type of Kapellebank mudflat are often distributed along the fringing of estuaries.

2.2 The Yangtze Estuary: Southeastern Chongming mudflat

The Yangtze River is the longest (6300 km) river in Asia and the third longest in the world. According to records from the Datong gauging station, which is the closest gauging station to the estuary (Figure 2.1), Yangtze ranks 5th globally in terms of water discharge ($9.05 \times 10^8\ \text{m}^3/\text{yr}$) and 4th in terms of sediment load ($4.70 \times 10^8\ \text{t}/\text{yr}$). Yangtze has the largest basin area ($1.80 \times 10^6\ \text{km}^2$) in southern Asia, ranking 12th globally (Milliman and Farnsworth, 2011). The Yangtze Basin is located in a subtropical humid climate zone. Approximately half of all precipitation (1100 mm, yearly average) joins the river

discharge towards the sea (Zhao et al., 2000).

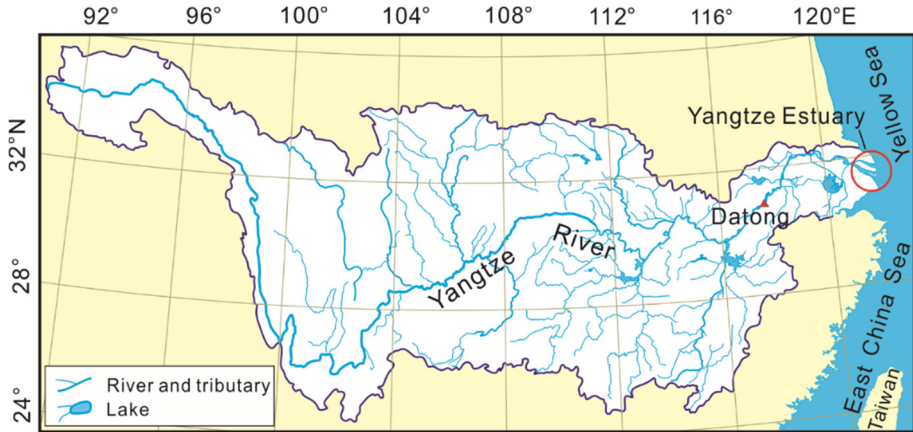


Figure 2.1: The Yangtze River Basin.

The morphology of the Yangtze Estuary formed after five development processes over the past 2000 years: the propagation (25 m/yr on average) of shoals near the southern bank; the attachment of shoals and small islands to the northern bank; the narrowing of the estuarine reach from 180 km to 90 km; the formation of the channels; and the deepening of the channel (Chen et al., 1979). The Yangtze Estuary is defined from Datong (Figure 2.1), where the tidal effect ends in dry season, to the area of the 30–50 m isobath in the delta front. After Xuliujing, the estuary is a three-level bifurcation system with four outlets into the sea (Figure 2.2A): Chongming Island divides the estuary into the South Branch and North Branch; Changxing Island and Hengsha Island divide the South Branch into the South Channel and North Channel; and the Jiuduansha shoal divides the South Channel into the South Passage and North Passage.

The Southeastern Chongming mudflat, which is a semi-exposed tidal mudflat, is located in the Yangtze River Delta. According to records from the Sheshan gauging station, which is located 20 km to the east of our study site, the tides in the Yangtze Estuary are mixed semi-diurnal with an average range of 2.5 m, reaching up to 3.5–4.0 m during spring tides (Figure 2.2A). The wind speed in this region is highly variable, with multi-year averages of 3.5–4.5 m/s and a maximum of 36 m/s (GSCI, 1988; Yang et al., 2008). Monsoon-driven winds are south-easterly in summer and north-westerly in winter. Several storms hit the study area annually, with the wind speeds of storms being approximately 13% greater than 25 m/s (Yang et al., 2003). Tropical cyclones impact the study area almost every summer (Hu et al., 2007). Wind speed and direction data for 31.5°N 122.3°E were obtained from the European Centre for Medium-range Weather Forecasts (ECMWF) every three hours throughout our study period.

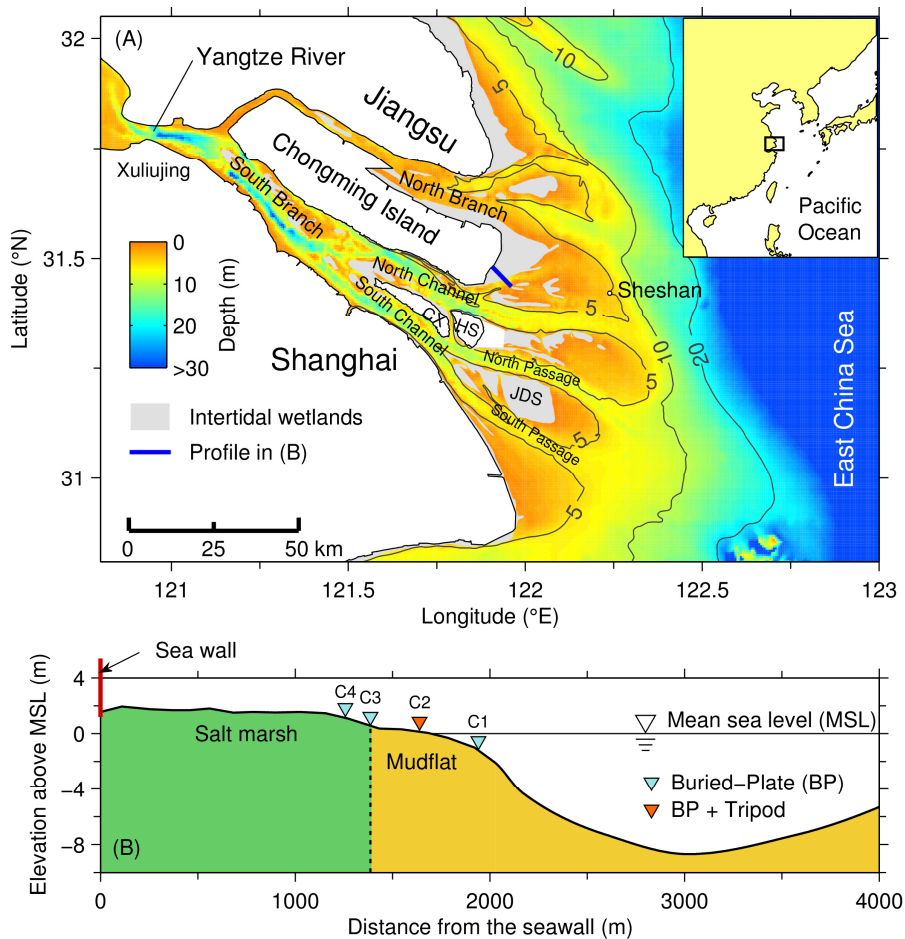


Figure 2.2: (A) Map of the Yangtze River Delta; (B) cross-shore bathymetric profile on which the observation sites stand. The abbreviations in (A) are as follows: CX — Changxing Island; HS — Hengsha Island; JDS — Jiuduansha shoal.

The cross-shore bathymetry profile is shown in Figure 2.2B, along with the position of our observation sites. Our transect crossed the centre of a secondary channel, which was approximately 2 km wide and 8 m deep. The intertidal flat profile is convex upward, with the innermost 1.4 km being covered by salt marshes and the remainder being unvegetated mudflats. We measured the bed-level changes on sites 1–4, with the elevations being -1.21 m (site C1; lower flat), 0.17 m (site C2; middle flat), 0.52 m (site C3; salt marsh front), and 1.15 m (site C4; salt marsh) above the mean sea level (MSL). The dominant species of salt marsh front was *Scirpus mariqueter*. The measured heights, stem diameters, and densities were 24.7 ± 10.3 cm, 1.2 ± 0.2 mm, and 2056 ± 113 no./m² at site

C3 and 9.1 ± 4.5 cm, 1.6 ± 0.5 mm, and 1870 ± 127 no./m² at site C4. We conducted systematic measurements of waves, currents, SSCs, bed level changes, and bed sediment properties at site C2, which was 1.65 km seaward of the sea wall.

The bed sediment on the mudflat generally consists of silt (median grain size <63 μm), more than 50% of which is coarse silt (32–64 μm) (Yang et al., 2008). When the tidal flat was exposed during the measurement periods, we observed only limited evidence of diatoms. In addition, bed ripple structures were not visibly affected by macro benthic species, which are relatively scarce at our site according to the low density of holes caused by their activities. Consequently, we consider the effects of such biological processes on our estimates of erosion and deposition rates to be minimal at this site.

2.3 The Hangzhou Bay: Nanhui Foreland mudflat

The Hangzhou Bay is situated to the south of the Yangtze Estuary (Figure 2.3B). The length and area of the bay are 99 km and 5100 km², respectively. The funnel-shaped bay leads to an increasing tidal range (maximum 7.6 m) and tidal current speed (maximum 2.0 m/s) from the mouth to the inner bay (Shi, 2001). Hangzhou Bay is famous for hosting a world-famous tidal bore, Qiantang Bore, which reaches 9 m in height and propagates in speed up to 40 km/h. Water and sediment exchanges between Hangzhou Bay and the Yangtze Estuary are frequent under the interaction of the Yangtze River plume, tidal forces and longshore current system (Cao et al., 1989; Su and Wang, 1989).

The Nanhui Foreland, which is located on the delta front of the Yangtze River Delta (Figure 2.3), is an exposed tidal mudflat. The Nanhui Foreland is located in a transition zone between the Hangzhou Bay and the Yangtze Estuary (Figure 2.3B). The water discharge and sediment load into Hangzhou Bay from the Qiantang River is only 4.2% and 1.4% of that from the Yangtze River, respectively (Chen, 2004), so the coastal evolution of the Nanhui Foreland is mainly governed by the Yangtze River. Over the past 2000 years, the Nanhui coast has prograded rapidly at a rate >10 m/yr (Yang et al., 2001). The combination of waves from east, and water and sediment discharge from Yangtze River and Qiantang River from north and south have resulted in Nanhui Foreland flat extending south-eastward (Chen et al., 2003). However, in recent years, especially since the closure of the Three Gorges Dam (TGD) in 2003, the sediment discharge from the Yangtze River has been drastically reduced, which has resulted in long-term erosion along the Nanhui coast (Yu and Lou, 2004; Yang et al., 2006).

The tides in the Hangzhou Bay are mixed semidiurnal, with the tidal range at Luchaogang, a gauging station close to our observation site (Figure 2.3B), being 3.2 m on average and greater than 4.0 m during spring tides. Monsoon-driven winds travel southeast in summer and northwest in winter. The multi-year averaged wind speed is 4

m/s on the land areas in Nanhui (GSCI, 1988) and 7 m/s on the open sea (at the 5-m bathymetric contour off the Nanhui Foreland) (Zhu et al., 1988). The maximum wind speed that has been recorded on the Yangtze Delta is 43 m/s (Zhu et al., 1988). The Nanhui coast is wave exposed. The mean and maximum wave heights that have been recorded at the 5-m bathymetric contour off the Nanhui Foreland are 1.0 m and 6.2 m, respectively (GSCI, 1988). Seasonal changes in the bed level of the tidal flat at Luchaogang reach 40 cm. The bed sediment of the tidal flat is generally silt (median grain size $<63 \mu\text{m}$), although very fine sand ($63\text{--}125 \mu\text{m}$) is occasionally found during seasons of strong erosion (Yang et al., 2008). The surface SSC at Luchaogang ranges from 0.46 kg/m^3 to 1.40 kg/m^3 , with an average of 0.99 kg/m^3 (Chen et al., 2006). The annual averaged surface SSC at Luchaogang has decreased by 25% since the closure of the TGD (Li et al., 2012).

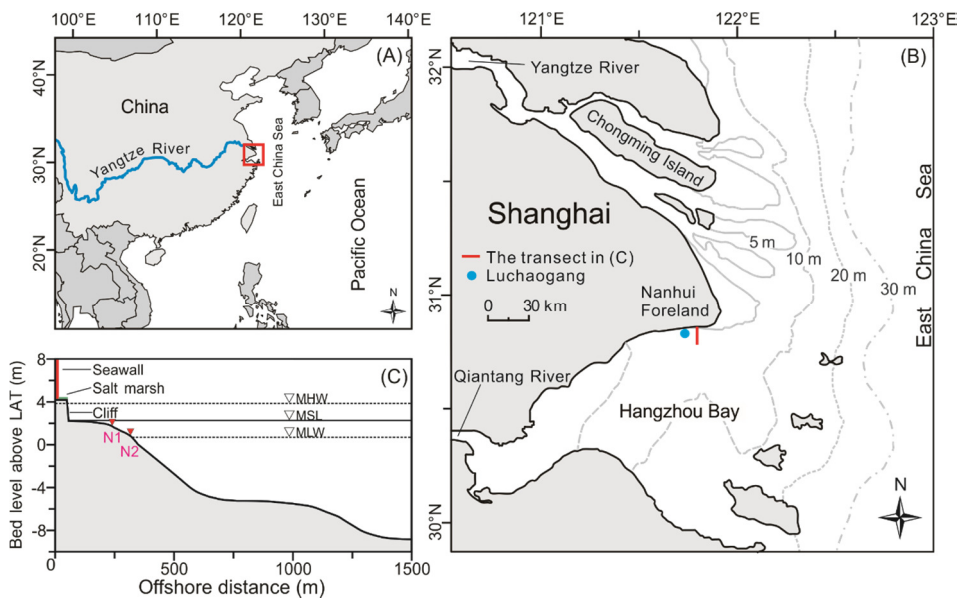


Figure 2.3: (A) Map of the Yangtze River and East China Sea. (B) Map of the Yangtze River Delta, which is shown by the red square in (A) and shows the study area and observation transect (red line). (C) Cross-shore bathymetric profile of the Nanhui Foreland mudflat (Chapter 5), on which the observation sites stand. Sites N1 and N2 are the study sites of measurements from 2009 and 2014, respectively. The elevation datum is based on the lowest astronomic tide (LAT).

The elevation of the presently studied mudflat (Figure 2.3C) is below the mean sea level (MSL). The presence of a 2-m-high cliff between the mudflat and an abandoned salt marsh (Figure 2.3C) indicates that the upper part of the mudflat is eroding. The mudflat is now less than 300 m wide. The cross-shore profile of the mudflat is convex upward,

with a mean gradient of $\sim 7\%$. The observation sites of the measurements in December 2010 and September 2014 were 200 m and 300 m seaward from the armoured cliff and were 0.7 m and 1.0 m below MSL (i.e., 0.9 m and 0.6 m above the mean low water level), respectively. The bed slopes on the seaward side of the observation site exceed 10% to a water depth of ~ 8 m below the lowest astronomic tide (LAT), which is located ~ 1500 m offshore (Figure 2.3C).

On the Nanhui Foreland mudflat, the amount of biomass derived from benthos is very low, and no salt marsh is present (GSCI, 1988). The study site shows no obvious evidence of diatom biofilms or sediment-mediated biological disturbances, such as holes and faecal casts from macro-benthos, which is probably because of the highly dynamic bottom sediments (Yang et al., 2008), high turbidity, and low elevation of the mudflat (submerged most of the time). Local variations, such as strong tidal currents, exposure to waves, and sediment instability, can restrict the development of benthic communities in intertidal zones (Ysebaert et al., 2003). Therefore, the biological effects on the near-bed sediment dynamics are considered to be minor in this study.

2.4 The Westerschelde Estuary: Kapellebank mudflat

Oosterschelde and Westerschelde, which are located in the Zeeland province in the southwestern Netherlands, used to be the estuaries of the Scheldt River. Since the closure of the Oosterschelde Storm Surge Barrier since 1986, Westerschelde has become the only direct route towards the sea. The Westerschelde Estuary consists of a freshwater zone between Ghent and Rupelmonde and a mixing zone between Rupelmonde and Vlissingen. The distance from Ghent to Vlissingen is 190 km. The annual river discharge ranges between 50 and 200 m^3/s , with a yearly averaged value of 110 m^3/s and maximum value >600 m^3/s between January and April. The sediment along the estuarine margins, i.e., intertidal area and salt marshes, is much finer than that in the channels and shoals. The surface sediments along the estuarine margins have a median grain size less than 125 μm , with a high percentage of mud (<50 μm in the report) (Kuijper et al., 2004).

Kapellebank is a semi-enclosed tidal flat along the northern bank of the Westerschelde Estuary in the Netherlands (Figure 2.4A). This tidal flat has a width of 1.8 km and a length of 0.9 km. The tidal flat faces a channel to the south. The tidal wave is semi-diurnal, with a mean tidal range around 4.5 m, which indicates a macrotidal flat. The bed slope of the flat is mild (ca. 3%). Measurements from 1993 showed that the bed sediment in this area is dominated by mud (Kuijper et al., 2004). From early spring until the onset of summer, 80% of the surface of the intertidal flat is covered by visible brown biofilm and forms a hummock-hollow pattern (Figure 2.5; Weerman et al., 2011).

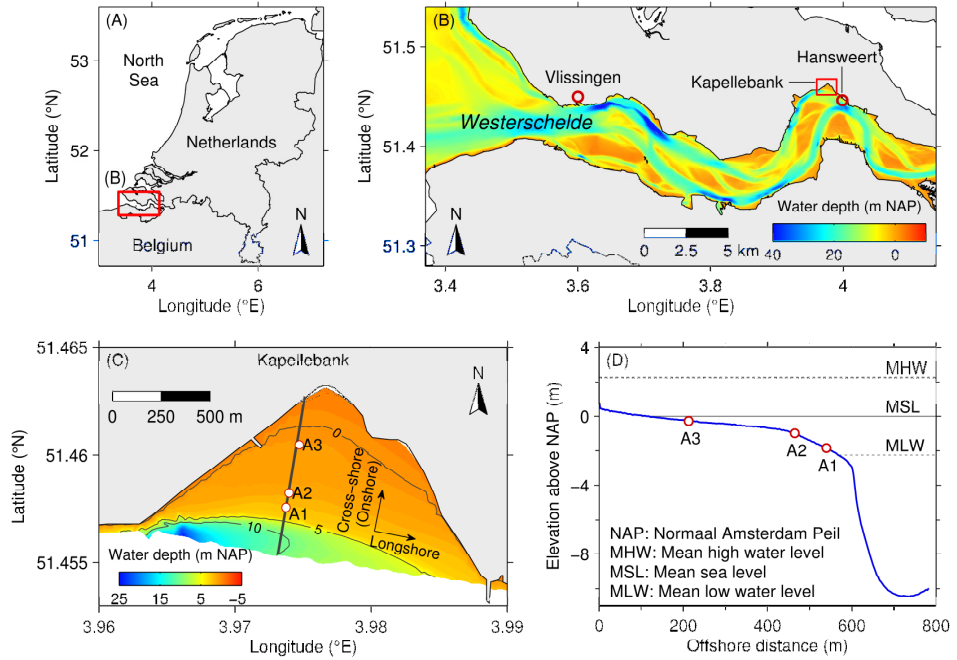


Figure 2.4: Map of study area. (A) Southeast coast of the North Sea; (B) Westerschelde Estuary showing the locations of studied mudflat (Kappellebank), meteorological station (Vlissingen) and tide station (Hansweert); (C) Sites of measurements on the Kappellebank mudflat; and (D) cross-shore bathymetry profile showing the elevations of the measurement sites.



Figure 2.5: Photograph of the Kappellebank intertidal flat, which shows a visible hummock-hollow pattern from diatoms (taken by B. C. van Prooijen).

The observation sites were located on a transect that was 100 m from the longest cross-shore transect (Figure 2.4C). The lowest site, A1, was located on the interface of the intertidal flat and the channel ($51^{\circ}27'24''\text{N}$, $3^{\circ}58'21''\text{E}$), with an elevation of -1.84 m NAP (Amsterdam Ordnance Datum, MSL) (Figure 2.4D). The elevations of sites A2 ($51^{\circ}27'30''\text{N}$, $3^{\circ}58'24''\text{E}$) and A3 ($51^{\circ}27'37''\text{N}$, $3^{\circ}58'27''\text{E}$) were -0.98 m and -0.25 m NAP, respectively.

3 Material and methods

This chapter introduces the methods of collecting data on the three mudflats, including *in situ* measurements setups (Section 3.1), sample collections and sample analysis in lab (Section 3.2). Section 3.3 describes the calculation models that establish the database of sediment dynamic parameters.



*Left: observation frame deployed on Southeastern Chongming mudflat (photo by Q. Zhu);
Right: observation frame deployed on Kapellebank mudflat (photo by B.C. van Prooijen).*

3.1 *In situ* measurements setup

3.1.1 Instrumentation setup

Measurement durations of the three mudflats were:

- Southeastern Chongming mudflat (Yangtze Estuary): July 23–August 3, 2011.
- Nanhui Foreland mudflat (Hangzhou Bay): December 18–19, 2009; September 9–30, 2014.
- Kapellebank mudflat (the Westerschelde Estuary): April 28–June 2, 2014.

Southeastern Chongming mudflat

Wave heights, wave periods, and water depths were measured using a self-logging sensor, the SBE-26plus Seagauge (Sea-Bird Electronics, Washington, USA), which was developed for wave monitoring using a data collection system comprising a 45-psia Paroscientific Digiquartz connected to an oil-filled tube via the pressure port (Sea-Bird Electronics, 2007). The instrument was horizontally placed on the sediment surface with the pressure probe located 8 cm above the sediment surface (Figure 3.1). The measuring burst interval was 10 minutes. Pressure data were collected at a frequency of 4 Hz over a duration of 256 seconds, yielding 1024 measurements per burst.

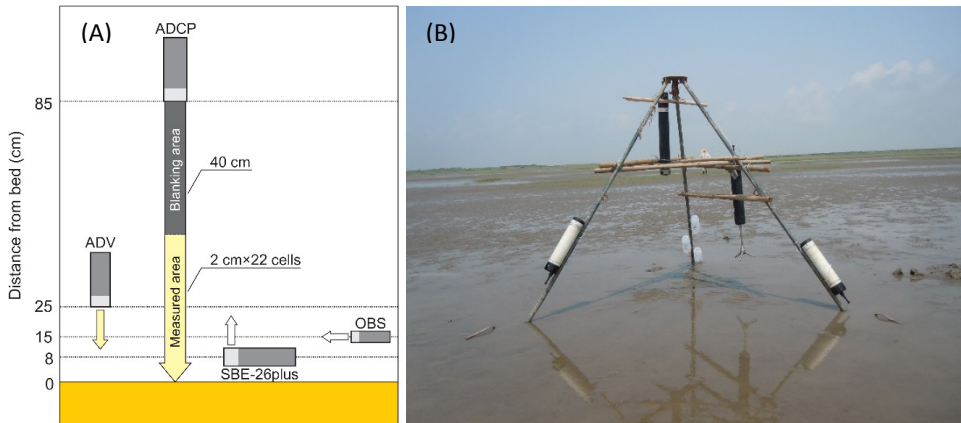


Figure 3.1: (A) Schematic representation of instrument deployment at Southeastern Chongming mudflat, and location with respect to the seabed. Lighter parts of the rectangles, which represent the locations of the instruments, indicate the locations of sensors. Arrows indicate the direction each sensor faced. (B) Photograph of measurement frame.

An ADCP (1.0 MHz high-resolution profiler, Nortek AS, Norway) was used to measure 3D current velocity profiles. The burst interval was 5 minutes. Each velocity profile is the mean value collected at a frequency of 1 Hz over a duration of 60 seconds.

The ADCP was attached to the tripod with the transmitters facing downwards and located 85 cm above the sediment surface. The blanking distance was 40 cm, and the cell size was set to 2 cm.

An ADV (6.0 MHz Vector current meter, Nortek AS, Norway) was used to measure the 3D velocity at a high sampling frequency in a small measurement volume (2.65 cm³). The sampling volume was located 9.3 cm above the bed. The ADV recorded velocities and pressure with a burst interval of 5 minutes, and for a period of 90 seconds at a frequency of 8 Hz. The water pressure in a high sampling rate, measured by a silicone piezoresistive pressure sensor (Nortek AS, 2005), was also used to analyse wave characteristics.

Turbidity in the water column was measured every five minutes using optical backscatter (OBS) sensors (OBS-3A, D&A Instrument Company, Washington, USA) attached to the tripod, with the probe positioned 15 cm above the sediment surface. Turbidity signals from the OBS sensors were converted into SSC values via calibration with *in situ* sediment samples. Regression between SSC and OBS-3A-derived turbidity yielded a correlation coefficient of 0.98. OBS-3A calibration of transferring turbidity to SSC is described in section 3.3.1, together with the calibration curves.

Finally, wind data at 122.25°E, 31.5°N were obtained from the ECMWF at an interval of three hours.

Nanhui Foreland mudflat 2009

Wave heights, wave periods and water depths were measured using a self-logging sensor, SBE 26plus Seagauge (Sea-Bird Electronics Inc., Washington, USA), which is specialized in wave monitoring. The instrument was placed horizontally on the sediment surface with the pressure probe located 8 cm above the sediment surface (Figure 3.2A). The probe logged mean water depth at 10-min intervals. At the same 10-min interval, waves were measured using 4-Hz pressure records obtained over a 256-second period, yielding 1024 measurements per burst (Shi et al., 2012). A 1.2-MHz Acoustic Doppler Current Profiler (ADCP) (Workhorse Sentinel, Teledyne RD Instruments, San Diego, USA) was fixed 12 cm above the sediment surface to obtain wave directions, which could not be measured by SBE 26plus Seagauge.

Although ADCP can be used to measure the current velocity profiles, its vertical special resolution and sampling interval were too big to be used in the study of bottom boundary flows on the intertidal flat. Instead, a 3.0-MHz Pulse-Coherent Acoustic Doppler Profiler (PCADP) (Sontek/YSI, San Diego, USA), which recorded data for 2 minutes every 5 minutes, was used to measure current velocity profiles. The PCADP was attached to a tripod and the transmitters were located 55 cm above the sediment surface. The blanking distance was 5 cm. Velocities were measured in 30 cells.

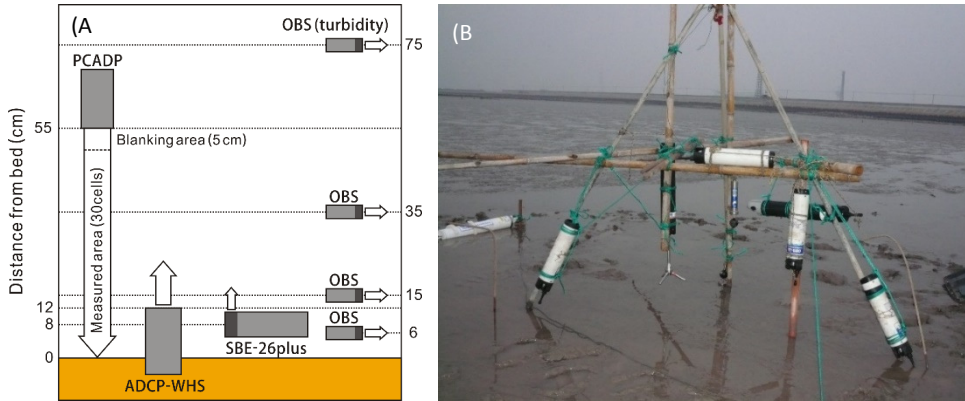


Figure 3.2: (A) Schematic figure of instruments deployment at Nanhui Foreland mudflat in 2009, and their position with respect to the seabed. Wide arrows for PCADP and ADCP-WHS show the direction of acoustic beams. Darker parts of the rectangles, which represent the locations of the instruments, indicate the locations of probes. Arrows indicate the facing direction of each probe. (B) Photograph of measurement frame.

Turbidity was measured every 1 minute using four Optical Back-Scatter (OBS) sensors (OBS-3A, D&A Instrument Company, Washington, USA) attached to the tripod at heights of 6, 15, 35, and 75 cm above the sediment surface. The turbidity signals from the OBS sensors were then transferred into SSC values on the basis of calibration measurements using *in situ* sediment samples.

Nanhui Foreland mudflat 2014

Wave heights, wave periods and water depths were measured using a self-logging sensor, SBE 26plus Seagauge (Sea-Bird Electronics Inc., Washington, USA), which is specialized in wave monitoring. The pressure probe located 45 cm above the sediment surface (Figure 3.3). The probe logged mean water depth at 10-min intervals. At the same 10-min interval, waves were measured using 4-Hz pressure records obtained over a 256-second period, yielding 1024 measurements per burst (Shi et al., 2012).

An ADV (6.0 MHz Vector current meter, Nortek AS, Norway) was used to measure the 3D velocity at a high sampling frequency in a small measurement volume (2.65 cm³). The sampling volume was located 15 cm above the bed. The ADV recorded velocities and pressure with a burst interval of 5 minutes, and for a period of 100 seconds at a frequency of 32 Hz.

An ADCP (2.0 MHz high-resolution profiler, Nortek AS, Norway) was used to measure 3D current velocity profiles. The burst interval was 5 minutes. Each velocity profile is the mean value collected at a frequency of 1 Hz over a duration of 18 seconds. The ADCP was attached to the tripod with the transmitters facing downwards and located

60 cm above the sediment surface. The blanking distance was 10 cm, and the cell size was set to 3 cm.

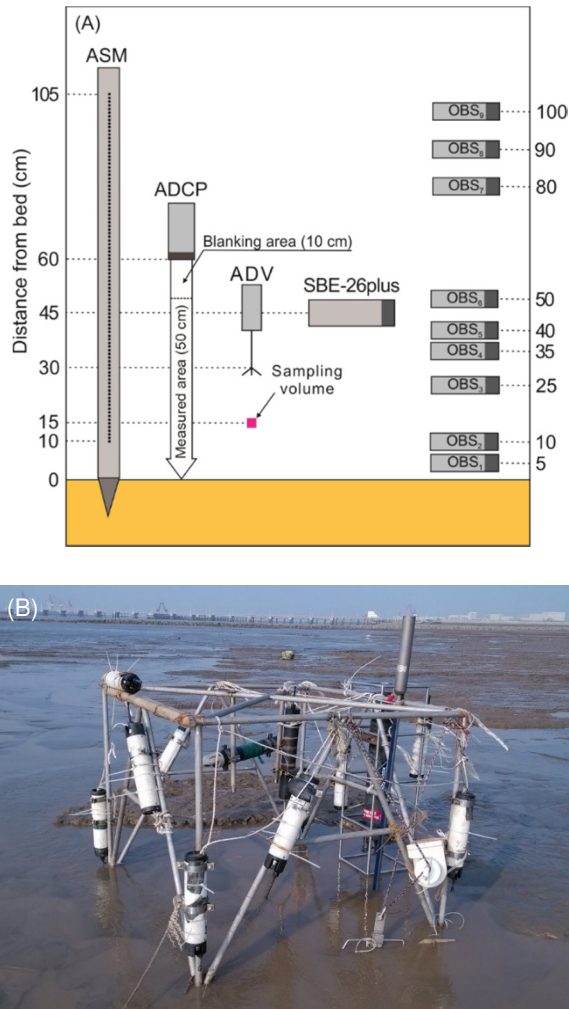


Figure 3.3: (A) Schematic representation of instrument deployment at Nanhui Foreland mudflat in 2014, and location with respect to the seabed. Darker parts of the rectangles, which represent the locations of the instruments, indicate the locations of sensors. (B) Photograph of measurement frame.

Turbidity was measured every 2.5 minute using nine Optical Back-Scatter (OBS) sensors (OBS-3A, D&A Instrument Company, Washington, USA) attached to the tripod at heights of 5, 10, 25, 35, 40, 50, 80, 90 and 100 cm above the sediment surface. Turbidity was also measured every 2.5 minute by ASM (Argus surface meter-IV, Argus

Environmental Instruments, Germany). Embedded with 96 OBS sensors in a titanium rod, at a distance of 1 cm between each other, ASM measured a turbidity profile in detail in each sampling burst.

Kapellebank mudflat

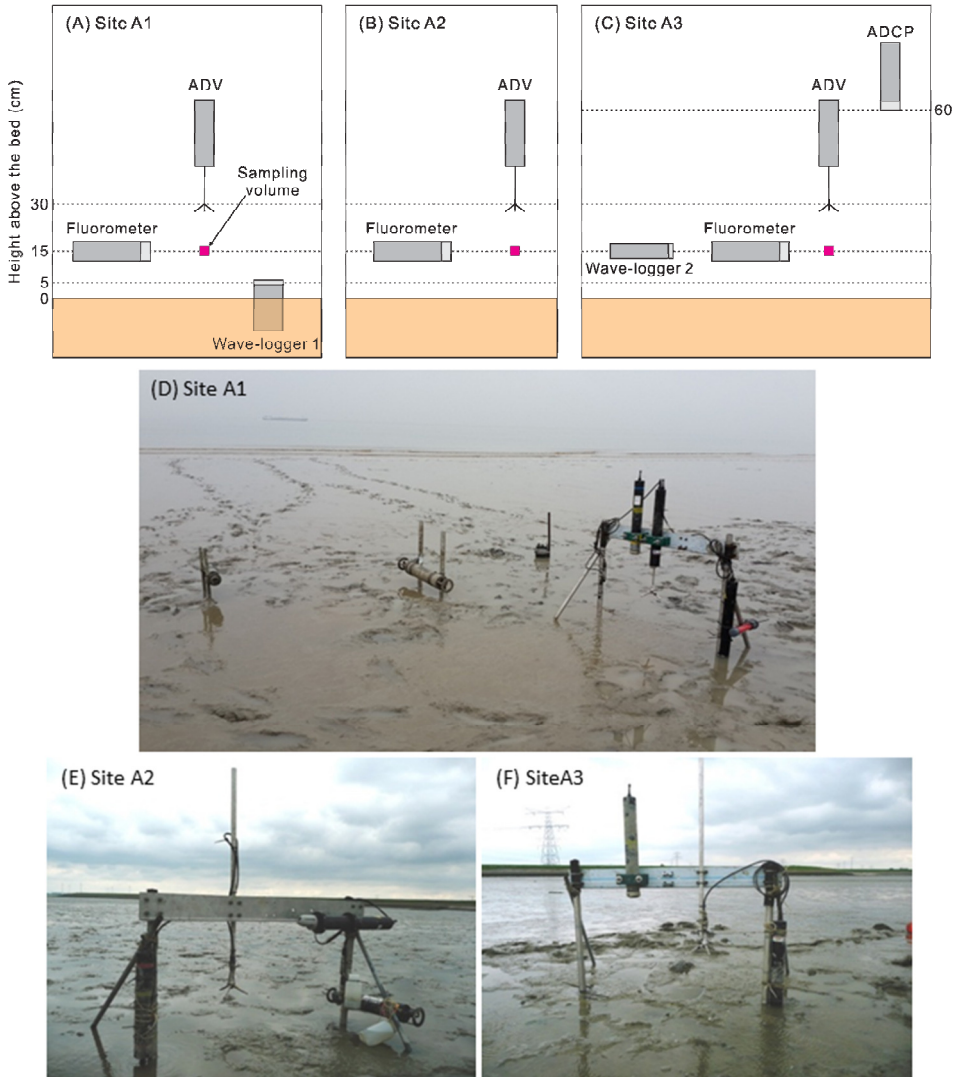


Figure 3.4: (A–C) Schematic representation of instruments deployment at Kapellebank mudflat, and their locations with respect to the seabed on each site. (D–F) The photographs of measurement frames.

Water level variations were measured on the Site A1. Wave-logger (OSSI-010-003C, Ocean Sensor Systems, Inc., USA) was deployed with its pressure probe fixed at 5 cm above the bed. The measurement interval was 20 min. 4096 data points were collected in each interval at a sampling rate of 10 Hz.

ADV (6.0 MHz Vector current meter, Nortek AS, Norway) was used to measure the 3D velocity at a high sampling frequency in a small measurement (2.65 cm^3) on each site. The velocity sampling volume was located at 15 cm above the original bed. From April 28 to May 2, the ADV recorded velocities with a burst interval of 5 minutes, in which 2048 data sets were collected in a sampling rate of 8 Hz. From May 3 to May 24, the ADV recorded at a burst interval of 10 minutes, in which 720 data sets were collected in a sampling rate of 8 Hz.

Fluorometer (C3TM Submersible Fluorometer, Turner Designs, USA) was used to measure turbidity, temperature and Chlorophyll *a* concentration every 5 min at 15 cm above the bed. Here we use the turbidity data for obtaining SSC by calibration.

3.1.2 Bed level measurements

Three methods were used to determine the bed-level variations: (1) the buried-plate method, (2) the tripod-rods method, and (3) the echo sounding function of the ADV/PCADP. The methods carried out in each study area are shown in Table 3.1.

The buried-plate method was used to measure relative bed-level changes between tidal cycles. Specifically, a $25 \times 25 \text{ cm}$ ceramic tile was buried horizontally beneath the sediment surface, with a stick at each of the four corners to mark the plate's position (Figure 3.5). We then measured the distance between the sediment surface and the plate using 16 thin sticks inserted vertically into the sediment. The first data were recorded a day (two tidal cycles) after burial of the plate, by which time the flat had been restored to its undisturbed state. Relative bed-level changes were calculated from the difference between the two measurements. To minimize the signal from the ripples, we positioned eight sticks on ripple crests and a further eight within ripple troughs. The measured ripple height and length at Site 2 were $5.8 \pm 1.3 \text{ mm}$ and $59.7 \pm 8.7 \text{ mm}$, respectively.

Table 3.1: Methods of determining bed-level changes in each study area.

	Buried-plate method	Tripod-rods method	Echo sounding
Southeastern Chongming	√		√ (ADV)
Nanhui Foreland		√	√ (PCADP)
Kapellebank			√ (ADV)

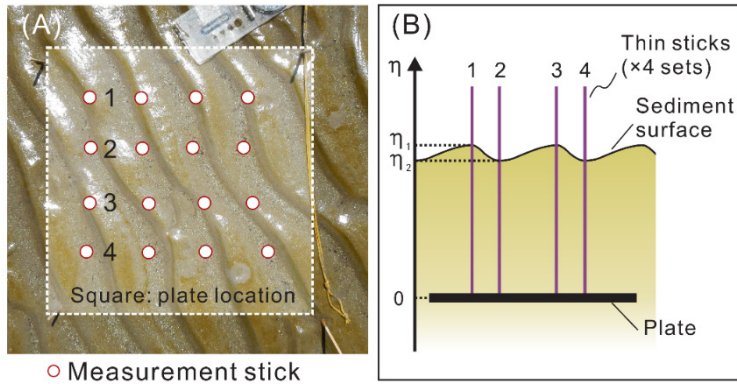


Figure 3.5: Buried-plate method measures relative bed level change. (A) is the plane view of a real sediment bed showing sticks assignment; transactional view (B) shows sticks are located evenly at ripple crests and troughs.

A triple-rods method, developed from the double-rods method (Yang et al., 2003) was used to measure relative bed-levels between tidal inundations, and thereby determine the net bed-level change that occurred during tidal cycles. The triple-rods system was composed of three rods that were set vertically in the sediments at an interval of 100 cm to form a triangle. Each rod was 3 cm in diameter and 100 cm in length (80 cm buried in the sediment, and 20 cm remaining above the sediment surface). In measuring the relative bed-levels, an alufer bar was put horizontally on the top of each two of the three rods and the vertical distance between the alufer bar and the sediment surface was measured at the middle of the interval between the two rods. The three readings were then averaged to determine the relative bed level at each measurement site. Using this method, the bed level was measured before and after the intra-tidal measurement period.

Relative bed-levels in high temporal resolution were measured by the ADV or PCADP using records of distance between the transmitter and the sediment surface with an accuracy of ± 1 mm (Andersen et al., 2006; Andersen et al., 2007; Shi et al., 2015). The distance was measured using echo ranging in the beginning of each measurement interval.

3.2 Sample collection and analysis

Southeastern Chongming mudflat

Each day we sampled surface sediment beneath the tripod during periods of daytime emergence. To avoid disturbing bed-level measurement area, we collected those samples at 2–3 m far away from the tripod centre, where the ADV was located. Samples consisted of a mixture of at least four scrapes of the topmost 1–2 mm of bed sediment. The grain

size distributions of each sample were analysed using a Coulter LS100Q laser diffraction particle size analyser (Beckman Coulter Inc., California, USA).

Additionally, we collected mini sediment cores (10 cm long) during typical spring (July 26) and neap (August 2) tides to analyse the vertical distribution of erodibility. Each core was divided into three sections, with the top section being 2 cm long, and the lower two sections each 4 cm long. Except for grain size analysis, water contents of the mini cores were measured. Wet sediment samples were first weighed and then dried at 50°C in an oven, before being reweighed for 48 hours or more to obtain stable weights. We then derived the water content W from the ratio of water (the difference between wet and dry sediment weights) to dry sediment weights.

Nanhui Foreland mudflat

In 2009, a total of 30 surficial sediment samples were collected in a 900-m² square area around the tripod, including one sample obtained directly beneath the tripod. In 2014, 2–mm surface sediment samples were collected. The grain size distributions of the sediments were analyzed using a Laser Diffraction Particle Size Analyzer, Coulter Ls100Q (Beckman Coulter Inc., California, USA).

Wet sediment samples were weighed and oven dried at a temperature of 50°C until a stable weight obtained (≥ 48 h). Water content was defined as the ratio of water (the difference between wet and dry sediment weights) to dry sediment weights (Taki, 2000).

Kapellebank mudflat

The surface sediment from each site was sampled by a mixture of several scrapes of the topmost 2 mm of the bed sediment at the three observation sites on April 29. The water content and grain size distribution of the fresh sediment samples were measured. Wet sediment samples were weighed and oven dried at a temperature of 60 °C until a stable weight was reached (≥ 96 h). The water content W was derived as the ratio of water (the difference between wet and dry sediment weights) to the dry sediment weights. The grain size distributions of the sediment samples were analysed by using a laser diffraction particle size analyser (Mastersizer 2000, Malvern Instruments Ltd., UK).

Chlorophyll a concentrations were measured as a proxy for microphytobenthic biomass. Sediment samples from the upper 2 mm of the sediment were collected near site A2 on April 28. The samples were taken at random points ($n=6$) and points that visually appeared to have a high ($n=2$) and low ($n=3$) diatom biomass. A pooled sample that consisted of ten cores with a surface area of 0.9 cm² was collected at each point. The samples were stored on ice until they were transferred to a –80°C freezer. Chlorophyll a concentrations were determined after freeze drying and extraction in 90% acetone by high-performance liquid chromatography (HPLC; Wright et al., 1991).

3.3 Data process and calculations

3.3.1 Data transformation from the instruments

SBE-26plus/wave-logger: In principle, the data process of the two wave gauges was to obtain wave parameters (wave height, wave period, and water depth) from the original pressure signals. Raw, high-frequency pressure data were first converted into pressure fluctuations in units of m-water, which indicates the distance of the water surface to the pressure probe. The mean pressure of each burst consisted of the water pressure and air pressure. The water depth (h) was obtained by removing the air pressure from the total pressure (Figure 3.6). Datasets during tidal submergence (i.e., $h=0$) were removed.

Second, the trend from low-frequency tides and other waves and the mean value were removed from the array of each burst before conducting spectrum analysis. The wave height (H) and wave period (T) were calculated based on the linear wave theory. The details are presented in Appendix VI in the manual of SBE-26plus Seagauge (Tucker and Pitt, 2001; Sea-Bird Electronics, 2007). The MATLAB scripts are provided in <http://neumeier.perso.ch/matlab/waves.html>.

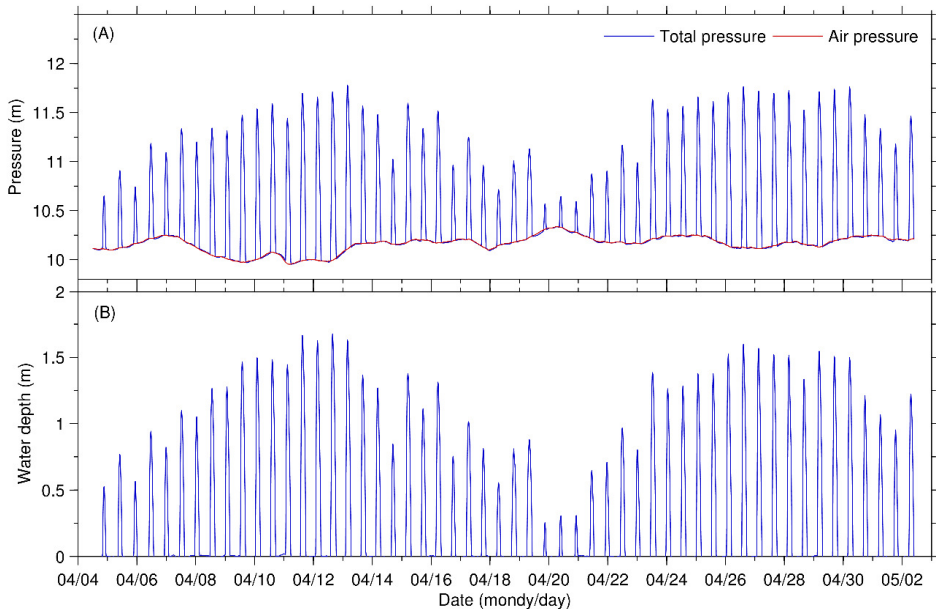


Figure 3.6: (A) Example of an SBE-26plus/wave-logger measured burst-averaged pressure. (B) The pure water depth can be obtained by extracting the air pressure from the total pressure.

The ‘SEASOFT for Waves’ software package could also obtain the bulk wave parameters by processing raw data files downloaded from the SBE-26plus. The default process of this software does not include a function to extracting the air pressure from the original pressure readings.

ADV: Three groups of data were processed from raw ADV datasets: three-dimensional velocities, wave parameters, and bed-level changes. The ADV is designed to obtain three-dimensional velocities of a small sampling volume. Additionally, pressure data with high temporal frequency (8 Hz or 32 Hz) were extracted and transformed into wave parameters by using a similar treatment to that for the pressure data from SBE-26plus and the wave-logger. Bed-level changes could be determined from the ‘distance from the probe/sampling volume to bottom’ data. Two extra acoustic beams were used at the beginning and end of each measurement burst to obtain this distance by using the principle of echo ranging.

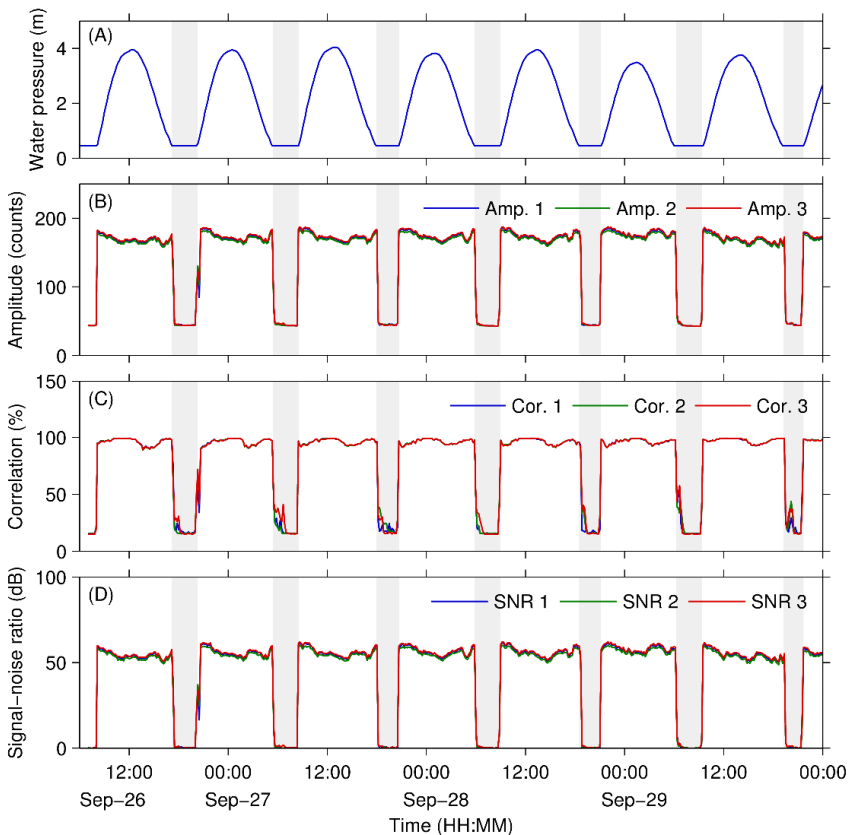


Figure 3.7: Example of acoustic parameters of ADV. When the sampling area was replaced by air during tidal emersion (highlighted with grey), the amplitude, correlation, and SNR became low.

Data filtration was conducted before further analysis to remove data during tidal emersion and data with low quality (i.e., unexpected bias). Three acoustic parameters could indicate if the velocity data had good quality: the amplitude, correlation, and signal-to-noise ratio. A low correlation (or low amplitude or SNR, which contains the amplitude information) indicates that the probe and measurement volume were exposed to the air or that pulse-to-pulse interference occurred. Generally, datasets with SNR < 20 dB or correlation < 70% were removed (Nortek AS, 2005); see the Nortek Forum (<http://www.nortek-as.com/en/knowledge-center/forum/>) for details.

PCADP/HR-Profiler: Similar to ADVs, the amplitude and correlation were used as indicators of data quality. After removing the datasets during tidal emersion, datasets below the sediment surface were also eliminated. The criteria for Sontek/YSI PCADP—the minimum values of the SNR and amplitude—are 15 dB and 80 counts (Sontek, 1996). In this thesis, we use amplitudes larger than 90–120 counts and correlations larger than 30–50% depending on the measurements.

OBS-3A/ASM/Fluorometer: The SSC in the water column is transferred from turbidity readings obtained by OBS-3A, ASM, or Fluorometer. The construction of the turbidity-SSC relationship is based on either indoor lab calibration or *in situ* calibration (Xue et al., 2004; Hoitink and Hoekstra, 2005). In this thesis, indoor lab calibration was used. The main procedures are as follows:

- Place the OBS-3A probe in the calibration tank, which is filled with tap water, with the probe at least 20 cm below the water surface. Trigger on the propeller in the tank bottom to continuously mix the water in the tank into a homogeneous state;
- Gradually add the highly concentrated suspended sediment sample collected in the field. When the real-time turbidity readings become close to constant, save 20 turbidity values and take a 600-ml water sample.
- Repeat the previous step several times until the readings can cover the highest value measured in the field.
- Determine the turbidity-SSC relationship from the regression between the mean value of each set of turbidity readings and the corresponding sediment concentrations from the water samples (Figure 3.8 – Figure 3.11).

A power function was used to establish the turbidity-SSC relationships in Southeastern Chongming, Nanhui Foreland 2009 cases. These turbidity readings are affected by the particle size, sediment concentration, water colour, light transmission of the water body, and bubbles (Campbell Scientific, 2007); piecewise fitting is sometimes required for areas with a high-SSC environment. For the Nanhui Foreland 2014 case, a power function was used in the low-turbidity region, while an exponential function was applied in the high-turbidity region (Figure 3.10). For Kapellebank case, a linear

regression with intercept of zero was used in the low-turbidity region, while a power function was used in the high-turbidity region (Figure 3.11).

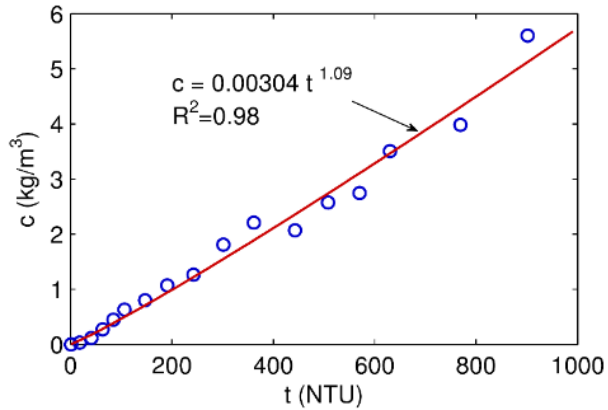


Figure 3.8: Relationship between OBS-3A measured turbidity (t) and suspended sediment concentration (c) for Southeastern Chongming case.

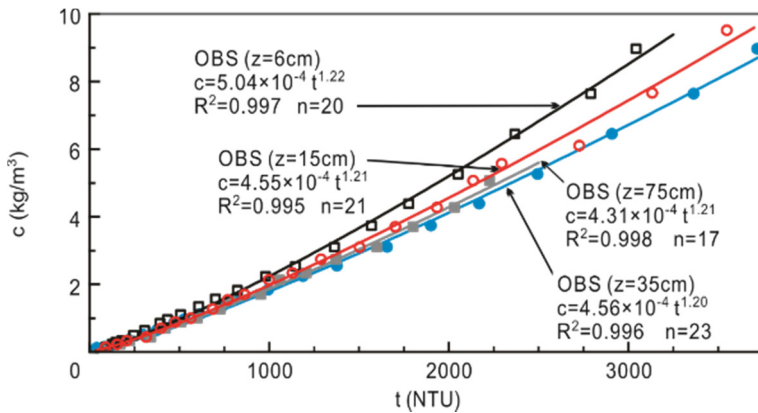


Figure 3.9: Relationship between OBS-3A measured turbidity (t) and suspended sediment concentration (c) for Nanhui Foreland mudflat 2009 case..

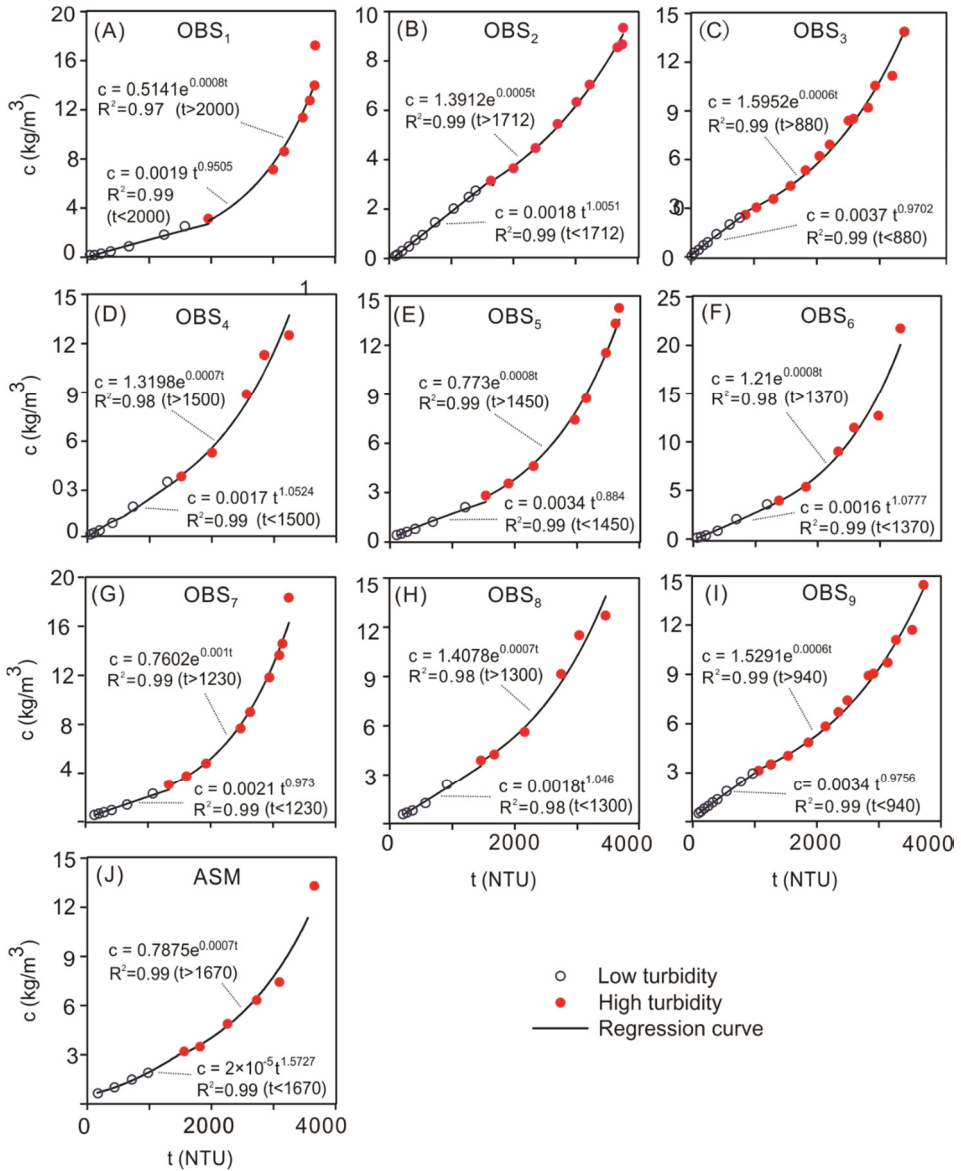


Figure 3.10: Relationship between OBS-3A measured turbidity (t) and suspended sediment concentration (c) for Nanhui Foreland mudflat 2014 case.

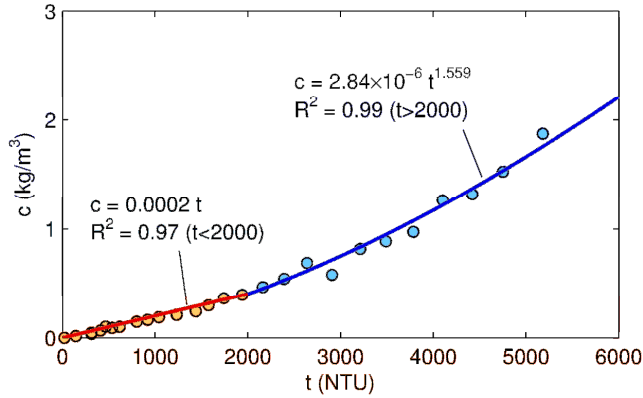


Figure 3.11: Relation between Fluorometer measured turbidity (t) and c for Kapellebank case.

In the analysis of indoor ASM calibration data, standard deviations of the calibrated probes under the same turbidity value were found to be much smaller than the mean value (3–5%). Therefore, we used the uniform turbidity-SSC relations of 96 OBS probe equipped in ASM referring to the manual (ARGUS, 2012).

3.3.2 Critical shear stresses

By assuming that the biological interaction with sediment dynamics was not significant, we calculated the critical bed shear stress for erosion of muddy sediments, τ_e (Pa), according to the method of Taki (2000):

$$\tau_e = 0.05 + \beta \left\{ \left[\frac{\pi}{6} (1 + sW) \right]^{\frac{1}{3}} - 1 \right\}^{-2} \quad (3.1)$$

where W is the measured water content (see section 3.2) and $s = \rho_s / \rho_w - 1$ is the submerged specific weight of bed sediment, in which ρ_s and ρ_w are the measured densities of sediments (2650 kg/m³) and seawater (1012–1014 kg/m³), respectively. The coefficient β ranges from 0.1 to 2.0, and in the present study we used $\beta = 1.0$.

3.3.3 Bed shear stresses

Wave-induced bed shear stress

Wave-induced bed shear stress, τ_w , was obtained by analysing surface-elevation monitoring data. Wave parameters (significant wave height H_s and significant wave period T_s) were derived from monitored high-frequency pressure data via linear wave theory (Tucker and Pitt, 2001). At the edge of the wave boundary layer, the peak orbital excursion (\hat{A}_δ) and peak orbital velocity (\hat{U}_δ) can be expressed as:

$$\hat{A}_\delta = \frac{H}{2 \sinh(kh)} \quad (3.2)$$

$$\hat{U}_\delta = \omega \hat{A}_\delta = \frac{\pi H}{T \sinh(kh)} \quad (3.3)$$

in which H is wave height (m), k ($= 2\pi/L$, $L = (gT^2/2\pi)\tanh(kh)$ is the wave length) is wave number (m^{-1}), h is water depth (m), ω is angular velocity (s^{-1}), and T is wave period (s). In practice, the significant wave height H_s and significant wave period T_s are used for H and T in the formulae.

Table 3.2: Approaches employed to obtain the wave parameters used in Equations (3.2) – (3.5).

		ADV	
	SBE-26plus	Zero-crossing method (Tucker and Pitt, 2001)	Spectral method (Wiberg and Sherwood, 2008)
Wave height, H		H_s : mean wave height of highest 33%	$H_s = 4 \sqrt{\sum_i S_h(f_i) \Delta f_i}$
Wave period, T	SEASOFT for Waves (Sea-Bird Electronics Inc.)	T_s : mean wave period of highest 33%	$1/T_{br} = f_{br} = \frac{\sum_i \left[f_i \frac{4\pi^2}{T_i^2 \sinh^2(k_i h)} \right]}{\sum_i \left[\frac{4\pi^2}{T_i^2 \sinh^2(k_i h)} \right] S}$
Bottom orbital velocity, U_δ		U_δ : Equation (4)	$U_\delta = 2 \sqrt{\sum_i \left[\frac{4\pi^2}{T_i^2 \sinh^2(k_i h)} S_{h,i} \Delta f_i \right]}$

The time-averaged (over half a wave cycle) bed shear stress due to waves, τ_w (Pa), can be expressed as:

$$\tau_w = \frac{1}{4} \rho_w f_w \hat{U}_\delta^2 \quad (3.4)$$

where ρ_w is the water density (kg/m^3) and f_w is the friction coefficient (-), which is determined by the hydraulic regime:

$$f_w = \begin{cases} 2 \text{Re}_w^{-0.5} & , \text{Re}_w \leq 10^5 \text{ (laminar)} \\ 0.0521 \text{Re}_w^{-0.187} & , \text{Re}_w > 10^5 \text{ (smooth turbulent)} \\ 0.237 r^{-0.52} & , \text{(rough turbulent)} \end{cases} \quad (3.5)$$

in which $Re_w = \frac{\hat{U}_s \hat{A}_s}{\nu}$ and $r = \frac{\hat{A}_s}{k_s}$ are the wave Reynolds number (-) and relative roughness (-), respectively. Parameter k_s is the Nikuradse roughness value given as $k_s = 2.5d_{50}$, where d_{50} is the median grain size of the bed sediment, and ν is the kinematic viscosity of sea water (m^2/s).

The wave parameters were obtained using the ‘SEASOFT for Waves’ software package for the SBE-26plus, and by analysing high-frequency water level elevation data obtained by ADV via zero-crossing and spectral estimates (Table 3.2).

Current-induced bed shear stress

The instantaneous velocity in a 3D orthogonal coordinate system can be expressed as $\mathbf{U} = u\hat{i} + v\hat{j} + w\hat{k}$, where u , v , and w are the instantaneous magnitudes in the three orthogonal directions \hat{i} , \hat{j} , and \hat{k} , respectively. The flow across tidal flats is subject to bed friction, resulting in a turbulent boundary layer that can extend to the water surface in the typically shallow conditions (Whitehouse et al., 2000). In this layer, current velocity is composed of a mean component ($*_m$) and a fluctuating component. The fluctuating component can be further decomposed into two parts: the wave orbital motion ($*_w$) and turbulence ($*_t$), resulting in the following:

$$\begin{aligned} u &= u_m + u_w + u_t \\ v &= v_m + v_w + v_t \\ w &= w_m + w_w + w_t \end{aligned} \quad (3.6)$$

In this thesis, each measurement period lasted for less than five minutes. Over such a short sampling duration, we assumed that the velocity series follows a linear increasing/decreasing trend. Five methods were applied to estimate the current-induced bed shear stress in Chapter 4: the LP (log-profile) method (being used in Nanhui Foreland case 2009) uses mean velocities, whereas the TKE (turbulent kinetic energy), TKEw (modified turbulent kinetic energy using vertical velocities only; being used in Nanhui Foreland 2014 and Kapellebank cases), RS (Reynolds stress), and ID (inertial dissipation) methods use fluctuating velocities.

The LP method is based on the assumption that the burst-mean horizontal current speed ($U_c = \sqrt{u_m^2 + v_m^2}$) profile in the boundary layer follows a logarithmic distribution:

$$U_c(z) = \frac{U_{*c}}{\kappa} \ln\left(\frac{z}{z_0}\right) \quad (3.7)$$

where $U_c(z)$ (m/s) is the current speed at the height above the bed, z (m); U_{*c} (m/s) is the friction velocity; κ is Von Kármán’s dimensionless constant ($= 0.4$); and z_0 (m) is the roughness length, which is the distance from the bed at which the flow reaches zero

if the flow profile strictly follows the logarithmic law. By regressing the current speed $U_c(z)$ against $\ln(z)$ using the least-squares method, U_{*c} and z_0 can be calculated from the gradient A and intercept B as follows:

$$\begin{aligned} U_{*c} &= \kappa A \\ z_0 &= e^{-\frac{B}{A}} \end{aligned} \quad (3.8)$$

We used internal consistency analysis (Collins et al., 1998) to examine whether the results derived from the $U_c(z) - \ln(z)$ relationship can be used to characterize boundary layer conditions. A linear relationship must exist between the shear velocity U_{*c} derived from Equation (3.7), and the current speed within the boundary layer ($U_{z'}$, here taken as U_{40} , which is the current speed at 40 cm above the bed), written as:

$$U_{*c} = aU_{z'} + b \quad (3.9)$$

To pass the internal consistency analysis, four requirements must be met: 1) the linear correlation between U_{*c} and $U_{z'}$ must exceed the appropriate significance level; 2) the regressed intercept should be small ($b \approx 0$); 3) z_0 obtained from the slope of the regression line should be similar to that derived using the $U_c(z) - \ln(z)$ regression:

$$a = \frac{\kappa}{\ln\left(\frac{z}{z_0}\right)} \quad (3.10)$$

and 4) the value of $C_D(z')$, which is the drag coefficient at a height of z' (40 cm in the present study), derived on the basis of slope a , should be consistent with

$$C_D(z') = \frac{U_{*c}^2}{U_{z'}^2} \quad (3.11)$$

The current-induced bed shear stress (τ_c , Pa) is subsequently calculated according as follows:

$$\tau_{c,LP} = \rho_w C_D(z') U_{z'}^2 \quad (3.12)$$

The second momentum methods are listed in Table 3.3. The TKE method and the TKEW method are based on the assumption that the bed shear stress scales linearly with the intensity of velocity fluctuations. To minimize the noise from the orbital motion of waves in the horizontal components, only the vertical fluctuations are used in the TKEW method. Minimizing the effects of waves has also been achieved using band-pass filtering (see Chapter 4). In the RS method, it is assumed that the measured covariance between horizontal and vertical fluctuations is close to the value near the bed. Soulsby and Humphery (1990) argued that it is not necessary to separate out the wave orbital velocities, as the vertical wave-induced velocity is both small and in quadrature with the horizontal

component.

Table 3.3: Second momentum methods used to estimate the current-induced bed shear stress, τ_c .

Method	Formula	Parameters and coefficients
TKE Turbulent kinetic energy	$TKE = \frac{1}{2} \rho_w (\overline{u_t^2} + \overline{v_t^2} + \overline{w_t^2})$ $\tau_{c,TKE} = C_1 \cdot TKE$	$C_1=0.19$ (Stapleton and Huntley, 1995)
TKEw Vertical turbulent kinetic energy	$\tau_{c,TKEw} = C_2 \rho_w \overline{w_t^2}$	$C_2=0.9$ (Kim et al., 2000)
RS Reynolds stress	$\tau_{c,RS} = \rho_w \sqrt{\overline{u_f w_f^2} + \overline{v_f w_f^2}}$	u_f, v_f, w_f : total fluctuating velocities, i.e., $u_f = u_w + u_t$
ID Inertial dissipation	$U_* = \left(\frac{2\pi\kappa z}{U_c} \right)^{1/3} \left(\frac{S_w(f) f^{5/3}}{\alpha_3} \right)^{1/2}$ $\tau_{c,ID} = \rho_w U_*^2$	$\kappa=0.4$ $\alpha_3 = 0.68$ (Green, 1992)

In the ID method, the friction velocity is derived by assuming a first-order balance between shear production and energy dissipation with deployment of the 1D spectrum applicable to the inertial dissipation range (Huntley, 1988; Kim et al., 2000), giving

$$U_* = (\kappa z)^{1/3} \left(\frac{S_i(k) k^{5/3}}{\alpha_i} \right)^{1/2} \quad (3.13)$$

where $\alpha_i (i=1,2,3)$ are 1D Kolmogorov constants, with $i=1$ and $i=2$ denoting directions parallel and transverse to the main flow, respectively, and $i=3$ denoting the vertical direction. In locally isotropic turbulence, $\alpha_1 = 0.51$, and $\alpha_2 = \alpha_3 = 4/3\alpha_1 = 0.68$ (Green, 1992). The frozen turbulence hypothesis, which assumes $S(k)k = S(f)f$ with $k = 2\pi f / U_c$, is then applied to transfer Equation (3.13) from the wave number (k) domain to the frequency (f) domain (Huntley, 1988). In the inertial subrange, $S_w(f) f^{5/3}$ is constant. In practice, the average value around the maximum value is used to represent $S_w(f) f^{5/3}$.

Wave and current directions

The current direction φ_c is derived from the mean value of the two horizontal velocity components u_m and v_m :

$$\varphi_c = \arctan\left(\frac{v_m}{u_m}\right) \quad (3.14)$$

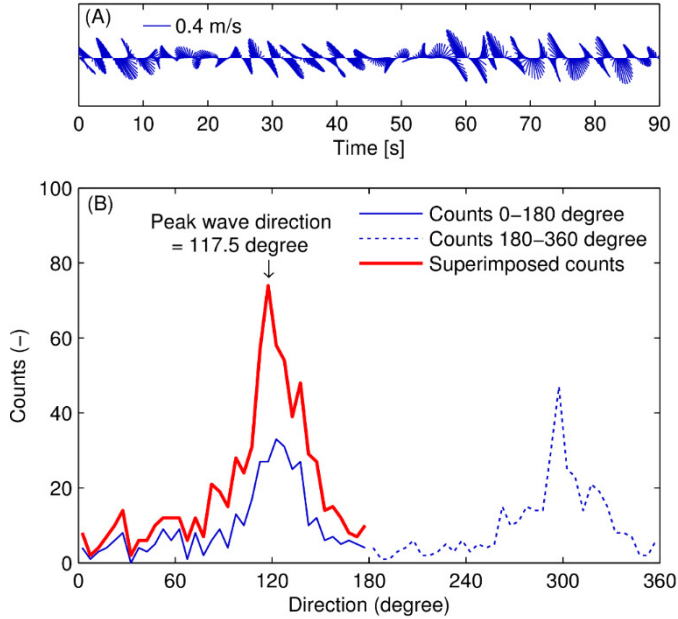


Figure 3.12: (A) Vector series of near-bottom wave orbital velocity filtered from the ADV in a burst, and (B) its direction (in Cartesian coordinates) count.

The wave direction φ_w is defined similarly, but based on the wave-induced orbital velocities u_w and v_w . Given a series of φ_w in a measurement burst, the wave direction is defined as the direction with the maximum number of counts. Two peaks in the direction counts, which are theoretically in a difference of 180° , can be found (Figure 3.12). As $|\cos \varphi_{cw}|$ and $|\sin \varphi_{cw}|$ are used in the WCI model, only one of the two peak directions is required. Accordingly, the counts between 180° and 360° are superimposed on those between 0° and 180° . A count every 5° was used in the present study.

Total bed shear stress

The bed shear stress due to waves and currents (τ_{cw} , N/m^2) was calculated using the

models of Grant and Madsen (1979) (Equation 3.15), van Rijn (1993) (Equation 3.16) and Soulsby (2005) (Equation 3.18).

The Grant–Madsen (1979) model is expressed as follows:

$$\tau_{cw} = \sqrt{(\tau_w + \tau_c |\cos \varphi_{cw}|)^2 + (\tau_c \sin \varphi_{cw})^2} \quad (3.15)$$

where τ_c is the bed shear stress due to currents, τ_w is the bed shear stress due to waves, and φ_{cw} is the angle between the wave (measured by ADCP-WHS or calculated using the method mentioned in the last section) and current (measured by PCADP/ADCP/ADV).

The van Rijn (1993) model is expressed as follows:

$$|\tau_{cw}| = \alpha_r \tau_c + |\tau_w| \quad (3.16)$$

$$\alpha_r = \left[\frac{\ln(30\delta/k_a)}{\ln(30\delta/k_s)} \right]^2 \left[\frac{-1 + \ln(30h/k_s)}{-1 + \ln(30h/k_a)} \right]^2 \quad (3.17)$$

where k_s is the Nikuradse roughness length, $k_s = z_0$, and δ is the thickness of the wave boundary layer. The bed shear stress reduction α_r is always ≤ 1 .

The Soulsby (2005) model is expressed as follows:

$$\tau_{cw} = \sqrt{(\tau_m + \tau_w |\cos \varphi_{cw}|)^2 + (\tau_w |\sin \varphi_{cw}|)^2} \quad (3.18)$$

where the averaged total shear stress τ_m is

$$\tau_m = \tau_c \left[1 + 1.2 \left(\frac{\tau_w}{\tau_c + \tau_w} \right)^{3.2} \right] \quad (3.19)$$

3.3.4 Sediment fluxes

In chapter 5, averaged near-bed (0.5 m) suspended sediment transport per unit wide (Equation 3.20) is used to represent for the whole water column, as majority of the sediment are transported in the near-bed layer.

$$Q_s^t = \sum_{i=1}^n u_i^t c_i^t \delta_i \Delta t \quad (3.20)$$

in which Q_s^t (kg/m) is the sediment transport per unit wide at time t , u_i^t (m/s) and c_i^t (kg/m³) are the velocity and SSC at the position i at time t , and δ_i (m) is the thickness of the layer at position i , Δt is the time interval between successive measurements (300 s).

3.3.5 Index of agreement

Intercomparisons among the bed shear stresses estimated using different approaches (Chapter 4) and among measured and simulated bed level changes (Chapter 7) were carried out using the index of agreement I . This index is introduced to quantitatively determine the similarity between two methods of estimating the same variable (Willmott, 1981):

$$I = 1 - \frac{\sum (x - y)^2}{\sum (|x - \bar{y}| + |y - \bar{y}|)^2} \quad (3.21)$$

where x and y are the two datasets being compared; $0 < I \leq 1$. The larger the value I is, the higher level of similarity the two datasets x and y is. $I = 1$ indicates perfect agreement.

4 Sediment dynamics of Southeastern Chongming mudflat

Accurate estimations of the bed shear stress are essential to predict the erosion and deposition processes in estuaries and coasts. Power spectra demonstrate that wind enhances the total bed shear stress as a result of the increases in both τ_w and τ_c generated by the greater wave height and reinforcing of vertical turbulence, respectively (section 4.1). From a comparison of the various methods obtaining τ_{cw} , section 4.2 draws an optimum solution of obtaining τ_{cw} from *in situ* ADV data. Sediment dynamic processes associated with bed level changes (section 4.3) show that the relative importance of waves and tides in intertidal wetland erosion and accretion can vary temporally (due to changes in balance between wave and tidal energies) and spatially (because of changes in elevation and vegetation in the cross-shore profile).

This chapter is based on the following manuscripts:

- Zhu, Q., van Prooijen, B.C., Wang, Z.B., Ma, Y.X., Yang, S.L., 2016. Bed shear stress estimation on an open intertidal flat using *in situ* measurements. *Estuarine, Coastal and Shelf Science*, 182 (Part A): 190-201.
- Zhu, Q., van Prooijen, B.C., Wang, Z.B., Yang, S.L., 2017. Bed-level changes on intertidal wetland in response to waves and tides: A case study from the Yangtze River Delta. *Marine Geology*, 385: 160-172.

4.1 Effect of waves to near-bed velocities

4.1.1 Wind condition and hydrodynamic background

Wind direction was variable during our field campaign. Prior to July 31 and after August 2, the prevailing wind direction was onshore (Figure 4.1A) and wind speed was generally moderate (6.8 ± 2.1 m/s). The maximum onshore wind velocity (11 m/s) occurred on July 27. A weak (2.6 ± 1.1 m/s) offshore wind flow characterised the period July 31–August 2.

The tides changed from neaps to springs during the measurement period. A maximum water depth of 2.2 m occurred during tidal cycle 14 (Figure 4.1B). ADV-derived mean near-bed current velocities ranged from 0.004 to 0.5 m/s, with an average value of 0.18 m/s (Table 3.3). The average significant wave height (calculated from ADV pressure measurements) was 0.25 m and 0.11 m during the windy and calm periods, respectively.

Table 4.1: Descriptive statistics for velocity speed (U_c), significant wave height (H_s), and bed shear stresses (τ_w , τ_c , τ_{cw}) of Southeastern Chongming study case.

BSS	Erosion stage			Recovery stage			Full period		
	Ave.	Max.	Min.	Ave.	Max.	Min.	Ave.	Max.	Min.
U_c (m/s)	0.17	0.51	0.004	0.19	0.41	0.02	0.18	0.51	0.004
H_s (m)	0.24	0.46	0.07	0.14	0.30	0.08	0.21	0.46	0.07
τ_w (Pa)	0.28	0.68	0.01	0.07	0.47	0.01	0.22	0.68	0.01
τ_c (Pa)	0.55	2.43	0.03	0.43	1.97	0.01	0.51	2.43	0.01
τ_{cw} (Pa)	0.72	2.47	0.07	0.48	1.99	0.03	0.66	2.47	0.03

4.1.1 Spectra of water elevations and velocities

Water level and velocity spectra were determined for each burst interval, and these spectral results are combined with contour plots in Figure 4.1B–E. As the measurement location falls dry at low water, no data were collected during these periods. Over the neap tides in the first part of the sampling period, some tides did not inundate the monitoring site. Three periods can be identified based on the wind conditions (Figure 4.1A): Period I (July 23–July 31); Period II (July 31–August 02), and Period III (August 02–August 03).

Figure 4.1B shows the contours of the energy density spectra of the water level fluctuations above the datum of the original bed level. In Period I, before July 31, a single peak is evident at a frequency around 0.32 Hz. No clear peaks are seen over Period II, indicating that wave heights were low. During Period III, two peaks occur around a

frequency at 0.32 and 0.1 Hz, and this indicates that the wave regime was dominated by locally generated waves over Period I, whereas offshore winds and swell dominated wave activity during Period III.

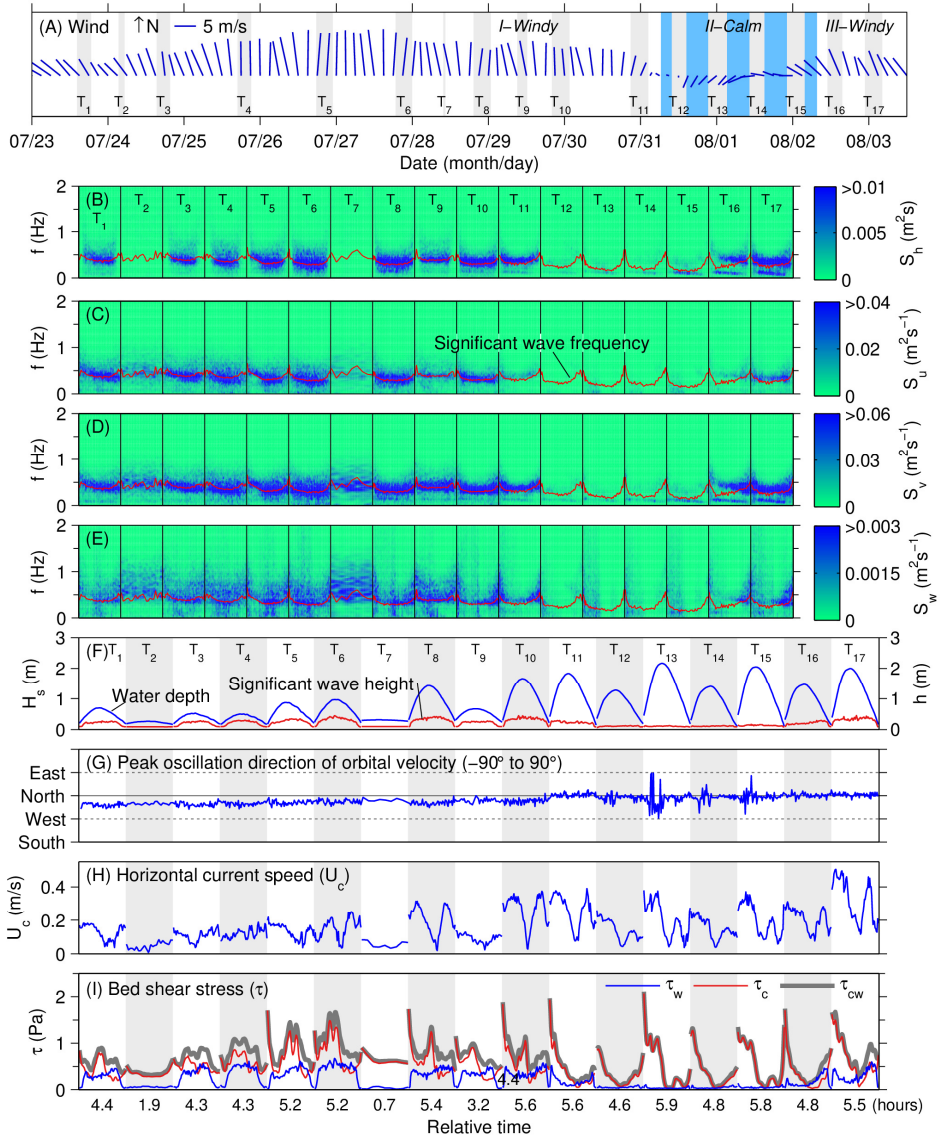


Figure 4.1: Time series of (A) wind vectors, (B) the energy spectrum of water depth, and (C–E) energy spectra of combined wave orbital and turbulent velocities in the east, north, and vertical up directions, (F) water depth (h) and significant wave height (H_s), (G) horizontal current speed (U_c), (H) wave oscillation directions, and (I) wave/current-induced bed shear stresses (τ_w and τ_c , respectively) and total bed shear stress (τ_{cw}). Each time series section covers the period of a single tidal inundation.

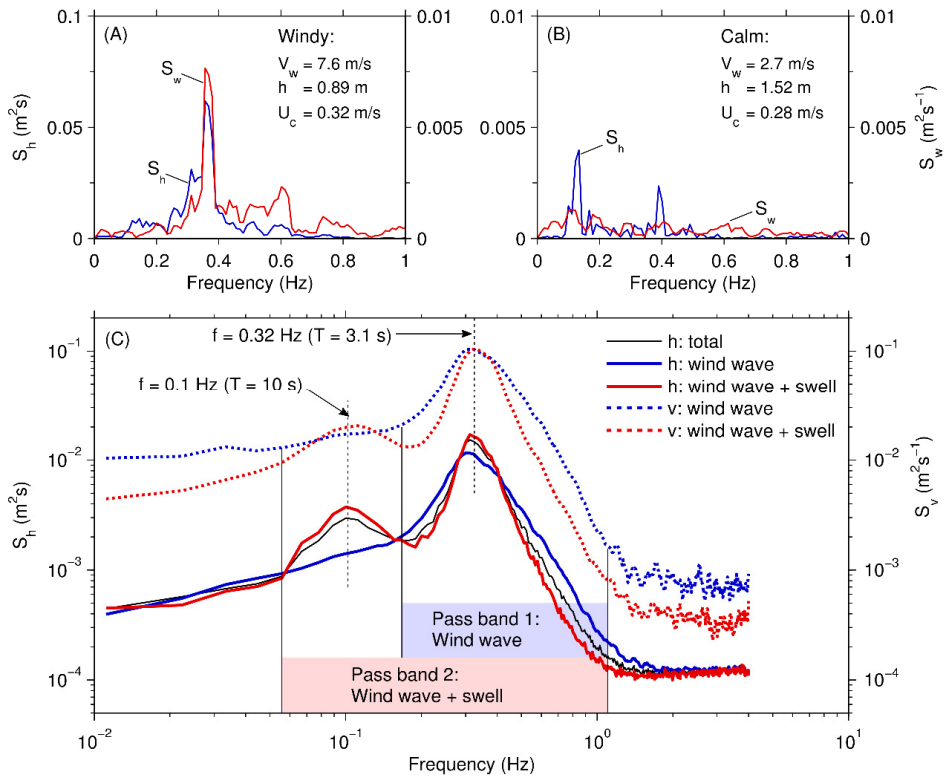


Figure 4.2: (A) and (B) show water depth and vertical velocity spectra in typical bursts of windy conditions and calm conditions, respectively. V_w , h , and U_c are wind speed, water depth, and horizontal current speed, respectively. (C) shows mean wave spectra showing that local waves are driven by wind during windy weathers (before T11), but by both wind and swells during calm weathers (after T11). Two corresponding pass-bands were used to carry out velocity spectra filtration.

Figure 4.1C–E shows the energy spectra derived from the velocity fluctuations in the three orthogonal directions. Similar to the water level spectra, a double-peaked spectrum is seen in Period III for the northward velocities (v), and this is more clearly highlighted in the averaged spectra (Figure 4.2C). The velocity spectra for the northward direction have a similar shape to the spectra of the water level fluctuations, which implies that the near-bed velocities in the wave propagation direction are significantly affected by wave motion. Waves contributed 84% to the spectral density of the total velocity energy spectrum in the wave propagation direction, with a maximum contribution of 97%. Based on the ‘wind wave’ and ‘wind wave + swell’ conditions, two corresponding pass-bands were applied to further wave–turbulence decomposition (Figure 4.2).

For the spectrum of the vertical velocity component, a peak occurs in the velocity spectrum at the same frequency as for the water level spectrum during Period I (Figure

4.2A). No clear peak is seen in the vertical velocity spectrum for the calmer Period II (Figure 4.2B). Furthermore, on average the waves contribute 40% to the spectral density of the vertical wave-turbulence energy spectrum in wavy period, with a maximum contribution of 93%.

Our results suggest that the near-bed velocity fluctuations were caused in part by waves. Even the vertical fluctuations, which are often assumed to be free of wave influence, are highly contaminated by the waves. Consequently, a decomposition of the velocity fluctuations is needed to separate waves and turbulent motion.

4.1.2 Wave-turbulence decomposition

The second momentum methods (TKE, TKEw, and ID) use the turbulent velocities only, so turbulent velocities are separated from the mixed wave-turbulent velocities. Two approaches were used to decompose the wave velocities from the turbulent velocities: a moving average (MA) (Williams et al., 2003) and energy spectrum analysis (ESA) (Soulsby and Humphery, 1990). The band-pass filter method of Meirelles et al. (2015) is similar to the ESA method and gives similar results.

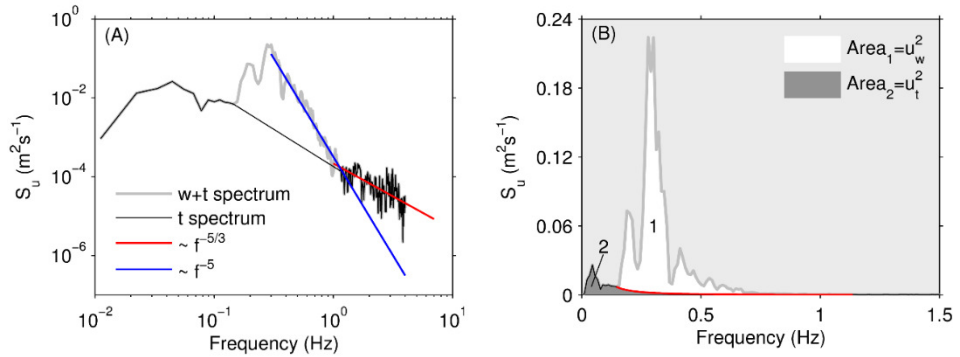


Figure 4.3: (A) Energy spectrum of combined wave orbital and turbulent velocities comprises a conventional turbulence spectrum (with a $f^{-5/3}$ power law behavior in the inertial subrange) and a wave velocity spectrum (with a f^{-5} power law behaviour at higher wave band). (B) shows the same spectra plotted in linear axes. The wave variance $\overline{u_w^2}$ is given by the area between dividing line, black line in (A), and the spectrum, while the rest is turbulent variance $\overline{u_t^2}$.

Williams et al. (2003) applied a simple MA filter that uses the mean of the previous N values to forecast the value at time t , as follows:

$$F_t = \frac{1}{N} \sum_{i=1}^N A_{t-i+1} \quad (4.1)$$

where F_t is the forecast value at time t , N is the number of previous data points to be

included in the MA, and A_t is the actual value at time t . Williams et al. (2003) used a 1-second MA to resample the original signal and extract the bulk wave-induced velocities.

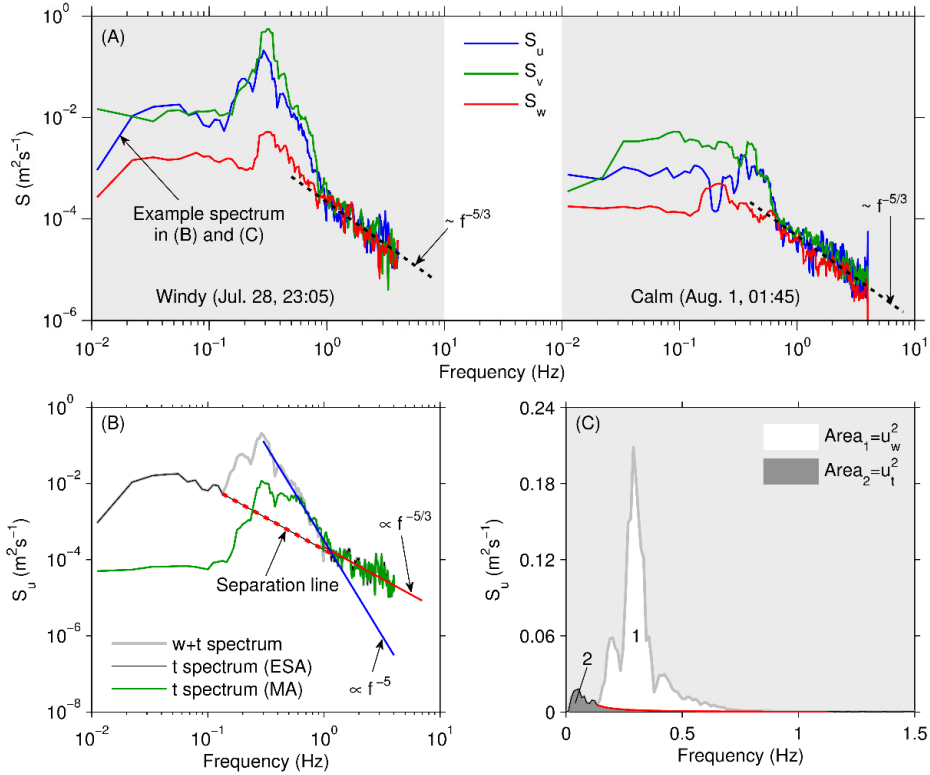


Figure 4.4: (A) Examples of energy spectra of combined wave orbital and turbulent velocities of three directions in windy and calm conditions, respectively. (B) An example of ESA and MA methods decomposed turbulent velocity spectra. (C) The same spectra as in (B) plotted on linear axes. The wave variance $\overline{u_w^2}$ is given by the area between the dividing line, the red dotted line in (B), and the spectrum, with the remaining area being the turbulent variance $\overline{u_t^2}$.

The ESA technique was developed by Soulsby and Humphery (1990) to split the variance without separating the instantaneous time series (Figure 4.3). The burst velocity series is first detrended to get combined wave–turbulent velocities u_w+u_t . The area under the energy spectrum $S_u(f)$ equals the total variance $\overline{(u_w+u_t)^2}$. A log–log plot (Figure 4.3A) reveals that the spectrum is a wave velocity spectrum, with a peak near 0.3 Hz and a characteristic f^{-5} power law decaying at higher wave frequencies, superimposed on a conventional turbulence spectrum, with a characteristic $f^{-5/3}$ slope in the inertial subrange.

This spectrum is further separated by a straight line, and the area above this line contributes to the wave variance $\overline{u_w^2}$, whereas the area below the line contributes to the turbulence variance $\overline{u_t^2}$ (Figure 4.3B). In the separated turbulent velocity spectrum, power densities of low frequency indicate the turbulent kinetic energy contributed by turbulence in energy containing range, while power densities in high frequency domain is in inertial range.

Figure 4.4B shows the velocity spectrum smoothed using an MA with a window of one second and the spectrum obtained after BP filtering with the pass-bands indicated in Figure 4.2.

A peak in the wave frequency band remains in the energy spectra of turbulent velocities obtained using the MA method. This indicates an incomplete separation of wave–turbulence decomposition. Moreover, in the low-frequency domain, the MA provides a low estimation of the turbulence spectral density.

4.2 Estimation of bed shear stress

4.2.1 Bed shear stresses

Wave-induced bed shear stress

The wave-induced bed shear stresses obtained using the different approaches were in good agreement with each other. The index of agreement (I) of each comparison was above 0.94 (Table 4.2). The ‘SEASOFT for Waves’ software package for the SBE-26plus obtained wave characteristics H_s and T_s using zero-crossing method (Sea-Bird Electronics, 2007). Theoretically, wave parameters obtained using pressure dataset from ADV and SBE-26plus using the zero-crossing method should be in accordance with each other. The instrument-dependent differences were probably caused by differences in the probe type and deployment settings (sampling frequency and duration). For the same ADV pressure dataset, zero-crossing and spectral estimation provide close τ_w values, with I reaching 0.98. Zero-crossing counts the water level going to equilibrium positions, while spectral estimation uses Fourier transform. They are expected to gain the similar values of wave parameters by signal processing approach. As the three approaches provide similar estimates of τ_w , the results obtained from the spectral estimations based on the ADV pressure data are used in the following analysis.

During windy conditions, the orbital velocity distribution indicates that waves propagate in a north-westnorth direction, which is the same direction as the prevailing wind. During the calm conditions around August 1st, the wave direction over one tidal cycle became divergent when the wind direction moved offshore (Figure 4.1G).

Table 4.2: Statistics and inter-comparison (index of agreement, I) of wave-induced bed shear stress, τ_w .

		SBE	ADV: 0-crossing	ADV: spectral
τ_w (Pa)	Mean	0.28	0.25	0.22
	Std.	0.16	0.22	0.18
I	SBE	1	0.94	0.94
	ADV: 0-crossing	0.94	1	0.98
	ADV: spectral	0.94	0.98	1

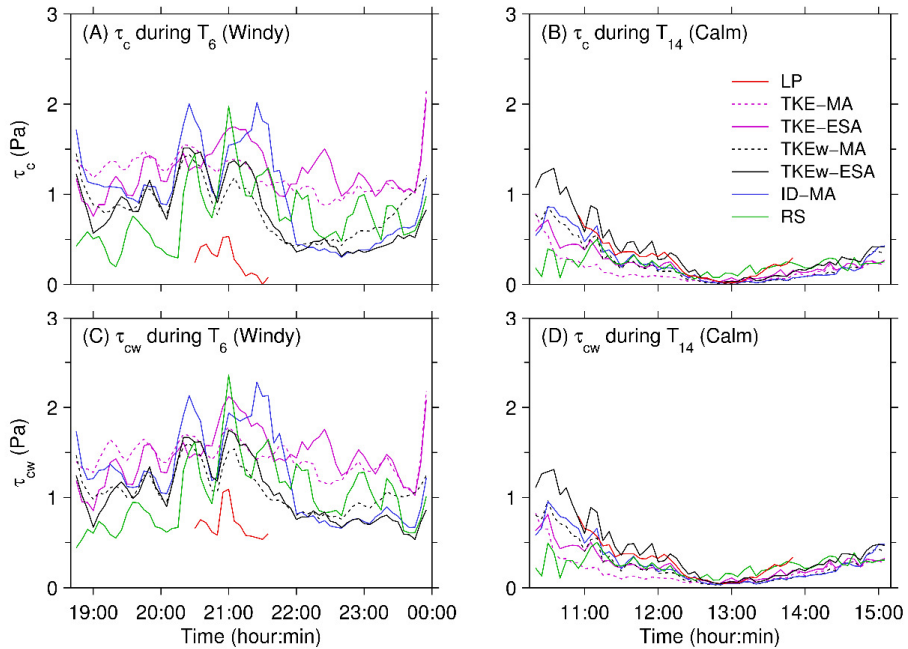


Figure 4.5: Expanded sections of the time series of τ_c and τ_{cw} obtained using the various approaches. The two tidal cycles are representative because tidal-average τ_{cw} in the cycle in T6 and T14 reaches maximum in windy period and minimum in calm period, respectively. Legends in panels (A), (C) and (D) are the same as that in panel (B).

Current-induced bed shear stress

The average value of the current-induced bed shear stress, τ_c , was 2.3 times larger than the wave-induced bed shear stress τ_w , indicating that currents and waves acted in competition in the present study area, whereas current-induced forces have a greater effect on the bed than do waves (Figure 4.1I).

Figure 4.5 demonstrates that the time series of τ_c obtained using different methods

show similar variation patterns during a tidal cycle. However, agreement in the magnitude of τ_c is weaker under windy conditions than under calm weather. According to our intercomparison analysis, indices of agreement vary around 0.86 (from 0.5 to 1) during calm conditions, but around 0.58 (from 0.25 to 0.86) during windy conditions (Table 4.1).

Total bed shear stress

The total bed shear stress under combined wave–current action obtained using the methods outlined above, varied from 0 to 3 Pa with an average of 0.65 Pa. The largest estimated value of averaged τ_{cw} was two times higher than the lowest estimate (Table 4.3). As with τ_c , values of τ_{cw} calculated using the different methods show more consistency under calm conditions (Figure 4.5B and D). Regarding the wave–turbulence decomposition methods, the MA method provides the higher estimates, and the ESA method provides the lower estimates.

The TKEw method, which uses ESA decomposition (TKEw-ESA), provided a moderate mean τ_{cw} value and generated the highest mean index of agreement, which is the average of the agreement level (J) values of this method with all the other methods. The mean value of τ_{cw} obtained from the TKEw-ESA method was 2.5 times greater under windy conditions than under calm conditions. Over a calm tidal cycle, τ_{cw} values decreased to the minimum value around high tide when current speeds are at their lowest (Figure 4.5D); however, τ_{cw} remained high over the course of a windy tidal cycle, even during slack water (Figure 4.5C).

4.2.2 Discussion on pro and cons of the approaches of estimating bed shear stresses

Several studies have compared the various approaches to estimating bed shear stress and have pointed out that each method has its advantages and disadvantages (Kim et al., 2000; Verney et al., 2006; Andersen et al., 2007; Salehi and Strom, 2012). They also concluded that in current-dominated environments, the different methods all tend to provide similar estimates, although the often-used LP method is better than other methods because it requires less data-set filtration (Andersen et al., 2007) and produces less scatter (Salehi and Strom, 2012). However, in the presence of waves it is difficult to identify the best method without knowing the true value of the bed shear stress. By focusing on the trends in time series, the magnitude of the estimation, degree of scatter, and the correlation with the SNR (signal-noise ratio), the TKE, TKEw, and RS methods have been identified as the most appropriate estimators of bed shear stress (Kim et al., 2000; Salehi and Strom, 2012). In the following discussion, we focus mainly on the limitations of each method in an attempt to identify the most appropriate method of estimating bed shear stress in combined wave–current environments.

Table 4.3: Inter-comparison (index of agreement, I) of τ_c in calm and windy conditions, and τ_{cw} in the whole measurement duration. In the WCI model, τ_w was obtained from spectral estimation using ADV measured pressure data. The following methods were used to estimate τ_c : TKE: turbulent kinetic energy; TKEw: modified TKE using vertical turbulent velocity only; ID: Inertial dissipation; and RS: Reynolds shear stress. The wave-turbulence decomposition methods used were moving averages (MA) and energy spectrum analysis (ESA).

	Method	LP	TKE		TKEw		ID	RS	Mean	
			MA	ESA	MA	ESA	MA			
$I-\tau_c$ Calm	LP	1	0.50	0.85	0.86	0.97	0.88	0.89	0.85	
	TKE	MA	0.57	1	0.82	0.83	0.64	0.78	0.62	0.75
		ESA	0.85	0.82	1	0.95	0.80	0.94	0.90	0.89
	TKEw	MA	0.86	0.82	0.95	1	0.89	0.98	0.81	0.90
		ESA	0.97	0.58	0.80	0.89	1	0.88	0.73	0.84
	ID	MA	0.88	0.77	0.94	0.98	0.88	1	0.81	0.89
	RS		0.89	0.61	0.90	0.81	0.74	0.80	1	0.82
$I-\tau_c$ Windy	LP	1	0.51	0.36	0.54	0.54	0.33	0.61	0.56	
	TKE	MA	0.51	1	0.67	0.71	0.58	0.66	0.38	0.64
		ESA	0.38	0.68	1	0.81	0.82	0.72	0.36	0.68
	TKEw	MA	0.55	0.72	0.81	1	0.86	0.79	0.39	0.73
		ESA	0.56	0.58	0.82	0.86	1	0.77	0.49	0.73
	ID	MA	0.36	0.65	0.72	0.79	0.77	1	0.37	0.67
	RS		0.62	0.35	0.34	0.37	0.46	0.35	1	0.50
$I-\tau_{cw}$ All	LP	1	0.72	0.64	0.73	0.75	0.58	0.76	0.74	
	TKE	MA	0.72	1	0.85	0.87	0.71	0.83	0.70	0.81
		ESA	0.65	0.86	1	0.91	0.87	0.85	0.65	0.83
	TKEw	MA	0.74	0.87	0.91	1	0.90	0.89	0.65	0.85
		ESA	0.76	0.73	0.87	0.90	1	0.84	0.63	0.82
	ID	MA	0.60	0.83	0.85	0.89	0.83	1	0.60	0.80
	RS		0.76	0.70	0.64	0.64	0.62	0.59	1	0.71
τ_{cw}	Mean	0.63	0.90	0.68	0.69	0.65	0.72	0.79	0.74 ^a	
(Pa)	Std.	0.50	0.56	0.41	0.41	0.39	0.49	0.59	0.48 ^a	

a. Results from the LP method are excluded as the related instrument ADCP covered less time measurement periods than ADV.

We used internal consistency analysis to examine whether the results derived from the $U_c(z) - \ln(z)$ relationship can be used to characterize boundary layer conditions. Estimations of τ_c by different approaches bring uncertainty in the definition of τ_{cw} . The LP method is a first moment method. This method requires a logarithmic velocity distribution, which may not be the case in reality. The present study shows a pass rate of 90% after internal consistency analysis, and most of the unpassed profiles were recorded at slack water, when the tidal current starts to rotate; this is in agreement with previous

studies (Collins et al., 1998; Wang et al., 2013; Zhu et al., 2014; Liu and Wu, 2015). Another limitation of the LP method is that it requires a fixed bed level that cannot vary with time. In reality, however, the bed level varies in the intertidal area. In energetic regions, where bed level change might be on the order of centimetres over a single tidal cycle, the error is caused by a vertical shift in the current velocity profile. For longer-duration measurements that incorporate extreme events, the error could be even larger when bed level variations may be on the order of decimetres.

Other mechanisms that violated the assumption of a logarithmic velocity distribution in shallow water include: unsteady flow (e.g., acceleration/deceleration of flow), stratification in the water column and transport of material as bed load, wind influencing the velocity profile by adding wave effects and producing variable velocity close to the water surface, and topography-induced secondary flows (Wilkinson, 1985; Gross et al., 1992; Friedrichs and Wright, 1997; Collins et al., 1998). For these reasons, the pass rate of internal consistency analysis may be lower, even reaching 0% at some locations (Collins et al., 1998). Note that a logarithmic velocity profile only guarantees the estimation of tidal-induced bed shear stress. The LP method would not detect the bed shear stress caused by wind-induced turbulent currents.

All estimates made using second momentum (TKE, TKE_w, ID, and RS) are sensitive to probe height. These techniques require the ADV sampling volume to be within the log layer, but high enough to avoid damping effects and near-bed stratification. Andersen et al. (2007) pointed out that placing the sampling volume at 1–4 cm above the bed might be too close to the bed and that fluctuations in vertical velocities would be dampened. This might be the reason why LP method was preferred rather than the second momentum methods. Among the second momentum methods, the ID method assumes that shear production and energy dissipation are equivalent. This means that an incomplete separation may lead to errors in the estimation of τ . Following the correction expression proposed by Huntley (1988), Kim et al. (2000) proposed a critical height of 35 cm, below which the full production–dissipation separation may not be ensured. In the present study, the ADV sampling volume height of 9.3 cm seems to be too low for ID estimation.

4.2.3 Impact of waves on estimating bed shear stresses

One of the key assumptions in the second momentum methods is that the fluctuating velocities measured in the vertical dimension are not contaminated by wave orbital motion, and this assumption has been used in many other studies (Kim et al., 2000; Andersen et al., 2007; Wang, 2007). This assumption has the largest impact on the TKE_w method, which only uses the vertical turbulent velocities. Without wave-turbulence decomposition, τ_{cw} could be overestimated by a factor of four (Figure 4.6A). The overestimation increases with enhanced wave strength, which is indicated by the H_s/h ratio, and 50% of the τ_{cw} values are overestimated by 1.6 times. When $H_s/h > 0.25$, the

possibility of τ_{cw} being overestimated by 1.6 times is greater than 50%; when $H_s/h > 0.5$, the possibility increases to 90% (Figure 4.6B). This indicates that under low-energy wave conditions, when H_s/h is low, the assumption is still valid. The TKEw method offers the easiest approach to estimating τ_c by applying $w_t = w - w_m$. It also implies that it is reasonable for Kim et al. (2000) using the assumption as their measurement were carried out in the deeper site where H_s/h ratio is very small.

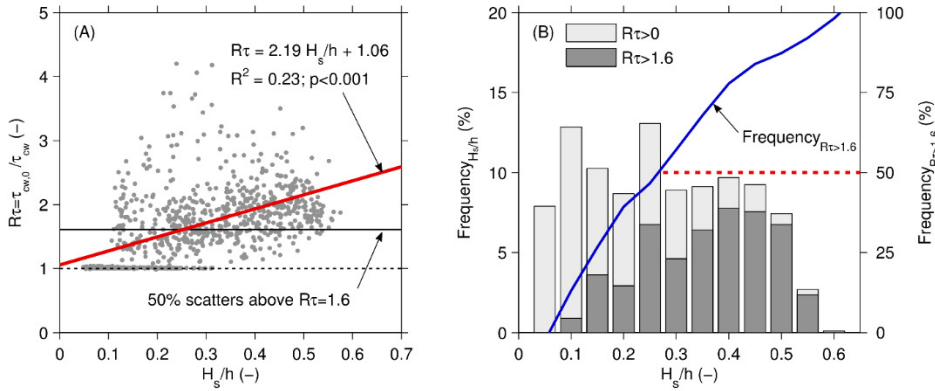


Figure 4.6: (A) The ratio of total bed shear stress without and with wave-turbulence decomposition ($R\tau = \tau_{cw,0}/\tau_{cw}$) increases with the ratio of significant wave height to water depth (H_s/h). Fifty percent of the τ_{cw} values are overestimated by 1.6 times. (B) Frequency diagram of H_s/h that $R\tau > 1.6$ probably occurs in the higher H_s/h domain. When $H_s/h > 0.25$, the possibility of the τ_{cw} value being overestimated by 1.6 times is greater than 50%.

Studies of the wind effect on bed shear stress help to improve our understanding of sedimentary processes in intertidal areas. It has been widely observed and accepted that high winds increase wave heights significantly and result in an increase in wave orbital velocity, and thus τ_w (Gross et al., 1992; Janssen-Stelder, 2000; Dalyander et al., 2013). In a field study on a mudflat in the Dutch Wadden Sea, Janssen-Stelder (2000) found that high bed shear stress occurs around high water, when current velocity is low, and this enhanced bed shear stress is dominated by the wave-induced component. Our study shows that the mean τ_w contributed 40% to the mean τ_{cw} in windy conditions, while 15% in calm condition.

In shallow-water environments, breaking wave is an important cause of bed erosion. However, τ_w is estimated under non-breaking conditions. Field and laboratory studies have shown that when depth-limit wave-breaking occurs, wave-breaking generates turbulence and setup flow that can agitate substantial amounts of bed sediment, which leads to increase in suspended sediment concentration (Levoy et al., 2000; de Vries et al., 2008; Callaghan and Wainwright, 2013). However, it remains difficult to quantify the

effect of breaking waves on bed erosion. In our case, the ratio of the height of largest 10% of waves to the water depth varies from 0.04 to 0.65; i.e., less than 0.73, and so indicates local non-breaking conditions (Battjes and Stive, 1985).

However, in addition to increasing the wave orbital motion, wind may affect the bed shear stress in another way because high values of τ_c were also found to occur around high water, when current velocities are low (Figure 4.5A). Using a regional-scale numerical modelling study of the Middle Atlantic Bight (USA), Dalyander et al. (2013) examined wind-driven currents by considering the correlation between non-tidal-induced stress and wind stress. This non-tidal term is usually caused by wind-driven flow. In our study, current speeds are still scaled with the water pressure gradient (Figure 4.1F and G). Therefore, in this case the wind-driven flow refers to turbulent flow rather than mean flow. The wind-driven turbulence cannot be captured by the LP method, which uses mean velocities, but it can be detected using the second momentum methods (TKE, TKEw, ID, and RS). These methods use the bulk turbulent velocities without separating the tidal-current-driven turbulence from the wind-driven turbulence. Therefore: (a) during slack water, the LP method results in low τ_c estimation, whereas the second momentum methods provide a τ_c of around 1 Pa (Figure 4.1I); and (b) under low-energy wave conditions, all methods are consistent, as the wind-driven motion is absent. This inference is supported by a recent wind-flume experiment, in which Su et al. (2015) pointed out that wind enhances the total bed shear stress by increasing the original vertical turbulence.

4.2.4 Impact of instrument settings on estimating bed shear stresses

According to the acoustic principle, ADV measurements suffer from Doppler noise (Lohrmann et al., 1995). The Doppler noise level increases as the height closer to the bed because of the random scatter and velocity shear in the sampling volume (Voulgaris and Trowbridge, 1998). Moreover, the noise error with respect to vertical velocity variance is smaller than that for the horizontal velocity variance, by at least an order of magnitude (Kim et al., 2000). From this point of view, the TKEw method is less sensitive to errors caused by Doppler noise.

In addition, attention should be given to sampling duration and frequency, regardless of which second momentum method is selected. High- and low-frequency losses are caused by inappropriate sampling rates and sampling durations, respectively (Soulsby, 1980). A sampling duration of 90 s provides about 30 waves. The spectrum analysed here (Figure 4.2C and Figure 4.4B) is complete in the low-frequency domain. A low limit of 5 Hz was estimated for the sampling rate by Kim et al. (2000). In the present study, a sampling rate of 8 Hz was sufficient to avoid high-frequency losses.

4.2.5 Optimum solution for estimating the total bed shear stress in intertidal areas

By considering the intercomparison results and limitations mentioned above, we suggest a optimum solution to estimate the total bed shear stress, τ_{cw} , from ADV measurement data following Figure 4.7.

Although the TKE_w method associated with the ESA wave-turbulence decomposition technique is ideal for estimating τ_{cw} , we still suggest that several approaches should be applied to obtain the most reliable estimate of bed shear stress.

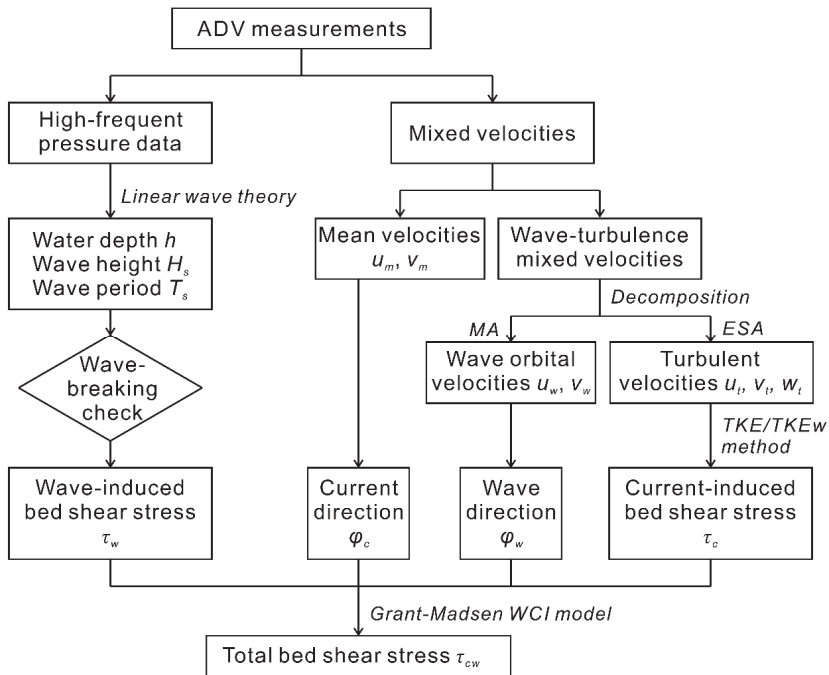


Figure 4.7: Protocols for estimating total bed shear stress under combined wave-current action, τ_{cw} , using *in situ* ADV data.

In the following analysis of Southeastern Chongming case, we use τ_{cw} calculated by the TKE_w method associated with the ESA wave-turbulence decomposition approach using ADV measured data.

4.3 Sedimentary processes and bed level changes

4.3.1 Sedimentary processes

Because near-bed SSC, c_b , varies over the course of a tidal cycle, to reduce complexity, we plotted the tide-averaged value (Figure 4.8D) at site C2. The average for tidal cycles 1–13 was $c_b = 0.4 \text{ kg/m}^3$, but increased to 1.7 kg/m^3 after cycle 14. We stress that the increase in SSC cannot be due to contamination of the OBS optical probe because the probe was cleaned daily with fresh water. The offshore surface SSC at Sheshan (see Figure 2.2) shows a similar pattern to our study site (Figure 4.8D), indicating that SSC increased on a regional scale towards the end of the first onshore wind stage.

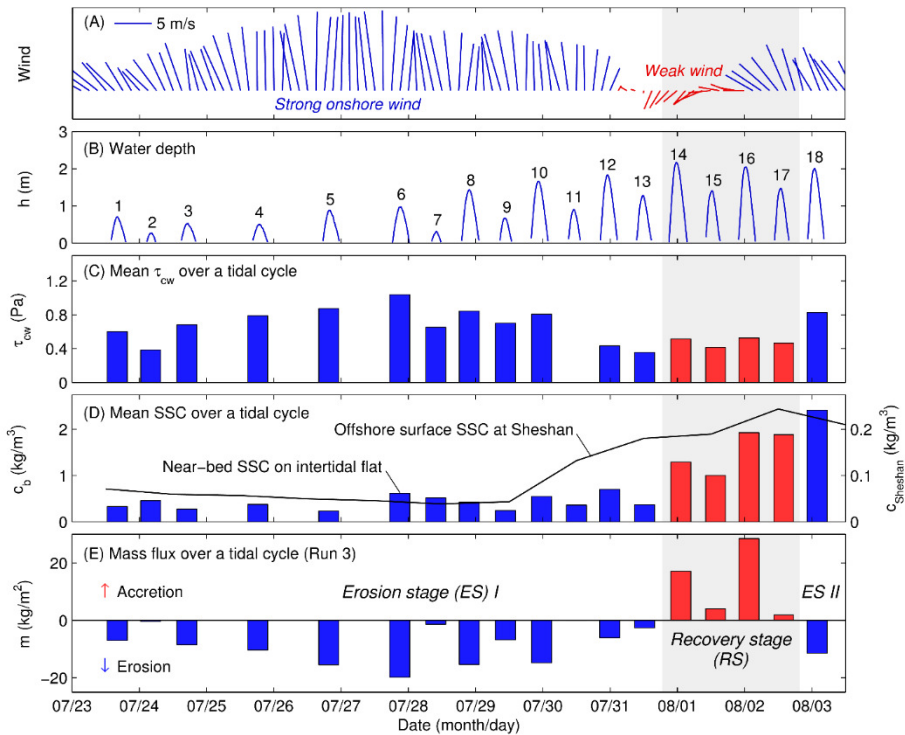


Figure 4.8: Time series of (A) wind vectors, (B) water depth (h), (C) tide-average value of combined wave-current bed shear stress (τ_{cw}), (D) tide-average near bed suspended sediment concentration (SSC, c_b) observed by OBS-3A, and surface SSC obtained at Sheshan ($c_{Sheshan}$, see Figure 2.2B), and (E) vertical sediment flux over each tidal cycle.

At C2, the critical bed shear stress for erosion, τ_e , was calculated as 0.29 Pa using Equation (3.1) and a constant water content of 32%. The average median grain size of

surficial sediment during the first onshore wind stage was 65 μm , with a mud (<62.5 μm) content of 46% (Figure 4.9). On August 1, during the period of weak offshore wind, median grain size decreased to 26 μm and the mud content rose to 100%.

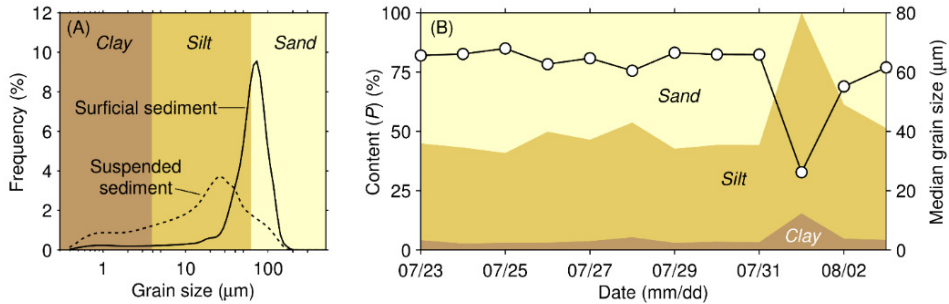


Figure 4.9: (A) Grain size distribution of surficial sediment sampled below the tripod and instantaneous suspended sediment sampled manually. Each line is the mean frequency curve of 12 surface bed samples and 4 suspended sediment samples, respectively. (B) Time series of clay, silt and sand components and median size of surficial sediment.

4.3.2 Measured bed level changes

Both the ADV and buried-plate measurements at Site C2 recorded bed degradation during strong wind conditions (tidal cycles 1–13) and bed accretion when the wind dropped and became offshore (tidal cycles 14–17; Figure 4.10A). We refer to these discrete periods of degradation and accretion as erosion stages (ES I; 1–13, and ES II; 18) and recovery stages (RS; 14–17), respectively, based on the behaviour of the bed level.

The ADV measurements showed that the bed level differs between the beginning and end of inundation periods (Figure 4.10A), indicating that bed-level variability occurs even in water depths less than 0.25 m. It indicated that hydrodynamic forces still act on the bed during very shallow waters. Dewatering process was considered to contribute to the bed-level variability in these stages when the bed position at beginning of a tidal inundation period was lower than that at the end of the previous tidal inundation period. However, because this process cannot be detected by direct measurement or modelling, we modified the ADV-measured bed levels by subtracting the intertidal difference in bed position for comparison with simulated values.

During the transition from the erosion to the recovery stage, we observed differences in the magnitude of bed-level change between the ADV and buried-plate derived measurements. The maximum erosion depths obtained by the buried-plate and ADV approaches were 6.9 and 10.6 cm, respectively, and occurred after tidal cycles 13 and 12, respectively (Figure 4.10). These differences were most probably caused by the slight difference in the positions at which the two techniques were used, the plate being

buried approximately 5 m from the ADV. Additionally, the ADV measurements were affected by scouring around the frame.

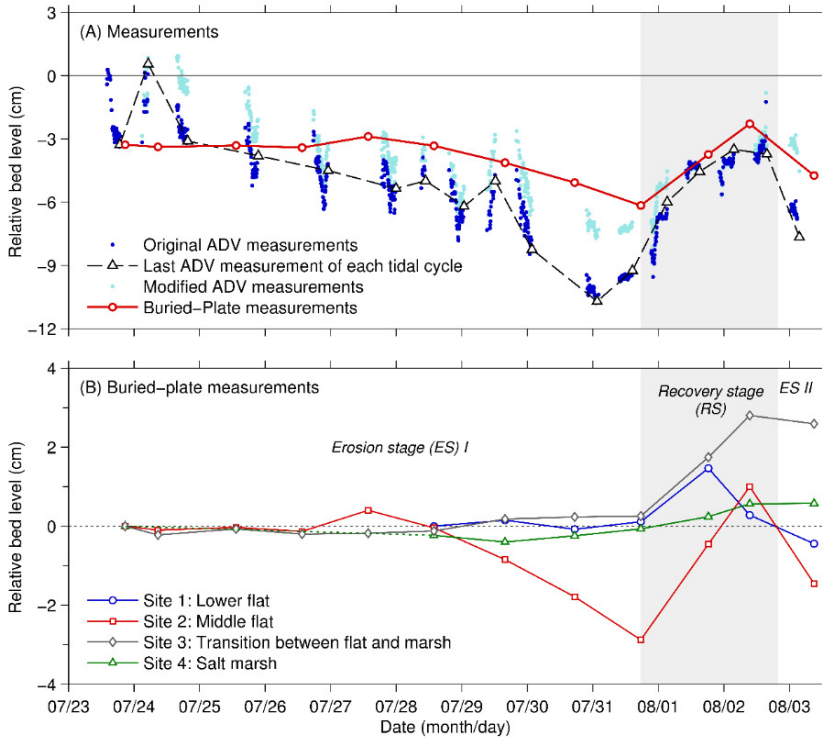


Figure 4.10: Time series of (A) measured bed level changes at Site C2, and (B) buried-plate measurements. To compare with simulated bed level later, ADV measurements are modified with removal the bed level difference between each two measured tidal cycles in (A).

Bed level changes on the mudflat were overall greater than on the salt marsh, and maximum bed level change was found at the middle flat (Site C2). During the first erosion stage, cumulative erosion at Site C2 (middle flat) reached ca. 3 cm, whereas bed level changes at the other sites were less than ± 0.5 cm. During the recovery, all the four sites experienced accretion, with maximum accretion found at Site C2 and minimum accretion found at Site C4 (salt marsh). During the second erosion stage, erosion was greatest at Site C2, second greatest at Site C1 (low flat), and third greatest at Site C3 (transition between flat and marsh), and almost no erosion was detected at the marsh site (Figure 4.10C).

4.3.3 The effect of strong winds on bed-level changes

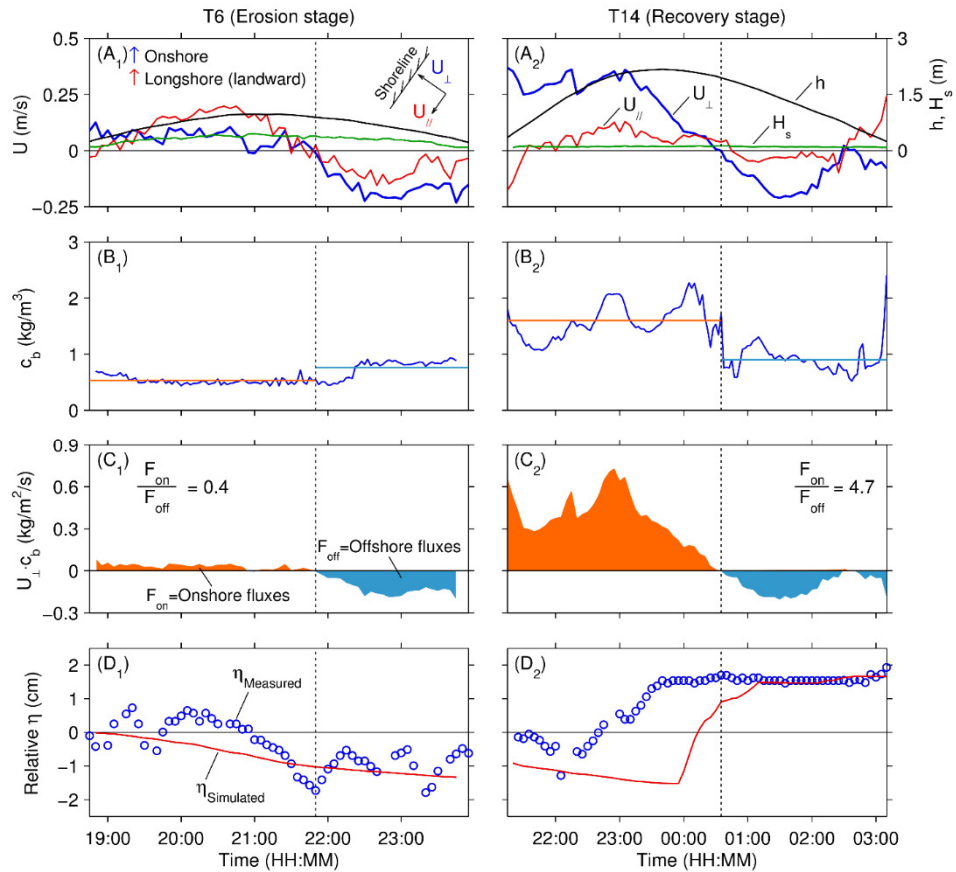


Figure 4.11: Time series of intra-tidal (A) onshore (U_{\perp}) and longshore velocities (U_{\parallel}), with water depth (h) and significant wave height (H_s), (B) Near-bed suspended sediment concentration (c_b), (C) Cross-shore near-bed sediment fluxes, and (D) ADV monitored (circle) and simulated (red line) relative bed level (η) in a typical erosion tidal cycle (T6) and a typical recovery tidal cycle (T14).

In contrast to storm conditions (wind speed >10.8 m/s), the morphological effects of strong wind conditions (wind speed <10.8 m/s) on meso- to macrotidal flats have not received much attention. Figure 4.11A₁–A₂ shows that the near-bed current speed varies with tidal range. Without the effect of waves, variations in current speed result in bed-level changes. Yang (1991) concluded that when wave forces exceed tidal forces, tidal cyclicity in bed-level changes is curtailed by waves. In our study, the mean wind speed during the measurement period was close to the year-averaged value, demonstrating that even normal wind conditions can modify the neap–spring cyclicity of bed-level changes.

Total bed shear stresses are higher over windy neap tides than during calm spring tides (Figure 4.8C). We note, however, that sediment concentrations are higher during spring tides than neap tides, a pattern that implies channel concentrations are following the spring–neap cycle.

Additionally, wind also serves to break the intratidal cyclicity of bed-level changes. On middle flats, tidal inundation begins with the peak flood flow, is characterised by slack water at high tide, and concludes with the peak ebb flow. According to Whitehouse et al. (2000), the bed alternates between degradation and accretion over the course of these three stages. In the present study, however, τ_{cw} values during over 90% of erosion stage were higher than the critical bed shear stress for erosion τ_e , indicating that erosion is a constant process whereas accumulation is comparatively rare. This imbalance results in net erosion of the bed during tidal inundation (Figure 4.11D₁).

The impacts of wind events on coastal bed-level changes can vary spatially and temporally. From the view of sediment balance, erosion some must correspond to accretion other where. For example, during a storm, erosion was observed on a mudflat, whereas accretion was found in the adjacent salt marsh and subtidal channel (Yang et al., 2003; Andersen et al., 2006). In general, the magnitudes of erosion and accretion on mudflats are larger than that on salt marshes. This is because salt marsh vegetation dissipates waves and weakens the action on bed sediments (Yang et al., 2012). Even on mudflat itself, erosion and accretion during a wind event can vary with elevation (Fan et al., 2006).

4.3.4 Bed recovery after wind event

Previous studies have shown that bed accumulation on intertidal wetlands follows wind-induced erosion (Pejrup, 1988; Yang et al., 2003; Andersen et al., 2006; Friedrichs, 2011). In our study, this recovery was rapid. After an eight-day period of erosion, for instance, the bed had nearly recovered its original position within two days. Sediment supply plays a fundamental role in bed recovery. The similar pattern of SSC variability between intertidal and subtidal flats (Figure 4.8D) suggests that there was an injection of sediment into both zones during the recovery stage. Pejrup (1988) demonstrated that onshore sediment fluxes are favourable under tide-dominated conditions. Sediment for bed recovery might also be supplied by the Yangtze River (Yang et al., 2003).

The increase in SSC and rapid bed recovery both occurred following tidal cycle 14, which marked the onset of a period of low wind speeds (Figure 4.10), rather than after tidal cycle 13. This is because the tidal range of cycle 14 exceeded that of cycle 13, resulting in a greater availability of tidal energy to erode and transport sediment from deeper waters. Additionally, we infer that the recovery stage coincided with the spring tide, which served to promote bed recovery.

The process of bed accretion occurs primarily through the settling-lag and scour-

lag (Van Straaten and Kuenen, 1958; Postma, 1961; Pejrup, 1988) associated with tidal asymmetry (Friedrichs, 2011). In Figure 4.11A₂–C₂, which shows the intratidal velocities, sediment concentration and near-bed sediment fluxes during a typical recovery tidal cycle, c_b was higher during the flood stage than the ebb stage. This pattern is the reverse of c_b variability during the erosion stage (Figure 4.11) and dominates the net onshore transport of sediment. Tidal asymmetry (Figure 4.11A₂) during the flood stage also serves to enhance net onshore sediment transport (Figure 4.11C₂). If sufficient distribution data are available, a detailed model of net sediment transport along a cross-shore transect can be derived from the analysis of grain size trends (Wang et al., 2012). On the one hand, enhanced high-energy flood flow will increase the bed shear stress, potentially resulting in bed erosion. However, as indicated by the layered bed model, deeper beds exhibit greater shear strength (Zhou et al., 2016), which, together with a decrease in τ_{cw} (Figure 4.8C), limits the magnitude of erosion. On the other hand, high-energy flood flow can transport considerable volumes of sediment onshore, whereas lower-energy ebb flow will remove comparatively less sediment offshore.

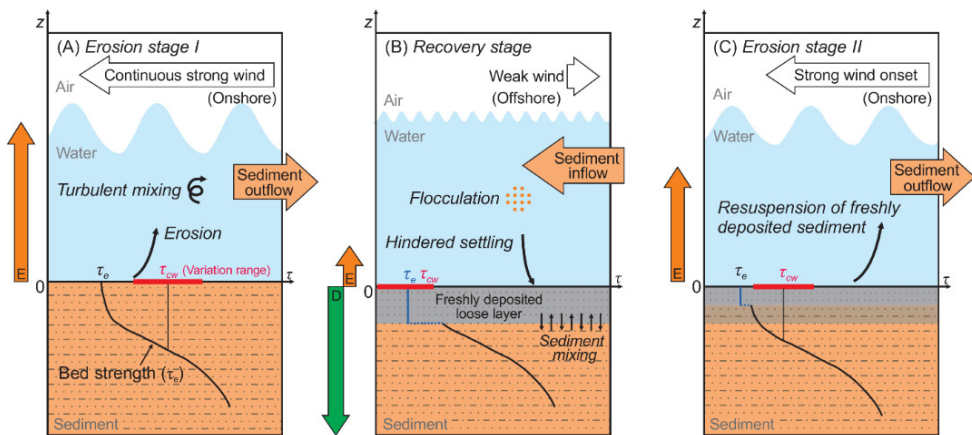


Figure 4.12: Schematic diagrams illustrate the key processes in three stages. Original vertical distribution of bed strength, representing τ_e , is redrawn after Winterwerp et al. (2012).

The settling time is also important to net bed accretion. In our study, sediment settling occurs 30% of measured tidal submergence in recovery stage by taking $\tau_d = 0.14$ Pa. Pejrup (1988) noted that the settling-lag and scour-lag processes are only effective during periods of high SSC (Figure 4.11B₂) when stimulated flocculation produces large settling velocities that serve to enhance deposition at slack water.

In summary, recovery is rapid when: (1) abundant sediment is delivered by high-energy tidal flows, probably during spring tides; (2) tidal asymmetry favours flood

dominance, leading to greater onshore sediment transport; (3) τ_d exceeds τ_{cw} long enough to promote sediment deposition; and (4) high SSC enhances flocculation, which also promotes settlement.

Figure 4.12 depicts the key processes operating in the three stages (ES I, RS, and ES II). The ADV-derived bed-level time series (Figure 4.10) shows rapid bed accretion during tidal cycle 14. Concurrently, the mud content increased from 50% in the erosion stage to 100% during the recovery stage (Figure 4.9). We suggest that the original coarser-grained bed became covered by a fresher, finer-grained layer. Such a change in bed condition undoubtedly affects the erodibility parameters M and τ_e in the recovery stage (Figure 4.12B). Water content W dictates τ_e according to Equation (3.1), and also serves to influence ρ_{dry} .

5 Sediment dynamics of Nanhui Foreland mudflat

Physical processes on Nanhui Foreland mudflat during normal weather and storm condition were investigated in this chapter. Study in normal weather indicates that bed shear stresses induced by waves can be important to sediment dynamics on the mudflat, even in periods of offshore winds. Relation of bed-level change, bed shear stress, critical shear stress for erosion and SSC is discussed in different intra-tidal stages. SSC-measurements close to the seabed revealed the presence of a highly dynamic fluid mud layer. Thickness of this layer depended on background SSC. Fluid mud layer occurred during high slack water was due to suspended sediment settling; resuspension induced fluid mud layer likely occurred caused by enhance combined wave–current action during storm condition. Existence of fluid mud layer further affected the sediment transport pattern. The studies therefore highlight the importance of employing combined wave–current action and measurements close to the sediment surface in coastal sediment dynamics.

Part of this chapter is based on the following manuscript:

Zhu, Q., Yang, S., Ma, Y., 2014. Intra-tidal sedimentary processes associated with combined wave–current action on an exposed, erosional mudflat, southeastern Yangtze River Delta, China. *Marine Geology*, 347: 95-106.

5.1 Physical processes during normal weather

5.1.1 Winds, tides, waves and currents (measurements in 2009)

Winds

During the observations, the overall wind direction was offshore (Figure 5.1A). The wind speed was moderate, at 6.7 ± 1.2 m/s during Tide 1 and 5.7 ± 1.1 m/s during Tide 2. Here Tide 1 and Tide 2 are defined as the two periods that the tidal flat was submerged. Tide 1 was roughly from 12-18 9:00 to 12-18 16:20, while Tide 2 from 12-18 21:40 to 12-19 3:40.

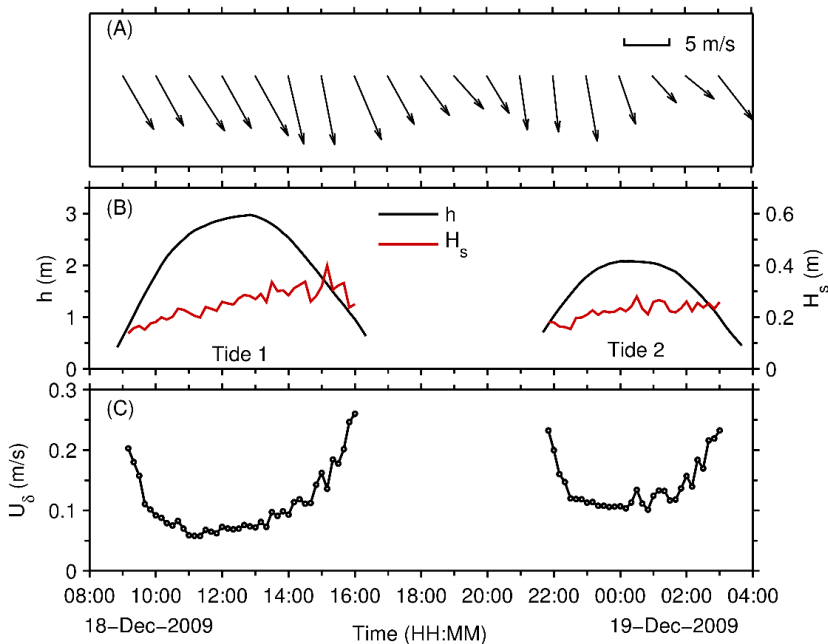


Figure 5.1: Time series of (A) wind vectors, (B) water depth (h) and significant wave height (H_s) obtained from SBE-26plus and processed by accompanied software SeasoftWave, and (c) peak orbital velocity, \hat{U}_s .

Tides

Both tides were approximately symmetrical. The maximum water depth at the high tide was 2.97 m during Tide 1 and 2.08 m during Tide 2 (Figure 5.1C). Given that the bed level of the observation site was 0.7 m below MSL, the tidal range was calculated to be 4.54 m for Tide 1 and 2.76 m for Tide 2. The large difference between the tidal ranges of the two tides reflects the characteristic of mixed semidiurnal tides in the study area.

Waves

The significant wave height (H_s) ranged from 0.14 to 0.40 m (Figure 5.1B). On average, H_s during the ebb stage (0.30 m for Tide 1 and 0.24 m for Tides 2) was 31% greater than that during the flood stage (0.21 m for Tide 1 and 0.20 m for Tides 2) (Table 5.1). Overall, the H_s during Tide 1 was slightly greater than that during Tide 2 (Table 5.1), which likely reflects the influence of wind speeds.

Table 5.1: Descriptive statistics for wave characteristics.

Tides	Period	Significant wave height (H_s) (m)			Peak orbital velocity (\hat{U}_δ) (m/s)			Relative wave height (H_s/h)		
		Max	Min	Ave \pm Std	Max	Min	Ave \pm Std	Max	Min	Ave \pm Std
Tide 1	Flood	0.29	0.14	0.21 \pm 0.04	0.20	0.06	0.09 \pm 0.04	0.17	0.07	0.10 \pm 0.02
	Ebb	0.40	0.24	0.30 \pm 0.04	0.26	0.07	0.14 \pm 0.06	0.27	0.09	0.16 \pm 0.06
	Whole tide	0.40	0.14	0.25 \pm 0.06	0.26	0.06	0.11 \pm 0.05	0.27	0.07	0.13 \pm 0.05
Tide 2	Flood	0.24	0.15	0.20 \pm 0.03	0.23	0.10	0.13 \pm 0.03	0.21	0.11	0.13 \pm 0.03
	Ebb	0.28	0.21	0.24 \pm 0.02	0.23	0.10	0.15 \pm 0.04	0.26	0.10	0.15 \pm 0.04
	Whole tide	0.28	0.15	0.22 \pm 0.03	0.23	0.10	0.14 \pm 0.04	0.26	0.10	0.14 \pm 0.04

Wave heights showed no significant correlation with water depth (Figure 5.1B). Because the water depth during Tide 1 was significantly greater than that during Tide 2, the relative wave heights and peak orbital velocities of the wave during Tide 1 were generally lower than those during Tide 2, although the wave heights showed an opposite trend (Table 5.1). However, during both tides, the peak orbital velocities showed an inverted phase mode with respect to water depth. That is, the tidal curve of the peak orbital velocity was U-shaped, with the largest values occurring at the beginning and the end of submergence and the lowest values occurring at high tides (Figure 5.1C).

The mean wave direction (the mean direction from which the waves arrived) was 206° during Tide 1 and 176° during Tide 2, which gives an average of 191° over the two tides. This indicates that the overall wave direction was onshore, as the coast faces the south (Figure 5.1B). As the wave direction was in disagreement with the wind direction, the waves were presumably derived from swells and refraction. At the study site, the total height of the seawall and the eroded cliff in front of the salt marsh was 6 m, and the

measurement of waves was conducted at a site only 300 m in front of the seawall. During our observations, the water at the measurement site was probably sheltered from the offshore winds by the seawall. That is, the wind-driven waves at this site, if they were formed, might be smaller than the waves caused by swells and refraction. As a result, the net wave direction was onshore.

Currents

Flow directions during both tides were generally north-westward during the flood stage and south-eastward during the ebb stage (Figure 5.2B). Because the coastline at the study site is oriented west–east (Figure 2.3C), the flow direction was between onshore and alongshore during the flood phase and between offshore and alongshore during the ebb phase.

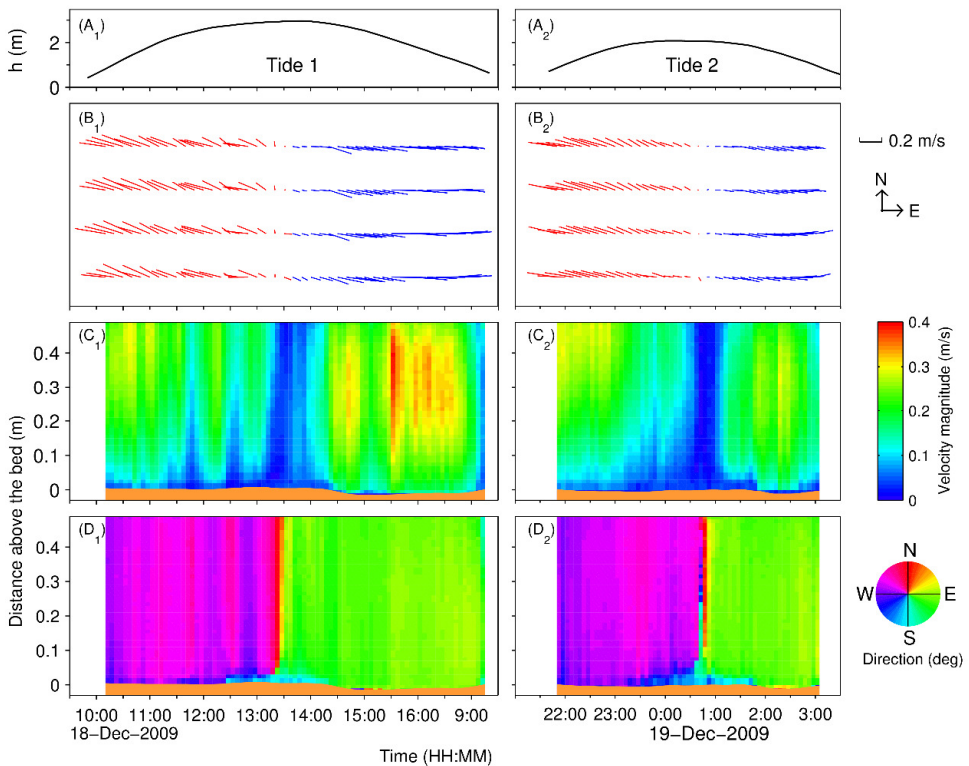


Figure 5.2: Time series of (A) water depth obtained from SBE-26plus SEAGAUGE, (B) current velocity vectors, (C) current velocity magnitudes and (D) directions obtained from PCADP. Subscripts 1 and 2 represent Tides 1 and 2, respectively. In panel (B), vector directions are: north is up; right is east. In panels (C) and (D), orange bottom represents sediment bed.

The flow velocity generally ranged from 1 to 32 cm/s (Figure 5.2C). The mean flow velocity decreased downwards from 19 cm/s at 45 cm above the seabed to 17 cm/s at 15 cm above the seabed and to 13 cm/s at 5 cm above the seabed (Figure 5.2B). Approximately 70% of the vertical velocity profiles passed the internal consistency analysis for a logarithmic distribution (Table 5.2); most of the profiles that did not pass the internal consistency analysis occurred at high tides when the flow velocities were very low.

Within tidal cycles, the flow velocities tended to be highest during early flood and late ebb, and lowest during high tides (Figure 5.2D). The averaged flow velocities were 16 cm/s during the flood phase and 20 cm/s during the ebb phase.

Table 5.2: Results of Internal Consistency Analysis of logarithmic distribution of vertical velocity profiles and derived parameters, the apparent roughness length z_0 and the drag coefficient C_D , of boundary layer.

Period	Number of profile			z_0 (10^{-3} m)	C_D
	Total	Pass	Rate of pass		
Tide 1 - flood	20	11	55%	3.04	$C_{D40}=0.0041$
Tide 1 - ebb	22	20	91%	0.26	$C_{D35}=0.0026$
Tide 1	42	31	74%	-	-
Tide 2 - flood	20	10	50%	7.06	$C_{D40}=0.0058$
Tide 2 - ebb	12	11	92%	0.53	$C_{D32}=0.0018$
Tide 2	32	21	66%	-	-

5.1.2 Bed sediment properties

The grain sizes of surficial sediments from just beneath the tripod ranged from 0.03 to 122 μm , with a median grain size (d_{50}) of 34 μm . The frequency curve of the grain size distribution was unimodal. The contents of sand, silt, and clay were 5%, 87% and 8%, respectively (Figure 5.3). The d_{50} of the other 29 samples collected in the 900- m^2 around the tripod was 33 ± 3 μm , suggesting that the sediment properties just beneath the tripod were representative of the study site. The water content of the sediment sample collected under the tripod was 72% in the uppermost 0.2 cm of fresh sediment and 34% for sediments 1 cm below the sediment surface.

Based on the method proposed by Taki (2001), τ_e was calculated to be 0.085 N/m^2 for the uppermost 0.2 cm of fresh sediment, and 0.119 N/m^2 for the sediments 1 cm below the sediment surface. As shown above, this method is applicable to muddy sediments with no significant biological disturbance, and the present study site met these preconditions.

Therefore, we believe that our calculated results are reliable.

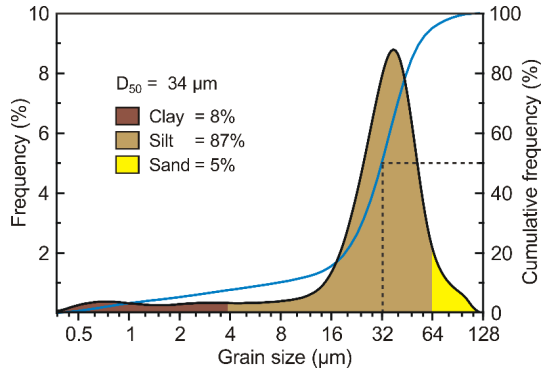


Figure 5.3: Grain size distribution of surface sediments sampled from directly beneath the tripod.

5.1.3 Bed shear stresses

Wave-induced bed shear stress (τ_w)

The τ_w ranged from 0.02 to 0.24 Pa (average, 0.07 Pa) during Tide 1 and from 0.04 to 0.31 Pa (average, 0.09 Pa) during Tide 2 (Figure 5.4B). During both tides, the time series of τ_w was U-shaped, with maximum values occurring at the beginning of flood and the end of ebb, whereas values were very low for the remainder of the submergence time, especially during high tide (Figure 5.4B).

Current-induced bed shear stress (τ_c)

Values of τ_c ranged from 0 to 0.4 Pa (average, 0.17 Pa) during Tide 1, and from 0 to 0.49 Pa (average, 0.18 Pa) during Tide 2 (Figure 5.4B). As for the flow velocity, the lowest values of τ_c occurred at high tides, whereas the highest values of τ_c occurred during the flood and ebb stages (Figure 5.4B). Values of τ_c were sometimes lower than τ_w at high tide and at the beginning of flood and at the end of ebb, but were higher than τ_w during the remainder (and most) of the time (Figure 5.4B). During Tide 1, the flood and the ebb time series of τ_c were approximately symmetrical. During Tide 2, however, values of τ_c during flood were significantly higher than during ebb (Figure 5.4B).

Bed shear stress due to combined wave–current action (τ_{cw})

The τ_{cw} values calculated using the three models were generally consistent with each other, although differences between them were occasionally substantial. The τ_{cw} values ranged from 0.03 to 0.78 Pa, with average values of 0.24, 0.25, and 0.25 Pa for the Grant–Madsen, van Rijn, and Soulsby models, respectively. Values of τ_{cw} were significantly greater than those of τ_c during the early flood and late ebb (Figure 5.4B); that is, during

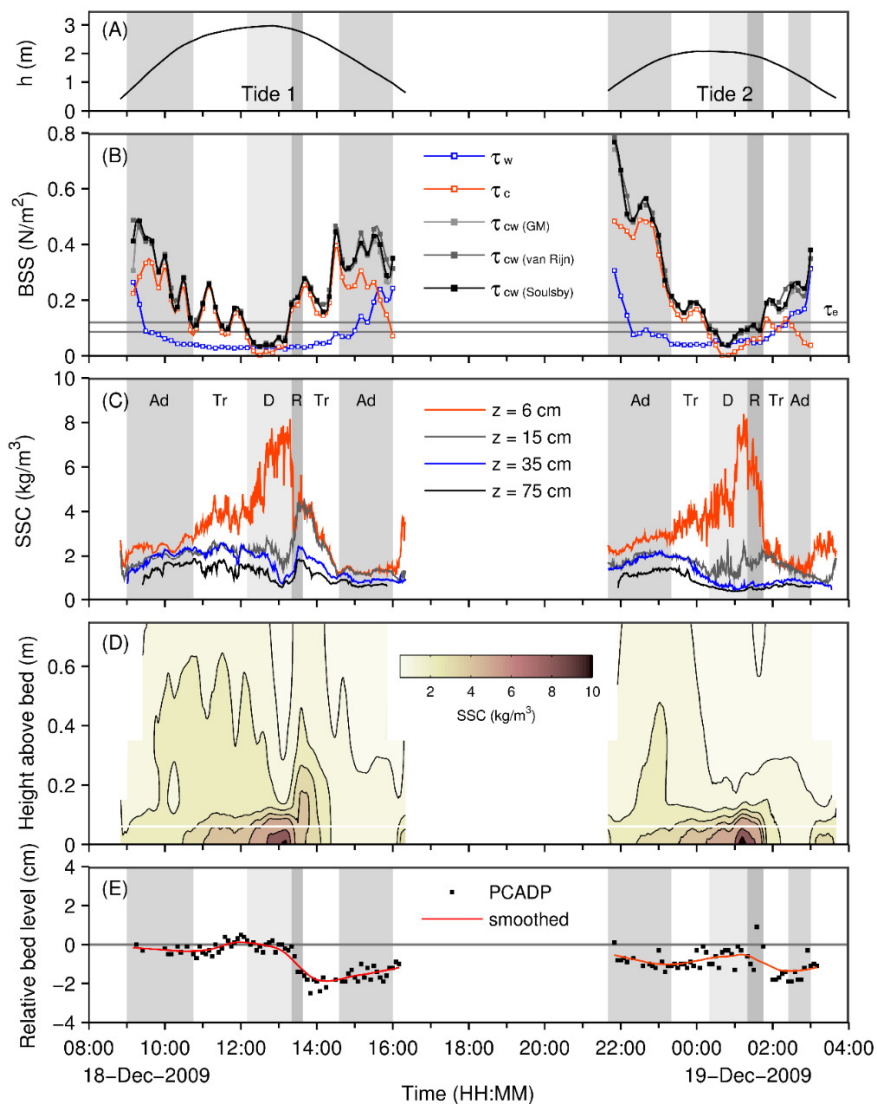


Figure 5.4: Time series of (A) water depth (h) obtained from SBE-26plus SEAGAUGE, (B) bed shear stresses (BSS), (C) suspended sediment concentration (SSC) obtained from the OBS-3As at different heights (z) above the sediment surface, (D) smoothed SSC contours, and (E) relative bed level changes (BLC) obtained from PCADP. **Ad**, **D**, and **R** in panel (C) represent the stages of advection, deposition, and resuspension stages, respectively, while **Tr** indicates transition stages. In panel (D), the SSCs below 6 cm above the bed surface (marked by a thin white band) were projected by interpolating the SSC from the given four heights. The dotted lines that bound the shaded contours indicate the end of SSC measurements due to fall in water level. The darkest cores in panel (D) indicates an SSC of >10 kg/m^3 .

shallow stages, waves play an important role in sediment dynamics. Values of τ_{cw} tended to decrease during flood, reaching their lowest values at high tide, and then increasing again during ebb. Values of τ_{cw} were noticeably less than those of τ_e for about 1 h around the time of high tides (Figure 5.4B).

5.1.4 SSC

The measured SSC ranged from 0.4 to 8.4 kg/m³ (Figure 5.4C). Vertical profiles show highest SSC just above the seabed, with values decreasing upwards (Figure 5.4D and Figure 5.5). The tide-averaged SSC at 6, 15, 35 and 75 cm above the seabed were 3.1, 2.0, 1.6, and 1.2 kg/m³, respectively, during Tide 1, and 3.2, 1.6, 1.8, and 0.8 kg/m³, respectively, during Tide 2. Vertical profiles of SSC during slack water at high tides were L-shaped, whereas SSC during typical flood and ebb stages increased more gradually with height, following a logarithmic trend (Figure 5.5).

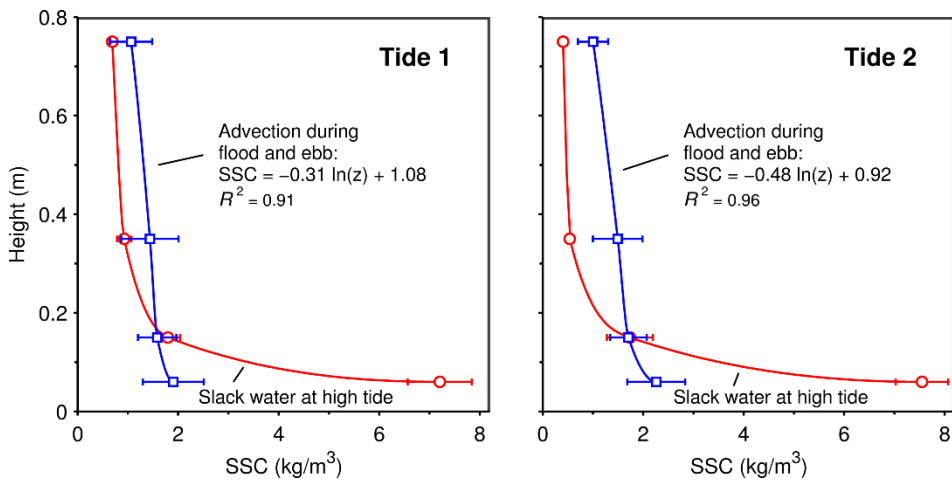


Figure 5.5: Vertical profiles of suspended sediment concentration (SSC) during slack water at high tide and during the advection stages of the flood and ebb tides. In the regression equations, z represents the height above the seabed.

The intra-tidal SSC time series shows that, during high tides, the SSC at 6 cm above the seabed is greatly increased, whereas the SSC farther above the seabed is reduced (Figure 5.4C). This suggests that settling of suspended sediments through the water column resulted in a fluidized mud layer in the lowest several centimeters of the water column. Based on the intra-tidal changes in current velocity and SSC, we identified three different stages of sediment transport: advection, deposition and resuspension. Advection indicates that the stage is characterized by the horizontal motion of suspended sediments and insignificant change in SSC under moderate currents. The deposition stage is

characterized by the settling out of suspended sediments and a significant increase in near-bed SSC at slack water. Finally, the resuspension stage is characterized by the reworking of previously deposited sediments and significant decrease in SSC due to the rebound of current velocity. During both tides, advection occurred during the flood, deposition occurred at high tide, resuspension occurred during the early ebb, and advection occurred during the full ebb stage (Figure 5.4C). The relationship between variations in SSC and hydrodynamic conditions is discussed below.

5.1.5 Bed-level changes

The net bed-level changes calculated on the basis of intra-tidal depositional and erosional mass fluxes using SSC and values of τ_{cw} and τ_e showed a net erosion of 6.0 mm (Grant–Madsen model), 6.9 mm (Soulsby model) and 7.6 mm (van Rijn model) over two tides. These values are close to net erosion observed using the triple-rods method (6.7 mm) and recorded by the PCADP probes (6.0 mm) after two tides (Table 5.3 and Figure 5.4E). In contrast, the bed-level changes calculated using τ_c showed a net accretion of 2.2 mm.

The details of intra-tidal bed-level changes were more complex than those involving net intertidal (between-tides) erosion. During both tides, numerous bed-level changes were recorded by the PCADP; a maximum cumulative erosion of 2 to 3 cm occurred at the beginning of ebb tides. In other words, the magnitude of gross intra-tidal erosion was much greater than that of net intertidal erosion.

Table 5.3: Comparison between cumulative erosion/deposition mass and bed level changes during the two tides.

		Deposition mass (kg/m ²)	Erosion mass* (kg/m ²)	Net bed level changes (mm)*
Based on combined wave- current action	Grant-Madsen model	1.9	7.2	-6.0
	Soulsby model	0.9	7.5	-6.9
	van Rijn model	1.4	7.7	-7.6
Observed using Triple-rods method**		-	-	-6.7
Observed using PC-ADP probe		-	-	-6.0
Based on current action only		6.9	4.8	+2.2

* Negative values represent net erosion.

**Difference between bed levels surveyed before Tide 1 (morning of 18 December) and after Tide 2 (morning of 19 December).

5.2 Relative importance of waves to sediment dynamics on exposed tidal flats

In a study of exposed tidal flats on Southeastern Chongming Island, Shi et al. (2012) noted the importance of waves to sediment dynamics, as tide-averaged τ_w values are as large as τ_c values on account of strong onshore winds, even during spring tides. In this study, although τ_w values were generally much lower than τ_c values under moderate offshore winds (vs. strong onshore winds) and spring tides, waves were still an important influence on sediment dynamics, for the following reasons: (1) τ_{cw} was much greater than τ_c during the shallow water stages (the beginning of flood and the end of ebb) when τ_w could exceed τ_c , and at slack water stages at high tides when flow velocities were nearly null. In some cases, τ_{cw} was several times greater than τ_c (Figure 5.4B). (2) More importantly, the calculated net bed-level change using τ_{cw} is in good agreement with the survey data, while the calculated result using τ_c is not. As indicated above, the calculated bed-level change using τ_c was 1.2 mm/tide (accretion), whereas the surveyed bed-level change and the calculated bed-level changes using τ_{cw} were ca. -3 mm/tide (erosion) (Table 5.3). (3) During our observations, the winds were offshore and wind speeds were about average. In the study area, the winds are onshore for half of the year, and several storms attack the coast each year (Yang et al., 2003). Under onshore wind conditions and in particular during storms, waves can play a much more important role in the sediment dynamics of the mudflats than in calm weathers (De Jonge and Van Beusekom, 1995; Yang et al., 2005a). Hence, it is absolutely necessary to incorporate waves into sediment dynamics models for exposed tidal flats in the area of this study, as well as on other open coasts worldwide (Yang et al., 2005b; Wang et al., 2006; Callaghan et al., 2010).

5.3 Intra-tidal bed-level changes

Bed-level changes on tidal flats surveyed between tidal submergences are useful for understanding neap-spring, seasonal, and long-term morphological evolution of tidal flats (Bassoullet et al., 2000; Andersen et al., 2006; Fan et al., 2006; Yang et al., 2011). However, such data do not elucidate the details of intra-tidal bed-level changes which, in combination with wave and current action data, are the keys to understanding the mechanisms of accretion and erosion. Measurements of intra-tidal bed-level changes have not been practical until the recent development of self-recording instruments. Although intra-tidal bed-level changes can be simulated mathematically, the models rely on actual measurements of intra-tidal current velocities, wave activities, water depths, and SSC (Whitehouse et al., 2000). Simulation results generally require calibration using surveyed bed-level data.

The present study using a PCADP, we observed bed-level changes, at 5-minute intervals. Most of the bed-level changes between burst intervals (5 min) ranged from 0 to 1 cm (Figure 5.4E), which is in good agreement with survey results of Anderson et al. (2006) on a Danish mudflat. Between-burst bed-level changes are frequent, which is presumably related to hydrodynamic and SSC variability (Figure 5.4). The data may also be partly influenced by the measurement errors. For example, the accuracy of the PCADP sensor for bed-level measurements is 1 mm (as explained above), while the accuracy of ALTUS is ± 2 mm (Andersen et al., 2006). However, temporal changes in bed-levels presumably filter out any interference attributed to the measurement errors, and thus accurately reflect the general patterns of erosion/accretion. Interestingly, during both tides, the temporal variations in bed-level are generally in phase with those of the near-bed SSC (at 6 cm above the seabed; Figure 5.4), suggesting that deposition of suspended sediment onto the seabed and resuspension of sediments from the seabed are reflected in the records of bed-level changes. The largest measure of intra-tidal erosion (2–3 cm) occurred during early ebb when the τ_{cw} increased rapidly and exceeded τ_e . The agreement of net bed-level changes surveyed within tidal cycles by the PCADP with the results of the other two methods (Table 5.3) also suggests that the PCADP could be an alternative approach to the measurement of intertidal bed-level changes.

The bed-level changes recorded by the PCADP suggest a maximum erosion depth of 2 cm during each of the tidal cycles (Figure 5.4E), which is much greater than the net intertidal bed-level changes of 3–4 mm per tide (Table 5.3). As the winds during our observations were offshore and moderate in speed, this maximum intra-tidal erosion depth only reflects the bed-level changes during calm weathers. During storms, the hydrodynamic conditions on tidal flats can change dramatically, and the intra-tidal maximum erosion depth would greatly increase. During Typhoon Paibian, for instance, erosional pits 30–40 cm deep (measured manually) were observed by the authors during the shallow stage of submergence on a tidal flat in eastern Nanhui, but these erosional pits had almost disappeared after the ebb (Yang et al., 2003). The author located (i.e., stumbled into) the submerged erosional pits as he walked across the mudflat (in several decimetres of water) during the storm; these pits had not been observed during previous observation (i.e., before the storm) at the same site. Water depth in the newly formed erosional pits was measured, as well as the water depth above the sediment surface around the pits, using a rod. The difference between these two water depths indicates the depth of the pits. Such strong intra-tidal erosion is likely to be extremely harmful to the benthos living in the sediments, if present, within the uppermost few decimetres on the tidal flats (Miller et al., 2002).

Although we observed net erosion rates of 3–4 mm per tide on the studied mudflat, these rates are not necessarily sustained; erosion/accretion rates are likely to vary when analyzed at different time scales, such as those of storm cycles, neap–spring cycles, and

seasonal cycles (Yang et al., 2008). It is possible that the erosion dominance observed in the present study is replaced by accretion dominance after neap tides with weaker winds. Nevertheless, the agreement of the simulated net intertidal bed-level changes with results of the other two methods implies that the mechanisms of erosion are well expressed in the calculation models, based on calculated and measured values of τ_{cw} , τ_e , SSC and properties of suspended sediments.

5.4 Physical processes under storm conditions

5.4.1 Sedimentary processes during the measurement period in 2014

The measurements at the Nanhui Foreland mudflat during the summer of 2014 lasted for 38 tidal cycles (number in Figure 5.6B). The short missing-data segments between tidal cycles indicate tidal emersion, and the longer (longer than one tidal cycle) segments were either caused by data retrieval or because of the instrument deployment schedule. The measurements covered a full spring-neap-spring cycle. The highest water depths in the neap and spring tidal cycles were 2.33 m and 4.12 m, respectively. The tidal ranges in the neap and spring cycles were calculated to be 1.5 m and 4.7 m based on the water depth and elevation of the measurement site.

The tidal-cycle-averaged wind speed during the measurement period ranged from 2.5 m/s to 11.7 m/s, measuring around 4–6 m/s during calm weather. The maximum wind speed (18.6 m/s) occurred at T26 (Figure 5.6A). The wind direction was southerly (onshore) at T5–6, T25–27, and T31–37 and northerly (offshore) at other times.

The near-bed (15 cm above the bed) current speed ranged from null to 0.51 m/s. The current speed during spring tides (0.25 m/s on average) was larger than that during neap tides (0.18 m/s). The significant wave height varied from 0.01 m to 3.9 m during the entire period, with an average value of 2.5 m. The wave height during typhoon ‘Fung-wong’ was much higher than those in calm weather. The effect of typhoons is discussed in the following section. Because of the effect of the spring-neap cycle and storm events, the total bed shear stress (τ_{cw}) during spring tides (0.65 Pa on average) was larger than that during neap tide (0.35 Pa on average), and even larger during storm events (2.13 on average; maximum of 4.79 Pa).

OBS-3A measured decreasing SSC from the bottom layer to the top layer: the average SSCs during the measurement period was 3.0 kg/m³, 1.4 kg/m³, and 0.7 kg/m³. In calm weather, the SSC showed a spring-neap cycle with high values during spring tides and low values during neap tide. During storms, the SSC values were 2.8 times larger than those in calm weather.

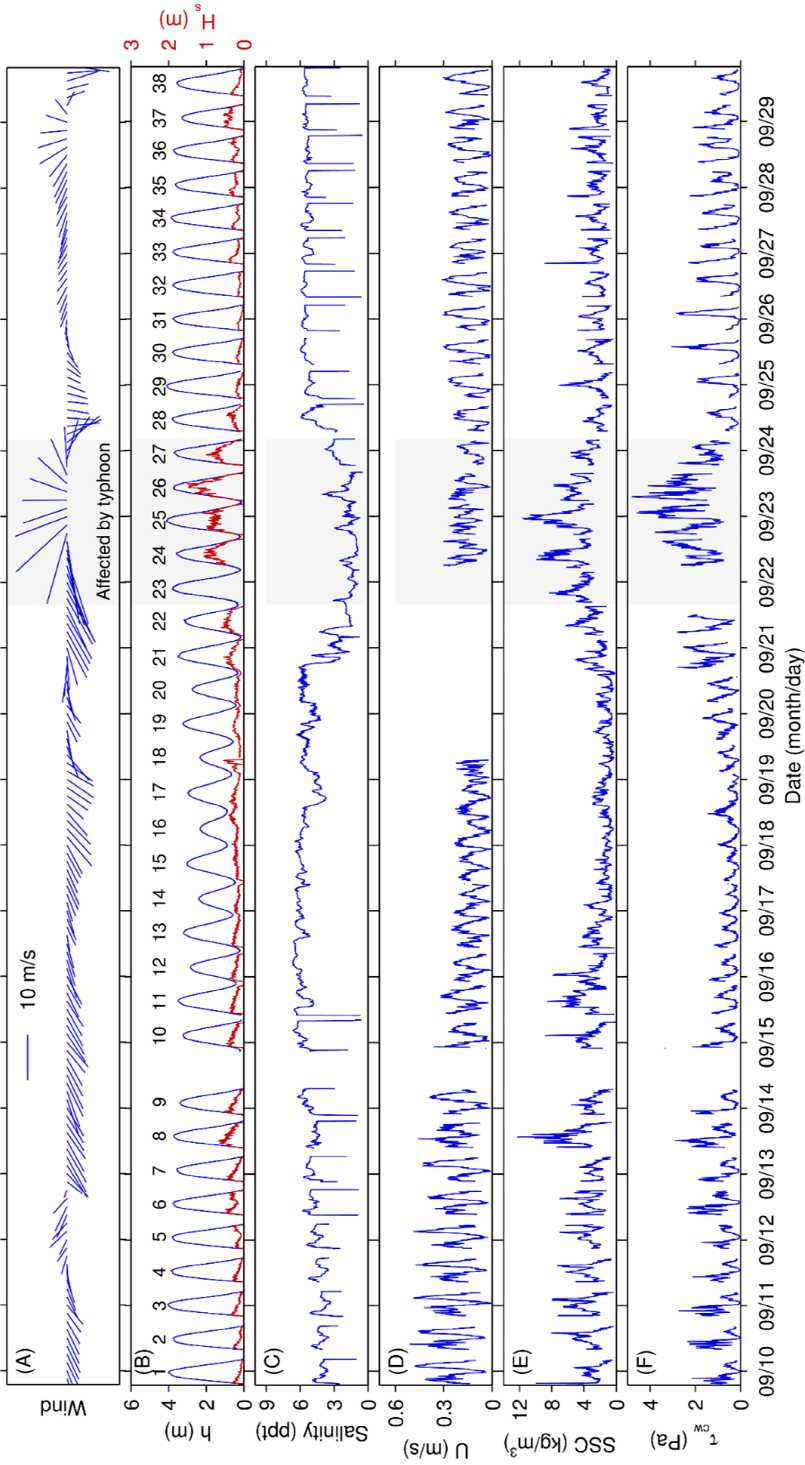


Figure 5.6: Time series of the (A) wind vector, (B) water depth (h), significant wave height (H_s), (C) salinity as measured by OBS-3A at 5 cm above the bed, (D) near-bed velocity (U) as measured by ADV, (E) suspended sediment concentration (SSC) as measured by OBS-3A at 25 cm above the bed, and (F) calculated total bed shear stress (τ_{ew}).

5.4.2 Variations in meteorological factors

The study area Nanhui experienced a typhoon, ‘Fung-wong’ (see its track in Figure 5.7), during the measurement period. The central maximum wind speed was 23 m/s during its landfall in Shanghai on 10:45, September 23, 2014. T29 was greatly affected by ‘Fung-wong’. Here, we chose T21–29 to discuss the storm’s impact on sedimentary processes in the study area.

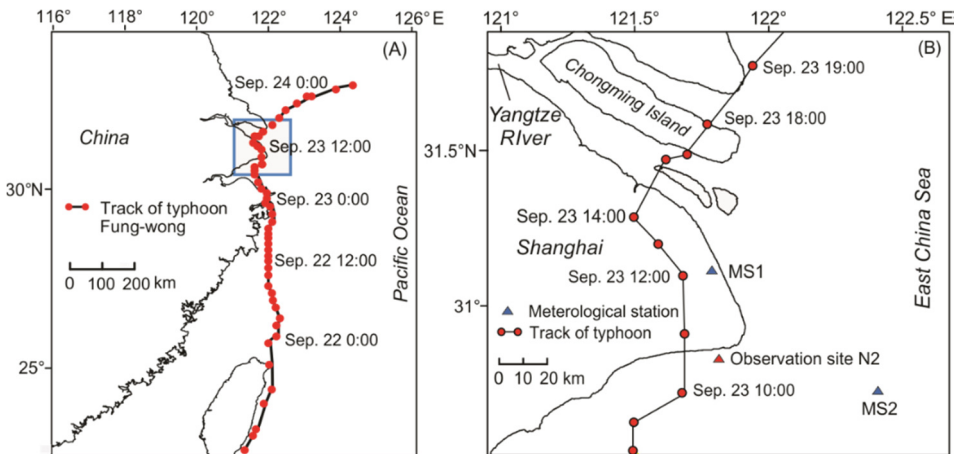


Figure 5.7: Track of typhoon ‘Fung-wong’.

When combining the wind data from Meteorological station 1 (MS1; Figure 5.7) and ECMWF near the study area, the wind speed increased from 6 m/s at T21 to 14 m/s at T26 and decreased to 3.0 m/s at T29. The hourly wind speed showed a maximum value of 19.1 m/s. The wind direction was onshore during the storm and offshore pre- and post-storm. We divided T21–29 into three sections according to the wind conditions in the study area:

- T21–22: pre-storm period;
- T23–27: during storm period;
- T28–29: post-storm period.

The air pressure was lower during the storm (minimum of 99.4 kPa) than that before (100.3 kPa on average) and after (100.5 kPa on average) the storm (Figure 5.8B). The variation in air pressure was caused by the movement of the typhoon because the central air pressure was lower than that of the surroundings. Precipitation was high during the storm, reaching 110 mm (24-hr accumulated) at T26.

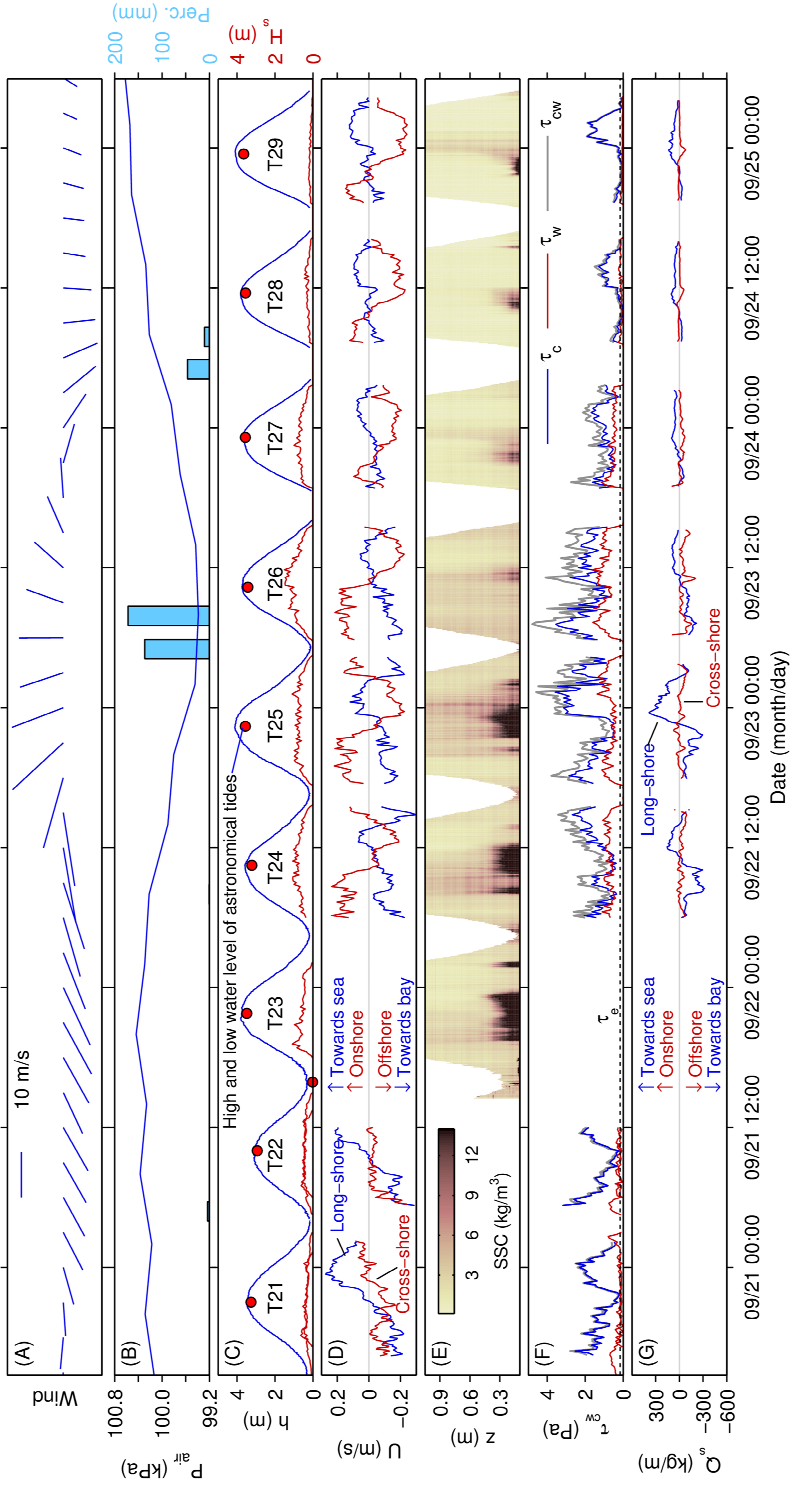


Figure 5.8: Time series in the tides around the storm: (A) wind vectors; (B) air pressure (P_{air}) and precipitation (Perc.); (C) measured water depth (h) and significant wave height (H_s), with the depth calculated from the predicted high and low water levels; (D) long-shore and cross-shore current velocities measured at 15 cm above the bed; (E) SSC profiles along height above the bed (z); (F) bed shear stresses; and (G) sediment transport rate per width within 0.5 m above the bed.

5.4.3 Tides, waves, currents and hydrodynamic forces

The maximum water depth increased from 3.2 m at T22 to 4.3 m at T29 (Figure 5.8C). These tides were in the transition from neap tides to spring tide (Figure 5.8B). A storm-induced tidal surge resulted in the difference between the measured and predicted (astronomical-tide-induced) water levels. The difference was 0.3 m on average, with a maximum value of 0.5 m at T26.

Table 5.4: Statistics of the meteorological and hydrodynamic parameters in response to the storm.

		Pre-storm			During storm			Post-storm	
		T21	T22	T24	T25	T26	T27	T28	T29
Water depth (m)	Mean	1.84	1.72	1.92	2.20	1.90	1.81	1.88	2.23
	Max.	3.50	3.17	3.60	4.12	3.74	3.70	3.80	4.10
	Min.	0.15	0.13	0.17	0.11	0.05	0.05	0.12	0.15
Wind speed (m/s)	Mean	7.79	10.21	15.49	13.38	8.92	8.99	6.56	4.19
	Max.	9.32	10.97	16.67	16.10	9.76	9.25	8.14	4.63
	Min.	6.68	9.74	13.51	10.06	8.53	8.85	4.91	3.29
H_s (m)	Mean	0.25	0.33	0.62	0.59	0.71	0.42	0.18	0.10
	Max.	0.54	0.60	1.06	1.10	1.50	1.00	0.46	0.22
	Min.	0.00	0.00	0.01	0.01	0.01	0.01	0.01	0.01
Current velocity* (m/s)	Mean	0.25	0.25	0.35	0.37	0.41	0.32	0.22	0.21
	Max.	0.36	0.42	0.51	0.61	0.78	0.52	0.35	0.42
	Min.	0.11	0.11	0.15	0.19	0.21	0.16	0.06	0.06
SSC* (kg/m ³)	Mean		3.86	5.91	6.22	3.78	2.83	1.83	1.90
	Max.		4.47	12.19	13.16	9.17	7.95	6.89	5.45
	Min.		2.73	2.04	1.59	1.82	0.94	0.52	0.45
τ_c (Pa)	Mean	1.26	1.27	1.27	1.83	1.89	0.96	0.44	0.54
	Max.	2.53	3.21	2.68	3.58	3.55	1.69	1.30	1.88
	Min.	0.19	0.21	0.35	0.45	0.63	0.24	0.02	0.03
τ_w (Pa)	Mean	0.22	0.24	0.65	0.63	0.83	0.38	0.09	0.05
	Max.	0.79	0.75	1.11	1.37	1.62	1.15	0.28	0.19
	Min.	0.02	0.02	0.00	0.00	0.00	0.00	0.00	0.00
τ_{cw} (Pa)	Mean	1.35	1.28	1.90	2.44	2.68	1.37	0.55	0.59
	Max.	2.79	2.80	3.43	4.59	4.79	2.75	1.50	1.93
	Min.	0.22	0.25	0.73	0.73	1.10	0.46	0.08	0.06
Q_s (kg/m)	Mean	59.8	69.5	163.0	217.5	140.7	64.0	43.6	55.7
	Max.	164.6	138.6	455.9	607.3	362.3	144.8	144.1	202.9
	Min.	21.9	2.3	28.4	47.1	36.4	15.2	2.1	3.1

* Average of the values in the near-bed 0.5 m.

The significant wave height (H_s) was below 0.5 m under calm conditions (T21–22 and T28–29; Figure 5.8C). During the storm, the H_s increased, with an average value of 0.64 m, which was 2.8 times higher than the average H_s in calm weather (0.23 m). T26 was greatly affected by the storm, showing a maximum H_s of 1.4 m. The mean H_s during T26 was 0.8 m, which was 3.5 times higher than the H_s in calm weather.

The near-bed current speed during the storm period was 1.6 times higher than that in calm weather (Table 5.4). The flow direction was generally westward during the flood stage and eastward during the ebb stage (Figure 5.8D). The long-shore velocity was larger than the cross-shore velocity because of the restraints of the shoreline. The flow velocity was low in high water and reached a maximum during flood/ebb peaks in calm weather, so the tidal wave was a propagation wave. During the storm period, however, both the long-shore and cross-shore flow velocities remained high around low water (T24–26; Figure 5.8D). The magnitude of the cross-shore velocities increased, which increased the total flow velocity.

Both τ_c and τ_w increased during the storm period (Figure 5.8; Table 5.4). The values of τ_c , τ_w and τ_{cw} were 1.7 times, 4.2 times and 2.2 times higher during the storm period than in calm weather (Table 5.4). The contribution of τ_c to τ_{cw} was over 90% under calm conditions, which indicates that tidal currents were dominant under normal calm conditions (Figure 5.8F). During the storm period, τ_w was significantly enhanced by increased wind strength from the storm. The mean τ_w (0.62 Pa) was larger than τ_e (0.16 Pa), and the waves at T26 may have greatly affected the bed sediment, with τ_w reaching 0.83 Pa. However, the increased flow velocity and turbulent level, which resulted in higher τ_c , may have been incorporated into waves to erode bed sediment. τ_c still contributed to approximately 70% of the τ_{cw} under storm conditions because this study area was a macro-tidal environment.

5.4.4 SSC

The SSC measured by OBS-3A and ASM better matched with the height increase (Figure 5.9). The index of agreement between the measurements of both instruments was above 0.9 for the height over 35 cm. This result indicates that the variation pattern in the SSC from the two instruments was close, although some differences did exist at small scales. This result might have depended on the instruments and probe type. OBS-3A was equipped with an OBS sensor that used the ultra-red band, whose wave length is 875 nm, while ASM's band was 850 nm. The accuracy of OBS-3A and ASM is $\pm 2\%$ and $\pm 5\%$, respectively (Scientific, 2007; ARGUS, 2012). In addition, turbidity measurements are affected by the grain size of the particles (Scientific, 2007). Sediment was frequently exchanged in the near-bed layer, so the grain size distribution might have varied greatly, causing the uncertainty in the turbidity measurements. This observation may explain the decreasing accordance of OBS-3A and ASM's measured SSC downward to the bed

(Figure 5.9). This analysis enables us to compare the SSC variations before (OBS-3A), during and after (ASM) the storm.

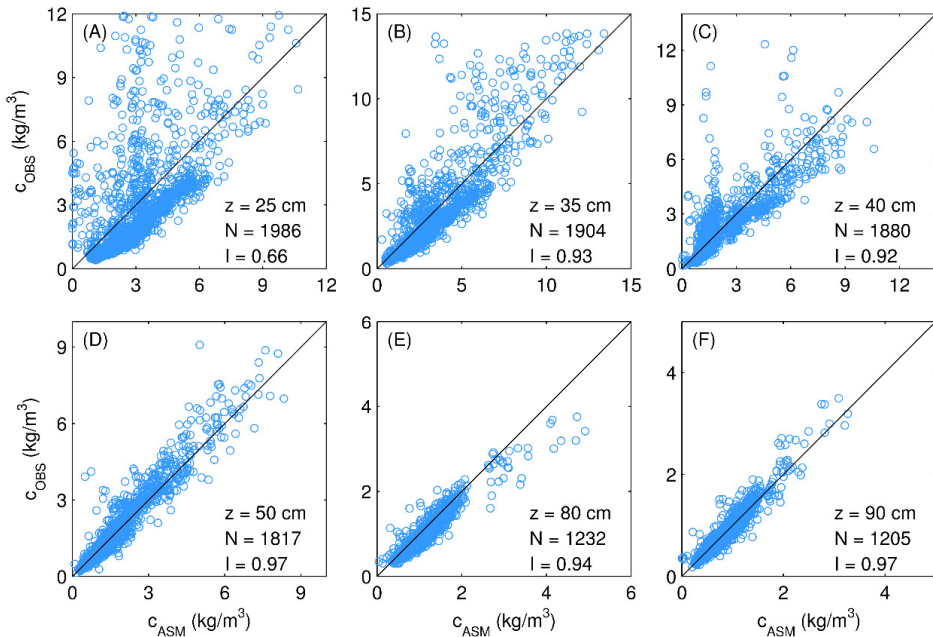


Figure 5.9: Comparison of the SSCs measured by OBS-3A and ASM at six heights (z). N is the number of valid measurements; I is the index of agreement. The black line is the 1:1 line.

The near-bed (50 cm) SSC during the storm period (4.7 kg/m^3) was 1.9 times higher than that in calm weather (2.5 kg/m^3). The tidal-averaged near-bed SSC was highest at T25, reaching 6.2 kg/m^3 (Table 4.2). During a tidal cycle, a high concentration layer ($>10 \text{ kg/m}^3$) often occurred within 50 cm under high slack water.

SSC variation showed a spring–neap cycle (Figure 5.6E) that near-bed SSC was high during typical spring tides (3.4 kg/m^3) and low during typical neap tides (0.9 kg/m^3). By modelling study, Chen and Gu (2000) concluded that SSC variation in the mouth of Hangzhou Bay was mainly controlled by water levels and current velocities in spring–neap cycle. However, storm event broke this spring–neap cyclicality. Storm in moderate tides lead to near-bed SSC increasing to 5.7 kg/m^3 , which was 1.5 times that in spring tides.

5.5 Variations in the near-bed SSC

5.5.1 High near-bed SSC layer on tidal flats during slack water

Extremely high near-bed SSC or fluid mud layers are widespread on continental shelves and in estuaries and bays; the thickness of these layers varies greatly (e.g., Kineke et al., 1996; Traykovski et al., 2000; McAnally et al., 2007). On the Amazon continental shelf, for instance, the thickness of the fluid mud layer can be greater than 1–2 m (Kineke et al., 1996). On the Eel River continental shelf in California, however, the thickness of the fluid mud layer is only 6–13 cm (Traykovski et al., 2000).

On tidal flats, fluid mud layers are sometimes reported following storms (Yang et al., 2003; Yang et al., 2005a; Yang et al., 2005b). Less is known about fluid mud layers on tidal flats under calm weather conditions. In the present study, fluid mud was clearly observed within the level of the lowest OBS during the slack water period at high tides, although its exact thickness is unknown.

In previous studies, near-bed turbidity sensors were usually mounted at heights of 10–30 cm above the seabed (e.g. Bassoullet et al., 2000; Andersen and Pejrup, 2001; Wang et al., 2006; Yang et al., 2007; Li and Yang, 2009; Dai et al., 2015b). At these heights, fluid mud layers existing just above the seabed would be undetected by the sensors. Although turbidity sensors have been occasionally mounted within 10 cm of the seabed on tidal flats, very little is known about the development of extremely high near-bed SSC or fluid mud layers. For example, on a mudflat in the Dollard Estuary, Netherlands, near-bed turbidity sensors were mounted at heights of 2.5 and 5 cm. However, because the mudflat is strongly sheltered from open sea waves, tidal currents are weak, and high-turbidity fluvial waters are absent, the near-bed SSC in this estuary were always less than 1 kg/m³ (Dyer et al., 2004). In a study of the mesotidal flats on the Jiangsu coast, China, Wang et al. (2006, 2012) mounted their lowest turbidity sensor at 8 cm above the seabed. They observed SSC of less than 2 kg/m³.

In the study of low flat of Nanhui Foreland mudflat (2009), background SSC were high. Before and after high tides, SSC in the water column within 75 cm of the seabed reached 1–2 kg/m³ or more, showing a logarithmically increasing trend approaching the seabed (Figure 5.4D; Figure 5.5). At high tides, flow velocities were null (Figure 5.2) and the wave action was at a minimum on account of the high water depth (Figure 5.1C and Figure 5.4B). As a result, τ_{cw} values decreased to their lowest levels within the tidal cycle, and were significantly less than the τ_e value, which presumably favours the deposition of suspended sediments. The pattern of abruptly increasing SSC in the water layers nearest to the seabed and decreasing SSC in upper water layers (Figure 5.4B) support this hypothesis.

The L-shaped SSC curve found during slack water at high tides suggests a layered

structure. Above the lutocline, SSC were low and well mixed, whereas below the lutocline, SSC increased rapidly towards the seabed. This layered structure also reflects the deposition of suspended sediments from the water column under weak hydrodynamic conditions. The high near-bed SSC or the fluid mud layer at high tide may be unstable; it may disappear during ebb tide when the value of τ_{cw} exceeds that of τ_e (Figure 5.4B and D), as a result of increased flow velocities and decreased water depth (Figure 5.2), resulting in sediment resuspension. In combination with earlier studies, such as that of Dyer et al. (2004), we conclude that under calm weather, high near-bed SSC or the fluid mud layer on tidal flats can either develop or not, depending on background SSC and hydrodynamic conditions. In other words, the thickness of the fluid mud layer can vary from null to substantial. Favourable conditions for the formation of high near-bed SSC or fluid mud layers include: (1) high background concentrations (e.g., $\geq 1\text{--}2 \text{ kg/m}^3$), supported by abundant fine-grained sediments from either fluvial or continental shelf resources; (2) macro tides leading to deep water at high tides; and (3) standing tidal waves resulting in slack water at high tides. As shown above, all of these conditions were present on the studied mudflat.

In many cases, very high SSC or fluid mud layers near the sediment surface may go undetected, on account of instrumental limitations or observational design. For example, using a 2-MHz acoustic bed-level sensor (ALTUS, described by Jestin et al., 1998), Anderson et al. (2006) observed a fluid mud layer 1–4 cm thick on a Danish mudflat. However, it is impractical to locate OBS sensors < 4 cm from the seabed. In the present study, if our lowest OBS was set 15 cm above the seabed, as per the normal design in earlier studies, we would have missed the extremely high near-bed SSC layer.

5.5.2 High near-bed SSC layer on tidal flats during a storm event

With the development of ASM, continuous turbidity measurements with high spatial resolution (1 cm) can provide great insight into the generation, development and disappearance of near-bed fluidized mud layers. The near-bed high concentrated mud layer in the lower flat (measured in 2014) was also found during high slack water, which was similar to the SSC measurement results in the middle flat (measured in 2009). However, the differences between these two cases are as follows:

(1) A shorter-duration near-bed fluid mud layer ($\text{SSC} > 10 \text{ kg/m}^3$) was found in the lower flat during flood/ebb peaks (Figure 5.8). The mechanisms of the generation of this fluid mud layer under high slack water and in the flood/ebb peak stages were different. The fluid mud layer in the flood/ebb peak stages occurred favourably during storm periods. The flow velocity was high and turbulence was strong at that time, so suspended sediment had little chance to settle to the bottom. Thus, the resource of the fluid mud layer must have been the bed sediment, which indicates that strong resuspension occurred under flood/ebb peaks during the storm stage as a result of enhanced hydrodynamic forces.

Another reason for this significant resuspension was that liquefaction might have occurred, which would have decreased the strength of the surface mud layer (van Kessel and Kranenburg, 1998). Liquefaction often occurs during storms and hurricanes (Teisson et al., 1993; van Kessel and Kranenburg, 1998; Jaramillo et al., 2009). Liquefaction occurs when the wave-induced stress inside the bed is larger than the yield strength of the bed. Under this condition, the surface sediment contains more water and is easily and quickly entrained by the increasing hydrodynamic forces, leading to a near-bed fluid mud layer (van Kessel and Kranenburg, 1998).

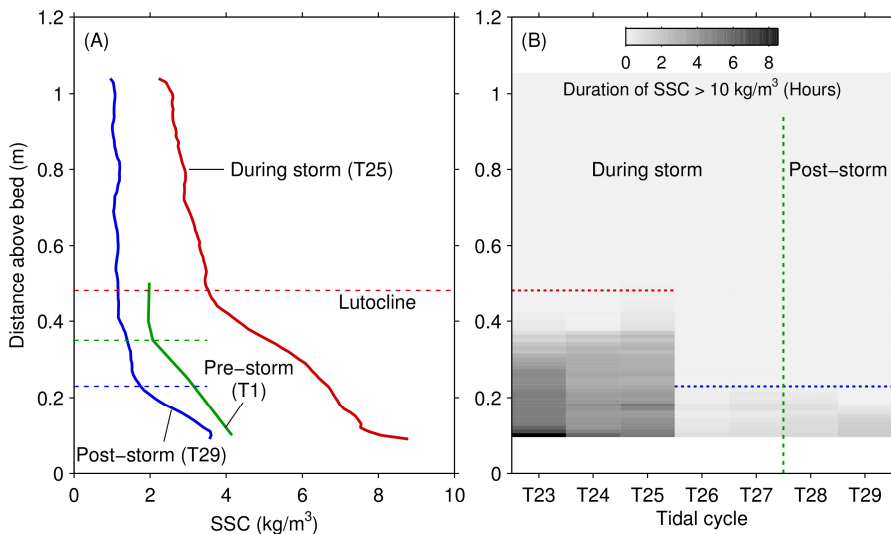


Figure 5.10: (A) Tidal-averaged SSC profiles before, during and after the storm. The SSC profiles at T25 and T29 were obtained by ASM, and that at T1 was obtained by OBS-3A. (B) Vertical distribution of the duration when the SSC > 10 kg/m³ at each tidal cycle (measured by ASM).

(2) Under calm conditions, the near-bed fluid mud layer in the lower flat was thicker than that in the middle flat. The ASM measurements showed that an upper SSC boundary > 10 kg/m³ in the lower flat was located 20–35 cm above the bed. In the middle flat, the OBS at 15 cm did not detect SSC values over 10 kg/m³, which indicates that the fluid mud layer in the middle flat was less than 15 cm. At T23–25 during the storm period, the SSC in the water column increased: i) the background SSC increased from 1.0–2.0 kg/m³ under calm weather conditions to 3.3 kg/m³ under storm conditions (Figure 5.10A); ii) the boundary of the fluid mud layer increased from 0.2–0.3 m under calm weather to more than 0.4 m (Figure 5.10). At T23, fluid mud occurred 0.09 m above the bed for 60% of the full tidal submergence. The lowest OBS probe of ASM was 0.09 cm, and the SSC increased downward to the bed. The occurrence of fluid mud within 10 cm above the bed

might have been even greater than 60%.

In the second phase of the storm period (T26–27), the background SSC, thickness and occurrence of the fluid mud layer decreased. The wave height reached a maximum and the tidal-averaged τ_{cw} was the greatest, especially at T26, but the mean SSC within 50 cm above the bed was the smallest. As bed erosion occurred, the deeper layer, which was more difficult to erode, was exposed to the flow. The bed was stratified, and the critical shear stress for erosion increases with depth, so this deeper bed provided less sediment supply to the water, leading to a smaller SSC. This depth-limited (or supply-limited) erosion was described as Type I erosion by Mehta and Partheniades (1982).

5.6 Sediment transport rate in response to storm event

The SSC profiles showed various shapes in the shallow and turbid area, while the majority of the SSC profiles were smoothly concave upward, with the SSC increasing towards the bed (Liu et al., 2014). More suspended sediment was transported in the near-bed layer. In our case (Nanhui Foreland mudflat 2009), 70% of the suspended sediment was transported in the near-bed 50 cm. Thus, we discuss the sediment transport by focusing on the sediment fluxes (Q_s) within 50 cm above the bed.

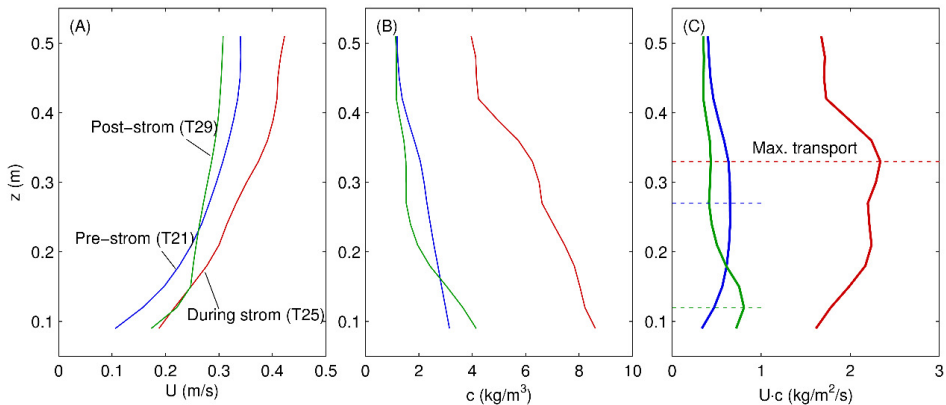


Figure 5.11: Tidal-averaged near-bed (50 cm) profiles of the (A) horizontal current speed (U), (B) suspended sediment concentration (c) and the multiplication of U and c before (T21), during (T25) and after (T29) the storm.

The sediment transport rate per width (Q_s) under storm conditions was 146.3 kg/m^3 , which was 2.6 times larger than that in calm weather (57.1 kg/m^3). T25 showed the largest Q_s , 3.8 times that in calm weather (Table 5.4). Because of the flow directions, the sediment transport rate along the long-shore direction was larger (2.5 times) than that

along the cross-shore direction. This observation indicates strong sediment exchange between Hangzhou Bay and the Yangtze Estuary under storm conditions.

Liquefaction and the resuspension of bed sediment, which generated a fluid mud layer, as mentioned in section 5.5.2, resulted in high transport rates during the storm event. The SSC increased towards the bed, while the current speed decreased along the depth. Multiplying the two profiles reflected the maximum sediment transport area in the water column. Under calm conditions, the maximum sediment transport area was within 0.3 m above the bed, typically ranging from 0.1 m to 0.25 m. The position of the maximum transport area was lifted up to 0.33 m above the bed because of the increase in the thickness of the near-bed fluid mud layer.

5.7 Discussion on sedimentary processes associated with hydrodynamic mechanisms on tidal flats

During two consecutive tides in 2009, we observed similar intra-tidal patterns of wave action (U-shaped time series of peak orbital velocity and τ_w), currents (oscillating flow directions, and V-shaped time series of flow velocity and τ_c), SSC (reverse V-shaped time series of near-bed SSC at 6 cm above the seabed, L-shaped vertical profiles at slack water at high tides and logarithmic vertical distributions during flood and ebb stages), and bed-level changes (slight erosion during flood, accretion during high tide, strong erosion during ebb, and net intertidal erosion). These similar intra-tidal patterns likely reflect common laws of hydrodynamics and sedimentary processes. However, hydrodynamic and sedimentary processes are likely more complex than what we have observed.

As with numerous earlier studies (e.g., Freeman et al., 1994; Jing and Ridd, 1996; Andersen and Pejrup, 2001; Hoitink and Hoekstra, 2005; Wang et al., 2006; Andersen et al., 2007; Quaresma et al., 2007; Wang et al., 2012), the study of Nanhui Foreland mudflat 2009 leaves ample room for further research, as follows. (1) Site-based and cross-shore comparisons of hydrodynamic and sedimentary processes in subtidal, low mudflat, middle mudflat (at MSL), and high mudflat zones are needed. Sedimentary processes at these sites may differ greatly. For example, in subtidal zone, stages of slack water and near-bed high SSC are expected to occur at both low and high tides. In contrast, on high mudflats, only one stage of slack water is expected, and the shallow water may limit the thickness of the high SSC layer. These types of comparisons will enhance our knowledge and understanding of both single-site and cross-shore sediment exchange. (2) Comparison of processes occurring on sheltered and exposed coasts, between progradational and erosional coasts, and between microtidal, mesotidal and macrotidal coasts are needed. (3) Temporal comparisons between calm and stormy weather conditions, incorporating high

resolution observations on currents, waves, SSC, and bed-level changes (especially during stormy conditions) are urgently needed. (4) Technical advancements to improve *in situ* measurements of near-bed hydrodynamic conditions, SSC, and bed-level changes are needed. Although substantive efforts have been made to investigate near-bed hydrodynamic and sedimentary processes, very few sensors have been set within 5 cm of the seabed. In many cases, the hydrodynamic boundary layer and the fluid mud layer may develop within this height. Smaller and more probes are required to establish the nature of the interface between near-bed layers and those in the upper water column. (5) Improvement of approaches for determination of parameters needed in calculations of erosion and deposition. For example, the calculation of the critical bed shear stress for erosion (τ_e) by Taki (2000) is based only on the water content of sediments, and is only applicable for muddy sediments. In fact, the lower parts of many tidal flats are sandy (e.g., Uncles et al., 1998; Fan et al., 2006; Yang et al., 2008). The determination of τ_e should incorporate both water content and grain size. Up till now, the determination of the critical shear stress for deposition (τ_d) has no widely accepted standard. For example, Milburn and Krishnappan (2003) used a τ_d value of 0.08 Pa (assumed to be 1/2 of the value of τ_e). Some other researchers used a τ_d value of 0.05 Pa (Wang, 2009; Shi et al., 2012). According to Lumborg (2005), τ_d ranges from 0.01 to 0.1 Pa and is typically around 0.05 Pa for mixtures of fine-grained mineral particles. Some studies have calculated erosion and deposition using a single critical shear stress measure (i.e. τ_e) (e.g., Christie et al., 1999), whereas other studies have employed separate critical shear stress values for erosion (τ_e) and deposition (τ_d) (Cancino and Neves, 1999; Lumborg, 2005; Andersen et al., 2007). Therefore, there is a need to establish uniform methods for calculating erosion and deposition, even though specific sedimentary parameters (such as τ_e) may vary between localities.

6 Sediment dynamics of Kapellebank mudflat

Concerning the cross-shore distribution we find that critical shear stress for erosion decreased from high to low intertidal flat. Bed degradation at lower intertidal flat was enhanced as the storm occurred during neap tides. It indicated that especially the bed at the elevation just below low water is highly sensitive for erosion during a storm event. This finding suggests that accurate simulation of intertidal bed evolution during very shallow water is necessary. Furthermore, enhanced wind-wave played limited role on bed erosion on semi-enclosed intertidal flat. The flow structure on the transition between tidal flat and channel substantially enhanced the bed erosion potential. Vertical distributions of critical shear stress for erosion (τ_e) is investigated and schematized. We also found that occurrence of diatom significantly enhanced the τ_e for surface sediment. This might be taken into account when the model is relevant for estimating the seasonal variability of sediment transport on intertidal flats. The findings in this chapter improve our insights into morphodynamics of tidal flat in response to wind events.

This chapter is based on the following manuscript:

Zhu, Q., van Prooijen, B.C., Maan, D.C., Wang, Z.B., Daggert, T., Yang, S.L., 2017. Cross-shore and vertical variability of mudflat erodibility: An integrated approach of in situ measurements and modelling. (Submitted)

6.1 Physical processes of sheltered mudflat

6.1.1 Tides and waves

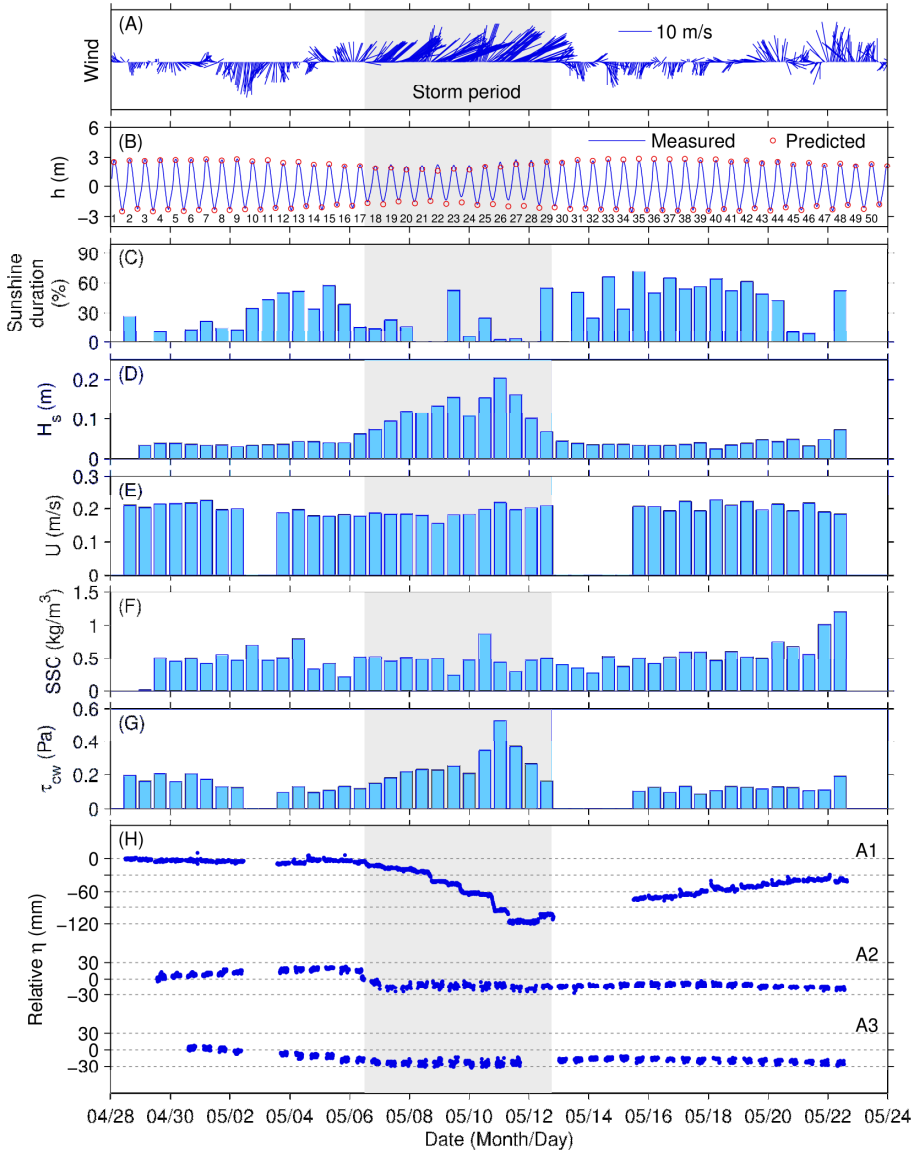


Figure 6.1: Time series of (A) wind vectors, (B) measured water level and predicted high and low water levels at the Hansweert gauge, (C) sunshine duration, (D) significant wave height (H_s), (E) current speed (U), (F) SSC, (G) total bed shear stress (τ_{cw}), and (H) bed level changes. Numbers in panel (B) represent order of tides. In panels (C)–(G), each bar indicates tidal averaged value. (D)–(G) are based on measurements at Site A1.

The water level at Hansweert showed that the maximum spring tidal range and minimum neap tidal range were 5.3 m and 3.3 m, respectively. During the measurement period, a storm event occurred from May 6 to 12. Onshore wind with speed >8 m/s is referred to as a storm period in this case (Figure 6.1A). The difference in the measured and predicted water levels indicated that the storm surge was 0.4 m on average, with a maximum value of 0.7 m (Figure 6.1B). Neap tides that coincided with the storm surge led to continuous inundation at the lowest site, A1, with a water depth of approximately 0.4 m during low waters.

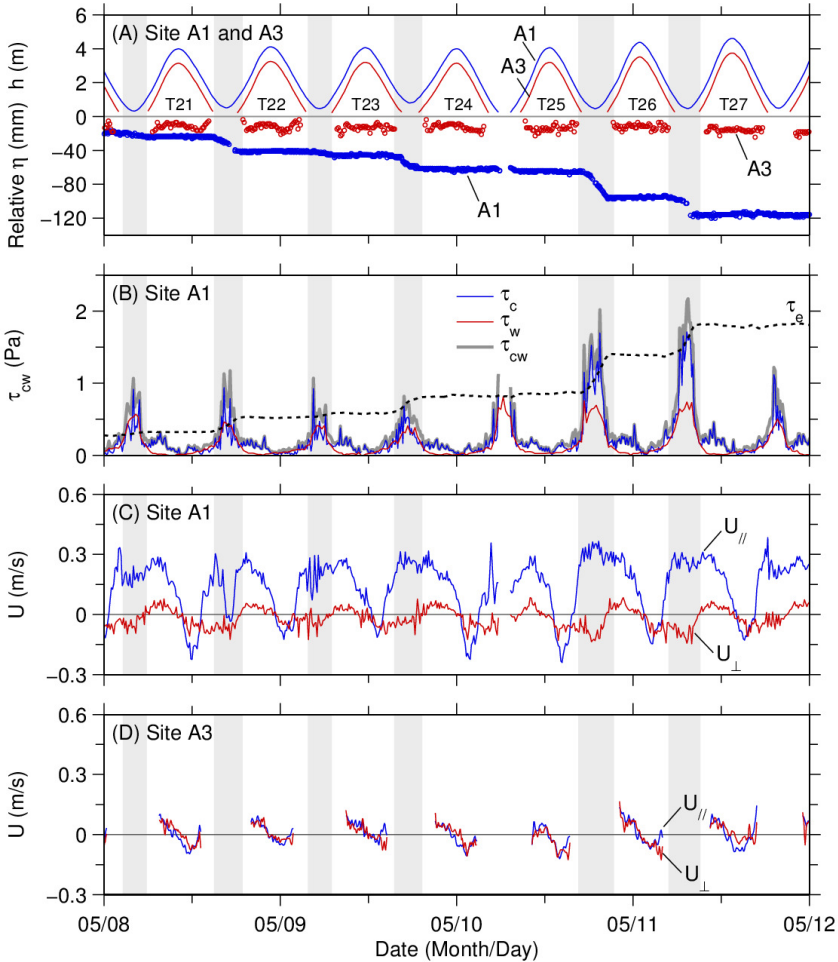


Figure 6.2: Time series of (A) water height (h), and relative bed level (η); (B) bed shear stress due to currents (τ_c), waves (τ_w), combined currents and waves (τ_{cw}), critical shear stress for erosion (τ_e); (C) and (D) current velocity ($U_{//}$: longshore component, positive values represent eastward velocities; U_{\perp} : onshore component, positive values represent onshore velocities).

During neap storm tides, the velocity values remained high at site A1 during low waters, which led to a high tidal averaged velocity (Figure 6.2C) but no obvious spring-neap cyclicality in the flow velocity magnitudes (Figure 6.1E).

The significant wave heights were significantly larger during the storm period (0.13 m on average) than under normal weather (0.04 m on average) (Figure 6.1). The maximum wave height was 0.43 m around May 10. According to the linear wave breaker index (Battjes and Stive, 1985), the waves at the three sites were non-breaking over the majority of the measurement period. The waves at site A1 were on the verge of breaking ($H_s/h > 0.6$) for low waters during the storm period (Figure 6.3).

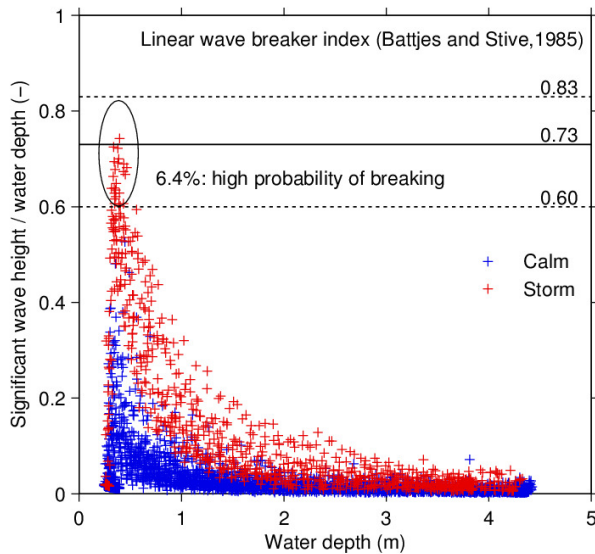


Figure 6.3: Breaking-wave check at Site A1.

6.1.2 Bed shear stresses

The average total bed shear stresses throughout the measurements increased offshore (Table 6.1). In calm weather, the total bed shear stress was 0.09 Pa and 0.08 Pa at A2 and A3, respectively. This value was less than the critical shear stress for surface sediment erosion, which was over 0.1 Pa. This phenomenon caused little disturbance in the sediment bed, so the bed levels at these two higher sites were relatively stable (Figure 3H). The average total bed shear stress at A1 was 0.15 Pa before the storm and 0.12 Pa after the storm.

Table 6.1: Statistics of the bed shear stresses.

Site	τ_c (Pa)	τ_w (Pa)	τ_{cw} (Pa)
A1	0.12	0.07	0.14
A2	0.07	0.03	0.09
A3	0.05	0.03	0.08

6.1.3 Suspended sediment concentration

The measured near-bed SSC varied from 0.01–8.55 kg/m³, with the average value of 0.52 kg/m³. Average SSC during normal weather was 0.48 kg/m³, and was 0.58 kg/m³ during storm period.

6.2 Bed level changes in response to the storm event

6.2.1 Cross-shore bed level changes

Studies of morphological changes on an open tidal mudflat showed that the distribution of erosion and accretion zones depends on the tidal range, and lower flats often belong to the erosion zone (Fan et al., 2006). Our study shows a similar pattern, in which significant bed erosion occurred during wind events around the lower flat (site A1), while the middle flat (sites A2 and A3) showed much smaller variations in the bed level (Figure 6.1H). Studies demonstrated that erosion zones coincide with wave-breaking zones because breaking waves generate turbulence and extra flows that stir up substantial bed material (Shi and Chen, 1996; Fan et al., 2006; de Vries et al., 2008).

Many high-temporal-resolution bed-level measurements showed that significant bed erosion often occurs under very shallow conditions because the bed level at the start of each inundation often differs significantly from that at the end of the previous inundation (O'Brien et al., 2000; Andersen et al., 2006; Shi et al., 2015). At site A1, the waves had a high probability of breaking over 6.4% of the storm period, mostly in shallow waters, because the ratio of the significant wave height over the water depth exceeded 0.60 and sometimes surpassed the threshold value for wave breaking (0.73; (Battjes and Stive, 1985). Consequently, significant erosion occurred during very shallow stages (Figure 6.2).

In summary, significant bed erosion was favourable at site A1 rather than the upper area for the following reasons: (1) the bed was exposed to large waves caused by wind/storm events; and (2) the water depth was shallow enough so that waves could deeply affect the bottom, even leading to wave breaking. In other words, the sensitivity to erosion was the highest at an elevation just below the low water level. However, this process was hardly detected in the field measurements. Under most conditions, acoustic instruments face downward to obtain the bed position by using ultrasonic echo-ranging

in an aqua environment (Jestin et al., 1998; O'Brien et al., 2000; Saulter et al., 2003; Andersen et al., 2006; Zhu et al., 2014). Thus, these devices cannot measure when the water surface drops below the echo transmitter (i.e., water depth < 0.3–0.45 m). Furthermore, numerical models sometimes miss erosion processes under very shallow conditions because of the existence of a threshold depth below which the model regards the bed as dry and stops simulating. This threshold depends on the tidal range and simulation time step and is often set to be centimetres to tens of centimetres (Deltares, 2010).

6.2.2 Effect of flow pattern to sediment transport during storm

Bed erosion has been considered to be increased by wave-induced bed shear stress, which is enhanced by storms (Janssen-Stelder, 2000; Yang et al., 2003; Fan et al., 2006; Dalyander et al., 2013). In recent years, the influence of wind-driven currents and turbulence has been emphasized (Banerjee et al., 2015; Su et al., 2015). In our study, τ_w increased significantly during shallow waters at storm-neap tides. τ_w , however, surpassed τ_e by a limited amount and was sometimes even smaller than τ_e . Figure 6.2B shows that τ_{cv} was dominated by the current-induced component of τ_e during significant erosion periods because strong flows occurred during low tides (Figure 6.2C and Figure 6.4B) and/or because storm wind enhanced the turbulence momentum of water surface and transformed the bottom layer (Su et al., 2015).

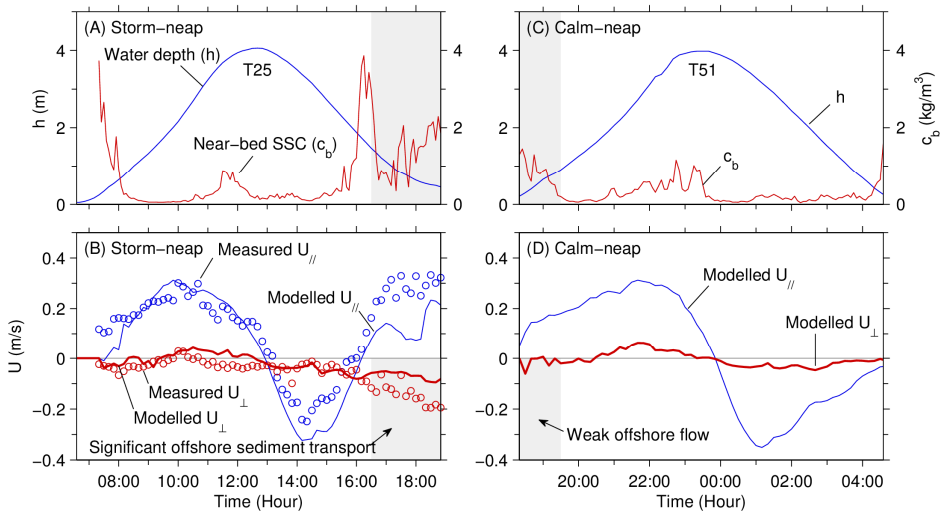


Figure 6.4: Time series of the water depth, near-bed suspended sediment concentration (c_b), and long-shore ($U_{||}$) and cross-shore (U_{\perp}) velocities in a storm-neap tidal cycle (A, B) and a calm-neap tidal cycle (C, D).

The tidal wave was nearly standing in the study area because low flow velocities occurred near high and low water levels. However, the velocity series during storm-neap tides in both the long-shore and cross-shore directions exhibited asymmetry: the ebb flow turned to the east when the ebb peak began, and the velocity magnitude was high; meanwhile, strong offshore flow appeared during low tides (Figure 6.4B). Comparing the numerical model's simulated velocities in the two neap-tide periods with and without the effect of storms, we found that this velocity asymmetry was caused by wind rather than the spring-neap cycle because this pattern was absent in the simulated velocities of the calm-neap tides (Figure 6.4D).

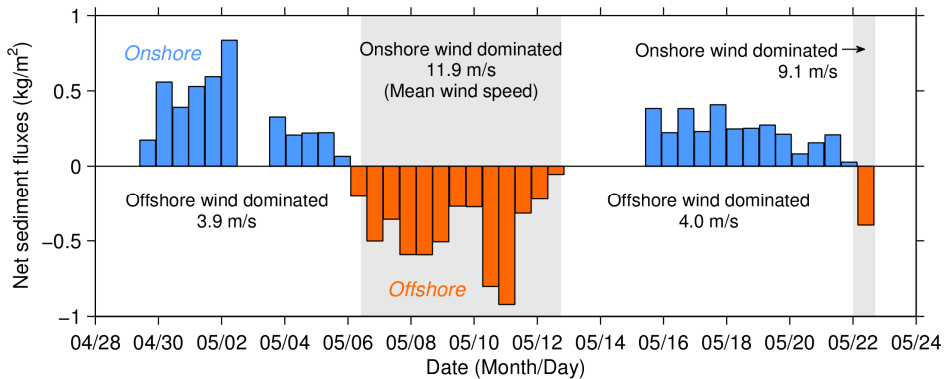


Figure 6.5: Net sediment transport fluxes per unit width at 15 cm above the (original) bed. Net offshore sediment transport occurred when strong onshore winds occurred, while net onshore sediment transport occurred in calm weather under spring tides.

The higher flows in shallow waters played an important role in sediment transport. In calm weather, SSC peaks appeared during the flood peak stage, so the net cross-shore sediment fluxes were onshore in calm tidal cycles (Figure 6.5). In stormy weather, the SSC peaks during low tides were much larger than those during floods (Figure 6.4A). Increased flows enhanced the bed shear stress, which eroded substantial amounts of sediment, and carried away this eroded sediment, leading to net offshore sediment transport (Figure 6.5). This net sediment transport model matches the results of open mudflats (Yang et al., 2003; Fan et al., 2006), which agrees with the theory that sediment moves from high-energy areas to low-energy areas along the energy gradient (Yang et al., 2003; Friedrichs, 2011).

6.3 Spatial variation in the erodibility of mudflats

6.3.1 Critical shear stress results

6.3.1.1 Vertical distribution of τ_e

The bed level variation at site A1 showed a stepwise time series: (i) increases were located in very shallow water, which occupied approximately 20% of the tidal cycle; and (ii) flatter portions were located in the other 80%, when the water depth was relatively high (Figure 6.1A).

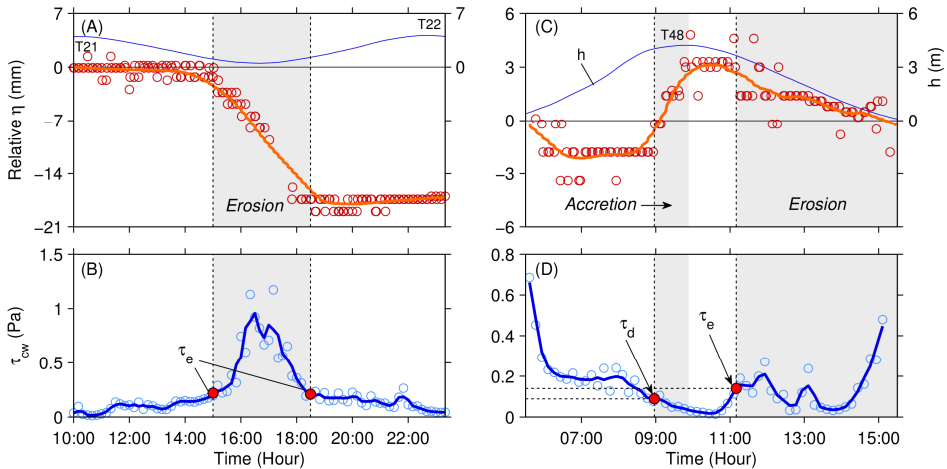


Figure 6.6: Examples of determining the critical shear stress for erosion (τ_e) and deposition (τ_d) from the ADV-measured bed level variabilities and total bed shear stress (τ_{cw}) under storm conditions (A, B) and calm conditions (C, D). Each solid line is the trend line of the scatters.

Time series of the bed level and total bed shear stress from a storm period on May 8 (T21 and T22) are illustrated in Figure 6.6A and B. The deposition rate at each shallow water stage, when the bed began to degrade, was zero, and the τ_{cw} became larger than the critical shear stress for the sediment at this depth. Afterward, the bed stopped degrading and returned to an equilibrium state when the τ_{cw} decreased to a certain threshold. These two thresholds can approximately represent the τ_e of the sediment at the bed levels when the system began to change its state from equilibrium to erosion and from erosion to equilibrium.

The τ_e for the original surface sediment, $z_b=0$ in Figure 6.7A, was determined by Taki's equation (Taki, 2001), as mentioned in section 3.5. The τ_e values decreased from 0.11 Pa at the sediment surface to 0.75 Pa at a depth of 0.11 m (Figure 6.7A). A linear

regression showed that τ_e and z_b had a linear relationship with a correlation coefficient of 0.86. However, τ_e is expected to become constant in the substrate layer rather than increase towards infinite depth. Thereby, we use a logarithmic function, whose gradient decreases with depth, to fit the scatters with the correlation coefficient of 0.70. For the topmost 1.5 cm, we suggest using S-distribution of τ_e (Figure 6.7C) which was proposed by Winterwerp et al. (2012).

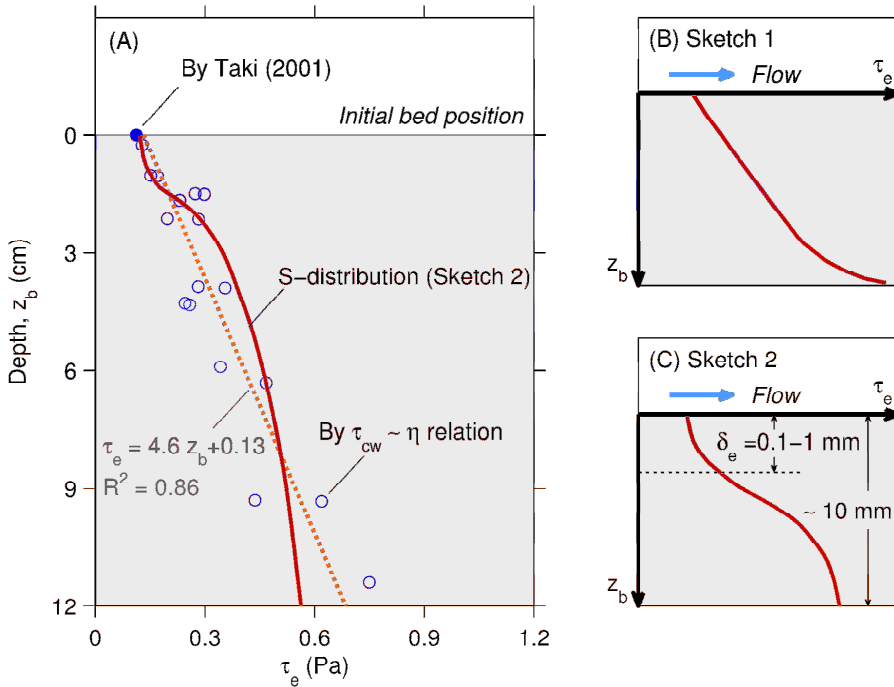


Figure 6.7: (A) Vertical distribution of τ_e , which linearly increases along the depth z_b of this study. The schematic diagrams of τ_e 's vertical distribution are redrawn after (B) Whitehouse et al. (2000; Sketch 1) and (C) Winterwerp et al. (2012; Sketch 2). The δ_e in Sketch 2 is the erodible depth within which the sediment is easily eroded by surface erosion.

6.3.1.2 τ_e and τ_d of freshly deposited sediment

The surface sediment was often freshly deposited mud. The water content of the surface sediment increased from the highest site, A3, to the lowest site, A1, leading to an offshore decrease in τ_e (Table 6.2) because mud beds at higher locations can undergo dewatering via evaporation and consolidation over longer periods.

After the storm, the bed at site A1 tended to recover, i.e., the bed level increased. This recovery of the bed did not occur throughout tidal inundation but only when the total bed shear stress dropped below a certain threshold, which is called the 'deposition

threshold, τ_d' . Sediment deposition occurred during high waters, which caused bed accretion (Figure 6.6C). Six tides showed a clear turning point when the bed level began to increase. The deposition threshold was 0.08 ± 0.01 Pa.

Table 6.2: Critical shear stress for the erosion (τ_e) of surface sediment along the cross-shore profile.

Site location	Elevation (m NAP)	d_{50} (μm)	W (%)	Mud content (%)	τ_e (Pa)
A1	-1.25	20.2	148	83	0.11
A2	-0.98	20.4	130	84	0.12
A3	-0.25	30.6	106	76	0.13

Significant bed erosion events rarely occurred during the recovery stage. Bed erosion of 3 mm only occurred during the ebb stage in the tidal cycle on May 22, when wind turned onshore with a speed of 8.4 m/s (Figure 6.1A and Figure 6.6C). The erosion threshold τ_e was 0.13 Pa. The erosion threshold under this condition represents freshly deposited sediment. This value was close to the calculated τ_e for the sampled surface sediment, which was 0.11 Pa.

The bed level changes at sites A2 and A3 were stable during tidal inundations, so determining the erosion and deposition thresholds of the sediment at these sites is difficult. This condition is identical to the condition at site A1 before the calm conditions.

6.3.2 Abiotic and biotic effect on τ_e of surface sediment

To date, determining the τ_e of surface mud, which is freshly deposited and has high water content, is based on empirical formulae that use the water content (Taki, 2001), bulk density (Mehta, 1988; Mitchener and Torfs, 1996), or dry density (Delo and Ockenden, 1992; Whitehouse, 2000). These three sediment characteristics are transferable. When using Taki's (2001) formula, the τ_e of the surface sediment at site A1 was estimated to be 0.11 Pa. This value matches that obtained by reading the τ_{cw} and η time series for the sediment at $z_b=2.5$ mm in the erosion stage and the freshly deposited mud in the recovery stage.

The aforementioned formulae fail to determine the τ_e of deeper, highly consolidated sediment. For instance, if we take $\tau_e=0.75$ Pa at $z_b=0.11$ m, W is deduced to be 12%. This value is even less than $W=13\%$ for highly compact grains if the porosity is 26% (Graton and Fraser, 1935), which rarely occurs in reality.

In addition, a diatom biofilm present on the mudflat, whose effect was not considered in the present empirical formulae. A diatom biofilm visibly covered the mudflat before the storm. Approximately 70 m from site A2, the average Chlorophyll a biomass of the surface 2-mm sediment layer was 180 mg/m^2 , which was close to the value of the reference sample with a high diatom biomass (208 mg/m^2 ; Figure 6.8). Diatoms

are known as a sediment stabilizer because diatoms produce extracellular polymeric substances (EPS), which can enhance the bed strength by binding bed sediment particles (Austen et al., 1999; Paterson et al., 2000; Herman et al., 2001). Andersen et al. (2010) found that τ_e increased linearly with EPS content. The Chlorophyll *a* concentration is a good proxy for diatom biomass on bare mudflats (Riethmüller et al., 2000; Kazemipour et al., 2012). Riethmüller et al. (2000) found a high correlation coefficient between the τ_e and Chlorophyll *a* concentration ($< 100 \text{ mg/m}^2$). In our study, the mean τ_{cw} and mean value of the topmost 10% τ_{cw} during the pre-storm stage were 0.15 Pa and 0.44 Pa, respectively. These values were higher than the abiotic τ_e value, which was 0.11 Pa. Bed erosion was expected to occur, but the bed level measurements showed no significant decrease (Figure 6.1H), which suggests that τ_e increased to at least 0.44 Pa with the existence of a diatom biofilm. On a mudflat in the East Frisian Wadden Sea, τ_e could reach 1.2 Pa when the Chlorophyll *a* concentration was 45 mg/m^2 (Andersen et al., 2010).

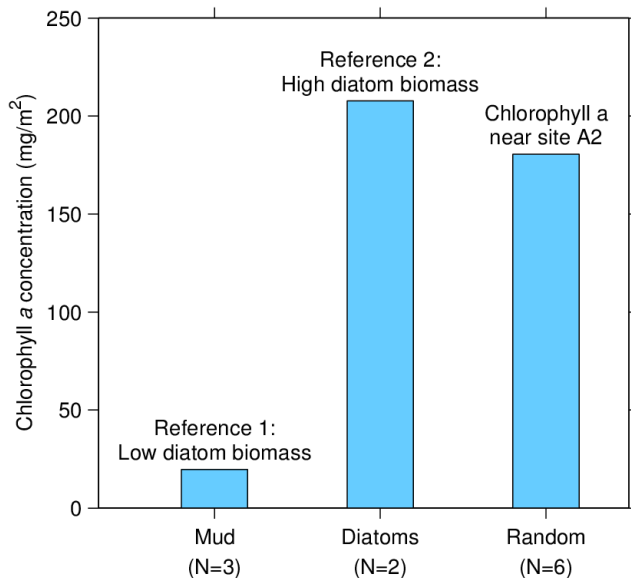


Figure 6.8: Chlorophyll *a* concentration near Site A2 at Kapellebank mudflat.

During the storm, some of the diatom biofilm may have been eroded as a result of high hydrodynamic forces. After the storm, increasing sunshine duration likely promoted the growth of diatoms, which prevented the bed erosion and may have promoted the bed-level recovery process. In addition to responding to storm events, diatoms show seasonal cyclicity on mudflats (Weerman et al., 2012). We suggest that the diatom distribution should be included in models to improve the understanding of seasonal variability in

sedimentation, whose magnitude is sufficient to affect the mud balance of estuaries (Herman et al., 2001).

6.3.3 Vertical distribution of erosion threshold

The determination of τ_e for sediment beds is a long-standing research topic in studies of morphodynamics because estimating the τ_e is fundamental to discussing sediment dynamics, especially the erosion rate. One erosion type identified by Mehta and Partheniades (1982) was Type I erosion, which describes a stratified bed that stops eroding when the bed shear stress equals the critical shear stress. The vertical distribution of τ_e explains this depth-limited erosion (also called ‘supply-limited erosion’). We can easily understand that τ_e increases with depth beneath the sediment surface because deeper sediment layers are better consolidated, i.e., larger bulk density (Townsend and McVay, 1990; Gomez and Amos, 2005; Zhou et al., 2016). However, how τ_e increases with depth has been less frequently reported compared to τ_e estimations for surface sediment.

In situ measurements enable us to learn the τ_e distribution of an undisturbed sediment bed. In the flume experiment by Mehta and Partheniades (1982), a deposited bed from suspension under a small shear stress was similar to a natural sediment bed. The variation in the τ_e with z_b showed a tilt-S distribution (Figure 6.7C) within 1–2 cm. After consolidating for 144 hours, τ_e reached 0.6 Pa at 1.4 cm below the sediment surface. This tilt-S distribution and length scale was later schematized by Mehta and Partheniades (1982) and Winterwerp et al. (2012). Another schematized τ_e distribution showed a linear decrease with z_b and a faster increase in deeper layers (Delo and Ockenden, 1992) (Figure 6.7B). The sediment beds in the above study were similar to but still differed from natural undisturbed sediment beds. Instead, an *in situ* benthic annular flume has been used to study resuspension characteristics (Amos et al., 1992; Thompson et al., 2011). These authors generated hydrodynamics forces within the flume, while we took advantage of natural tide and wave forces. In addition, the aforementioned studies were restricted to the τ_e distribution in the topmost 1–2 cm, while we extended this range to 12 cm.

6.3.4 Summary of spatial variation in erodibility of sheltered mudflat

The erosion potential, i.e., bed stability, of mudflats is essential to predict morphological changes and the sediment budget. In this paper, the cross-shore and vertical distribution of an undisturbed semi-enclosed mudflat was determined by using *in situ* measurements. The bed stability decreased along the offshore direction as τ_e decreased, and the hydrodynamic force increased from higher to lower tidal flats (Figure 6.9). Wave-breaking and abnormal flow structures have a high probability to occur at the interface between intertidal flats and channels, so bed stability is significantly weakened

in this area.

We presented the first empirical evidence of the vertical distributions of τ_e in an undisturbed cohesive sediment bed. The empirical formulae of τ_e by water content failed when the sediment bed was highly consolidated, similar to deeper beds. Without diatoms, τ_e decreased linearly towards deeper beds, while M showed no obvious trends.

Diatoms with seasonal distributions are common on mudflats. Diatoms notably increase the critical bed shear stress for the erosion of surface sediment on intertidal flats. These creatures change the cross-shore distribution of bed stability by enhancing the τ_e of the surface sediment and increase the τ_e of the topmost 1–2 mm in the vertical distribution.

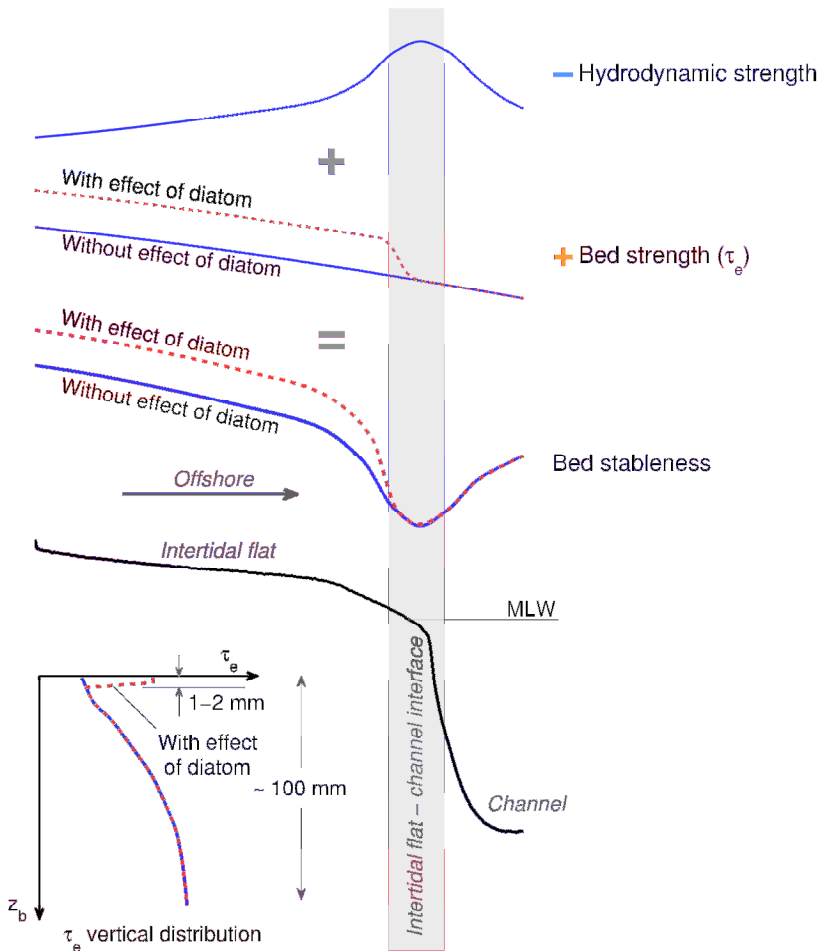


Figure 6.9: Schematic diagram of the bed stability distribution of a tidal mudflat in both the cross-shore and vertical dimensions.

7 BLC model

Based on the findings in above chapters, a bed-level change (BLC) model is constructed, incorporating *in situ* measured parameters of hydrodynamics (waves and currents), suspended sediment concentrations, and bed sediment properties. Bed-level changes in high resolution in Chapters 4 and 6 were reconstructed using this model. We present the first empirical evidence in obtaining vertical distributions of erosion coefficient (M) of the undisturbed cohesive sediment bed. Variation of τ_e and M in response to wind event was calibrated using the integrated approach of measurements and numerical modelling. Debating on existence of τ_d is investigated by this integrated approach. Finally, section 7.5 demonstrates limitations of the BLC model.

This chapter is based on the following manuscripts:

- Zhu, Q., van Prooijen, B.C., Maan, D.C., Wang, Z.B., Daggars, T., Yang, S.L., 2017. Cross-shore and vertical variability of mudflat erodibility: An integrated approach of *in situ* measurements and modelling. (Submitted)
- Zhu, Q., van Prooijen, B.C., Wang, Z.B., Yang, S.L., 2017. Bed-level changes on intertidal wetland in response to waves and tides: A case study from the Yangtze River Delta. *Marine Geology*, 385: 160-172.

7.1 Model description

In this chapter, a BLC (bed level change) model is established to reproduce the bed level changes in the studies mentioned in the previous chapters. The model uses the hydrodynamic variables and sedimentary parameters obtained in the *in situ* measurements (Figure 7.1). By comparing the measured and simulated bed level changes, this model is used to: (1) quantify and study the impact of wind event on variations of bed properties (τ_e and M ; section 7.2); (2) learn the vertical distribution of M (section 7.3); (3) improve the understanding of deposition process by discussing the rationality of critical shear stress for deposition, τ_d (section 7.4).

For easier reading without referring back to the previous chapters, we describe the model in a systematic presentation in this section, even if some of the formulations have already been mentioned above. The model is setup based on the classic Partheniades-Krone erosion-deposition model. Changes in bed level are defined by the rates of erosion, E , and deposition, D ($\text{kg}/\text{m}^2/\text{s}$):

$$\frac{\Delta\eta}{\Delta t} = \frac{1}{\rho_{dry}} (D - E) \quad (7.1)$$

where ρ_{dry} is the dry density of the bed sediment in kg/m^3 . The variables used in the model are defined in Table 7.1.

Table 7.1: Selected notations in the single-point bed level change (BLC) model.

Notation	Variable name	Illustration
η	Bed level	Simulated / Measured
ρ_{dry}	Dry density	$f(W)$
W	Water content	Measured from sediment cores
E	Erosion rate	Simulated, $f(\tau_{cw}, \tau_e, M)$
τ_{cw}	Total bed shear stress under combined wave–current action	Simulated using <i>in situ</i> measured hydrodynamic parameters
τ_e	Critical bed shear stress for erosion	$f(W)$
M	Erosion coefficient	Calibrated from the model
D	Deposition rate	Simulated, $f(\omega_s, c_b, \tau_d)$
ω_s	Settling velocity	Simulated, $f(c_b)$
c_b	Near-bed suspended sediment concentration	In situ measured
τ_d	Critical bed shear stress for deposition	$= 0.5 \tau_e$

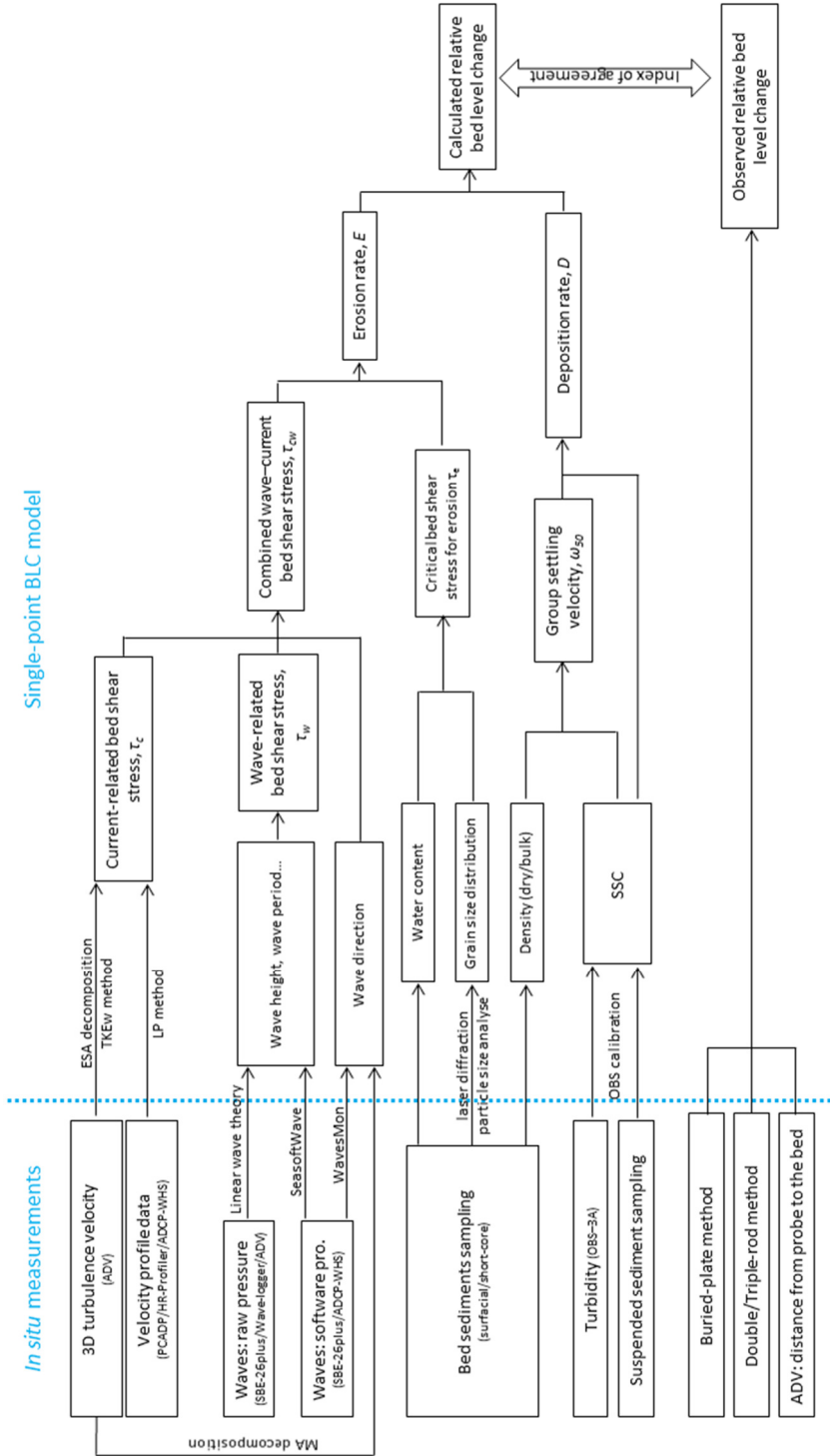


Figure 7.1: Overview of the BLC model setup, and the approaches from which the variables in the model are obtained.

7.1.1 Erosion rate

Based on the stochastic nature of bed shear stress, van Prooijen and Winterwerp (2010) proposed an erosion-rate formula in which the third-order polynomial fit is expressed as in Equation (7.2). Although this formula is derived for flow only, we extended its application to combined wave–current conditions, which is similar to the treatment of the Ariathurai-Partheniades equation (Partheniades, 1965; Ariathurai, 1974):

$$E = M \tau_e \begin{cases} 0 & , \frac{\tau_{cw}}{\tau_e} \in [0, 0.52) \\ a_1 \left(\frac{\tau_{cw}}{\tau_e} \right)^3 + a_2 \left(\frac{\tau_{cw}}{\tau_e} \right)^2 + a_3 \left(\frac{\tau_{cw}}{\tau_e} \right) + a_4 & , \frac{\tau_{cw}}{\tau_e} \in [0.52, 1.7] \\ \left(\frac{\tau_{cw}}{\tau_e} - 1 \right) & , \frac{\tau_{cw}}{\tau_e} \in (1.7, +\infty) \end{cases} \quad (7.2)$$

in which the constants $a_1 = -0.144$, $a_2 = 0.904$, $a_3 = -0.823$, and $a_4 = 0.204$; M (s/m) is the erosion rate coefficient, and τ_{cw} (Pa) is the total bed shear stress due to the combined effects of wave and current action. For easier reading without referring back to the previous chapter, we summarize the formulation mentioned above and present them in a systematic presentation.

Total bed shear stress due to combined wave and current action, τ_{cw} (Pa), was calculated using the Grant and Madsen (1979):

$$\tau_{cw} = \sqrt{(\tau_w + \tau_c |\cos \varphi_{cw}|)^2 + (\tau_c |\sin \varphi_{cw}|)^2} \quad (7.3)$$

Wave-induced bed shear stress

Wave-induced bed shear stress, τ_w , was obtained by analysing surface-elevation monitoring data either by SBE-26plus/ADV/wave-logger. Wave parameters (significant wave height H_s and significant wave period T_s) were derived from monitored high-frequency pressure data via linear wave theory (Tucker and Pitt, 2001). At the edge of the wave boundary layer, the peak orbital excursion (\hat{A}_δ) and peak orbital velocity (\hat{U}_δ) can be expressed as:

$$\hat{A}_\delta = \frac{H}{2 \sinh(kh)} \quad (7.4)$$

$$\hat{U}_\delta = \omega \hat{A}_\delta = \frac{\pi H}{T \sinh(kh)} \quad (7.5)$$

in which H is wave height (m), k ($= 2\pi/L$, $L = (gT^2/2\pi)\tanh(kh)$ is the wave length) is wave number (m^{-1}), h is water depth (m), ω is angular velocity (s^{-1}), and T is wave period (s). In practice, the significant wave height H_s and significant wave period T_s are

used for H and T in the formulae.

The time-averaged (over half a wave cycle) bed shear stress due to waves, τ_w (Pa), can be expressed as:

$$\tau_w = \frac{1}{4} \rho_w f_w \hat{U}_\delta^2 \quad (7.6)$$

where ρ_w is the water density (kg/m^3) and f_w is the friction coefficient (-), which is determined by the hydraulic regime:

$$f_w = \begin{cases} 2 \text{Re}_w^{-0.5} & , \text{Re}_w \leq 10^5 \text{ (laminar)} \\ 0.0521 \text{Re}_w^{-0.187} & , \text{Re}_w > 10^5 \text{ (smooth turbulent)} \\ 0.237 r^{-0.52} & , \text{(rough turbulent)} \end{cases} \quad (7.7)$$

in which $\text{Re}_w = \frac{\hat{U}_\delta \hat{A}_\delta}{\nu}$ and $r = \frac{\hat{A}_\delta}{k_s}$ are the wave Reynolds number (-) and relative roughness (-), respectively. Parameter k_s is the Nikuradse roughness value given as $k_s = 2.5d_{50}$, where d_{50} is the median grain size of the bed sediment, and ν is the kinematic viscosity of sea water (m^2s^{-1}).

Current-induced bed shear stress

Variability in turbulent velocity fluctuation in the vertical dimension $\overline{w_t^2}$ is used to infer bed shear stress via the following equation (in SI units):

$$\tau_c = C \rho_w \overline{w_t^2} \quad (7.8)$$

in which ρ_w is the sea water density and the constant C is 0.19, after (Stapleton and Huntley, 1995). As high-resolution measurements of near-bed velocity might be affected by surface wave motion, we used wave–turbulence decomposition. Specifically, we used the energy spectrum analysis (ESA) approach, which is a technique developed by (Soulsby and Humphery (1990) to split the variance without separating the instantaneous time series.

Wave and current direction

Current direction φ_c is determined from the arctangent of burst-mean velocities in easterly and northerly orientations, whereas wave direction φ_w is probably determined from the arctangent of wave orbital velocities. The wave orbital velocity is decomposed from wave–turbulent velocities using MA filtration.

Critical shear stress for erosion

The variable τ_e (Pa) is the critical bed shear stress for erosion calculated as (Taki, 2001):

$$\tau_e = 0.05 + \beta \left\{ \left[\frac{\pi}{6} (1 + sW) \right]^{\frac{1}{3}} - 1 \right\}^{-2} \quad (7.9)$$

where W is the measured water content and $s = \rho_s / \rho_w - 1$ is the submerged specific weight of bed sediment, in which ρ_s and ρ_w are the measured densities of sediments and, respectively. The coefficient β ranges from 0.1 to 2.0, and in the present study we used $\beta = 1.0$.

7.1.2 Deposition rate

The deposition rate, D , in Equation (7.1) is derived from the sediment flux at the bed according to the following two deposition modes:

$$D = c_b \omega_s \quad (7.10)$$

or

$$D = \begin{cases} 0 & , \tau_{cw} > \tau_d \\ c_b \omega_s & , \tau_{cw} \leq \tau_d \end{cases} \quad (7.11)$$

where c_b (kg/m^3) is the near-bed SSC measured by the OBS-3A, ω_s (m/s) is the settling velocity of suspended sediment, and τ_d (Pa) is the critical bed shear stress for deposition.

The group settling velocity of cohesive sediment, ω_s (m/s), is strongly dependent on the SSC and can be estimated as:

$$\omega_s = E_1 c_b^{E_2} \quad (7.12)$$

in which E_1 and E_2 are constants that vary among estuaries (Whitehouse et al., 2000). In Southeastern Chongming mudflat case, E_1 and E_2 were set to 0.002 and 1.5, respectively, for Equation (7.12).

Increased sediment concentration over a certain limit results in decreased settling velocity, which is described as hindered settling. This process must be accounted for when estimating deposition fluxes in shallow water, as layers of high sediment concentration are common in estuaries and bays, as well as on continental shelves and intertidal flats (Kineke et al., 1996; Traykovski et al., 2000; McAnally et al., 2007; Zhu et al., 2014). To determine ω_s while also considering hindered settling, we followed the formula of Whitehouse et al. (2000). The effective diameter, d_e , of a floc increases with the volume concentration $C = c_b / \rho_s$ via the following relationship:

$$d_e = l C^{\frac{E_2}{2}} \quad (7.13)$$

where the length-scale l is given by:

$$l = \left[\frac{19.8 \rho_w \nu \rho_s^{E_2} E_1}{g(\rho_e - \rho_w)} \right]^{0.5} \quad (7.14)$$

in which constants E_1 and E_2 are the same as in Equation (7.12), ν is the kinematic viscosity of water, g is gravitational acceleration, ρ_w and ρ_s are the densities of water and sediment, respectively, and $\rho_e = \rho_w + 0.03(\rho_s - \rho_w)$ is the effective density of the floc. The volume concentration of flocs is given as:

$$C_f = \frac{(\rho_s - \rho_w) C}{\rho_e - \rho_w} \quad (7.15)$$

Therefore, settling velocity ω_s can be expressed as:

$$\omega_s = \frac{d_e}{\nu} \left\{ \left[10.36^2 + 1.049 (1 - C_f)^{4.7} D_s^3 \right]^{0.5} - 10.36 \right\} \quad (7.16)$$

where D_s is the dimensionless floc diameter given by:

$$D_s = d_e \left[\frac{g(\rho_e - \rho_w)}{\rho_w \nu^2} \right]^{\frac{1}{3}} \quad (7.17)$$

7.2 Application 1: Determining of erosional parameters in wind event

This section is based on the results and simulations of Southeastern Chongming mudflat. In this study, effort is made on the simulations shown in Table 7.2.

Table 7.2: Simulation codes with different conditions of Southeastern Chongming case.

Run ID	Erosion				Deposition		Recovery stage (RS) modification				
	M (s/m)	W (%)	τ_e (Pa)	ρ_{dry} (kg/m ³)	Model	τ_d (Pa)	M (s/m)	W (%)	τ_e (Pa)	ρ_{dry} (kg/m ³)	τ_d (Pa)
1	0.0019	32	0.29	1414	Eq. (4)	/			off		
2	0.0014	32	0.29	1414	Eq. (5)	0.15			off		
3	0.0014	32	0.29	1414	Eq. (5)	0.15	0.00056	98	0.14	736	0.07
4	0.0014× (1±50%)	32	0.29	1414	Eq. (5)	0.15	0.00056× (1±50%)	98	0.14	736	0.07

7.2.1 M of surface sediment

Bed level can be calculated using the BLC model by incorporating velocity, wave, and sediment concentration measurements. Using the constant M and τ_e , we simulated bed-level changes during the first erosion stage (Table 7.1B, Runs 1 and 2). From tidal cycle 14 onwards, the accretion in Run 1 was considerably faster than the measured accretion. By the end of the simulation period, the relative bed level increases by as much

as 40 cm, which is far greater than the observed values. For Run 2, we applied a deposition threshold of $\tau_d = 0.14$ Pa, with the result that the excessive accretion no longer occurred. We also note that the simulated bed-level series for each tidal cycle are smoother than those measured by the ADV, indicating that ADV-derived intratidal bed levels exhibited greater variability than the simulated bed levels.

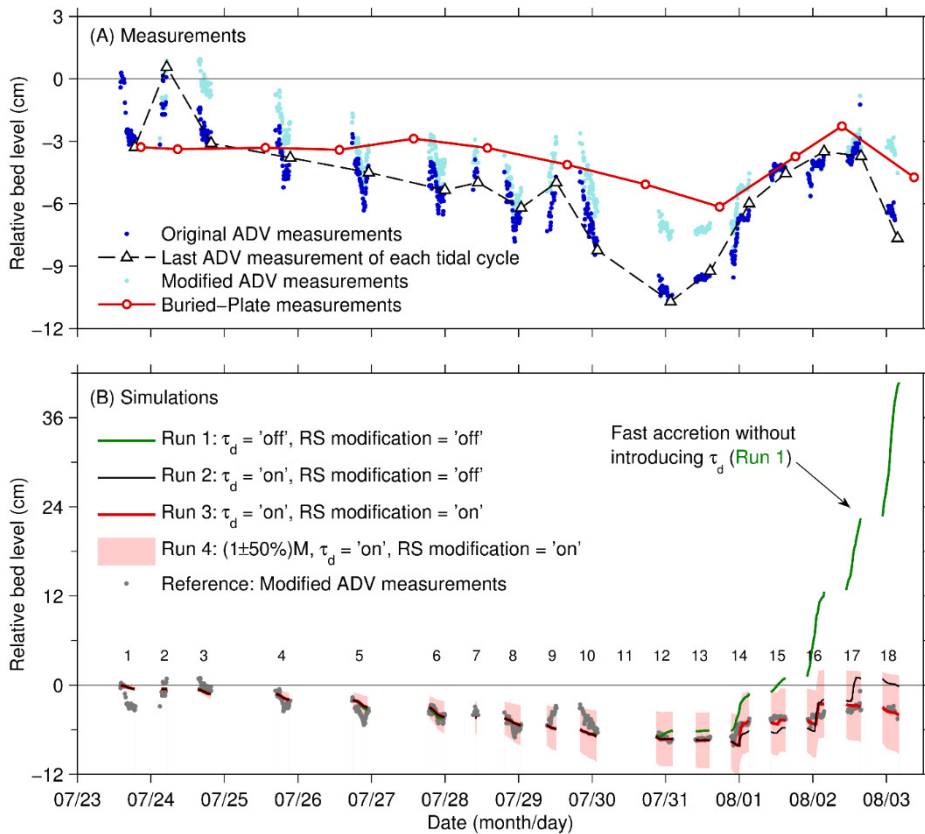


Figure 7.2: Time series of (A) measured and (B) simulated bed level changes. To compare with simulated bed level later, ADV measurements are modified with removal the bed level difference between each two measured tidal cycles. ‘RS modification’ in (B) indicates if erosion parameter M and W are modified in the recovery stage.

In a recent study of hurricane-induced sediment transport on the Louisiana shelf, Xu et al. (2015) concluded that near-bed sediment fluxes are sensitive to model parameters. The erosion coefficient M , one of the key parameters in the erosion model Equation (7.2), is typically obtained by extensive laboratory testing (Whitehouse et al., 2000). In this study, we propose an approach to calibrating M that uses *in situ* measurements. Specifically, we introduced the index of agreement I (Willmott et al., 1985; Equation

(3.21)) to compare bed-level series simulated using different M to ADV measurements.

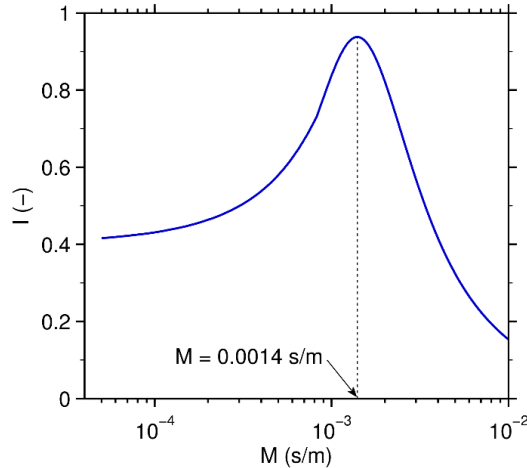


Figure 7.3: Diagram showing erosion coefficient M in Equation (2) determining the accordance, indicated by index of agreement I , of simulated bed level with ADV measurements. $M=0.0014$ s/m provides the best estimation in the first erosion stage (see Figure 4.8).

Our analysis of the mini-core samples revealed that the sediment water content, W , was stable in the upper 10 cm but decreased slightly from 32% to 30% with depth down core. This pattern indicates that the erosion coefficients M and τ_e might be considered constants during first erosion stage (see Figure 4.8). Based on this assumption, we calculated M as 0.0014 s/m (Figure 7.3).

7.2.2 Variation of τ_e and M in response to wind event

A systematic means for calculating M , presented by Winterwerp and van Kesteren (2004), requires several key soil mechanical parameters. In the present study, however, data pertaining to the recovery stage W and sediment water content were unavailable. Consequently, we conducted a model-based test to evaluate the degree to which M and W (τ_e and ρ_{dry}) vary during the recovery stage. Our most recent sediment sample from the bed surface indicates that the bed-sediment component during the final cycle was similar to that of the first erosion stage (Figure 4.10B). Measurements of water content exhibit a similar pattern. Therefore, we consider that the bed sediment properties during the last tidal cycle were similar to those of the first erosional stage, with the result that M and W modifications need to be applied only to tidal cycles 13–17 (Figure 4.8).

Figure 7.4A shows that to obtain bed levels that are in close agreement with our measurements, M decreases from 0.0014 s/m to 0.00056 s/m during the erosion stage,

while W increases from 32% to 98%. The increase in W is responsible for the decrease in τ_e , as a high water content results in a looser particle structure and more erodible sediment. During the recovery stage, τ_e becomes 0.14 Pa, which is consistent with the findings of Whitehouse et al. (2000) that τ_e for recently deposited mud is only 0.1–0.2 Pa. Sediment mass fluxes are also lower (Figure 7.4B), leading to improved simulations of bed level (Table 7.1B, Run 2 vs. Run 3).

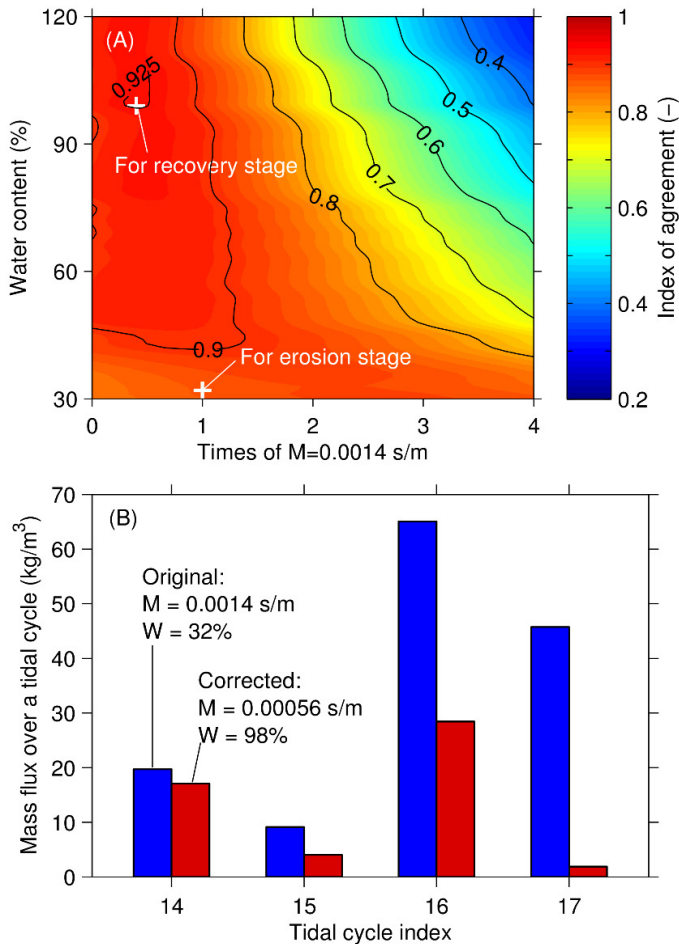


Figure 7.4: (A) Calibration of erosional parameters M and W for recovery stage. It provides best bed level simulation when M decreases by 60% and W turns from 32% to 98%; (B) Mass fluxes over tidal cycles in recovery stage. Net accreted sediment mass is 2.7 times overestimated without M and W being modified.

In practice, we consider M to be constant within a certain period when bed

properties do not change significantly. Typical values for $M \cdot \tau_e$ vary from 10^{-5} to 5×10^{-4} kg/m²/s (Winterwerp and van Kesteren, 2004). In our study, values for $M \cdot \tau_e$ were 4.1×10^{-4} kg/m²/s and 7.8×10^{-5} kg/m²/s during the erosion and recovery stages, respectively. We note that although M and W both changed over the course of the experiment, it is plausible that these changes are related. For example, M is determined in part by the dry density and volume concentration of bed sediment, both of which are related to W (Winterwerp and van Kesteren, 2004).

The strength of surface mud layer may also be weakened by liquefaction, which is always along with enhanced wave strength caused by storms/hurricanes (Teisson et al., 1993; van Kessel and Kranenburg, 1998; Jaramillo et al., 2009). Laboratory study showed that liquefaction takes place when wave-induced stress inside the bed is larger than the yield strength of the bed. With the liquefaction process, a fluid mud layer, which is transformed from the surface sediment layer, may occur (van Kessel and Kranenburg, 1998). This further result in high transport rates during wind events. Liquefaction induced increase in water content of bed sediment may decrease the bed erodibility, and directly affect the bed level by changing bulk density. Although the effect of liquefaction was not included in the model, as no evidence (i.e., increase in near-bed SSC; Fig. 4D) was found, it is important to estimate sediment fluxes in mud-rich areas with high wave energy from other studies.

7.3 Application 2: Obtaining a vertical profile of the erosion coefficient (M)

This section is based on the results and simulation of the Kapellebank case. When the τ_{cw} exceeds the τ_e , deposition stops, i.e., $D = 0$ in Equation (7.1). The bed level change rate $\Delta\eta / \Delta t$ becomes

$$\frac{\Delta\eta}{\Delta t} = \frac{1}{\rho_{dry}} \cdot (-E) = -\frac{1}{\rho_{dry}} \cdot M \cdot \delta(\tau_{cw}, \tau_e) \quad (7.18)$$

The M value could be determined by

$$M = -\frac{\Delta\eta}{\Delta t} \cdot \rho_{dry} \cdot \frac{1}{\delta(\tau_{cw}, \tau_e)} \quad (7.19)$$

In Equation (7.19), the bed level change rate $\Delta\eta / \Delta t$ is obtained by ADV measurements, ρ_{dry} is fixed as 800 kg/m³ given a water content of 90%, and the τ_{cw} is calculated through Equation (7.3).

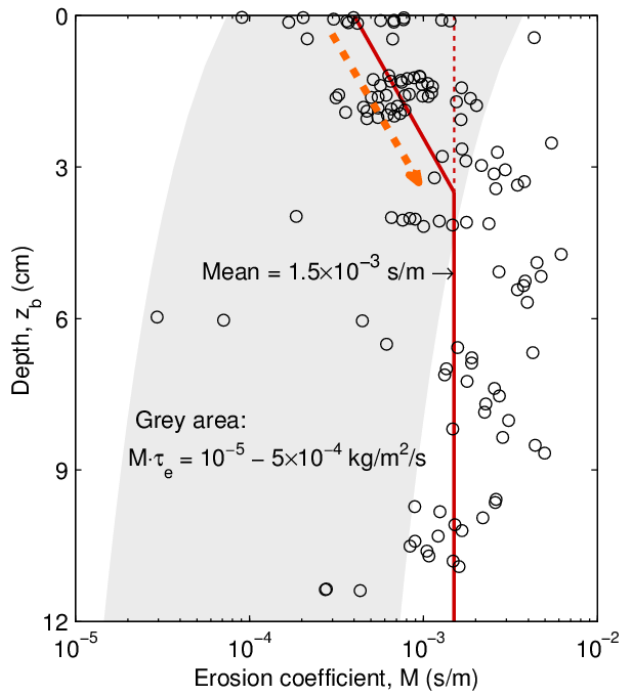


Figure 7.5: Vertical distribution of the erosion coefficient (M) and suggested values provided by Winterwerp and van Kesteren (2012).

The simulation shows that the M value within the topmost 12 cm of the sediment layers varied from 0.03×10^{-3} to 6.2×10^{-3} s/m, with an average value of 1.5×10^{-3} s/m. Except for a decreasing trend in the top 3 cm layer, no significant trend in M with depth z_b was found (Figure 7.5).

The M value of mud beds is often considered to be constant but varies on the scale of orders of magnitude (Table 7.3). M is a parameter that describes bed characteristics and thus varies with the grain size distribution, consolidation and bio-chemical effects (Mehta and Partheniades, 1982; Amos and Mosher, 1985; Amos et al., 1992; Winterwerp et al., 2012). A formulation to determine M was proposed by Winterwerp and van Kesteren (2004). This method requires systematic measurements of soil mechanical parameters, including the consolidation coefficient, initial volume concentration, dry density, median grain size, and sediment's remoulded shear stress. Again, this approach requires laboratory tests. Sediment samples may change their properties through dewatering and consolidation between the time they are collected and the time they are tested.

Table 7.3: Comparison of characteristics and erosion parameters, namely, the critical shear stress (τ_c) and erosion coefficient (M), of the muds in the selected literature and those of the Kapellebank mudflat.

Sample remarks	d_{50} (μm)	ρ_b (kg/m^3)	P_{mud} (%)	τ_c (Pa)	M (10^{-3} s/m)	$M' = M \cdot \tau_c$ (10^{-4} kg/m ² /s)	Reference
Kaolinite in tap water	1	1093–1218	100	–	–	0.13	Mehta & Partheniades (1982)
Kaolinite in salt water	1	1116–1239	100	–	–	0.07	
HR Wallingford – Grangemouth	–	1370	89–90	–	0.5–1.4	–	Whitehouse et al. (2000)
HR Wallingford – Harwich	–	1250	88–95	–	0.7	–	
HR Wallingford – Hongkong	–	–	65–80	–	0.6–1.5	–	
HR Wallingford – Ipswich	–	1320	–	–	0.9–3.0	–	
HR Wallingford – Kelang	–	–	65–80	–	0.2–0.9	–	
HR Wallingford – Kingsnorth	–	1375	64	–	0.7	–	
HR Wallingford – Medway	–	1220	80	–	0.7	–	
HR Wallingford – Mersey Eastham	–	1140	80	–	0.5	–	
HR Wallingford – Poole	–	1500	80–85	–	0.7–1.4	–	
HR Wallingford – Tees Seal Sands	–	1550	75	–	0.2–1.4	–	
HR Wallingford – Tees dredged	–	1430	75	–	0.5–1.8	–	van Prooijen et al. (2010)
Jacobs (2009) test	–	1784	16	0.4	9	36	
Amos et al. (1992) test	–	1500	80	2.35	3.4	80	
Ketelmeer – measured	7.3	1167–1626	–	0.2–2.1	0.0006–4.2	1.9–8.4	Winterwerp et al. (2012)
Ijmuiden – measured	2.5	1127–1610	–	1.0–1.3	0.0009–1.9	12–19	
Kembs – measured	21	1512	–	2.4	1.3	31	
Ketelmeer – computed	7.3	1167–1626	–	0.2–2.1	0.004–0.52	1.0–2.8	
Ijmuiden – computed	2.5	1127–1610	–	1.0–1.3	0.003–0.46	2.9–4.6	
Kembs – computed	21	1512	–	2.4	0.17	4.1	
Kapellebank – Site A1	20	1492	83	0.1–0.8	0.03–6.2	0.1–26	This thesis

This study used *in situ* measurement datasets to deduce the M values of an undisturbed sediment bed. The M values agree with those in the literature in terms of their order of magnitude (Table 7.3). However, comparing the vertical distribution of M values is difficult because previous studies only showed the results within the topmost 1–2 cm. Our study showed an increase in M in the topmost 3 cm, while no significant variation trend in M with z_b in deeper layer. Top centimeters in layered bed model could be considered using an increase distribution, and increase speed of M should be slower than that of τ_e . This is because when τ_{cw} is set as a constant, $E = M \cdot \delta(\tau_{cw}, \tau_e)$ should decrease downward, indicating a supply-limited erosion. M could be kept as a constant in deeper layer in layered bed model.

7.4 Application 3: Debate on critical shear stress for deposition (τ_d)

Several arguments have been raised concerning critical bed-shear stress during deposition, τ_d . Although some have argued that erosion and deposition occur simultaneously (Winterwerp, 2007), other studies of sediment dynamics have incorporated τ_d into their assessments (Krone, 1962; Dyer, 1986; Christie et al., 1999; Lumborg, 2005). As shown in Figure 7.2B, our results support the model of deposition occurring when total bed shear stress is smaller than τ_d . However, it is also likely that sediment particles settle because of gravity. Here, we define the falling motion of sediment as ‘settling’ and the product as ‘deposition’: sediment is always settling under the influence of gravity, whereas deposition is not constant. For example, if bed shear stress is insufficiently low to allow deposition, sediment can remain in suspension in the near-bed water column, resulting in no change in bed level.

Table 7.4: Values of selected parameters in three stages.

	Erosion process			Deposition process	
	M (s/m)	τ_e (Pa)	τ_{cw} (Pa)	c_b (kg/m ³)	ω_s (mm/s)
1st erosion stage	0.00101	0.29	1.07±0.48	0.4±0.2	0.6±0.3
Recovery stage	0.00172	0.16	0.35±0.33	1.3±0.7	2.8±1.7
2nd erosion stage	0.00101	0.29	1.07±0.49	2.4±0.5	5.5±1.2

This scenario, which is incorporated into Equation (7.11), supports the model of bed degradation during the second erosion stage. Table 7.4 shows that the magnitude of erosion parameters (τ_{cw} , τ_e , and M) in the two erosion stages is similar, whereas deposition parameters c_b and ω_s are 6 and 9.2 times larger, respectively, in the second erosion stage

than in the first erosion stage. Were the deposition rate not controlled by τ_d (i.e., constant deposition), bed level would increase considerably and degradation would not occur during the second erosion stage.

7.5 Limitations of the model

7.5.1 Mass erosion of mudflat

The erosion process in Equation (7.2) only refers to surface erosion. In reality, four erosion modes exist for cohesive sediment (Winterwerp and van Kesteren (2004): the entrainment of mud layers, floc erosion, surface erosion, and mass erosion. When the bed's shear stress exceeds a certain threshold (i.e., the remoulded bed strength), local failure occurs within the bed, resulting in the formation of cracks. This type of erosion is often observed as sheet erosion on intertidal flats (Figure 7.6A and Figure 7.7). Although sheet erosion did not occur immediately adjacent to the observation frame, we did observe this phenomenon in the vicinity of the measurement site and throughout the lower intertidal flat. This mass erosion process proved to be crucial to estimates of the total sediment transport inside and outside the tidal flat system because mass erosion typically occurs during wave attacks (Winterwerp and van Kesteren, 2004). On Nanhui Foreland mudflat, disagreement between measured bed-level changes using buried-plate method and ADV echo ranging might be due to sheet erosion. Figure 7.7B shows that fast bed degradation in the speed of 20–36 mm/cycle, which was one order of magnitude larger than the normal net bed-level changes per tidal cycle, occurred September 22 (ADV echo ranging) and September 29 (buried-plate method).

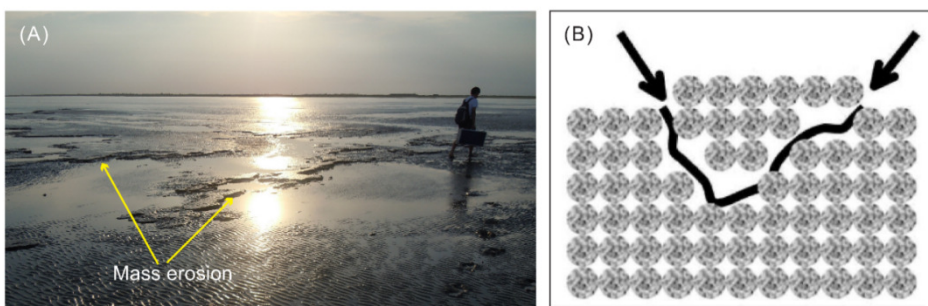


Figure 7.6: (A) Photo that shows mass erosion on a mudflat (taken at 17:30 on July 30th, low flat of the Southeastern Chongming mudflat); (B) schematic figure that shows mass erosion as classified by Winterwerp and van Kesteren (2004, Figure 9.1d).

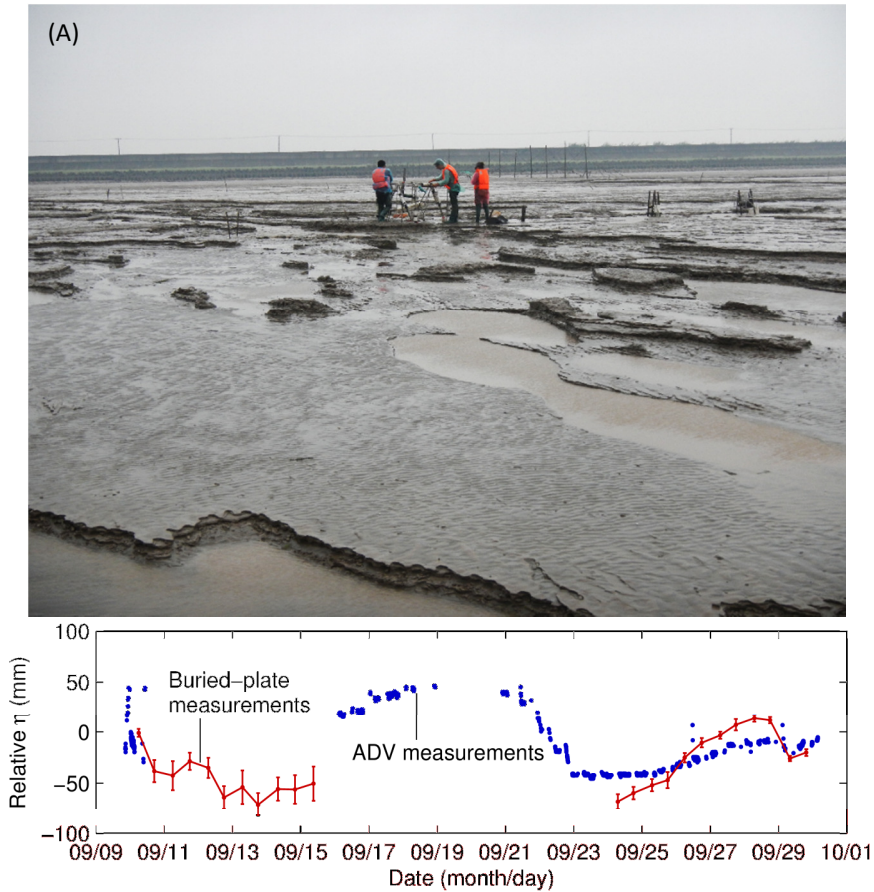


Figure 7.7: (A) Photo that shows mass erosion on a mudflat after the typhoon ‘Fung-wong’ (taken by S. L. Yang at 17:00 on September 23, 2014, in the Nanhui Foreland mudflat). Figure (B) presents measured relative bed-level changes.

7.5.2 Sediment reworking

Sediment reworking has been often reported in tidal flats in different temporal scales (Andersen and Pejrup, 2001; Maire et al., 2008; Webster et al., 2013). By bed-level measurements of more than three years and isotope dating, Andersen and Pejrup (2001) found that reworking of the sediment occurred within 3–8 cm in depth. Sediment reworking in shorter temporal scale may be caused by bedform migration (Webster et al., 2013), which is difficult to reproduce using the BLC model. This is shown by the difference between measured and simulated changes in bed level (Figure 4.10B).

The observed fluctuations in the measured bed level may have been caused partly by measurement errors (Figure 7.8). For example, the ADV records bed-level changes

every five minutes. In most burst intervals, bed-level variations ranged from 0 to 10 mm, with the majority (96%) ranging from 0 to 5 mm. This rate of variability is similar to the accuracy (1 mm) of the ADV sensor used for bed-level measurement. By incorporating a moving average, this noise can be minimised. However, such smoothed bed-level series obtained from the ADV exhibit a periodic signal, which is absent in our simulations, and we hypothesise that this disparity is related to the migration of bed ripples. The magnitude of this fluctuation (10–13 mm) is indicative of the bed ripple height, H_r . Manual measurements show that H_r varied from 3 to 20 mm and L_r varied from 28 to 107 mm (Table 7.5). Our values agree with those of Baas et al. (2013), who reported that H_r values in their flume-based experiments using sand-mud mixture were of the order of millimetres, with ripple lengths L_r measured in centimetres.

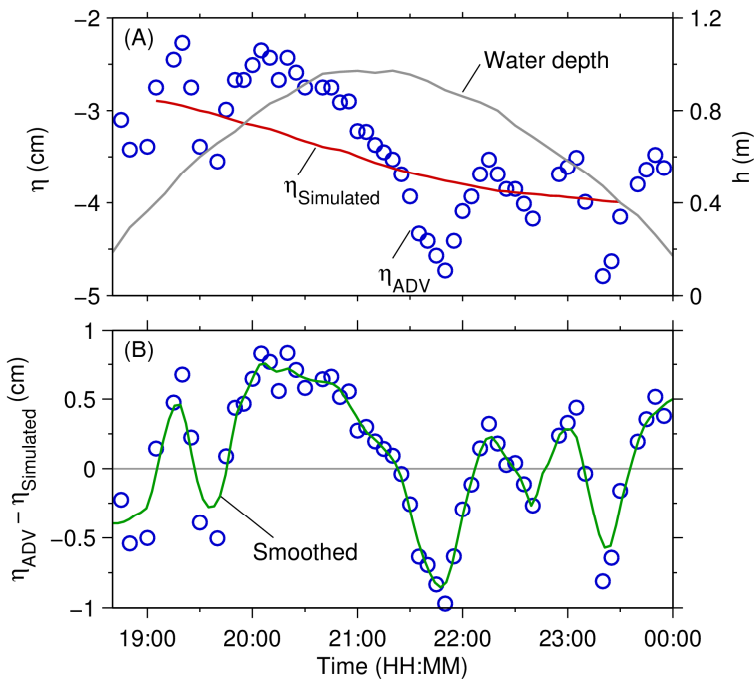


Figure 7.8: An example tidal cycle in 2011/07/27 shows that ADV monitored bed level is composed by a ripple-averaged component and an ripple-induced component. (A) shows ADV monitored (circle) and simulated (red line) relative bed level (η), with corresponding water depth (h). (B) shows time series of $\eta_{\text{ADV}} - \eta_{\text{simulated}}$, indicating ADV recorded bed ripple migration.

The ratio of ripple length to periodicity reflects the ripple migration rate V_r (Table 7.5). Lin and Venditti (2013) derived an empirical relationship between V_r and other physical parameters:

$$\frac{V_r}{\omega_s} = 0.00127 \left(\frac{\theta}{\theta_e} \right)^{0.989} \times BCF \quad (7.20)$$

in which ω_s is the settling velocity of the sediment concentration near the bed, $\theta = \tau_{cw} / [(\rho_s - \rho_w)gD_{50}]$ and $\theta_e = \tau_e / [(\rho_s - \rho_w)gD_{50}]$ are the Shields number and critical Shields number, respectively, for sediment entrainment, and BCF is a bias correction factor dependent on the ratio of water depth to sediment grain size, h/D_{50} . BCF was determined after Lin and Venditti (2013). In our study, the calculated rate of ripple migration was approximately 10^{-5} m/s, which aligns with the estimates based on the ADV-monitored bed level and measured ripple length (Table 7.5). We note the difference in magnitude is caused partly by the uncertainty associated with the ripple length. As manual measurements of ripple length are temporally sparse, $L_{r,meas}/T_{r,ADV}$ is estimated from the closest measurement of $L_{r,meas}$.

Table 7.5: Results of bed ripple size (height, H_r , and length, L_r), period (T_r) and migration rate (V_r). Simulated ripple migration rate is tidally averaged.

Tidal cycle ID	Ripple height		Ripple length		Period		Ripple migration rate			
	Manually meas.	ADV monitored	Manually meas.	ADV monitored	T_r (s)	N	$L_{r,meas}/T_r$, ADV	Simulated		
	H_r (mm)	N	H_r (mm)	N	L_r (mm)	N				
3	–	–	5.4±1.3	5	–	–	4258±483	4	1.1	1.2
5	5.9±1.6	20	5.0±0.4	3	47.9±5.6	20	–	–	–	1.1
6	–	–	7.9±2.1	6	–	–	2926±284	6	1.6	5.3
8	–	–	3.4±1.3	6	–	–	2050±326	3	2.3	2.7
9	–	–	–	–	43.0±8.5	24	–	–	–	–
10	–	–	11.8±1.6	5	–	–	3692±1129	6	1.3	3.7
11	–	–	3.9±1.2	3	59.2±7.1	48	–	–	–	2.9
12	12.6±3.2	16	1.6±0.4	4	86.5±12.7	36	3719±965	2	2.3	0.6

7.5.3 Horizontal processes

In addition, the BLC model described in this study cannot solve morphological problems along horizontal spatial scales. For instance, this model cannot describe the advection process, which changes the SSC and further affects the deposition rate. However, the erosion and deposition processes described by this model can be embedded into 2D/3D morphological models.

8

Synthesis

This chapter summarizes the main conclusions of the thesis, which accomplish the objectives raised in Chapter 1 (section 1.3). Novelties are given in section 8.2. Section 8.3 provides recommendations for future study according to findings and limitations of this thesis.



Photos taken by camera equipped on drone. Left: transition zone between salt marsh and mudflat at Southeastern Chongming mudflat (by Q. Zhu and Q.X. Liu); Right: coherent flow structure indicated by suspended sediment on the interface between tidal flat and channel at Kapellebank mudflat (by R.L. Brouwer).

8.1 Conclusions

This study aims to further our understanding of sediment dynamic processes occurring on intertidal mudflats, and to improve the bed-level change modelling strategies. In summarizing the context presented and answering questions listed in section 1.3, the most important findings of this thesis are as follows:

8.1.1 Sediment dynamic processes in intertidal mudflats of different open levels

Total bed shear stress was dominated by tidal currents on meso-macrotidal flats, with waves had significant impact when water depth was less than 1m. The more open the flat was, the stronger tidal currents impact on hydrodynamic forces, as τ_c/τ_w was 4.8 in open tidal flat, while was around 2 in moderate-open and sheltered flats. In temporal, τ_{cw} was larger during spring tides than during neap tides. When wind events occurred, τ_{cw} were more than 3 times larger than that in normal spring tides.

Duration of $\tau_{cw} < \tau_e$ during neap tides was longer (1.4–1.6 times) than that during spring tides. Duration of $\tau_{cw} < \tau_e$ in open and moderate-open intertidal flats in normal weather was 23%, indicating an erosion tendency; while was 70% on sheltered flats, indicating a deposition tendency. In open and moderate-open flat, strong wind resulted in duration of $\tau_{cw} < \tau_e$ decreasing to 6.1%; even dropped to 0% when storm occurred. Diatom presence disturb the erosion-deposition pattern by enhancing τ_e , which could be 4 times the value of abiotic τ_e .

Intra-tidal SSC variation normally followed a V-shaped patten: SSC was high during flood and ebb peaks, and SSC was low during high slack water. Since near-bed SSC was controlled by erosion, deposition and advection processes, there was no unified variation pattern in response to strong wind/storm event. For instance, SSC during strong wind condition was higher than that during normal weather in the Nanhui Foreland mudflat; lower in the Southeastern Chongming mudflat; and there was no obvious increase or decrease in SSC in the two wind scenarios in Kapellebank mudflat. Vertically, SSC profiles identified during typical flood and ebb stages increased gradually with height following a logarithmic trend whereas they were L-shaped during slack water periods. With a high background SSC in the Nanhui Foreland mudflat, substantial volumes of suspended sediment that settled during slack water periods formed a near-bed fluid mud layer. The thicknesses of fluid mud layers lasting for 0.5–1 h under normal weather conditions in middle- and low-lying flats were < 6 cm and 20–40 cm, respectively. During storm periods, the thickness of fluid mud layers increased to 48 cm when the background

SSC value increased to 3.3 kg/m^3 . In addition, 30 cm fluid mud layers likely formed during peak flood/ebb periods.

Intra-tidal bed-level changes in the Nanhui Foreland mudflat show that erosion occurred during peak flood and ebb periods while accretion occurred under high slack water conditions during periods of normal weather. The maximum erosion depth was 2–3 cm, exceeding the net intertidal bed-level changes of 0.7 cm. On low flats, during storm periods, bed-level changes measured via ADV and buried-plate methods showed maximum variations of 8–9 cm, but they were found to be in poor agreement due to the occurrence of sheet erosion. These processes were closely related to the formation and migration of edges resulting from sheet erosion. On the Southeastern Chongming mudflat, bed degradation of 10.6 cm occurred over 11 tidal cycles during strong wind events, whereas bed accretion levels of 8.3 cm occurred in the following 5 recovery tidal cycles. Overall, bed-level changes in the mudflat were more significant than those found along the salt marsh, with maximum values observed in the middle flat area. Buried-plate measurements show that during erosion, 3 cm of bed degradation occurred in the middle flat area, whereas lower and upper flat areas showed bed-level variations of $\pm 0.5 \text{ cm}$; during recovery stages, accretion was greatest in the middle flat area (2.3 cm), followed by those in the lower flat area (1.5 cm) and in the transitional zone between flat and marsh areas (0.8 cm). The lowest value was found in the salt marsh area (0.4 cm). On Kapellebank mudflat, the maximum variations decrease towards upper flat. Significant bed degradation processes occurred only in low flat areas during storm events. Intra-tidal bed-level changes show that bed degradation only occurred when water depths were less than 1 m, and the bed levels were stable during the remaining tidal submergence period.

8.1.2 Relationships between sediment dynamic processes in intertidal flats

Sediment dynamic processes respond to tides, wind conditions and sediment properties at intra-tide, neap–spring tides, and storm time scales. Erosion and deposition stages alternate due to the balance between τ_{cw} and τ_e and as a result of background SSC values. During tidal submergence periods, erosion occurred during peak flood and ebb periods, whereas deposition generally occurred during slack water periods. Deposition stages were shortened and even disappeared under storm conditions. Sediment dynamic processes on intertidal flats also exhibit neap–spring cyclicity in calm weather conditions. Wind events, which are random, interrupt this neap–spring cyclicity pattern. Our study shows that even moderate wind strengths can overturn intra-tidal and neap–spring cyclicities of bed-level changes even on meso–macrotidal mudflats. The effects of waves become more pronounced when flats are open.

Bed degradation during storm periods results from an increase in τ_{cw} . Wind enhances τ_{cw} in the following two ways: (1) wave orbital velocities are increased due to enhanced

wave heights driven by winds, which lead to an increase in τ_w ; and (2) wind driven flows increase τ_c in the τ_{cw} model. One form of wind-driven flow involves extra turbulence superimposed on original turbulence resulting from tidal currents, with mean flow speeds maintaining the neap–spring cyclicity. The other form involves wind-driven flows resulting from the abnormal flow structures found on at interface of a flat and channel, which breaks the intra-tidal cyclicity of current speeds. Bed recovery is rapid when large volumes of sediment are transported by high-energy spring tidal flows. More specifically, such conditions increase SSC values and enhance settling through flocculation. Bed recovery is also promoted by tidal asymmetry and with sufficient time for $\tau_{cw} < \tau_d$. This rapid deposition process greatly affects bed conditions.

8.1.3 BLC model and its applications

Based on our understanding both of the relationships among τ_{cw} , τ_e , τ_d , SSC and bed-level changes and of the classical Partheniades-Krone erosion-deposition model, we constructed a BLC model using the measured parameters as inputs. Measurements and simulations were used to investigate effects of strong wind events on sediment dynamics in intertidal mudflats, to quantify the erosion parameter τ_e and M (erosion coefficient) and to study the influence of wind events on these variables. Our results show that sediment freshly deposited after wind events is much looser: the water content was found to be 3 times that of more consolidated bed sediment before the examined wind event, and M decreased by 60%. Vertically, τ_e decreased following a power function, and the magnitude of M was $10^{-3} \sim 10^{-4}$ s/m without presenting a significant tendency with depth. This result indicates that τ_e cannot be simplified as a constant in erosion-deposition and morphological models and that M can be used as a constant.

The BLC model was used to determine whether τ_d should be introduced into the deposition model. We define falling sediment motion as ‘settling’ and the product as ‘deposition’: sediment always settles under the influence of gravity, whereas sediment deposition resulting in bed accretion occurs when τ_{cw} falls below a certain threshold, which is τ_d . Therefore, we suggest employing τ_d , which is valued at $0.5-1 \tau_e$.

8.2 Novelties

The novelties of this thesis are as follows:

1. We proposed and deployed a combined approach involving the use of *in situ* measurements and numerical modelling to improve ways of studying sediment dynamics in intertidal mudflats. First, the technical difficulties experienced when measuring simultaneous waves, current velocities, SSC values and bed-level changes in intertidal flats at a high resolution were addressed. Second, the BLC

model was designed to apply τ_{cw} , τ_e , τ_d , E and D calculations based on *in situ* measured data, and the simulated BLC values were found to be in good agreement with the measured BLC values. The combination of measurements and simulations was successfully applied to determine the effects of winds on bed sediment properties and bed-level changes. By this approach, we were able to present the first empirical evidence on the vertical distribution of τ_e and M of an absolute natural mud bed.

2. We focused on wind effects not only at the storm level but also at weaker levels (strong wind; speed < 10 m/s). We found that even for semi-open tidal flats, strong winds significantly affect sediment dynamics on intertidal flats. The often-applied assumption that ‘vertical velocities are not contaminated by surface waves’ was tested. This assumption fails when $H_s/h > 0.25$, which is quite common in intertidal areas and, in particular, in open flats.

8.3 Recommendations for future work

This thesis presents sediment dynamic processes of intertidal mudflats based on *in situ* measurements associated with the BLC model. According to our findings, recommendations for future research and suggested measurement and modelling strategies are outlined as follows:

1. Deployment settings, including sampling durations and frequencies, are essential for *in situ* measurements based on the calculation of hydrodynamic forces. Because the wave periods in intertidal flats are short (seconds), the sampling frequencies should be sufficiently high to record wave cycle patterns. The sampling durations must be long enough to record a sufficient quantity of waves for wave statistics. These two settings are also key to constructing a velocity power spectrum without high and low frequency losses (*Chapter 4*).
2. Measurements that are made close to sediment surfaces (millimetres to tens of millimetres above the sediment surface) are recommended. This layer is important for sediment transport because (i) highly dynamic fluidized mud layers may exist (*Chapter 5*); (ii) acoustic instruments fail to record bed-level changes under very shallow conditions, thus creating differences between any two measured tidal cycles in measured time series (*Chapter 6*); and (iii) significant sediment fluxes can occur under very shallow conditions (*Chapter 6*).
3. The maximum intra-tidal erosion levels are often several times greater than the tidal cycle net erosion levels. This finding presumably has implications for the principles of benthic ecology.
4. Waves are indeed important in intertidal flats. Wave processes must always be

considered when examining open intertidal flats because bed-level simulations without waves are different from measured results, even under moderate offshore wind conditions on a current-dominated flat (*Chapters 4 and 5*). Sheltered flats in estuaries normally suffer from low levels of wave energy, and the effects of waves are only considered during storm events (*Chapter 6*).

5. An integrated approach involving measurements and simulations is recommended for detecting the effects of wind on bed-level changes and calibrating erosion parameters (*Chapter 7*).
6. It is recommended that bottom boundary descriptions used in numerical models be improved. (i) very shallow conditions should be better simulated by improving wet-dry treatments; (ii) vertical distributions of τ_e should be considered, especially for extreme events, which expose deeper well-consolidated layers; and (iii) appropriate descriptions of diatom effects should be considered as part of the bottom boundary conditions.

However, this thesis still presents limitations to be addressed in future work:

1. Specific measurements and calculations of settling velocities require further study. Flocculation occurs when fine-grained sediments are present. With an increase in SSC, hindered settling processes occur. The settling velocity that we introduce in the thesis and was proposed by Whitehouse (2000) takes these two aspects into account. However, flocs are dynamic and are best observed by using in situ measurements, e.g., LISST (Wang et al., 2013). Parameterizations of hindered settling velocities also involve conducting several tests (Winterwerp and van Kesteren, 2004; te Slaa et al., 2015).
2. Mechanisms of fluidized mud dynamics must be better understood. We demonstrate the occurrence and disappearance of lutocline near the bed in *Chapter 5*. More *in situ* measurements, flume tests and model studies must be conducted to quantify the concentration distribution and thickness of this highly concentrated layer because it affects sediment transport rates.
3. The erosion model applied in this thesis refers to surface erosion. During storm events with wave attack processes, however, mass erosion occurs when the bed shear stress exceeds a certain threshold and when cracking occurs (Winterwerp and van Kesteren, 2004). This form of erosion is often observed as sheet erosion on intertidal flats. This mass erosion process affects volumes of sediment moving in and out of tidal flat systems.
4. The effects of bed-level changes on hydrodynamic forces (Figure 1.2) are not discussed in this thesis. This process is often discussed in studies on long-term tidal flat and tidal inlet system development and equilibrium features (de Swart and Zimmerman, 2009; Friedrichs, 2011), whereas the time scale applied in this thesis is relatively shorter (tidal cycles to days). Evaluations of the key processes identified

in a certain study are dependent on the time scale used.

5. Natural deposits on intertidal flats occasionally include a mixture of sand and mud. Cohesive and non-cohesive sediments are generally managed separately. However, interactions between these fractions should be considered in suspended sediment concentration distribution, erosion and deposition processes (Le Hir et al., 2011). Therefore, it is recommended that sand-mud mixture dynamic modelling strategies be applied when studying the morphodynamics of tidal flats.

References

- Allen, J.R.L., Duffy, M.J., 1998. Medium-term sedimentation on high intertidal mudflats and salt marshes in the Severn Estuary, SW Britain: the role of wind and tide. *Marine Geology* 150 (1-4), 1-27.
- Amos, C.L., Daborn, G., Christian, H., Atkinson, A., Robertson, A., 1992. In situ measurements on fine-grained sediments from the Bay of Fundy. *Marine Geology* 108 (2), 175-196.
- Amos, C.L., Mosher, D.C., 1985. Erosion and deposition of fine-grained sediments from the Bay of Fundy. *Sedimentology* 32 (6), 815-832.
- Amos, C.L., Tee, K.T., 1989. Suspended sediment transport processes in Cumberland Basin, Bay of Fundy. *Journal of Geophysical Research-Oceans* 94 (C10), 14407-14417.
- Andersen, T.J., Fredsoe, J., Pejrup, M., 2007. In situ estimation of erosion and deposition thresholds by Acoustic Doppler Velocimeter (ADV). *Estuarine Coastal and Shelf Science* 75 (3), 327-336.
- Andersen, T.J., Lanuru, M., van Bernem, C., Pejrup, M., Riethmueller, R., 2010. Erodibility of a mixed mudflat dominated by microphytobenthos and *Cerastoderma edule*, East Frisian Wadden Sea, Germany. *Estuarine Coastal and Shelf Science* 87 (2), 197-206.
- Andersen, T.J., Lund-Hansen, L.C., Pejrup, M., Jensen, K.T., Mouritsen, K.N., 2005. Biologically induced differences in erodibility and aggregation of subtidal and intertidal sediments: a possible cause for seasonal changes in sediment deposition. *Journal of Marine Systems* 55 (3-4), 123-138.
- Andersen, T.J., Pejrup, M., 2001. Suspended sediment transport on a temperate, microtidal mudflat, the Danish Wadden Sea. *Marine Geology* 173 (1-4), 69-85.
- Andersen, T.J., Pejrup, M., 2002. Biological mediation of the settling velocity of bed material eroded from an intertidal mudflat, the Danish Wadden Sea. *Estuarine Coastal and Shelf Science* 54 (4), 737-745.

- Andersen, T.J., Pejrup, M., Nielsen, A.A., 2006. Long-term and high-resolution measurements of bed level changes in a temperate, microtidal coastal lagoon. *Marine Geology* 226 (1-2), 115-125.
- ARGUS, 2012. User manual of ASM-IV Argus Surface Meter. Argus Gesellschaft für Umweltmesstechnik mbH, Ritterhude, Germany.
- Ariathurai, C., 1974. A finite element model for sediment transport in estuaries. University of California, Berkley, USA.
- Armanini, A., 1995. Non-uniform sediment transport: dynamics of the active layer. *Journal of Hydraulic Research* 33 (5), 611-622.
- Armentano, T.V., Woodwell, G.M., 1975. Sedimentation rates in a Long Island marsh determined by 210 Pb dating 1. *Limnology & Oceanography* 20 (3), 452-456.
- Austen, I., Andersen, T.J., Edelvang, K., 1999. The influence of benthic diatoms and invertebrates on the erodibility of an intertidal mudflat, the Danish Wadden Sea. *Estuarine Coastal and Shelf Science* 49 (1), 99-111.
- Baas, J.H., Davies, A.G., Malarkey, J., 2013. Bedform development in mixed sand-mud: The contrasting role of cohesive forces in flow and bed. *Geomorphology* 182, 19-32.
- Banerjee, T., Muste, M., Katul, G., 2015. Flume experiments on wind induced flow in static water bodies in the presence of protruding vegetation. *Advances in Water Resources* 76, 11-28.
- Barbier, E.B., Koch, E.W., Silliman, B.R., Hacker, S.D., Wolanski, E., Primavera, J., Granek, E.F., Polasky, S., Aswani, S., Cramer, L.A., Stoms, D.M., Kennedy, C.J., Bael, D., Kappel, C.V., Perillo, G.M.E., Reed, D.J., 2008. Coastal ecosystem-based management with nonlinear ecological functions and values. *Science* 319 (3561), 321-323.
- Bassoullet, P., Le Hir, P., Gouleau, D., Robert, S., 2000. Sediment transport over an intertidal mudflat: field investigations and estimation of fluxes within the "Baie de Marennes-Oleron" (France). *Continental Shelf Research* 20 (12-13), 1635-1653.
- Battjes, J.A., Stive, M.J.F., 1985. Calibration and verification of a dissipation model for random breaking waves. *Journal of Geophysical Research* 90 (C5), 9159-9167.
- Bi, N.S., Yang, Z.S., Wang, H.J., Xu, C.L., Guo, Z.G., 2014. Impact of artificial water and sediment discharge regulation in the Huanghe (Yellow River) on the transport of particulate heavy metals to the sea. *Catena* 121, 232-240.
- Bird, E.C.F., 1986. Mangroves and intertidal morphology in Westernport Bay, Victoria, Australia. *Marine Geology* 69 (3-4), 251-271.
- Blum, M.D., Roberts, H.H., 2009. Drowning of the Mississippi Delta due to insufficient sediment supply and global sea-level rise. *Nature Geoscience* 2 (7), 488-491.
- Bohling, B., 2009. Measurements of threshold values for incipient motion of sediment particles with two different erosion devices. *Journal of Marine Systems* 75 (3-4),

- 330-335.
- Cai, Y.M., Zhou, Y.X., Tian, B., 2014. *Shanghai Wetlands*, second ed., Shanghai Century Publishing (Group) Co., Ltd and Shanghai Scientific and Technical Publishers, Shanghai.
- Callaghan, D.P., Bouma, T.J., Klaassen, P., van der Wal, D., Stive, M.J.F., Herman, P.M.J., 2010. Hydrodynamic forcing on salt-marsh development: Distinguishing the relative importance of waves and tidal flows. *Estuarine Coastal and Shelf Science* 89 (1), 73-88.
- Callaghan, D.P., Wainwright, D., 2013. The impact of various methods of wave transfers from deep water to nearshore when determining extreme beach erosion. *Coastal Engineering* 74, 50-58.
- Cancino, L., Neves, R., 1999. Hydrodynamic and sediment suspension modelling in estuarine systems - Part I: Description of the numerical models. *Journal of Marine Systems* 22 (2-3), 105-116.
- Cao, P., Dong, Y., Yan, S., Gu, G., 1989. Basic Characteristics of the tidal flat on the north coast of Hangzhou Bay. *Oceanologia et Limnologia Sinica* 20 (5), 412 - 422. (in Chinese)
- Chen, J.Y., Yun, C.X., Xu, H.G., Dong, Y.F., 1979. The Development Model of the Chang Jiang River Estuary during last 2000 years. *Acta Oceanologica Sinica* 1 (1), 103-111. (in Chinese)
- Chen, S.L., 2004. Hydrological and sediment features and fluxes in Nanhui nearshore waters, Hangzhou Bay. *Marine Sciences* 28 (3), 18-22. (in Chinese)
- Chen, S.L., Gu, G.C., 2000. Modeling suspended sediment concentrations in the mouth of Hangzhou Bay. *Journal of Sediment Research* (5), 45 - 50. (in Chinese)
- Chen, S.L., Zhang, G.A., Gu, G.C., 2003. Geomorphic evolution of Nanhui Nearshore of the Yangtze Estuary and its sediment dynamic mechanism. *Shanghai Geology* 2003 (4), 1-4. (in Chinese)
- Chen, S.L., Zhang, G.A., Yang, S.L., Shi, J.Z., 2006. Temporal variations of fine suspended sediment concentration in the Changjiang River estuary and adjacent coastal waters, China. *Journal of Hydrology* 331 (1-2), 137-145.
- Christie, M.C., Dyer, K.R., Turner, P., 1999. Sediment flux and bed level measurements from a macro tidal mudflat. *Estuarine Coastal and Shelf Science* 49 (5), 667-688.
- Christoffersen, J.B., Jonsson, I.G., 1985. Bed friction and dissipation in a combined current and wave motion. *Ocean Engineering* 12 (5), 387-423.
- Chu, Z.X., Sun, X.G., Zhai, S.K., Xu, K.H., 2006. Changing pattern of accretion/erosion of the modern Yellow River (Huanghe) subaerial delta, China: based on remote sensing images. *Marine Geology* 227, 13-30.
- Chu, Z.X., Zhai, S.K., 2008. Yangtze River sediment: In response to Three Gorges Reservoir (TGR) water impoundment in June 2003. *Journal of Coastal Research* 24

- (1A), 30-39.
- Collins, M.B., Ke, X., Gao, S., 1998. Tidally-induced flow structure over intertidal flats. *Estuarine Coastal and Shelf Science* 46 (2), 233-250.
- Campbell Scientific, 2007. User manual of OBS-3A Turbidity and Temperature Monitoring System, in: Campbell Scientific, I. (Ed.), 4/28 ed. Campbell Scientific, Inc., North Loga, Utah.
- Cooper, N.J., 2005. Wave dissipation across intertidal surfaces in the Wash tidal inlet, eastern England. *Journal of Coastal Research* 21 (1), 28-48.
- Costanza, R., d'Arge, R., deGroot, R., Farber, S., Grasso, M., Hannon, B., Limburg, K., Naeem, S., Oneill, R.V., Paruelo, J., Raskin, R.G., Sutton, P., vandenBelt, M., 1997. The value of the world's ecosystem services and natural capital. *Nature* 387 (6630), 253-260.
- Dai, S.B., Lu, X.X., 2014. Sediment load change in the Yangtze River (Changjiang): A review. *Geomorphology* 215, 60-73.
- Dai, S.B., Yang, S.L., Cai, A.M., 2008. Impacts of dams on the sediment flux of the Pearl River, southern China. *Catena* 76 (1), 36-43.
- Dai, Z.J., Liu, J.T., 2013. Impacts of large dams on downstream fluvial sedimentation: An example of the Three Gorges Dam (TGD) on the Changjiang (Yangtze River). *Journal of Hydrology* 480, 10-18.
- Dai, Z.J., Liu, J.T., Wei, W., Chen, J.Y., 2014a. Detection of the Three Gorges Dam influence on the Changjiang (Yangtze River) submerged delta. *Scientific Reports* 4, 1-7.
- Dai, Z.J., Liu, J.T., Xiang, Y.B., 2015a. Human interference in the water discharge of the Changjiang (Yangtze River), China. *Hydrological Sciences Journal-Journal Des Sciences Hydrologiques* 60 (10), 1770-1782.
- Dai, Z.J., Liu, J.T., Xie, H.L., Shi, W.Y., 2014b. Sedimentation in the Outer Hangzhou Bay, China: The Influence of Changjiang Sediment Load. *Journal of Coastal Research* 30 (6), 1218-1225.
- Dai, Z.J., Zhu, W.W., Li, W.H., Li, J.F., 2015b. Research on recent changes of fluid mud and its impacted factors in the north passage of the Changjiang Estuary. *Journal of Sediment Research* 2015 (1), 49-54.
- Dalyander, P.S., Butman, B., Sherwood, C.R., Signell, R.P., Wilkin, J.L., 2013. Characterizing wave- and current- induced bottom shear stress: U.S. middle Atlantic continental shelf. *Continental Shelf Research* 52, 73-86.
- Davies, A.M., Gerritsen, H., 1994. An intercomparison of three - dimensional tidal hydrodynamic models of the Irish Sea. *Tellus A* 46 (2), 200-221.
- de Brouwer, J.F.C., Bjelic, S., de Deckere, E., Stal, L.J., 2000. Interplay between biology and sedimentology in a mudflat (Biezelingse Ham, Westerschelde, The Netherlands). *Continental Shelf Research* 20 (10-11), 1159-1177.

- de Brouwer, J.F.C., Wolfstein, K., Ruddy, G.K., Jones, T.E.R., Stal, L.J., 2005. Biogenic stabilization of intertidal sediments: The importance of extracellular polymeric substances produced by benthic diatoms. *Microbial Ecology* 49 (4), 501-512.
- De Jonge, V.N., Van Beusekom, J.E.E., 1995. Wind- and tide-induced resuspension of sediment and microphytobenthos from tidal flats in the Ems estuary. *Limnology and Oceanography* 40 (4), 766-778.
- de Swart, H.E., Zimmerman, J.T.F., 2009. Morphodynamics of Tidal Inlet Systems. *Annual Review of Fluid Mechanics* 41, 203-229.
- de Vries, J., van Gent, M.R.A., Walstra, D.J.R., Reniers, A., 2008. Analysis of dune erosion processes in large-scale flume experiments. *Coastal Engineering* 55 (12), 1028-1040.
- Delo, E., Ockenden, M., 1992. Estuarine muds manual. HR Wallingford Report SR 309. Oxfordshire, UK.
- Deltares, 2010. User Manual Delft3D-FLOW, Delft, The Netherlands, pp. 93.
- Dickhudt, P.J., Friedrichs, C.T., Schaffner, L.C., Sanford, L.P., 2009. Spatial and temporal variation in cohesive sediment erodibility in the York River estuary, eastern USA: A biologically influenced equilibrium modified by seasonal deposition. *Marine Geology* 267 (3-4), 128-140.
- Ding, P., Hu, K., Kong, Y., Hu, D., 2003. Numerical Simulation of Storm-induced Erosion/Deposition in Yangtze Estuary --A Case Study of Typhoon Jelawat. *Journal of Sediment Research* (6), 18-24. (in Chinese)
- Du, J.-L., Yang, S.-L., Feng, H., 2016. Recent human impacts on the morphological evolution of the Yangtze River delta foreland: A review and new perspectives. *Estuarine, Coastal and Shelf Science* 181, 160-169.
- Dyer, K.R., 1986. *Coastal and Estuarine Sediment Dynamics*. John Wiley & Sons Inc, pp. 173.
- Dyer, K.R., Christie, M.C., Manning, A.J., 2004. The effects of suspended sediment on turbulence within an estuarine turbidity maximum. *Estuarine Coastal and Shelf Science* 59 (2), 237-248.
- Eisma, D., 1998. *Intertidal Deposits: River Mouth, Tidal Flats, and Coastal Lagoons*. CRC Press, Boca Raton.
- Emanuel, K., 2005. Increasing destructiveness of tropical cyclones over the past 30 years. *Nature* 436 (7051), 686-688.
- Fan, D.D., Guo, Y.X., Wang, P., Shi, J.Z., 2006. Cross-shore variations in morphodynamic processes of an open-coast mudflat in the Changjiang Delta, China: With an emphasis on storm impacts. *Continental Shelf Research* 26 (4), 517-538.
- Fang, H.W., Shang, Q.Q., Chen, M.H., He, G.J., 2014. Changes in the critical erosion velocity for sediment colonized by biofilm. *Sedimentology* 61 (3), 648-659.
- Fredsøe, J., 1984. Turbulent boundary layer in wave-current motion. *Journal of Hydraulic*

- Engineering 110 (8), 1103-1120.
- Freeman, D.P., Coates, L.E., Ockernden, M.C., Roberts, W., West, J.R., 1994. Cohesive sediment transport on an inter-tidal zone under combined wave-tidal flow. *Netherlands Journal of Aquatic Ecology* 28 (3-4), 283-288.
- Friedrichs, C.T., 2011. Tidal flat morphodynamics: a synthesis, in: Hansom, J.D., Flemming, B.W. (Eds.), *Treatise on Estuarine and Coastal Science*. Elsevier.
- Friedrichs, C.T., Wright, L.D., 1997. Sensitivity of bottom stress and bottom roughness estimates to density stratification, Eckernforde Bay, southern Baltic Sea. *Journal of Geophysical Research-Oceans* 102 (C3), 5721-5732.
- Friedrichs, C.T., Wright, L.D., 2004. Gravity-driven sediment transport on the continental shelf implications for equilibrium profiles near river mouths. *Coastal Engineering* 51 (8-9), 795-811.
- Friedrichs, C.T., Wright, L.D., Hepworth, D.A., Kim, S.C., 2000. Bottom-boundary-layer processes associated with fine sediment accumulation in coastal seas and bays. *Continental Shelf Research* 20 (7), 807-841.
- Frihy, O.E., Debes, E.A., El Sayed, W.R., 2003. Processes reshaping the Nile delta promontories of Egypt: pre- and post-protection. *Geomorphology* 53 (3-4), 263-279.
- Gallagher, E.L., Boyd, W., Elgar, S., Guza, R.T., Woodward, B., 1996. Performance of a sonar altimeter in the nearshore. *Marine Geology* 133 (3-4), 241-248.
- Gao, S., 2009. Geomorphology and sedimentology of tidal flats, in: Perillo, G.M.E., Wolanski, E., Cahoon, D.R., Brinson, M.M. (Eds.), *Coastal Wetlands: An Intergrated Ecosystem Approach*. Elsevier, Amsterdam, pp. 259-316.
- Ge, J.Z., Shen, F., Guo, W.Y., Chen, C.S., Ding, P.X., 2015. Estimation of critical shear stress for erosion in the Changjiang Estuary: A synergy research of observation, GOCI sensing and modeling. *Journal of Geophysical Research-Oceans* 120 (12), 8439-8465.
- Gomez, E.A., Amos, C.L., 2005. Dewatering effects on the erodibility of newly deposited cohesive beds by unidirectional currents. *Sedimentology* 52 (1), 183-189.
- Goodwin, P., Mehta, A.J., Zedler, J.B., 2001. Tidal wetland restoration: An introduction. *Journal of Coastal Research* 27, 1-6.
- Grant, W.D., Madsen, O.S., 1979. Combined wave and current interaction with a rough bottom. *Journal of Geophysical Research-Oceans and Atmospheres* 84 (NC4), 1797-1808.
- Graton, L.C., Fraser, H.J., 1935. Systematic Packing of Spheres: With Particular Relation to Porosity and Permeability. *The Journal of Geology* 43 (8, Part 1), 785-909.
- Green, M.O., 1992. Spectral estimates of bed shear stress at subcritical Reynolds numbers in a tidal boundary layer. *Journal of Physical Oceanography* 22 (8), 903-917.
- Green, M.O., Black, K.P., Amos, C.L., 1997. Control of estuarine sediment dynamics by interactions between currents and waves at several scales. *Marine Geology* 144 (1-

- 3), 97-116.
- Green, M.O., Coco, G., 2007. Sediment transport on an estuarine intertidal flat: Measurements and conceptual model of waves, rainfall and exchanges with a tidal creek. *Estuarine Coastal and Shelf Science* 72 (4), 553-569.
- Green, M.O., Coco, G., 2014. Review of wave-driven sediment resuspension and transport in estuaries. *Reviews of Geophysics* 52 (1), 77-117.
- Gross, T.F., Isley, A.E., Sherwood, C.R., 1992. Estimation of stress and bed roughness during storms on the Northern California Shelf. *Continental Shelf Research* 12 (2-3), 389-413.
- Group of Shanghai Coastal Investigation (GCSI), 1988. Report of Shanghai Coastal Comprehensive Investigation. Shanghai Scientific and Technological Press, Shanghai (in Chinese).
- Gust, G., Morris, M.J., 1989. Erosion Thresholds and Entrainment Rates of Undisturbed in situ Sediments. *Journal of Coastal Research*, 87-99.
- Han, Z., Yun, C.X., 2003. Deposition and erosion remote-sensing reverse of Dachan Bay beach in Lingdingyang estuary. *Acta Geographica Sinica* 25 (5), 58-64. (in Chinese)
- Harley, C.D.G., Hughes, A.R., Hultgren, K.M., Miner, B.G., Sorte, C.J.B., Thornber, C.S., Rodriguez, L.F., Tomanek, L., Williams, S.L., 2006. The impacts of climate change in coastal marine systems. *Ecology Letters* 9 (2), 228-241.
- Herman, P.M.J., Middelburg, J.J., Heip, C.H.R., 2001. Benthic community structure and sediment processes on an intertidal flat: results from the ECOFLAT project. *Continental Shelf Research* 21 (18-19), 2055-2071.
- Hoitink, A.J.F., Hoekstra, P., 2005. Observations of suspended sediment from ADCP and OBS measurements in a mud-dominated environment. *Coastal Engineering* 52 (2), 103-118.
- Holthuijsen, L.H., 2007. *Waves in oceanic and coastal waters*. Cambridge University Press.
- Hooke, J.M., Bray, M.J., Carter, D.J., 1996. Sediment transport analysis as a component of coastal management - A UK example. *Environmental Geology* 27 (4), 347-357.
- Houwing, E.J., 1999. Determination of the critical erosion threshold of cohesive sediments on intertidal mudflats along the Dutch Wadden Sea Coast. *Estuarine Coastal and Shelf Science* 49 (4), 545-555.
- Hu, B.Q., Yang, Z.S., Wang, H.J., Sun, X.X., Bi, N.S., Li, G.G., 2009. Sedimentation in the Three Gorges Dam and the future trend of Changjiang (Yangtze River) sediment flux to the sea. *Hydrology and Earth System Sciences* 13 (11), 2253-2264.
- Hu, K., Ding, P., Ge, J., 2007. Modelling of storm surge in the coastal waters of Yangtze Estuary and Hangzhou Bay, China. *Journal of Coastal Research* 245, 527-533.
- Hu, Z., Lenting, W., van der Wal, D., Bouma, T.J., 2015a. Continuous monitoring bed-level dynamics on an intertidal flat: Introducing novel, stand-alone high-resolution

- SED-sensors. *Geomorphology* 245, 223-230.
- Hu, Z., Wang, Z.B., Zitman, T.J., Stive, M.J.F., Bouma, T.J., 2015b. Predicting long-term and short-term tidal flat morphodynamics using a dynamic equilibrium theory. *Journal of Geophysical Research-Earth Surface* 120 (9), 1803-1823.
- Huntley, D.A., 1988. A modified inertial dissipation method for estimating seabed stresses at low Reynolds numbers, with application to wave/current boundary layer measurements. *Journal of Physical Oceanography* 18 (2), 339-346.
- Huyng-Thanh, S., Temperville, A., 1990. A numerical model of the rough turbulent boundary layer in combined wave and current interaction. *Coastal Engineering Proceedings* 1 (22).
- Jacobs, W., Le Hir, P., Van Kesteren, W., Cann, P., 2011. Erosion threshold of sand–mud mixtures. *Continental Shelf Research* 31 (10), S14-S25.
- Jangir, B., Satyanarayana, A.N.V., Swati, S., Jayaram, C., Chowdary, V.M., Dadhwal, V.K., 2016. Delineation of spatio-temporal changes of shoreline and geomorphological features of Odisha coast of India using remote sensing and GIS techniques. *Natural Hazards* 82 (3), 1437-1455.
- Janssen-Stelder, B., 2000. The effect of different hydrodynamic conditions on the morphodynamics of a tidal mudflat in the Dutch Wadden Sea. *Continental Shelf Research* 20 (12-13), 1461-1478.
- Jaramillo, S., Sheremet, A., Allison, M.A., Reed, A.H., Holland, K.T., 2009. Wave-mud interactions over the muddy Atchafalaya subaqueous clinof orm, Louisiana, United States: Wave-supported sediment transport. *Journal of Geophysical Research-Oceans* 114.
- Jestin, H., Bassoullet, P., Le Hir, P., L'Yavanc, J., Degres, Y., 1998. Development of ALTUS, a high frequency acoustic submersible recording altimeter to accurately monitor bed elevation and quantify deposition and erosion of sediments, *Oceans'98*, pp. 189 - 194.
- Jing, L., Ridd, P.V., 1996. Wave-current bottom shear stresses and sediment resuspension in Cleveland Bay, Australia. *Coastal Engineering* 29 (1-2), 169-186.
- Kazemipour, F., Launeau, P., Meleder, V., 2012. Microphytobenthos biomass mapping using the optical model of diatom biofilms: Application to hyperspectral images of Bourgneuf Bay. *Remote Sensing of Environment* 127, 1-13.
- Kim, S.C., Friedrichs, C.T., Maa, J.P.Y., Wright, L.D., 2000. Estimating bottom stress in tidal boundary layer from Acoustic Doppler Velocimeter data. *Journal of Hydraulic Engineering-Asce* 126 (6), 399-406.
- Kineke, G.C., Sternberg, R.W., Trowbridge, J.H., Geyer, W.R., 1996. Fluid-mud processes on the Amazon continental shelf. *Continental Shelf Research* 16 (5-6), 667-696.
- Kirby, R., Bleakley, R., Weatherup, T., Raven, P.J., Donaldson, D., 1992. Effect of

- episodic events on tidal mud flat stability, Ardmillan Bay, Strangford Lough, Northern Ireland, in: Mehta, A.J. (Ed.), *Nearshore and estuarine cohesive sediment transport*. Pacific Rim Congress, Washington, pp. 378-392.
- Krone, R.B., 1962. Flume studies of the transport of sediment in estuarial shoaling processes.
- Kuijper, C., Steijn, R.C., Roelvink, J.A., van der Kaaij, T., Olijslagers, P., 2004. Morphological modelling of the Western Scheldt: validation of Delft3D.
- Lawler, D.M., 2008. Advances in the continuous monitoring of erosion and deposition dynamics: Developments and applications of the new PEEP-3T system. *Geomorphology* 93 (1-2), 17-39.
- Le Hir, P., Cann, P., Waeles, B., Jestin, H., Bassoullet, P., 2008. Erodibility of natural sediments: experiments on sand/mud mixtures from laboratory and field erosion tests. *Proceedings in Marine Science* 9, 137-153.
- Le Hir, P., Cayocca, F., Waeles, B., 2011. Dynamics of sand and mud mixtures: A multiprocess-based modelling strategy. *Continental Shelf Research* 31 (10), S135-S149.
- Le Hir, P., Monbet, Y., Orvain, F., 2007. Sediment erodability in sediment transport modelling: Can we account for biota effects? *Continental Shelf Research* 27 (8), 1116-1142.
- Le Hir, P., Roberts, W., Cazaillet, O., Christie, M., Bassoullet, P., Bacher, C., 2000. Characterization of intertidal flat hydrodynamics. *Continental Shelf Research* 20 (12-13), 1433-1459.
- Lesser, G.R., Roelvink, J.A., van Kester, J., Stelling, G.S., 2004. Development and validation of a three-dimensional morphological model. *Coastal Engineering* 51 (8-9), 883-915.
- Levoy, F., Anthony, E.J., Monfort, O., Larssonneur, C., 2000. The morphodynamics of megatidal beaches in Normandy, France. *Marine Geology* 171 (1-4), 39-59.
- Li, H., Yang, S.L., 2009. Trapping Effect of Tidal Marsh Vegetation on Suspended Sediment, Yangtze Delta. *Journal of Coastal Research* 25, 915-936.
- Li, P., Yang, S.L., Milliman, J.D., Xu, K.H., Qin, W.H., Wu, C.S., Chen, Y.P., Shi, B.W., 2012. Spatial, Temporal, and Human-Induced Variations in Suspended Sediment Concentration in the Surface Waters of the Yangtze Estuary and Adjacent Coastal Areas. *Estuaries and Coasts* 35 (5), 1316-1327.
- Lin, C.Y.M., Venditti, J.G., 2013. An empirical model of subcritical bedform migration. *Sedimentology* 60 (7), 1786-1799.
- Liu, H., Wu, J.X., 2015. Estimation of bed shear stresses in the pearl river estuary. *China Ocean Engineering* 29 (1), 133-142.
- Liu, J.H., Yang, S.L., Zhu, Q., Zhang, J., 2014. Controls on suspended sediment concentration profiles in the shallow and turbid Yangtze Estuary. *Continental Shelf*

- Research 90 (0), 96-108.
- Lohrmann, A., Cabrera, R., Gelfenbaum, G., Haines, J., 1995. Direct measurements of Reynolds stress with an acoustic Doppler velocimeter. *Proceedings of the IEEE Fifth Working Conference on Current Measurement (Cat. No.95CH35734)*, 205-210.
- Lumborg, U., 2005. Modelling the deposition, erosion, and flux of cohesive sediment through Oresund. *Journal of Marine Systems* 56 (1-2), 179-193.
- Ma, Y.X., Friedrichs, C.T., Harris, C.K., Wright, L.D., 2010. Deposition by seasonal wave- and current-supported sediment gravity flows interacting with spatially varying bathymetry: Waiapu shelf, New Zealand. *Marine Geology* 275 (1-4), 199-211.
- Maa, J.P.Y., Sanford, L., Halka, J.P., 1998. Sediment resuspension characteristics in Baltimore Harbor, Maryland. *Marine Geology* 146 (1-4), 137-145.
- Maan, D.C., van Prooijen, B.C., Wang, Z.B., De Vriend, H.J., 2015. Do intertidal flats ever reach equilibrium? *Journal of Geophysical Research: Earth Surface* 120 (11), 2406-2436.
- Maire, O., Lecroart, P., Meysman, F., Rosenberg, R., Duchene, J.C., Gremare, A., 2008. Quantification of sediment reworking rates in bioturbation research: a review. *Aquatic Biology* 2 (3), 219-238.
- Mancini, F., Dubbini, M., Gattelli, M., Stecchi, F., Fabbri, S., Gabbianelli, G., 2013. Using Unmanned Aerial Vehicles (UAV) for High-Resolution Reconstruction of Topography: The Structure from Motion Approach on Coastal Environments. *Remote Sensing* 5 (12), 6880-6898.
- McAnally, W.H., Friedrichs, C., Hamilton, D., Hayter, E., Shrestha, P., Rodriguez, H., Sheremet, A., Teeter, A., Flu, A.T.C.M., 2007. Management of fluid mud in estuaries, bays, and lakes. I: Present state of understanding on character and behavior. *Journal of Hydraulic Engineering-Asce* 133 (1), 9-22.
- Mehta, A., 1988. Laboratory studies on cohesive sediment deposition and erosion, *Physical processes in estuaries*. Springer, pp. 427-445.
- Mehta, A.J., McAnally, W.H., 2008. *Fine-Grained Sediment Transport*. American Society of Civil Engineers.
- Mehta, A.J., Partheniades, E., 1982. Resuspension of deposited cohesive sediment beds. *Coastal Engineering Proceedings* 1.
- Meirelles, S., Henriquez, M., Hornerdevine, A.R., Souza, A.J., Pietrzak, J., Stive, M., 2015. Bed shear stress on the middle shoreface of the South-Holland coast. *Coastal Sediments 2015*. DOI: http://dx.doi.org/10.1142/9789814689977_0210
- Milburn, D., Krishnappan, B.G., 2003. Modelling erosion and deposition of cohesive sediments from Hay River, Northwest Territories, Canada. *Nordic Hydrology* 34 (1-2), 125-138.
- Millard, K., Redden, A.M., Webster, T., Stewart, H., 2013. Use of GIS and high resolution

- LiDAR in salt marsh restoration site suitability assessments in the upper Bay of Fundy, Canada. *Wetlands Ecology and Management* 21 (4), 243-262.
- Miller, D.C., Muir, C.L., Hauser, O.A., 2002. Detrimental effects of sedimentation on marine benthos: what can be learned from natural processes and rates? *Ecological Engineering* 19 (3), 211-232.
- Milliman, J.D., Farnsworth, K.L., 2011. *River Discharge to the Coastal Ocean: A Global Synthesis*. Cambridge University Press, Cambridge, 384 pp.
- Mitchener, H., Torfs, H., 1996. Erosion of mud/sand mixtures. *Coastal Engineering* 29, 1-25.
- Montserrat, F., Suykerbuyk, W., Al-Busaidi, R., Bouma, T.J., van der Wal, D., Herman, P.M.J., 2011. Effects of mud sedimentation on lugworm ecosystem engineering. *Journal of Sea Research* 65 (1), 170-181.
- Myrhaug, D., Slaattelid, O.H., 1990. A rational approach to wave-current friction coefficients for rough, smooth and transitional turbulent flow. *Coastal Engineering* 14 (3), 265-293.
- Nagihara, S., Mulligan, K.R., Xiong, W., 2004. Use of a three-dimensional laser scanner to digitally capture the topography of sand dunes in high spatial resolution. *Earth Surface Processes and Landforms* 29 (3), 391-398.
- Neumeier, U., Lucas, C.H., Collins, M., 2006. Erodibility and erosion patterns of mudflat sediments investigated using an annular flume. *Aquatic Ecology* 40 (4), 543-554.
- Nolte, S., Koppenaar, E.C., Esselink, P., Dijkema, K.S., Schuerch, M., De Groot, A.V., Bakker, J.P., Temmerman, S., 2013. Measuring sedimentation in tidal marshes: a review on methods and their applicability in biogeomorphological studies. *Journal of Coastal Conservation* 17 (3), 301-325.
- Nortek AS, 2005. *Vector Current Meter User Manual*, Norway, p. 15.
- O'Brien, D.J., Whitehouse, R.J.S., Cramp, A., 2000. The cyclic development of a macrotidal mudflat on varying timescales. *Continental Shelf Research* 20 (12-13), 1593-1619.
- O'Connor, B.A., Yoo, D., 1988. Mean bed friction of combined wave/current flow. *Coastal Engineering* 12 (1), 1-21.
- O'Shea, M., Murphy, J., 2013. Predicting and Monitoring the Evolution of a Coastal Barrier Dune System Postbreaching. *Journal of Coastal Research* 29 (6A), 38-50.
- Ogston, A.S., Cacchione, D.A., Sternberg, R.W., Kineke, G.C., 2000. Observations of storm and river flood-driven sediment transport on the northern California continental shelf. *Continental Shelf Research* 20 (16), 2141-2162.
- Palanques, A., de Madron, X.D., Puig, P., Fabres, J., Guillen, J., Calafat, A., Canals, M., Heussner, S., Bonnin, J., 2006. Suspended sediment fluxes and transport processes in the Gulf of Lions submarine canyons. The role of storms and dense water cascading. *Marine Geology* 234 (1-4), 43-61.

- Paphitis, D., Collins, M.B., 2005. Sand grain threshold, in relation to bed 'stress history': an experimental study. *Sedimentology* 52 (4), 827-838.
- Partheniades, E.A., 1965. Erosion and Deposition of Cohesive Soils. *World Journal of Biological Psychiatry the Official Journal of the World Federation of Societies of Biological Psychiatry* 2 (4), 190-192.
- Paterson, D.M., Tolhurst, T.J., Kelly, J.A., Honeywill, C., de Deckere, E., Huet, V., Shayler, S.A., Black, K.S., de Brouwer, J., Davidson, I., 2000. Variations in sediment properties, Skeffling mudflat, Humber Estuary, UK. *Continental Shelf Research* 20 (10-11), 1373-1396.
- Pejrup, M., 1988. Suspended sediment transport across a tidal flat. *Marine Geology* 82 (3-4), 187-198.
- Postma, H., 1961. Transport and accumulation of suspended matter in the Dutch Wadden Sea. *Netherlands Journal of Sea Research* 1 (1), 148-190.
- Quaresma, V.d.S., Bastos, A.C., Amos, C.L., 2007. Sedimentary processes over an intertidal flat: A field investigation at Hythe flats, Southampton Water (UK). *Marine Geology* 241 (1-4), 117-136.
- Riethmüller, R., Heineke, M., Kühl, H., Keuker-Rüdiger, R., 2000. Chlorophyll a concentration as an index of sediment surface stabilisation by microphytobenthos? *Continental Shelf Research* 20 (10-11), 1351-1372.
- Riggs, S.R., Ambrose, W.G., Cook, J.W., Snyder, S.W., 1998. Sediment production on sediment-starved continental margins: The interrelationship between hardbottoms, sedimentological and benthic community processes, and storm dynamics. *Journal of Sedimentary Research* 68 (1), 155-168.
- Salehi, M., Strom, K., 2012. Measurement of critical shear stress for mud mixtures in the San Jacinto estuary under different wave and current combinations. *Continental Shelf Research* 47, 78-92.
- Sanchez-Arcilla, A., Jimenez, J.A., Valdemoro, H.I., 1998. The Ebro delta: Morphodynamics and vulnerability. *Journal of Coastal Research* 14 (3), 754-772.
- Sarmiento, G.N.R., Cipolletti, M.P., Perillo, M.M., Delrieux, C.A., Perillo, G.M.E., 2016. Methodology for classification of geographical features with remote sensing images: Application to tidal flats. *Geomorphology* 257, 10-22.
- Saulter, A.N., Russell, P.E., Gallagher, E.L., Miles, J.R., 2003. Observations of bed level change in a saturated surf zone. *Journal of Geophysical Research-Oceans* 108 (C4).
- Schünemann, M., Kühl, H., 1993. Experimental Investigations of the Erosional Behavior of Naturally Formed Mud from the Elbe Estuary and Adjacent Wadden Sea, Germany. *Nearshore & Estuarine Cohesive Sediment Transport* (1-2), 314-330.
- Schoellhamer, D.H., Mumley, T.E., Leatherbarrow, J.E., 2007. Suspended sediment and sediment-associated contaminants in San Francisco Bay. *Environmental Research* 105 (1), 119-131.

- Sea-Bird Electronics, I., 2007. SBE 26plus Seagauge wave and tide recorder operating manual, Washington, USA, pp. 5; 92.
- Shi, B., Wang, Y.P., Du, X., Cooper, J.R., Li, P., Li, M.L., Yang, Y., 2016. Field and theoretical investigation of sediment mass fluxes on an accretional coastal mudflat. *Journal of Hydro-Environment Research* 11, 75-90.
- Shi, B.W., Wang, Y.P., Yang, Y., Li, M.L., Li, P., Ni, W.F., Gao, J.H., 2015. Determination of Critical Shear Stresses for Erosion and Deposition Based on In Situ Measurements of Currents and Waves over an Intertidal Mudflat. *Journal of Coastal Research* 31 (6), 1344-1356.
- Shi, B.W., Yang, S.L., Wang, Y.P., Bouma, T.J., Zhu, Q., 2012. Relating accretion and erosion at an exposed tidal wetland to the bottom shear stress of combined current-wave action. *Geomorphology* 138, 380-389.
- Shi, Z., 2001. Observations of fluid mud in the deepwater navigational channel of Hangzhou Bay. *Marine Science Bulletin* 20 (6), 40 - 50.
- Shi, Z., Chen, J.Y., 1996. Morphodynamics and sediment dynamics on intertidal mudflats in China (1961-1994). *Continental Shelf Research* 16 (15), 1909-1926.
- Shields, A., 1936. Application of similarity principles and turbulence research to bed-load movement (English translation of the original German manuscript). Hydrodynamic Laboratory, California Institute of Technology, Pub. No. 167.
- Siadatmousavi, S.M., Jose, F., 2015. Winter storm-induced hydrodynamics and morphological response of a shallow transgressive shoal complex: Northern Gulf of Mexico. *Estuarine Coastal and Shelf Science* 154, 58-68.
- Sontek, 1996. Acoustic Doppler Profiler (ADP) Principles of Operation. Sontek technical notes, San Diego, CA.
- Soulsby, R., Humphery, J., 1990. Field observations of wave-current interaction at the sea bed, *Water wave kinematics*. Springer, pp. 413-428.
- Soulsby, R.L., 1980. Selecting record length and digitization rate for near-bed turbulence measurements. *Journal of Physical Oceanography* 10 (2), 208-219.
- Soulsby, R.L., 2005. Bed shear-stresses under combined waves and currents on smooth and rough beds., HR Wallingford Report
- Stapleton, K., Huntley, D., 1995. Seabed stress determinations using the inertial dissipation method and the turbulent kinetic energy method. *Earth Surface Processes and Landforms* 20 (9), 807-815.
- Su, J.L., Wang, K.S., 1989. Changjiang river plume and suspended sediment transport in Hangzhou Bay. *Continental Shelf Research* 9 (1), 93-111.
- Su, M., Yao, P., Wang, Z.B., Chen, Y.P., Zhang, C.K., Stive, M.J.F., 2015. Laboratory studies on the response of fine sediment to wind, IAHR World Congress 2015. IHAR, the Netherlands.
- Taki, K., 2001. Critical shear stress for cohesive sediment transport. In: McAnally, W.H.,

- Mehta, A.J. (Eds.), Coastal and Estuarine Fine Sediment Processes. Elsevier Science, pp. 53–61.
- Thornton, E.B., Swayne, J.L., Dingler, J.R., 1998. Small-scale morphology across the surf zone. *Marine Geology* 145, 173-196.
- te Slaa, S., van Maren, D.S., He, Q., Winterwerp, J.C., 2015. Hindered Settling of Silt. *Journal of Hydraulic Engineering* 141 (9), 13.
- Teisson, C., Ockenden, M., Le Hir, P., Kranenburg, C., Hamm, L., 1993. Special Issue Coastal Morphodynamics: Processes and Modelling Cohesive sediment transport processes. *Coastal Engineering* 21 (1), 129-162.
- Temmerman, S., Meire, P., Bouma, T.J., Herman, P.M.J., Ysebaert, T., De Vriend, H.J., 2013. Ecosystem-based coastal defence in the face of global change. *Nature* 504 (7478), 79-83.
- Thompson, C.E.L., Couceiro, F., Fones, G.R., Helsby, R., Amos, C.L., Black, K., Parker, E.R., Greenwood, N., Statham, P.J., Kelly-Gerreyn, B.A., 2011. In situ flume measurements of resuspension in the North Sea. *Estuarine Coastal and Shelf Science* 94 (1), 77-88.
- Thorne, P.D., Agrawal, Y.C., Cacchione, D.A., 2007. A comparison of near-bed acoustic backscatter and laser diffraction measurements of suspended sediments. *Ieee Journal of Oceanic Engineering* 32 (1), 225-235.
- Thornton, E.B., Swayne, J.L., Dingler, J.R., 1998. Small-scale morphology across the surf zone. *Marine Geology* 145 (3-4), 173-196.
- Tolhurst, T.J., Black, K.S., Shayler, S.A., Mather, S., Black, I., Baker, K., Paterson, D.M., 1999. Measuring the in situ erosion shear stress of intertidal sediments with the Cohesive Strength Meter (CSM). *Estuarine Coastal and Shelf Science* 49 (2), 281-294.
- Townsend, F., McVay, M., 1990. SOA: Large Strain Consolidation Predictions. *Journal of Geotechnical Engineering* 116 (2), 222-243.
- Traykovski, P., Geyer, W.R., Irish, J.D., Lynch, J.F., 2000. The role of wave-induced density-driven fluid mud flows for cross-shelf transport on the Eel River continental shelf. *Continental Shelf Research* 20 (16), 2113-2140.
- Tucker, M.J., Pitt, E.G., 2001. *Waves in ocean engineering*. Elsevier ocean engineering book series vol. 5, Elsevier, Amsterdam.
- Turner, I.L., Russell, P.E., Butt, T., 2008. Measurement of wave-by-wave bed-levels in the swash zone. *Coastal Engineering* 55 (12), 1237-1242.
- Uncles, R.J., Stephens, J.A., Harris, C., 1998. Seasonal variability of subtidal and intertidal sediment distributions in a muddy, macrotidal estuary: the Humber-Ouse, UK, in: Black, K.S., Paterson, D.M., Cramp, A. (Eds.), *Sedimentary Processes in the Intertidal Zone*. Geological Society, London, pp. 211-220.
- van Kessel, T., Kranenburg, C., 1998. Wave-induced liquefaction and flow of subaqueous mud layers. *Coastal Engineering* 34 (1-2), 109-127.

- van Ledden, M., 2003. Sand-mud segregation in estuaries and tidal basins, Civil Engineering and Geosciences. Delft University of Technology, the Netherlands.
- van Maren, D.S., Winterwerp, J.C., Wang, Z.Y., Pu, Q., 2009. Suspended sediment dynamics and morphodynamics in the Yellow River, China. *Sedimentology* 56 (3), 785-806.
- van Prooijen, B.C., Monserrat, F., Herman, P.M.J., 2011. A process-based model for erosion of Macoma balthica-affected mud beds. *Continental Shelf Research* 31 (6), 527-538.
- van Prooijen, B.C., Winterwerp, J.C., 2010. A stochastic formulation for erosion of cohesive sediments. *Journal of Geophysical Research-Oceans* 115, 15.
- van Rijn, L.C., 1993. Principles of sediment transport in rivers, estuaries and coastal seas. Aqua Publication, Amsterdam, the Netherlands.
- Van Straaten, L., Kuenen, P.H., 1958. Tidal action as a cause of clay accumulation. *Journal of Sedimentary Research* 28 (4).
- Verney, R., Brun-Cottan, J.C., Lafite, R., Deloffre, J., Taylor, J.A., 2006. Tidally-induced shear stress variability above intertidal mudflats in the macrotidal Seine estuary. *Estuaries and Coasts* 29 (4), 653-664.
- Villaret, C., Latteux, B., 1992. Long-term simulation of cohesive sediment bed erosion and deposition by tidal currents. Long-term simulation of cohesive sediment bed erosion and deposition by tidal currents, 19 pp.
- Voulgaris, G., Trowbridge, J.H., 1998. Evaluation of the acoustic Doppler velocimeter (ADV) for turbulence measurements. *Journal of Atmospheric and Oceanic Technology* 15, 272-289.
- Walling, D.E., 2006. Human impact on land-ocean sediment transfer by the world's rivers. *Geomorphology* 79 (3-4), 192-216.
- Walstra, D.J.R., Ruessink, B.G., Reniers, A., Ranasinghe, R., 2015. Process-based modeling of kilometer-scale alongshore sandbar variability. *Earth Surface Processes and Landforms* 40 (8), 995-1005.
- Wang, A.J., 2009. Environmental dynamic processes of coastal salt marsh wetlands. PhD thesis, Nanjing University, Nanjing, China. (in Chinese)
- Wang, A.J., Gao, S., Jia, J.J., Pan, S.M., 2005. Contemporary sedimentation rates on salt marshes at Wanggang, Jiangsu, China. *Acta Geographica Sinica* 60 (1), 61-70. (in Chinese)
- Wang, H., Yang, Z., Saito, Y., Liu, J.P., Sun, X., Wang, Y., 2007. Stepwise decreases of the Huanghe (Yellow River) sediment load (1950-2005): Impacts of climate change and human activities. *Global and Planetary Change* 57 (3-4), 331-354.
- Wang, Y.P., Gao, S., Jia, J., Thompson, C.E.L., Gao, J., Yang, Y., 2012. Sediment transport over an accretional intertidal flat with influences of reclamation, Jiangsu coast, China. *Marine Geology* 291, 147-161.

- Wang, Y.P., Gao, S., Jia, J.J., 2006. High-resolution data collection for analysis of sediment dynamic processes associated with combined current-wave action over intertidal flats. *Chinese Science Bulletin* 51 (7), 866-877.
- Wang, Y.P., Voulgaris, G., Li, Y., Yang, Y., Gao, J.H., Chen, J., Gao, S., 2013. Sediment resuspension, flocculation, and settling in a macrotidal estuary. *Journal of Geophysical Research-Oceans* 118 (10), 5591-5608.
- Wang, Y.P., Zhang, R.S., Gao, S., 1999. Geomorphic and hydrodynamic responses in salt marsh-tidal creek systems, Jiangsu, China. *Chinese Science Bulletin* 44 (6), 544-549.
- Wang, Y.Y., 2007. The Observations and Models of Bottom Boundary Layer for Fine Sediment, PhD thesis, State Key Laboratory of Estuarine and Coastal Research. East China Normal University, Shanghai, China. (in Chinese)
- Wang, Z., Van Maren, D., Ding, P., Yang, S., Van Prooijen, B., De Vet, P., Winterwerp, J., De Vriend, H., Stive, M., He, Q., 2015. Human impacts on morphodynamic thresholds in estuarine systems. *Continental Shelf Research* 111 (Part B), 174-183.
- Warner, J.C., Sherwood, C.R., Signell, R.P., Harris, C.K., Arango, H.G., 2008. Development of a three-dimensional, regional, coupled wave, current, and sediment-transport model. *Computers & Geosciences* 34 (10), 1284-1306.
- Webster, K.L., Ogston, A.S., Nittrouer, C.A., 2013. Delivery, reworking and export of fine-grained sediment across the sandy Skagit River tidal flats. *Continental Shelf Research* 60, S58-S70.
- Webster, P.J., Holland, G.J., Curry, J.A., Chang, H.R., 2005. Changes in tropical cyclone number, duration, and intensity in a warming environment. *Science* 309 (5742), 1844-1846.
- Weerman, E.J., Herman, P.M.J., Van de Koppel, J., 2011. Top-down control inhibits spatial self-organization of a patterned landscape. *Ecology* 92 (2), 487-495.
- Weerman, E.J., Van Belzen, J., Rietkerk, M., Temmerman, S., Kefi, S., Herman, P.M.J., Van de Koppel, J., 2012. Changes in diatom patch-size distribution and degradation in a spatially self-organized intertidal mudflat ecosystem. *Ecology* 93 (3), 608-618.
- Whitehouse, R., 2000. Comparison of mud tested at HR Wallingford – erosional/depositional properties determined in laboratory test, in: *muds_test_HRWallingford* (Ed.), *Dynamics of estuarine muds: a manual for practical applications*. Thomas Telford, Victoria.
- Whitehouse, R., Soulsby, R., Roberts, W., Mitchener, H., 2000. *Dynamics of estuarine muds: A manual for practical applications*. Tomas Telford Limited, 1 Heron Quay, London.
- Wiberg, P.L., Sherwood, C.R., 2008. Calculating wave-generated bottom orbital velocities from surface-wave parameters. *Computers & Geosciences* 34 (10), 1243-1262.

- Widdows, J., Brinsley, M.D., Bowley, N., Barrett, C., 1998. A benthic annular flume for in situ measurement of suspension feeding/biodeposition rates and erosion potential of intertidal cohesive sediments. *Estuarine Coastal and Shelf Science* 46 (1), 27-38.
- Widdows, J., Brown, S., Brinsley, M.D., Salkeld, P.N., Elliott, M., 2000. Temporal changes in intertidal sediment erodability: influence of biological and climatic factors. *Continental Shelf Research* 20 (10-11), 1275-1289.
- Wilkinson, R., 1985. Variation of roughness length of a mobile sand bed in a tidal flow. *Geo-Marine Letters* 5 (4), 231-239.
- Williams, H.F.L., Hamilton, T.S., 1995. Sedimentary dynamics of an eroding tidal marsh derived from stratigraphic records of ¹³⁷Cs fallout, Fraser Delta, British Columbia, Canada. *Journal of Coastal Research* 11 (4), 1145-1156.
- Williams, J.J., Bell, P.S., Thorne, P.D., 2003. Field measurements of flow fields and sediment transport above mobile bed forms. *Journal of Geophysical Research-Oceans* 108 (C4), 36.
- Willmott, C.J., 1981. On the validation of models. *Physical geography* 2 (2), 184-194.
- Willmott, C.J., Ackleson, S.G., Davis, R.E., Feddema, J.J., Klink, K.M., Legates, D.R., O'Donnell, J., Rowe, C.M., 1985. Statistics for the evaluation and comparison of models. *Journal of Geophysical Research: Oceans* 90 (C5), 8995-9005.
- Willows, R.I., Widdows, J., Wood, R.G., 1998. Influence of an infaunal bivalve on the erosion of an intertidal cohesive sediment: A flume and modeling study. *Limnology and Oceanography* 43 (6), 1332-1343.
- Winterwerp, J.C., 2007. On the sedimentation rate of cohesive sediment, in: J.P.Y. Maa, L.P.S., Schoellhamer, D.H. (Eds.), *Proceedings in Marine Science*. Elsevier, pp. 209-226.
- Winterwerp, J.C., van Kesteren, W.G.M., 2004. *Introduction to the Physics of Cohesive Sediment Dynamics in the Marine Environment*. Elsevier Science, Amsterdam, The Netherlands.
- Winterwerp, J.C., van Kesteren, W.G.M., van Prooijen, B., Jacobs, W., 2012. A conceptual framework for shear flow-induced erosion of soft cohesive sediment beds. *Journal of Geophysical Research-Oceans* 117, 17.
- Wright, L.D., Wiseman, W.J., Bornhold, B.D., Prior, D.B., Suhayda, H.N., Keller, G.H., Yang, Z.S., Fan, Y.B., 1988. Marine dispersal and deposition of Yellow River silts by gravity-driven underflows. *Nature* 332 (6165), 629-632.
- Wright, S.W., Jeffrey, S.W., Mantoura, R.F.C., Llewellyn, C.A., Bjornland, T., Repeta, D., Welschmeyer, N., 1991. Improved HPLC method for the analysis of chlorophylls and carotenoids from marine phytoplankton. *Marine Ecology-progress Series* 77, 183-196.
- Xu, K., Mickey, R.C., Chen, Q., Harris, C.K., Hetland, R.D., Hu, K., Wang, J., 2015. Shelf sediment transport during hurricanes Katrina and Rita. *Computers &*

- Geosciences 8 (26).
- Xue, Y.Z., He, Q., Wang, Y.Y., 2004. The method and application of OBS in the measurement of sediment concentration. *Journal of Sediment Research* (4), 56-60.
- Yang, B.C., Dalrymple, R.W., Chun, S.S., 2005a. Sedimentation on a wave-dominated, open-coast tidal flat, south-western Korea: summer tidal flat-winter shoreface. *Sedimentology* 52 (2), 235-252.
- Yang, S.L., 1991. Impact of wind driven wave on short-period erosion of tidal flat. *Marine Sciences* 3 (2), 59 - 64. (in Chinese)
- Yang, S.L., Ding, P.X., Chen, S.L., 2001. Changes in progradation rate of the tidal flats at the mouth of the Changjiang (Yangtze) River, China. *Geomorphology* 38 (1-2), 167-180.
- Yang, S.L., Friedrichs, C.T., Shi, Z., Ding, P.X., Zhu, J., Zhao, Q.Y., 2003. Morphological response of tidal marshes, flats and channels of the outer Yangtze River mouth to a major storm. *Estuaries* 26 (6), 1416-1425.
- Yang, S.L., Li, H., Ysebaert, T., Bouma, T.J., Zhang, W.X., Wang, Y., Li, P., Li, M., Ding, P., 2008. Spatial and temporal variations in sediment grain size in tidal wetlands, Yangtze Delta: On the role of physical and biotic controls. *Estuarine Coastal and Shelf Science* 77 (4), 657-671.
- Yang, S.L., Li, M., Dai, S.B., Liu, Z., Zhang, J., Ding, P.X., 2006. Drastic decrease in sediment supply from the Yangtze River and its challenge to coastal wetland management. *Geophysical Research Letters* 33 (6).
- Yang, S.L., Li, P., Gao, A., Zhang, J., Zhang, W.X., Li, M., 2007. Cyclical variability of suspended sediment concentration over a low-energy tidal flat in Jiaozhou Bay, China: effect of shoaling on wave impact. *Geo-Marine Letters* 27 (5), 345-353.
- Yang, S.L., Milliman, J.D., Li, P., Xu, K., 2011. 50,000 dams later: Erosion of the Yangtze River and its delta. *Global and Planetary Change* 75 (1-2), 14-20.
- Yang, S.L., Shi, B.W., Bouma, T.J., Ysebaert, T., Luo, X.X., 2012. Wave Attenuation at a Salt Marsh Margin: A Case Study of an Exposed Coast on the Yangtze Estuary. *Estuaries and Coasts* 35 (1), 169-182.
- Yang, S.L., Zhang, J., Zhu, J., Smith, J.P., Dai, S.B., Gao, A., Li, P., 2005b. Impact of dams on Yangtze River sediment supply to the sea and delta intertidal wetland response. *Journal of Geophysical Research-Earth Surface* 110 (F3).
- Ysebaert, T., Herman, P.M.J., Meire, P., Craeymeersch, J., Verbeek, H., Heip, C.H.R., 2003. Large-scale spatial patterns in estuaries: estuarine macrobenthic communities in the Schelde estuary, NW Europe. *Estuarine Coastal and Shelf Science* 57 (1-2), 335-355.
- Yu, Z.Y., Lou, F., 2004. The evolvement characteristics of Nanhuizui foreland in the Changjiang Estuary, China. *Acta Oceanologica Sinica* 26 (3), 47-53. (in Chinese)
- Zhang, S.R., Lu, X.X., Higgitt, D.L., Chen, C.T.A., Han, J.T., Sun, H.G., 2008. Recent

- changes of water discharge and sediment load in the Zhujiang (Pearl River) Basin, China. *Global and Planetary Change* 60 (3-4), 365-380.
- Zhao, C.H., Zhu, Z.H., Zhou, D.Z., 2000. *Worldwide Rivers and Dams*. China Water & Power Press, Beijing. (in Chinese)
- Zhou, Z., van der Wegen, M., Jagers, B., Coco, G., 2016. Modelling the role of self-weight consolidation on the morphodynamics of accretional mudflats. *Environmental Modelling & Software* 76, 167-181.
- Zhu, H., Yun, C., Mao, Z., Wang, S., 1988. Characteristics and empirical relationships of wind generated wave in the Changjiang Estuary., in: Chen, J., Shen, H., Yun, C. (Eds.), *Processes of Dynamics and Geomorphology of the Changjiang Estuary*. Shanghai Scientific and Technological Press, Shanghai, pp. 166-177. (in Chinese)
- Zhu, Q., Yang, S., Ma, Y., 2014. Intra-tidal sedimentary processes associated with combined wave–current action on an exposed, erosional mudflat, southeastern Yangtze River Delta, China. *Marine Geology* 347, 95-106.

Notations

a	Slope of $U_{sc} - U_z$ regression
a_i	Coefficient in Equation (7.2) ($i=1, 2, 3, 4$)
A	Slope of $\bar{U}_c(z) - \ln(z)$ regression
\hat{A}_δ	Peak orbital excursion
b	Intercept of $U_{sc} - U_z$ regression
B	Intercept of $\bar{U}_c(z) - \ln(z)$ regression
c	Suspended sediment concentration
c_b	Near bed suspended sediment concentration
c_{gel}	Gelling concentration
C_i	Constant in τ_c calculation using TKE and TKEw method ($i=1, 2$)
C_D	Drag coefficient
D	Deposition rate
D_{50}	Median grain size of sediment particles
D_*	Dimensionless particle size
E	Erosion rate
f	Frequency
f_w	Wave-related friction coefficient
g	Gravity acceleration
h	Water depth
H	Wave height
H_r	Ripple height
H_s	Significant wave height
I	Index of agreement
k	Wave number
L	Wave length
L_r	Ripple length
M	Erosion rate coefficient
Q_s	Suspended sediment flux / Suspended sediment transport per unit width
r	Relative bed roughness
Re_w	Wave-related Reynolds number

s	Effective density, $s = \rho_s / \rho_w - 1$
t	Turbidity
T	Wave period
T_r	Ripple period
T_s	Significant wave period
T_0	Time when $t=0$
u, v, w	East, north, and up component of instantaneous velocity
u_m, v_m, w_m	Mean components of east, north, and up velocities
u_w, v_w, w_w	Wave-orbital-motion components of east, north, and up velocities
u_t, v_t, w_t	Turbulent fluctuating components of east, north, and up velocities
\bar{U}_c	Burst-mean horizontal current speed
\hat{U}_δ	Peak orbital velocity
U_{*c}	Friction velocity
V_r	Ripple migration rate
W	Water content
x, y	Parameters in index of agreement
z	Vertical coordinate
z_0	Bed roughness length
β	Coefficient in Equation (3.1) and Equation (7.9)
η	Bed level
θ	Shields parameter
θ_e	Critical Shields parameter for sediment entrainment
κ	Von Kármán's constant
ν	Kinematic viscosity
ρ_s	Sediment density
ρ_w	Sea water density
τ_d	Critical bed shear stress for deposition
τ_e	Critical bed shear stress for erosion
τ_c	Current induced bed shear stress
τ_w	Wave induced bed shear stress
τ_{cw}	Total bed shear stress due to combined wave–current action
τ_m	Wave-cycle averaged total bed shear stress
ϕ_c	Current direction
ϕ_w	Wave direction
ϕ_{cw}	Angle between wave and current directions
ω	Angular velocity
ω_s	Settling velocity
$\omega_{s,0}$	Settling velocity of individual aggregates
ω_{50}	Group settling velocity

Abbreviations

ADCP	Acoustic Doppler Current Profiler
ADV	Acoustic Doppler Velocity meter
ASM	Argus Surface Meter
BLC	Bed-Level Change
BP	Buried-Plate method
ECMWF	European Centre for Medium-range Weather Forecasts
EPS	Extracellular Polymetric Substances
HPLC	High-Performance Liquid Chromatography
ID	Inertial Dissipation
LAT	Lowest Astronomic tide
LP	Logarithmic Profile
MHW	Mean High Water level
MLW	Mean Low Water level
MNHWL	Mean Neap High Water Level
MNLWL	Mean Neap Low Water Level
MSHWL	Mean Spring High Water Level
MSLWL	Mean Spring Low Water Level
MSL	Mean Sea Level
NAP	Normaal Amsterdam Peil (Dutch)
OBS	Optical Back-Scatter sensor
PCADP	Pulse-Coherent Acoustic Doppler Profiler
RS	Reynolds Stress
RTK-GPS	Real-Time Kinematic Global Positioning System
SSC	Suspended sediment concentration
TKE	Turbulent Kinetic Energy
WCI	Wave–Current Interaction

Acknowledgements

This dissertation was supported by a bilateral agreement between Delft University of Technology (TUD) and East China Normal University (ECNU). The training and Doctoral Education took place under the joint supervision and responsibility of the two universities. Following financial sponsorships are acknowledged: the Natural Science Foundation of China (NSFC; 41130856, 41576092, 51320105005, 41071014), the NSFC-Shandong Joint Fund for Marine Science Research Centers (U1606401), the Chinese Scholarship Council (CSC), Royal Dutch Academy of Science and Arts (NWO-JSTP: 842.00.007, NWO-PSA: 08-PSA-E-001/2008DFB90240), and “Het Lamminga Fonds”.

What I harvest at the end of PhD is more than this dissertation. Heartfelt thanks go to all the people who have supported me and helped me during my PhD.

First of all, I would like to thank my promotors, prof. Shi Lun Yang and prof. Zheng Bing Wang. They both affected me profoundly by their extensive knowledge, strict attitude in research and passion in their scientific career. Prof. Yang directed me to the field of geoscience. He has provided guidance, trust and patience throughout my whole PhD life. My scientific habitat has been established by his inspiration and requirements on every detail. In addition, the field campaigns would not be successful without his nearly-40-year experience that he has shared. Prof. Wang has made me move forward by his constructive suggestions when I encountering difficulties. I still remember that in the first talk with him, he provided his idea to the problem which I had struggled for a long time.

My sincere gratitude also goes to my co-promotor Bram van Prooijen for his supervision, encouragement and consideration. He enabled me to pursue the research in TUD, and has helped dealing with the administration documents. The structures and details of the papers and this thesis are confirmed after countless meetings with him. Bram also helps me with translating the propositions and long abstract into Dutch. His enthusiasm to both research and daily life has made a lot of fun during my staying in the

Netherlands.

I also want to thank my advisors prof. Shenliang Chen and prof. Zhijun Dai from SKLEC for their professional suggestions on the thesis and the proposal. Prof. Yaping Wang from Nanjing University is acknowledged for his professional suggestion in thesis review. I thank Dr. Kehui Xu and Dr. Yanxia Ma from Louisiana State University for their advices to part of Chapters 3 and 4.

Special thanks are given to the head of TUD-CiTG prof. Marcel Stive, and heads of SKLEC prof. Pingxing Ding and prof. Yunxuan Zhou, who facilitated the dual-degree agreement. It is a great honour to be the first one benefit from this agreement, which is also under the efforts of administration departments (e.g., Rector Offices, Graduate Schools and International Offices) of the two universities. The Vice Rector Peter Wieringa of TUD, the director of ECNU International Exchange Division, Yunxuan Zhou, and prof. Xiuzhen Li from SKLEC are acknowledged for their support to this agreement.

I greatly acknowledge SKLEC which is a platform that allows chances and good resources. Thank prof. Shu Gao, prof. Qing He, prof. Weiguo Zhang, prof. Jianrong Zhu and all the other teachers for sharing their knowledge and comments in my research career. Thank Ping Wang, Shi'en Yu, Guo'an Zhang, Di Hua, Wei Li, Junhong Li, Can Jin, Xiaoli Huo, Li Tan and Hong Jiang for their administrative support. Thank Dr. Wenxiang Zhang for his help and useful discussion in field work, research and daily life; thank Yuanzhong Xue and Jinghua Gu for their help in instrument use; thank Ruiming Wu and Lingxiang Wang for their technical support. Special thank goes to my lovely 425 officemates: Benwei Shi for his introducing me to the tidal flat research; Peng Li, Xiangxin Luo, Chuangshou Wu, Jianhua Liu, Longhao Yan, Zhen Zhang, Yanpig Chen, Yingwen Liu and Yajuan Li for sharing their experience in graduate study and research; Chaoyang Zhang, Haifeng He, Xiaoya Zhang, Han Wu, Qing Tian, Rusheng Wang, Yefeng Lu, Haifei Yang, Limin Miao, Qiang Zhu, Tian Yang, Haobing Wang, Saisai Zhang, and Jiqing Fan for their accompany in everyday life and support in experiments. Thank the SKLEC students with whom I had a lot of fun in these years.

I indeed would like to thank many nice colleagues at TUD. My sincere gratitude goes to Han, Wim, Claire, Cynthia, Steven, Hong, Miguel, Clara, Mohamed, Shahid, Andres, Joris and many other Water Labers for creating an academic and friendly atmosphere. Special thank goes to my officemate Cynthia Maan for a lot of useful discussions and making me enjoy rather than survive in the Netherlands. I also thank the following faculty colleagues in an incomplete list: Zhan Hu, Saulo Meirelles, Xuexue Chen, Min Su, Peng Yao, Mariette van Tilburg, Gensheng Zhao, Ao Chu, Qian Ke, Victor Chavarrías, Wei Li, Lixia Niu, Peng Dai, Dongju Wu, Ronald Brouwer; Xuedong Zhang, Xin Tian, and Feifei Wang for every discussion and joyous moment with you. Thank Marcel Zijlema and Pieter Smit for their help in SWASH. Thank CICAT, University and Faculty Graduate Schools for their administrative support.

One-year life in Yerseke was also unforgettable. Thank the staffs in Spatial Ecology Department of NIOZ for letting me know the world of ecologists. Thank prof. Peter Herman, prof. Tjeerd Bouma and prof. Johan van de Koppel for letting me join the department discussion. Thank Christian Schwarz, Quanxing Liu, Tisja Dagggers for their fruitful discussion related to ecology. Thank Bas and Jos for sharing a lot of practical knowledge of field work. Thank Lennart van IJzerloo and Jurian Brasser for their assistant in the Kapellebank experiment. Thank the administrative staff in NIOZ-Yerseke for taking care of my accommodation and administration affairs in NIOZ and the guest house De Kêête. Thank all those lovely De Kêêeters. I am afraid that I can't name you all here, because it might use more than half a page. I pretty enjoyed the parties, dinners, beers, movies and games with you. Special thanks to the Chinese friends in Yerseke: Zhigang Ma, Hui Cheng, Haobing Cao, Ronghua Wang, Jianwei Zhang, Haoxin Fan, Hui Qi, Zhuo Xu, Nanyang Chu, Tao Hong and Jiaguo Yan. I felt much less homesickness with your company. Thank Maomao and Norbert for their hospitality and taking care me when I got hurt.

Finally, I want to express my deep gratitude to my family and family-in-law for your support and every happy moment you are with me. 感谢父母对我无微不至的关心，你们的支持是我努力前进的最大动力。独生子女在外求学经常忽略你们的感受，希望今后能对你们多一些陪伴。Thank you Zhenchang, you are not only a good husband in daily life, but also a best mate in academic research. It is wonderful to meet you in my life!



Qin Zhu
at Yerseke, the Netherlands

January 31st, 2017

List of publications

Journal articles

- Zhu, Q.**, van Prooijen, B.C., Maan, D.C., Wang, Z.B., Dagers, T., Yang, S.L., 2017. Cross-shore and vertical variability of mudflat erodibility: An integrated approach of in situ measurements and modelling. (Submitted)
- Zhu, Q.**, van Prooijen, B.C., Wang, Z.B., Yang, S.L., 2017. Bed-level changes on intertidal wetland in response to waves and tides: A case study from the Yangtze River Delta. *Marine Geology*, 385: 160-172.
- Zhu, Z., van Belzen, J., Chu, N., **Zhu, Q.**, Ysebaert, T., Herman, P.J.M., Bouma, T., 2016. Climate-change intensified wave forcing risks the meltdown of coastal seed banks. (Submitted)
- Zhu, Q.**, van Prooijen, B.C., Wang, Z.B., Ma, Y.X., Yang, S.L., 2016. Bed shear stress estimation on an open intertidal flat using in situ measurements. *Estuarine, Coastal and Shelf Science*, 182 (Part A): 190-201.
- Zhang, W.X., **Zhu, Q.**, Hu, J., Gu, J.H., Yang, S.L., 2015. Experimental Study of the Multifrequency Acoustic Backscatter System using Field Sediment. *Universal Journal of Geoscience*, 3: 188 - 194. doi: 10.13189/ujg.2015.030602.
- Liu, J.H., Yang, S.L., **Zhu, Q.**, Zhang, J., 2014. Controls on suspended sediment concentration profiles in the shallow and turbid Yangtze Estuary. *Continental Shelf Research*, 90: 96-108.
- Zhu, Q.**, Yang, S., Ma, Y., 2014. Intra-tidal sedimentary processes associated with combined wave–current action on an exposed, erosional mudflat, southeastern Yangtze River Delta, China. *Marine Geology*, 347: 95-106.
- Shi, B.W., Yang, S.L., Wang, Y.P., Bouma, T.J., **Zhu, Q.**, 2012. Relating accretion and erosion at an exposed tidal wetland to the bottom shear stress of combined current-wave action. *Geomorphology*, 138: 380-389.
- Miao, L.M., Yang, S.L., **Zhu, Q.**, Shi, B.W., Li, P., Wu, C.S., 2016. Variations of suspended sediment concentrations and transport in response to a storm and its dynamic mechanism—A study case of Nanhui tidal flat of the Yangtze River Delta.

Acta Ocenologia Sinica, 38 (5), 158-167. (in Chinese)

Liu, J.H., Chen, S.L., Yang, S.L., **Zhu, Q.**, 2014. Study on the change of suspended sediment concentration during tidal cycle and its dynamic mechanism near the Changjiang Estuary. *Advances in Marine Science*, 31(2): 188-199. (in Chinese)

Conference proceedings, abstracts and talks

First author:

Zhu, Q., van Prooijen, B.C., Maan, D.C, Yang, S.L., 2015. High resolution bed level changes on an intertidal mudflat. *13th International Conference on Cohesive Sediment Transport Processes*, 7–11 September 2015, Leuven, Belgium, poster.

Zhu, Q., Yang, S.L., 2014. Multi-approach based study of bed level changes of an intertidal mudflat. *Annual conference of Chinese Society for Oceanology and Limnology*, 26–28 October 2014, Nanjing, Jiangsu, China, oral presentation. (in Chinese)

Zhu, Q., 2014. Kapellebank Campaign 2014. *China-Dutch cooperation project workshop*, 26 May 2014, TU Delft, the Netherlands, oral presentation.

Zhu, Q., S.L., Yang, 2013. Morphodynamics on an exposed intertidal mudflat-adjacent channel system. *AGU Fall Meeting*, 9–13 December 2013, San Francisco, California, USA, poster.

Zhu, Q., B.C. van Prooijen, 2013. Eddies in shallow mixing layers of tidal zone. *Workshop: PSA project Impact of human activities on eco-morphological development of rivers and estuaries & JSTP project Fate of future of tidal flats in estuaries*, 15–17 April 2013, TU Delft, the Netherlands, oral presentation.

Zhu, Q., van Prooijen, B.C., Yang, S.L., 2013. Intra-tidal sedimentary processes associated with combined current–wave action on an exposed, erosional mudflat. *NCK days 2013*, 16–18 March 2013, Kuikduin, the Netherlands, poster.

Zhu, Q., 2013. In situ observation of intra-tidal sedimentary processes on exposed mudflat. *Hydraulic Engineering Department Colloquium*, 9 April 2013, TU Delft, the Netherlands, oral presentation.

Co-author:

Van Prooijen, B.C., Zhu, Q., Brouwer, R.L., He, Q., 2015. Horizontal coherent structure between tidal flat and channel. *Proceedings of Coastal Sediments 2015*. 11– May 2015, San Diego, California, USA.

Zhang, W.X., Liu, J.H., **Zhu, Q.**, Yang, S.L., 2013. Study of in situ acoustic measurements

of waves. *Proceeding in 16th China Ocean Engineering symposium*, 5–7 August 2013, Dalian, China. (in Chinese)

Curriculum Vitae

Qin Zhu was born on 12th of June 1988 in Shanghai, China. She studied physics and teaching skills at Physics department of East China Normal University (ECNU) from 2006 to 2010. In June 2010, she obtained Bachelor degree of Physics. At the same year, she got the certificate for teaching in middle school.

Since September of 2010, Qin was recommended to directly continue her PhD study in Physical Geography at State Key Laboratory of Estuarine and Coastal Research (SKLEC) at ECNU, promoted by prof. dr. Shi Lun Yang. Since August of 2011, she received the funding from Chinese Scholarship Council (CSC) and became a two-year joint-educated PhD student in Department of Hydraulic Engineering at TU Delft, under the supervision of dr. ir. Bram van Prooijen and prof. dr. ir. Zheng Bing Wang. Her research topic is the sediment dynamics and erosion-deposition processes of intertidal mudflat based on *in situ* measurements and numerical modelling.